國立交通大學

材料科學與工程學系

博士論文

含氫鍵之香蕉型液晶超分子之研究
Study of Hydrogen-Bonded Banana-Shaped
Supramolucular Liquid Crystals

研究生：王怜詠 (Ling-Yung Wang)

指導教授：林宏洲 (Hong-Cheu Lin) 博士

中華民國九十八年十一月

誌謝

大家常說，要撐完整個博士班的過程非常煎熬，因為耗時甚鉅，不過這段日子終究是結束了，想起以往經常於研究中絞盡腦汁的樣子，頓時倍感有趣。在研究中燃燒生命的同時，也常想起家人不厭其煩的叮嚀，要我注意身體，做事要慢慢來，有空要回家看長輩。雖然這些轟炸式提醒我都沒做好半樣，不過回首往事，這些話卻是最讓我覺得溫馨的，也是最感動的話語，都勝過無數的加油與鼓勵。我懂你們的期待，也了解你們的關懷，再多的學術發表都無法映襯出你們對我的關愛，我想說，從今以後，你們可以以我的博士學位為榮，而我會視你們的嘮叨為最大的驕傲！四年前，我將人生第一本論文獻給了自己，四年後，我將人生求學生崖中最後一本論文獻給你們。感謝我家中偉大的爸爸、媽媽與長輩。

回到實驗室座位整理行李，偶然發現一份背面已被當作計算紙的論文，熟悉的論文內容讓我看到一個碩士班學生的影子。在那裡，任何瘋狂的想法都可以被包容被討論，賦予自由性的研究環境造就出一個對任何研究都充滿興趣的人格，也訓練出對題目設計充滿靈敏度與豐富度的學生。這論文的指導老師是任職於暨南大學的賴榮豐教授，而那熟悉的影子正是在打這串文章的我。感謝賴老師在碩士班期間帶領學生了解做研究的興趣，讓我了解對研究應有的態度與認知。也感謝碩班求學中的書報老師，他們總是期望學生能以最嚴格的姿態去閱讀論文，秉持這樣的信念，學生才能在現今做出豐碩的成果。因為你們，讓我覺得研究是一種謹慎，也是種幸福。在此對各位指導過學生的暨大老師敬上最至誠的感謝。

四年前，我放下了研究生生崖中第一顆攪拌石，四年後我將那顆已經被染到發黑的磁石收起，收拾的過程，一瓶裝了些許不純物的樣品瓶被打翻了，那正是博班實驗過程中第一個合成的產物，也是第一個合成的失敗品，一瓶帶著對新環境青澀且徬徨的回憶。我保留著它，只期望能夠記取教訓，能於博班求學過程中謹慎地對待每份被設計出來的題目。抬起頭來，回憶被忙碌於實驗室學弟妹們給打斷，實驗室裡每台旋轉濃縮機被充分的運轉著，在帶有濃厚「合成氣味」的環境裡，他們帶著期待的心，去期盼等下能做出更純的產物，好能在接下來的純化過程中偷個懶。看著他們，我微笑的將那瓶失敗品丟入了玻璃回收槽，因為我相信這絕對不是要留給你們的東西，被留下的應當是除了這本往後會被弄髒的博論外，還有我們一起奮鬥過的痕跡。在此獻上對實驗室夥伴們最熱切的祝福與期勉。(你們可以放心的拿我的瓶子去用了阿！)

實驗室的電話一如往常的常常響起，有人賊笑的拍拍被點名的夥伴，也意味著電話那彼端是我們的老闆。林宏洲老師如家父般的叮嚀總是讓學生帶著苦笑掛上電話，回想起，我也曾經這樣過，林老師提供學生一個看似輕鬆可是卻嚴格的求學環境，為有自己不斷的努力奮鬥與涉取知識，才能滿足老師的要求，這是一種恨鐵不成鋼期盼。在臨走前，記得老師還不忘叮嚀屬囑咐，教誨中，一股暖流

上心頭，謝謝老師在論文上的指導，還有英文寫作上的要求，讓我了解到寫好一篇論文應該有的態度。讓您操心了四年，除了一聲抱歉，還有更多的感謝，抱歉讓你對我的憂慮又讓白頭髮又多了一根，感謝您四年來的教導，學生會懷念再您身旁一起改論文討論研究內容的日子，這是珍貴的回憶。

　　感謝口試委員趙如蘋老師、賴重光老師、王文竹老師、徐秀福老師、陳皇銘老師，由於您們的參予可以讓學生的論文更加完善，學生永遠會記得在台上被溫馨砲轟的兩個多小時的口試，在仔細嚴屬的指導下，學生才能有機會再度了解自己的缺點，能在往後更加突破，超越自己，套句別人說過的話「即使試後會遍體麟傷，我依然會笑的很燦爛」。學生感謝趙老師與陳老師對於論文架構上的修飾，感謝徐秀福老師與賴重光老師在 X-ray 繞射實驗上的指正與教導，也感謝王文竹老師納啟發性的提問，讓學生意識到差點失去的思考靈活度，學生會在往後更加的努力，才能不辜負老師們於百忙中抽空的指導。

　　給溫柔嫻淑的千惠，多多將十一月十號拿到的學位獻予當生日禮物，感謝你這些年來的陪伴與照顧，讓我在高興、生氣、哀傷、憂愁的時候都能有最後的避風港，壓力來了，我不需要再去埔里散心，因為你就是我的開心果。你也要加油，別再替自己的懶惰找藉口囉！以後，我還想再吃你的火腿炒飯耶。

　　打下論文的最後一段，不是文章的修飾，也不再是論文的摘要，這是一種充滿對生活週遭的感謝，我很榮幸也很高興可以替四年的求學生活做這樣的結論，不是最好的，卻能讓我永遠留在心中的回憶。老爸要我在離開的時候好好感謝鎮守於交大正門的土地公，感謝祂保佑求學生活的順利，我倒是覺得，不謝天、也不謝地，因為即使生活在風大、潮濕、物價高的新竹，我還是覺得很快樂，因為有你們的陪伴，所以我不孤單。

含氫鍵之香蕉型液晶超分子之研究

學生：王怜詠　　　　　　　　　　　　　　指導教授：林宏洲

摘要

　　香蕉型(彎曲型)液晶是不具旋光中心結構卻具有光學活性(或稱對掌異構性質)的液晶材料，本研究著重於氫鍵超分子引入至彎曲型液晶結構時，所產生的液晶性質與光電性質的影響。分子設計上分為：含單雙氫鍵之香蕉型液晶超分子、氫鍵與共價鍵共聚之香蕉型側鏈液晶高分子、含氫鍵之香蕉型主鏈液晶雙/高分子，若又包含了混摻效應討論，總共分為五個章節(討論點)在本文中討論。

　　由研究結論得知，氫鍵的引入會降低垂直於分子軸向的偶極距，因此彎曲型分子引入雙氫鍵官能機時會因分子整體偶極距降低而無法得到自發極化能力。若引入單氫鍵官能基，因為不對稱結構，雖然垂直於分子軸的偶極距下降，可其他軸向的偶極會提升，所以分子整體偶極距會保有一定的向量，當分子有適當的彎曲角度、適當的硬段與軟段長度時，可以誘導出自發極化能力以及光學活性。

　　以氫鍵連結之香蕉型液晶雙分子與主鏈高分子是世界首例的分子設計，並且量測到自發極化能力。鐵電/反鐵電行為與消旋/對掌特性可藉由分子結構內的矽氧基團數目不同而調控，因氫鍵而對電壓敏感之特性也在此研究中觀測得到。

　　於側鏈型高分子而言，因為高分子結構內分子堆疊較為緊密的關係，純共價鍵之彎曲型側鏈高分子無法有效的誘導出自發極化能力，可是卻可藉由共聚氫鍵結構來調控分子間疏密的堆疊行為。在氫鍵分子較多共價鍵分子較少的情況下，彎曲型側鏈共聚高分子可以有效的誘導出自發極化能力。

　　混摻系統而言，可以延展與降低具極化能力的液晶相溫寬與相發生溫度，穩定自發極化能力，而溫度範圍與自發極化值也可藉由混合不同氫鍵與共價鍵彎曲型分子的比值進行調控，不論在共價/氫鍵小分子混摻系統或者共價/氫鍵高/小分子混摻系統皆有上述類似性質。

　　含氫鍵之香蕉型液晶超分子的液晶與光電特性皆在本文中被充分探討。

Study of Hydrogen-Bonded Banana-Shaped Supramolucular Liquid Crystals

Student: Ling-Yung Wang   Advisor: Dr. Hong-Cheu Lin

Abstract

Banana-shaped (so called bent-core) liquid crystals are achiral structures with spontaneous polarization and chirality properties. In this thesis, the identifications and classifications of banana-phase types, electro-optical properties, and bent-core structural configurations were introduced. Meanwhile, the influences of H-bonded functional insertions in bent-core supramolecular materials on the mesomorphic and electro-electric properties were investigated in this doctoral dissertation as well.

In chapter 2, the existence of polar switching behavior in the polar smectic (SmCP) phase of bent-core asymmetric hetero-dimers (with one H-bond) was proven to be associated by their configurations with higher dipole moments and suitable bent angles. In addition, the lack of polar switching behavior in supramolecular bent-core symmetric trimers (with two H-bonds), which exhibited the regular SmC phase with weak electrical stabilities, might be related to their configurations with smaller dipole moments.

In chapter 3, the novel examples of supramolecular bent-core dimers and main-chain polymers with various siloxyl units of central linking spacer, which exhibited voltage-sensitive removable and reassemble (anti)ferroelectric polar switching behavior of spontaneous polarization, were established due to the reorganized H-bonded designs. The ferroelectricity and chirality properties could be adjusted by the controlling of siloxyl units, where the anticlinic tilt in the antiferroelectric ground state (SmC_AP_A) of chiral domain and anticlinic tilt in the ferroelectric ground state (SmC_AP_F) of racemic domain were displayed in bent-core

supramolecules with less siloxyl units (di-siloxyl unit) and more siloxyl units (tri-siloxyl unit), respectively.

In chapter 4, the voltage-dependent anti-ferroelectric properties of spontaneous polarization behavior in the polar smectic phase, which were displayed in H-bonded bent-core side-chain copolymers, were also reported influenced by tuning of proper intermolecular stacking in bent-core covalent- and H-bonded components. A special approach to constructing (or stabilizing) the SmCP phase was first developed by copolymerization of bent-core covalent- and H-bonded units in side-chain polymer complexes with proper molar ratios from both bent-core covalent- and H-bonded monomers without the SmCP phase.

With respect to mesomorphic and electro-optical properties of the bent-core H-bonded dopant systems, more stable SmCP mesophases and low phase tansition temperatures were achieved and the mesophasic range and Ps value of H-bonded complexes could be tuned by the modulating of covalent- and H-bonded doping ratio due to the softer intermolecular arrangement of H-bonded structural dopants. The phenomena were revealable in both small molecular and small molecule/polymer dopant systems as shown in chapters 5 and 6.

Overall, the details of influences by H-bonded and configuration effects in bent-core supramolecules, containing small molecules, imers, and main-chain polymers, and side-chain polymers, on the mesomorphic, molecular stacking, and electro-optical propeties were futher studied in this article.

Outline of Contents

List of Tables

List of Figures

without electric field applying; (f) the racemic (SmC$_A$P$_F$) domains under triangular wave electric field applying; (g) the racemic (SmC$_A$P$_F$) domains after the removing of triangular wave electric field applying. (White arrows are the directions of polarizers and analyzers, and red arrows are the indicators of chiral (SmC$_A$P$_A$ or SmC$_S$P$_F$) domains.)

electric field applying: (a) $+100$ V; (b) 0 V (voltage removing); (c) -100 V for complex IV-C with antiferroelectric switching property to show racemic domain (exchanging between SmC_SP_A and SmC_AP_F).

Chaper 1

Introduction

1.1. Introduction of Banana-Shaped Liquid Crystals

Ferroelectric and anti-ferroelectric liquid crystals (FLCs and AFLCs) become more important due to their fast response of electro-optical properties by applying external electric fields. At early stages, the molecular design of FLCs was only confined to molecular structures having chiral c enter derivatives. However, since the first example of the achiral bent-core (banana-shaped) molecule possessing switchable behavior has been explored,[1] many kinds of bent-core liquid crystals were developed and conferred fascinating optical and electrical properties.

Banana-shaped liquid crystals, which are the achiral structures, display interesting and special electro-optical properties such as spontaneous polarization and chirality duo to the bent molecular shape and polar linking functions. In general, bent-core mesogenic configurations consist of a central core and two rigid wing segments linking through polar functional groups with a suitable bent angle where appropriate lengths of flexible chains are attached linking groups (see Figure 1.1).[2] According to the bent molecular shape and the polar functions, a total dipole force perpendicular to molecular direction is produced by the coupling of three dimension dipoles (see Figure 1.2), and the spontaneous polarization behaviors of bent-core liquid crystals can be induced through the polar directions of layer structures. Furthermore, the chirality (including racemic and homochiral domains) is also accomplished according to the polar direction and the molecular tilted direction (see Figure 1.3).[3]

1.2. Mesophasic Types of Banana-Shaped Liquid Crystals

Regarding the mesophasic types of banana-shaped liquid crystals, the particular mesophases, including columnar stacking, tilted smectic phases, and three dimensional structures, named as B_1 to B_8 phases were explored and identified (see Figure 1.4).[3,4] These can be divided into four main types (i) layer modulation, (ii) modification of layer correlation, (iii) helix formation and (iv) splay modulation. The classification of "B phases" has been collected by C. Tschierske and R. A. Reddy as shown in Table 1.1,[5] and the detail introduction of individual "B phases" is described as following.
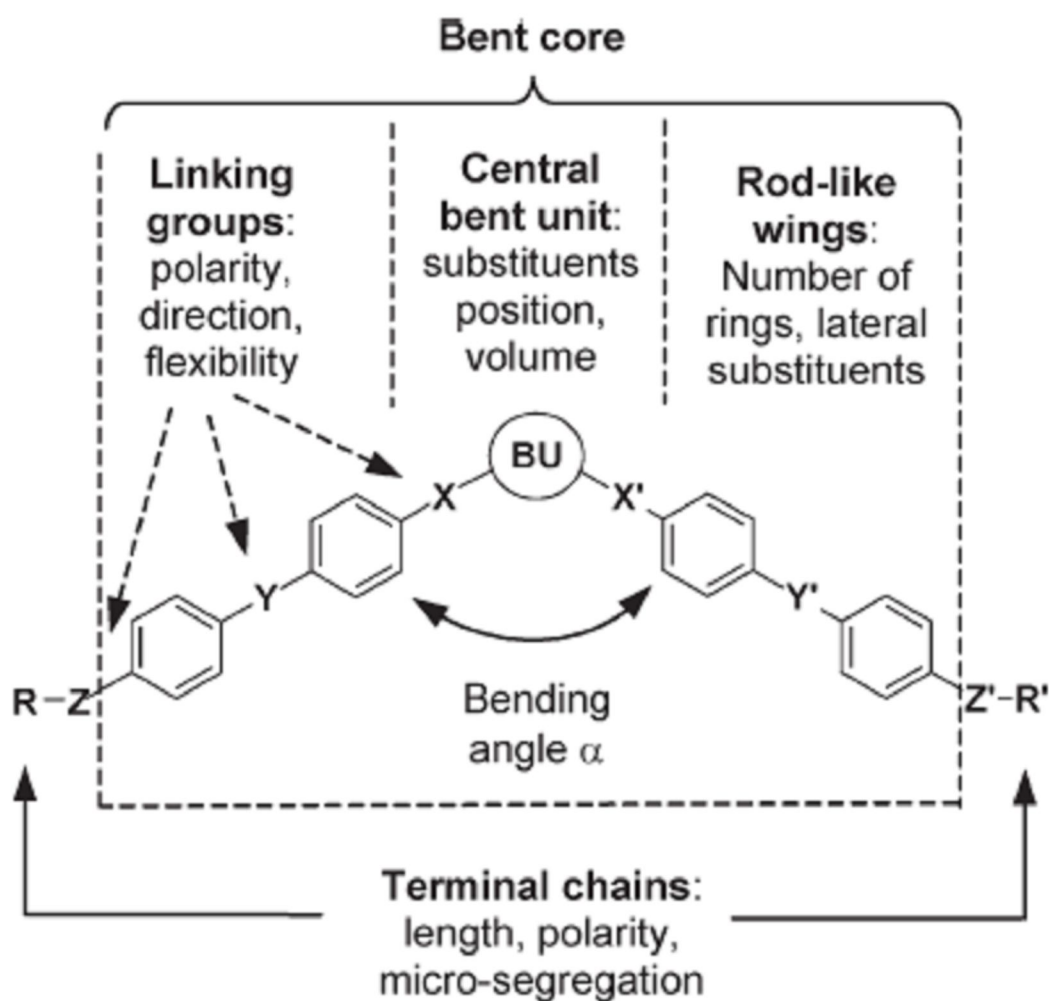
Figure 1.1. The molecular formation of bent-core liquid crystalline designs. [2]
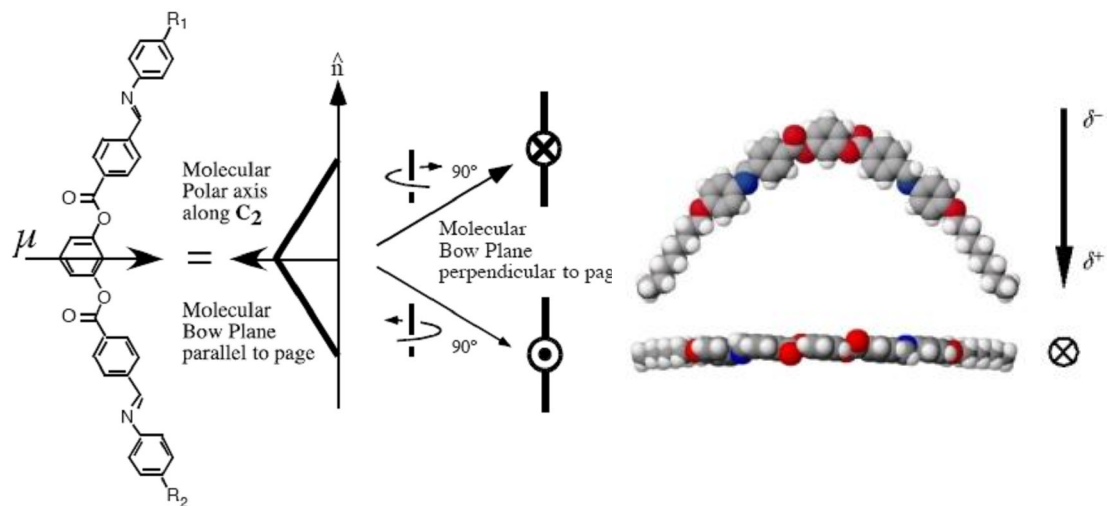
Figure 1.2. The dipole direction of bent-core structure.
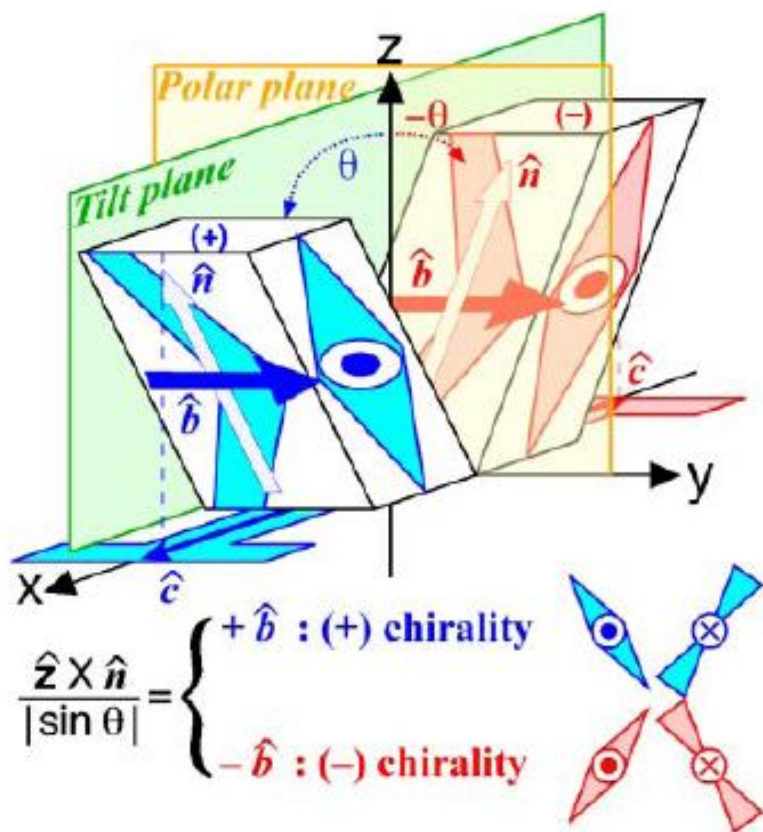
Figure 1.3. The chirality of bent-core structures according to the polar direction and tilt direction. [3]
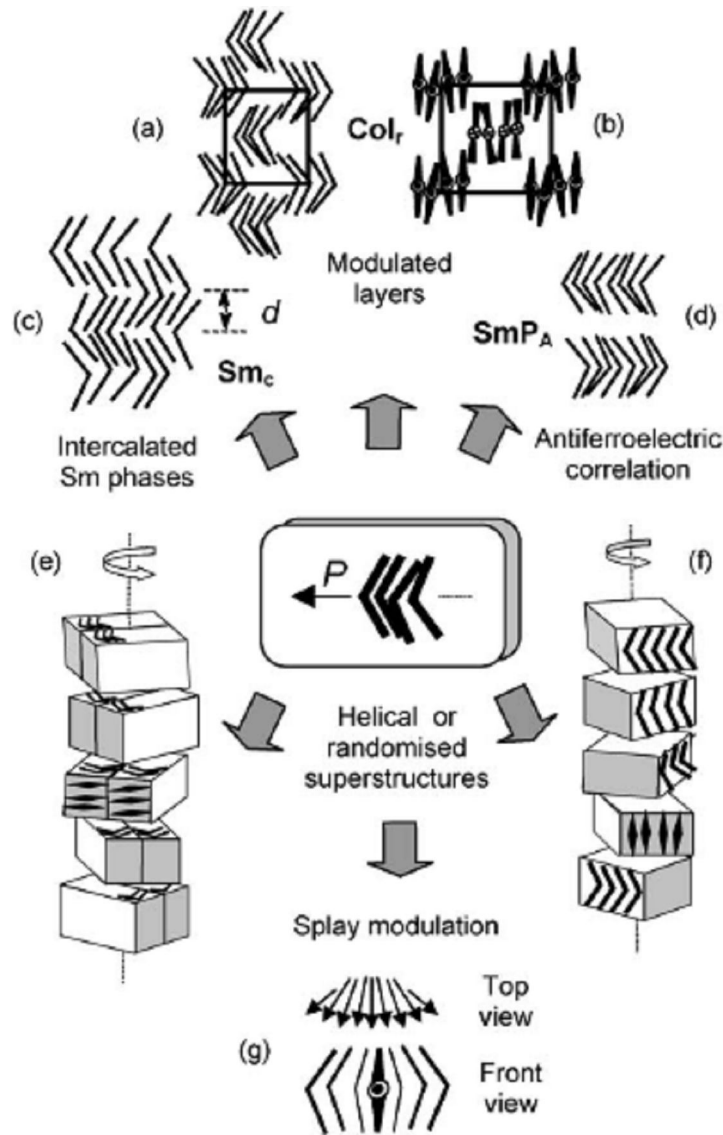
Figure 1.4. The mesophasic types of banana-shaped liquid crystals. [3,4]

1.2.1. B_1 phase

The B_1 phase, which is generally obtained in the bent-core structures with longer and shorter molecular length ratio of rigid core and flexible chain, respectively, was generalized as a columnar (Col) phase because of the two dimension columnar layer modulation. As shown in Figure 1.5,[6] dendritic-like and mosaic textures were revealable in B_1 phase. Based on the traditional identification of B_1 phases via XRD investigations, a broad diffuse scattering peak in wide angle region and several sharp peaks in small angle region were observed. In previous studies, the Col_r of B_1 phase,

which is the non-tilted columnar arrangement as the undulated wavy molecular stacking, generally exhibited no spontaneous polarization behavior. However, in contrast to the conventional Col_r phase, two other kinds of polar switchable B_1 phases named as Col_{rev} and Col_{ob} ($Col_{rev,tilt}$) were developed under a suitable applying of an electric field, and those different tilted modulated columnar molecular arrangements and 3D structures were shown and compared in Figure 1.5 as well.

Table 1.1. The positional ordered mesophases formed by bent-core molecules[5]

Mesophase type	Organization of the molecules	B-nomenclature[50]	Non-switching phases	AF switching	FE switching	Helical filaments
						—
Intercalated smectic and no in-plane order	Orthogonal	B6	SmA_c			—
	Tilted	B6	SmC_c			—
Smectic monolayer and no in-plane order	Orthogonal	—	SmA_b	$SmAP_A$	$SmAP_R$	—
	Tilted	B2		$SmCP_A$	$SmCP_{FE}$	(+)
	Tilted	—		$SmCP_A^{[*]b}$	$SmCP_{FE}^{[*]b}$	(+)
	Tilted	—			$SmCP_R$	—
Smectic monolayer with in-plane order, but no interlayer correlation	Tilted	B5		$B5_{AF}$	$B5_{FE}$	—
Smectic bilayer	Double tilted	B8		$SmCG_2P_A$		(+)
Undulated smectic	Tilted	—		$USmCP_{AF}$	$USmCP_{FE}$	(+)
Undulated modulated smectic	Tilted	B7-subtype (B7′)		$U^mSmC_sP_{AF}$	$U^mSmC_sP_F$	+
Mesophase with 2D or 3D lattice (?)	Tilted	B7	B7	$B7_{AF}$		+
Modulated smectic (columnar ribbon phases)	Orthogonal	B1	$Col_r/p2mg$	Col_rP_{AF}		—
	Orthogonal	$B1_{rev}$	$Col_r/pmmn$ (SmÃP) Col_{ob} (SmČ$_s$P)	$Col_{ob}P_{AF}$	$Col_{ob}P_{FE}$	(+)
	Tilted	$B1_{rev,tilted}$				(+)
	Double tilted	—		$SmČ_sG_2P_{AF}$		(+)
Hexagonal columnar		—	Col_h	Col_hP_{AF}		—
Soft crystalline mesophase	Orthogonal (TGB-like)	$B4^{[*]}$	$B4^{[*]}$			—
Soft crystalline or hexatic mesophase	?	B3	B3			—

[a] Abbreviations: SmA = untilted smectic phase without in-plane order, SmC = tilted smectic phase without in-plane order, SmCG = double-tilted smectic phase, USm = undulated (sinusoidal deformed) smectic phase, U^mSm = modulated undulated smectic phase, SmÃ, SmČ = modulated smectic phases (the layers are broken into ribbons), Col = columnar mesophase; P = mesophase with polar order; subscripts: b = biaxial, c = intercalated; A = AF order, F = FE order, AF = AF switching, FE = FE switching, s = synclinic orientational correlation between adjacent layers, a = anticlinic correlation between layers, R = random (no orientational correlation between layers), r = rectangular 2D lattice, ob = oblique 2D lattice, h = hexagonal 2D lattice, rev = reversed, rev,tilted = reversed tilted; $p2mg$ = plane group and $pmmn$ = layer group which characterise the columnar phases in more detail; the superscript [*] indicates a mesophase with supramolecular chirality, characterised by the spontaneous formation of a conglomerate of domains of opposite chirality sense whereby the molecules themselves are configurational achiral or racemic; − = not observed, (+) observed in few exceptional cases, + = typical feature of the mesophase; [b] these phases are also assigned as "dark conglomerate phases".
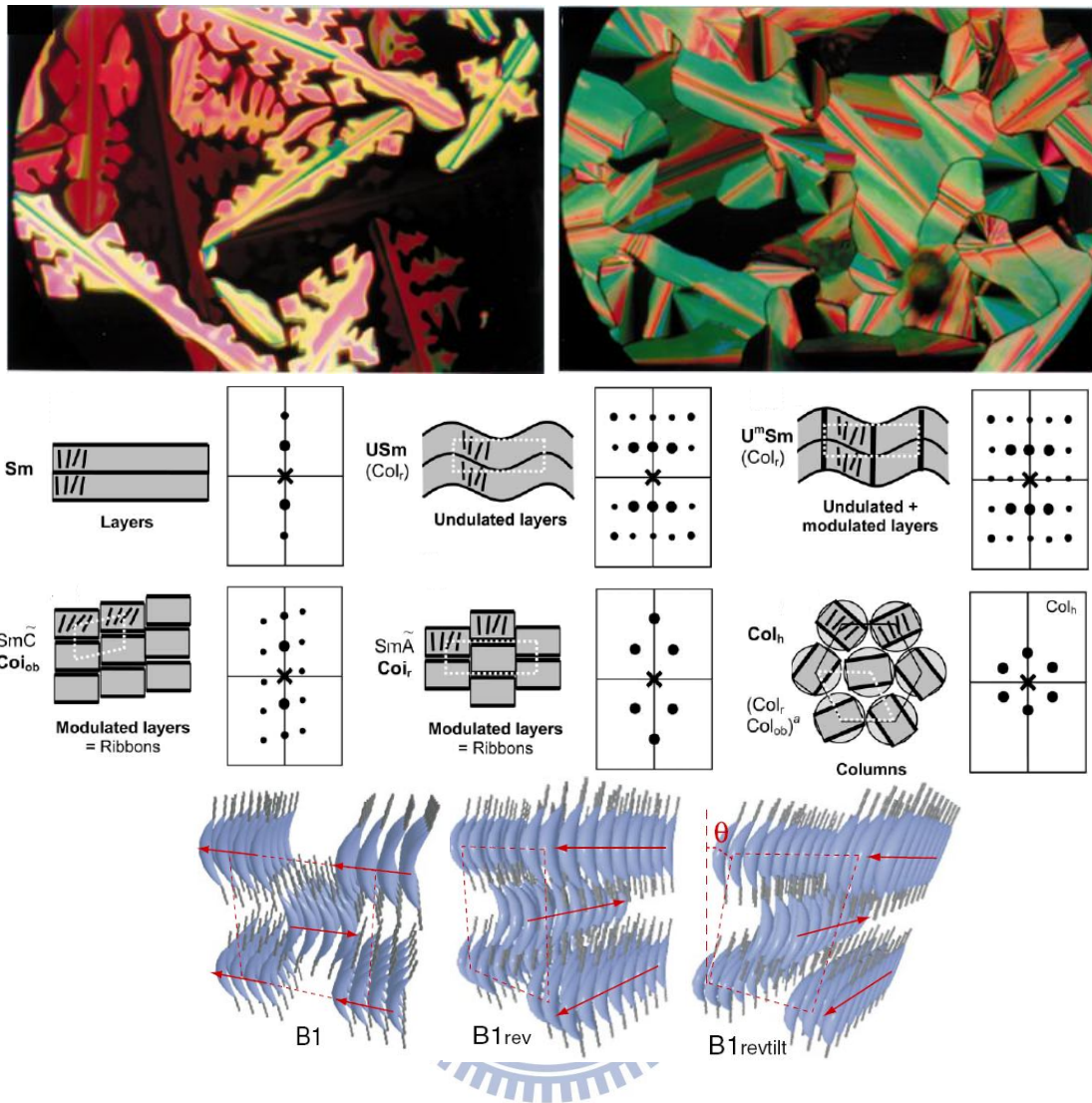
Figure 1.5. The mesophase textures, XRD models and molecular arranged models of B_1 phase. [3,6]

1.2.2. B_2 phase

The B_2 phase (so called SmCP phase) is still the most extensively studied banana phase. The spontaneous polarization behavior is obtainable in this phase, which is explained the polar order based on close packing of molecules in a smectic layer with a unique bending along a C_{2V} symmetry axis. The schileren, broken fan, and circular textures were possessed in this phase (see Figure 1.6).[7] The most prevailingly investigated B_2 phase revealed ferroelectric (FE)/antiferroelectric (AF) properties, which possessed identical/inverse polarizations, and synclinic (S)/anticlinic (A)

arrangements with alike/opposite molecular tilted aspects between layer to layer, respectively.[8] Hence, depending on the polar directions and molecular tilted directions in neighboring layers, four kinds of different molecular architectures denoted as SmC_AP_A, SmC_SP_A, SmC_AP_F, and SmC_SP_F were categorized to homochiral (SmC_AP_A and SmC_SP_F) and racemic (SmC_SP_A and SmC_AP_F) conditions, respectively. In the XRD investigations of B_2 phase, the smallest and next-smallest angle peaks are related to the first and second order diffractions corresponding to the smectic layer with about 30° to 45° molecular tilted angles.
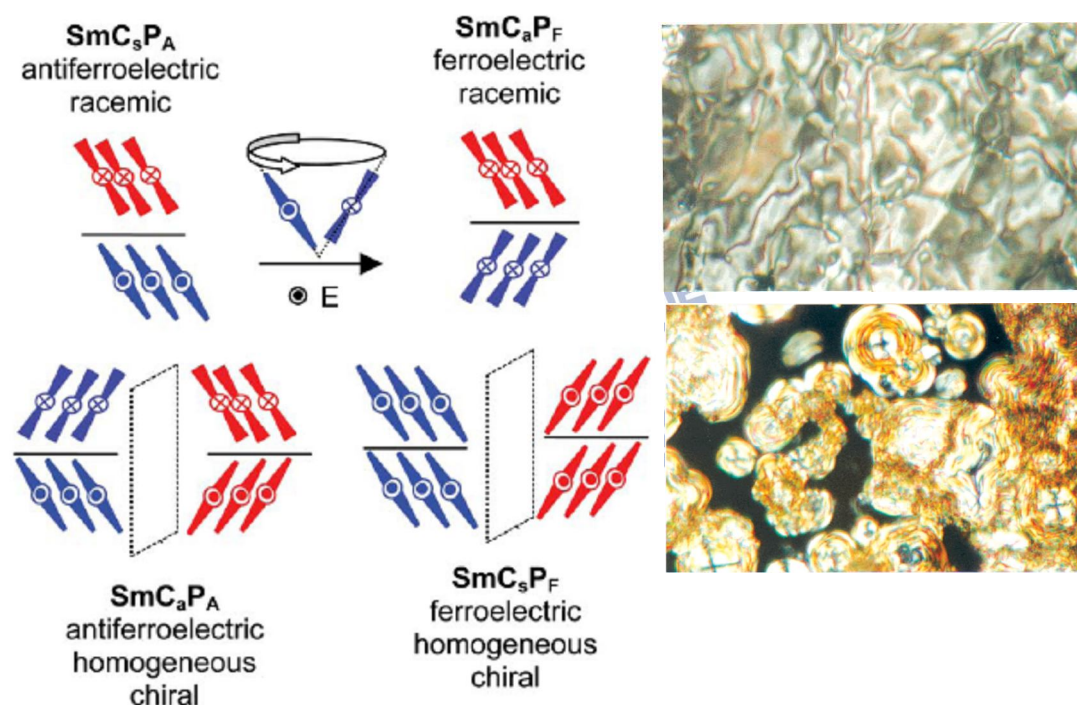
Figure 1.6. The mesophase textures and molecular arranged models of B_2 phase. [7]

1.2.3. B$_3$ phase

The B_3 phase is a kind of higher-order lamellar arrangement, which often exhibits in lower temperature cooling from B_2 phase (see Figure 1.7). Even if the spontaneous polarization behavior was received in a previous paper,[9] however the electro-optical identification was uncertainly duo to the non-confirmed second harmonic generation (SHG) activity and low dielectric constant phenomena.[10] As

shown in Figure 1.7, the XRD investigation of B_3 phase, revealed several diffraction peaks at small and wide angle regions to describe it is similar with a crystalline structure,[9,11] and the layer spacing in B_3 phase was the same as that in a crystal state, longer than that in B_2 phase, and shorter than that in B_4 phase.

No	R	Cr		B4		B3		B2		B1		I	ref.
1a	$C_5H_{11}O$	•	176	—		—		—		•	181	•	[5]
1b	$C_6H_{13}O$	—		•	143.6 [6.46]	•	159.1 [3.71]	—		•	173.4 [5.11]	•	[4,5]
1c	$C_7H_{15}O$	—		•	141.3 [5.62]	•	155.2 [2.81]	•	171.7 [5.53]	—		•	[4,5,]
1d	$C_8H_{17}O$	—		•	139.7 [5.53]	•	151.9 [3.32]	•	173.9 [5.73]	—		•	[4,5,7]
1e	$C_{10}H_{21}O$	—		•	138.4 [4.51]	•	144.4 [4.75]	•	172.9 [6.20]	—		•	[4,5]
1f	$C_{12}H_{25}O$	—		•	140.9 [6.20]	—		•	169.9 [4.17]	—		•	[4,5]
1g	$C_{16}H_{33}O$	—		•	136.9 [12.5]	—		•	163.7 [6.97]	—		•	[4,5]
1h	$C_8^*H_{17}O$	•	81	—		—		—		—		•	[5]
1i	C_5H_{11}	•	105.7 [2.27]	—		•	143.2 [2.08]	•	149.9 [4.16]	—		•	[4,5]
1j	C_6H_{13}	•	83.3 [1.80]	—		•	148.8 [2.45]	•	155.6 [4.40]	—		•	[4,5]
1k	C_8H_{17}	•	72.2 [4.80]	—		•	139.9 [2.74]	•	158.1 [5.29]	—		•	[4,5]
1l	$C_{10}H_{21}$	•	68.3 [5.91]	—		•	136.3 [5.35]	•	158.5 [9.70]	—		•	[4,5]
1m	$C_{12}H_{25}$	•	62.6 [3.80]	—		•	130.2 [3.32]	•	156.0 [5.62]	—		•	[4,5]
1n	$C_{14}H_{29}$	•	50.4 [2.86]	—		•	122.7 [3.43]	•	151.3 [5.48]	—		•	[4,5]

Figure 1.7. The bent-core chemical structure and XRD patterns of B_3 phase. [3,9,11]

1.2.4. B_4 phase

The B_4 phase, so called "smectic blue", often appears in lower temperature cooling from B_2 and B_3 phases. In previous studies, the lattice distance of B_4 phase was longer than that of B_3 phase. Textures of B_4 phase under a polarizing microscope appeared as transparent dark blue colored domains, as shown in Figure 1.8. This blue

color was first considered to be caused by selective reflection due to the helical structure like a twist-grain-boundary (TGB) phase.[11,12] In the POM observations of B_4 phase, the dark and bright domains were demonstrated, which could be exchanged by the rotating one of the polarizers clockwise and counterclockwise. A CD spectrum with an opposite sense was also obtained to indicate the chirality structure.[13] Although the B_4 phase was not switchable by an electric field and its dielectric constant was low, SHG was observed even without the electric field. This indicated the existence of a spontaneous non-centrosymmetric order.[4] In the XRD investigations of B_4 phase (see Figure 1.8), the number of diffraction peaks decreased in wide angle region and the peaks became wider than that of B_3 phase, which suggested that the B_4 phase has an in-plane order.
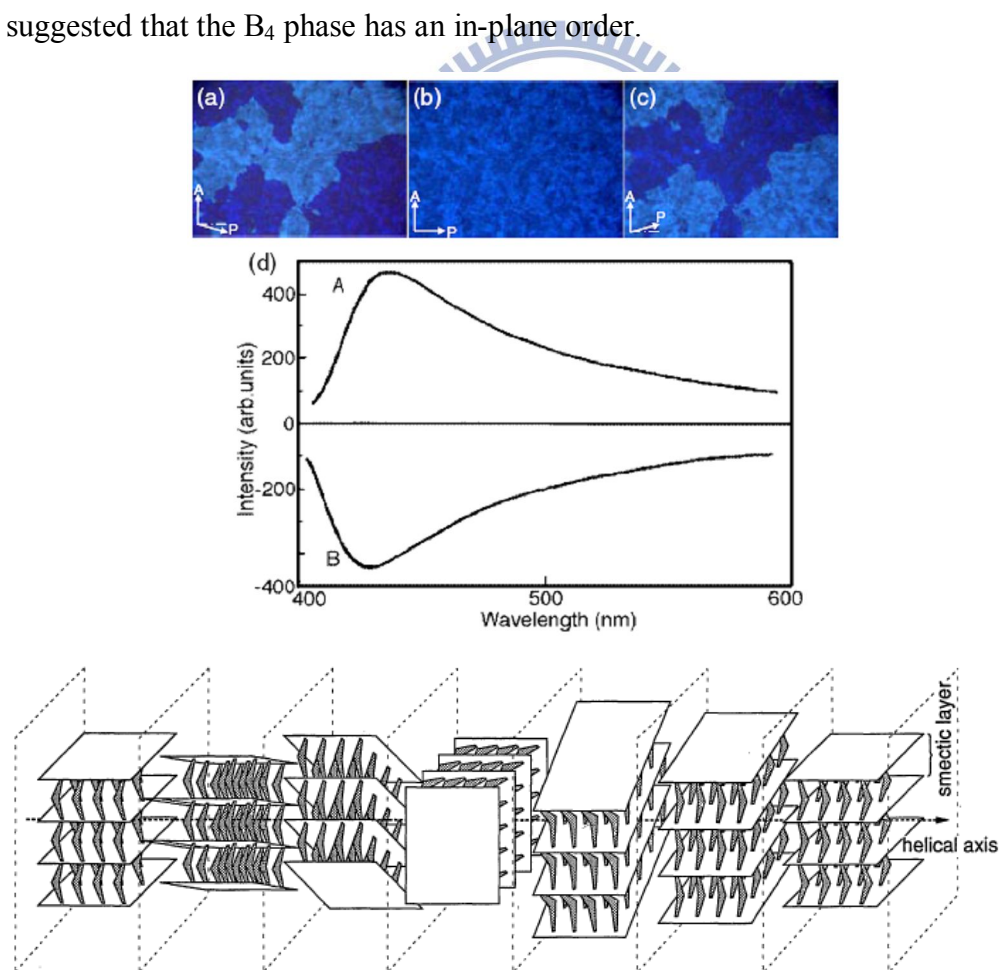
Figure 1.8. The POM textures, CD spectra, and molecular arranged model of B_4 phase. [3,11-13]

1.2.5. B₅ phase

According to the previous articles, B_5 phase was performed in the bent-core structures which bear CH_3 and F substitutes at the central-ring and the F substitute at both terminal rings (see Figure 1.9).[14] In previous studies, this phase appeared below the B_2 phase, and the transition enthalpy between them was small. In electro-optical studies, the FE and AF switching of spontaneous polarization behaviors in B_5 phase were observable. Even if the electro-optical properties and mesophase texture of B_5 phase were similar with those of B_2 phase, however their XRD investigations from the surface oriented samples were distinguishable. In a small angle region, highly order reflections peaks corresponding to the smectic layer spacing could be observed. Moreover, the model of in-plane molecular arrangement was established as well.
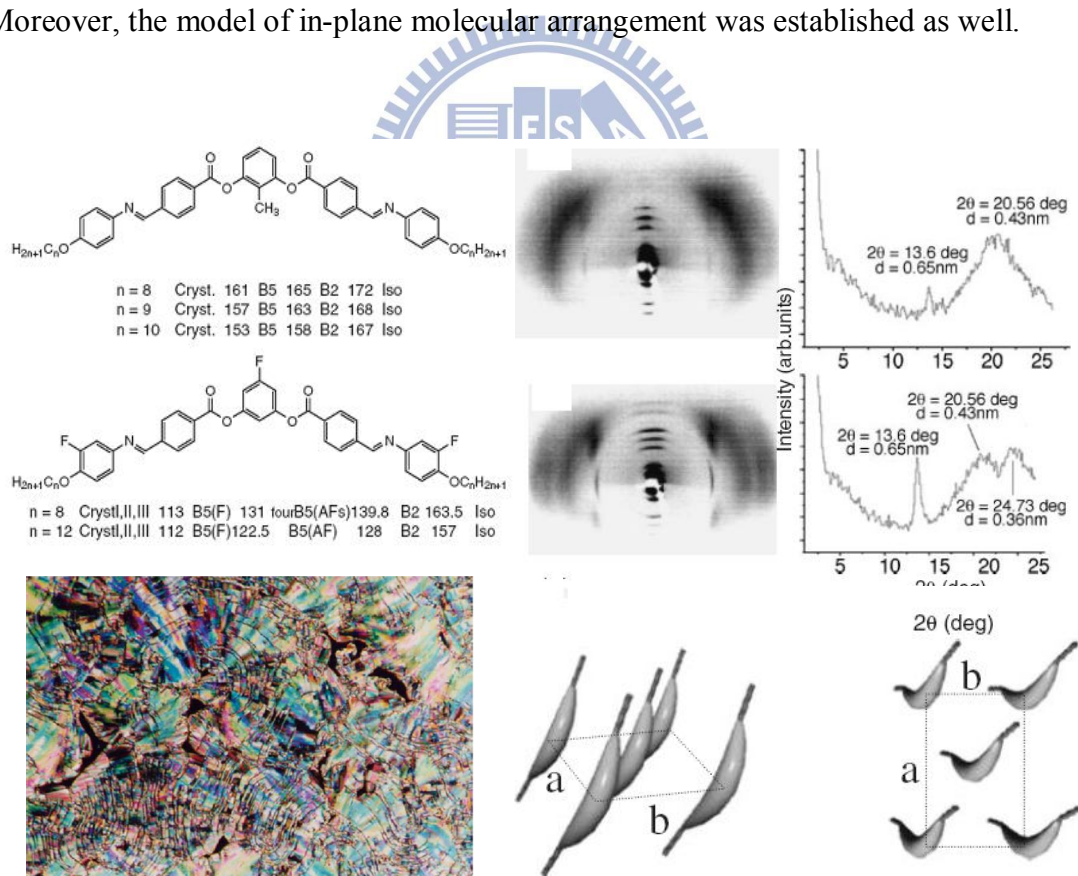
Figure 1.9. The bent-core chemical structures, POM texture, XRD patterns, and molecular arranged models of B_5 phase. [3,14]

1.2.6. B_6 phase

As shown in Figure 1.10, the B_6 phase exhibited a fan-like texture as the smectic A phase but a homeotropic texture could never be obtained. In XRD investigations, only one reflection peak smaller than half of molecular length was obtained in the small angle region to indicate the intercalated molecular arrangement tilted in a layer. In addition, four broad diffuse peaks were observed in the wide angle region, suggesting liquid-like in-plane order. [15]
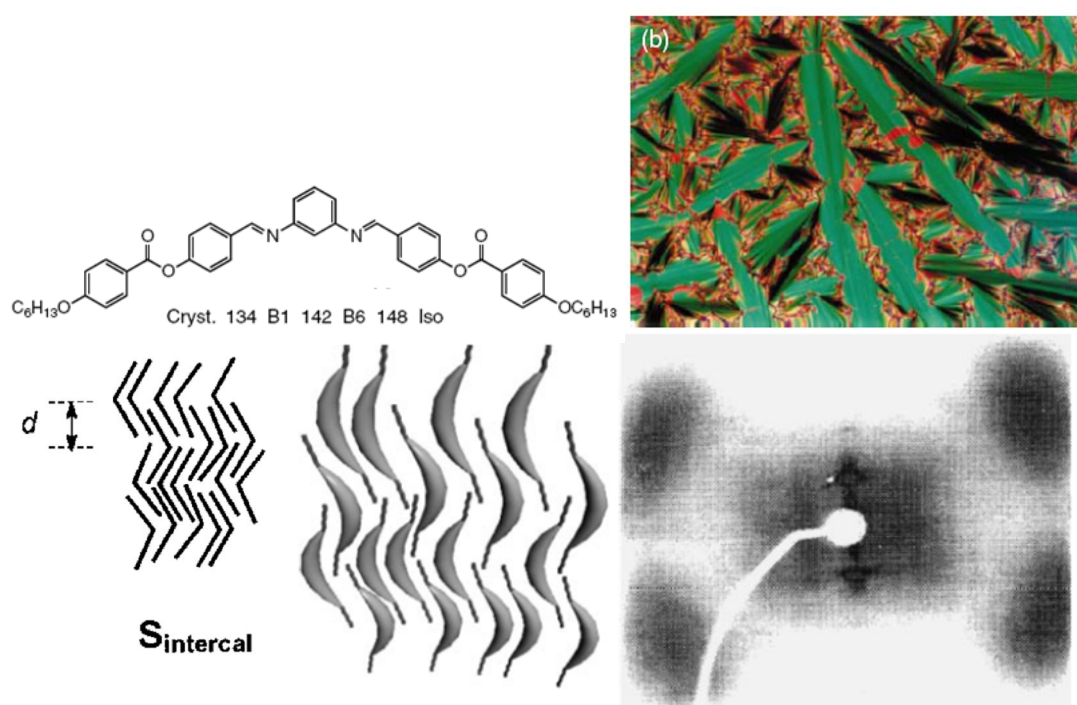
Figure 1.10. The bent-core chemical structures, POM texture, XRD patterns, and molecular arranged models of B_6 phase. [3,15]

1.2.7. B_7 phase

Based on the previous articles, the B_7 phase often revealed in the bent-core structures with a NO_2 or CN substitutes at the positions of central ring.[16] Many kinds of POM textures could be observed in B_7 phase such as spiral filament (coexistence of left- and right-handed spirals), chiral micro-mosaic domain, myeliniclike, accordion-like, checker-board-like, banana-leaf-like, and circular domain textures as

shown in Figure 1.11.[4,17] The FE and AF switching of spontaneous behaviors in B_7 phase were obtainable. In XRD investigations, a liquid-like broad diffuse peak and several sharp reflection peaks were obtained in wide and small angle regions, respectively, and the sharp reflection peaks were also identified by the high resolution X-ray diffraction, suggesting the 2D ordered modulated layer structures. The immediate image of modulated layer structures was also observable by freeze fracture transmission electron microscopy (see Figure 1.12).[18] On the other hands, the B_7 phase was called SmC_G phase within triclinic symmetry as well. Depending on tilting of the molecular planes (called clinic) and of the layer polarization (called leaning) where the layer polarizations further exhibited in-layer and out-layer conditions, eight different general tilted structures were framed as shown in Figure 1.12.[19]
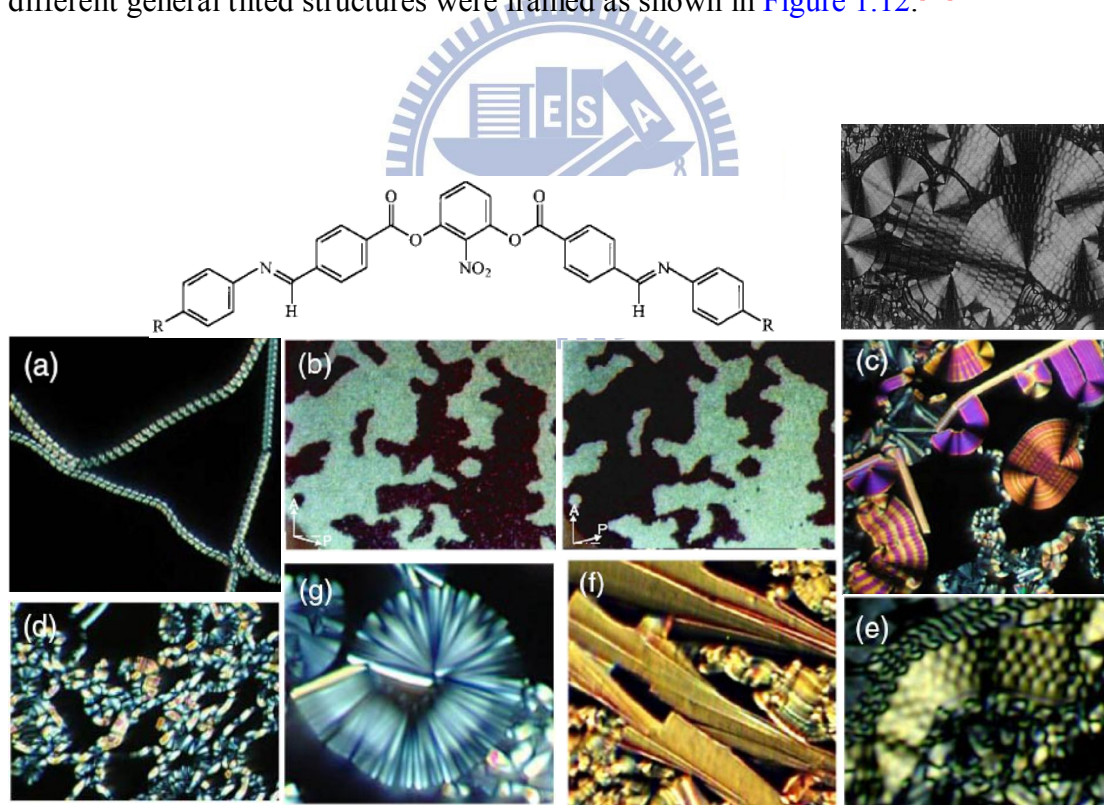
Figure 1.11. The bent-core chemical structures and several kinds of POM textures of B_7 phase. [3,4,16,17]
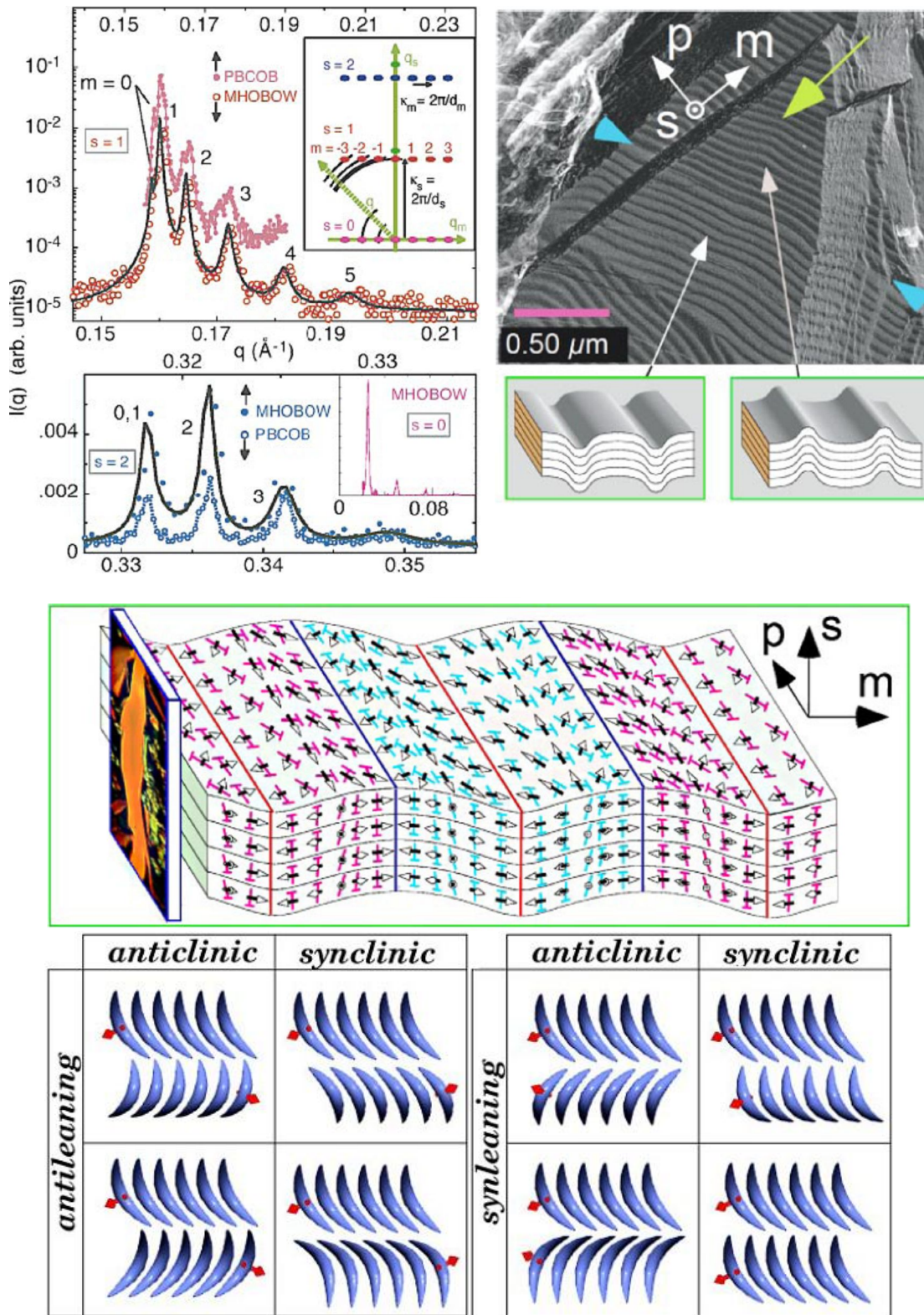
Figure 1.12. The high resolution XRD patterns, FFTEM image, and molecular arranged model of B_7 phase.[3,18,19]

1.2.8. B_8 phase

The B_8 phase was displayed in the bent-core chemical structures as shown in

Figure 1.13. The spiral and fan-like domains were examined in this phase by gradual and further cooling from isotropic phase, respectively. The AF switching of spontaneous behaviors in B_7 phase was obtainable, and the bi-layer structure was also recognized by XRD investigations.[20]

In recent years, some kinds of mesophases such as nematic, smectic A, and crystalline phases, which displayed their own spontaneous switching behaviors and chirality were discovered in novel bent-core liquid crystals (those properties are not contributed form chiral-center possessed rod-like structures). It is suggested that the original "B phase" classified rules may be not satisfied for subsequently researches. Otherwise, complete classification of the B_n-related phases is a subject for future research.
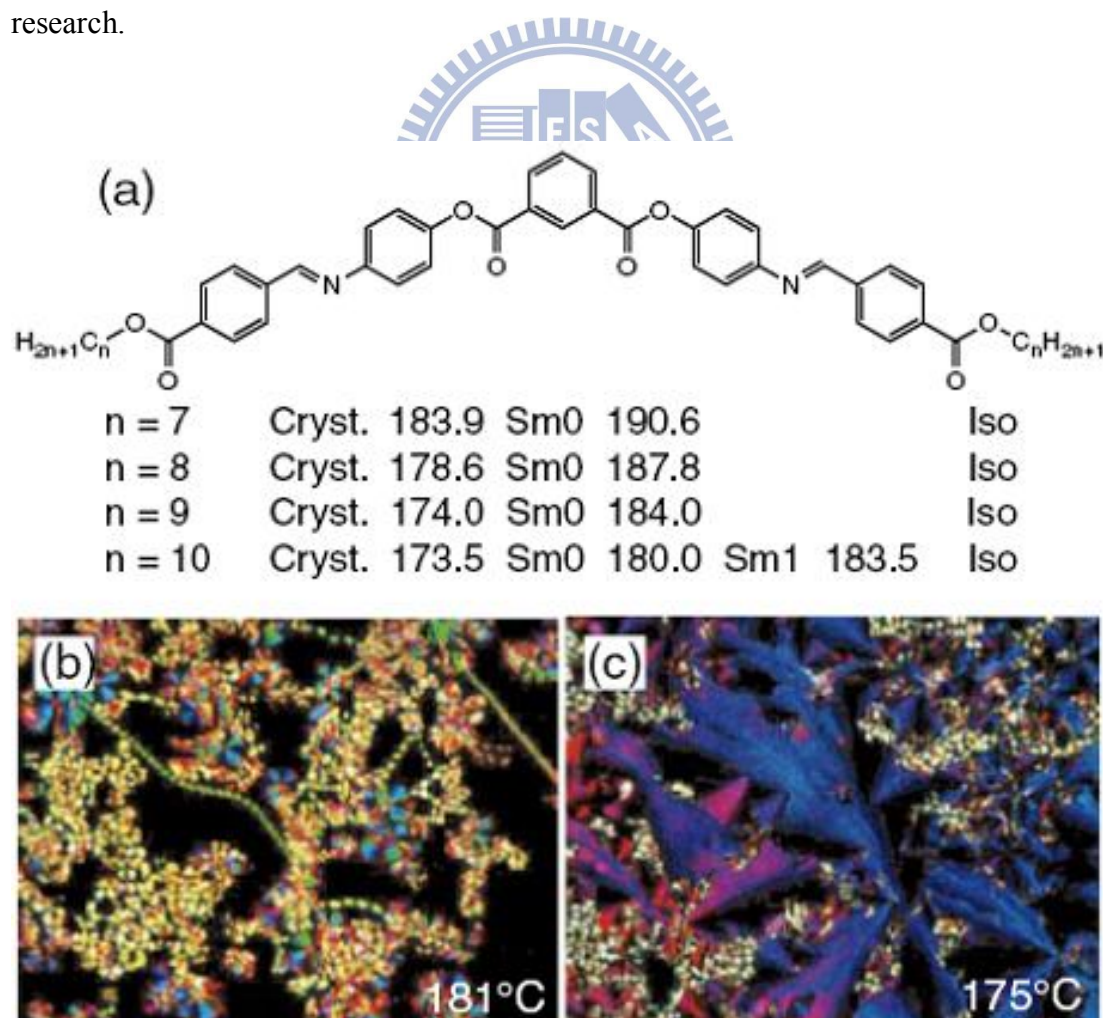
Figure 1.13. The chemical bent-core structure and POM textures of B_8 phase. [3,20]

1.3. Identifications of AF/FE Spontaneous Polarizations in B$_2$ Phase

In this dissertation, we focus the mainly researches in the investigations and characterizations of the B$_2$ phase of bent-core structures. The electro-optical properties are deservedly the important investigations for banana-shaped liquid crystals. Regarding the spontaneous polarization behaviors of B$_2$ phase, the equal and opposite polar directions between layer to layer micro-polar directions are detected. As shown in Figure 1.14, two kinds of polar switching conditions were defined.[21] The ferroelectric (FE) switching behavior means a polar smectic ground state (SmP$_{F1}$) with equal inter-layer polar directions switches to a reverse polar smectic excited state (SmP$_{F2}$) with equal inter-layer polar directions under a sufficient applied electric field. On the other hands, the anti-ferroelectric (AF) switching behavior means a polar smectic ground state (SmP$_{AF}$) with opposite inter-layer polar directions switches to the polar smectic excited state with equal inter-layer polar directions. Then, the spontaneous polarization behaviors can be enhanced due to the inter-molecular micro-aggregation of AF/FE polar switching conditions.
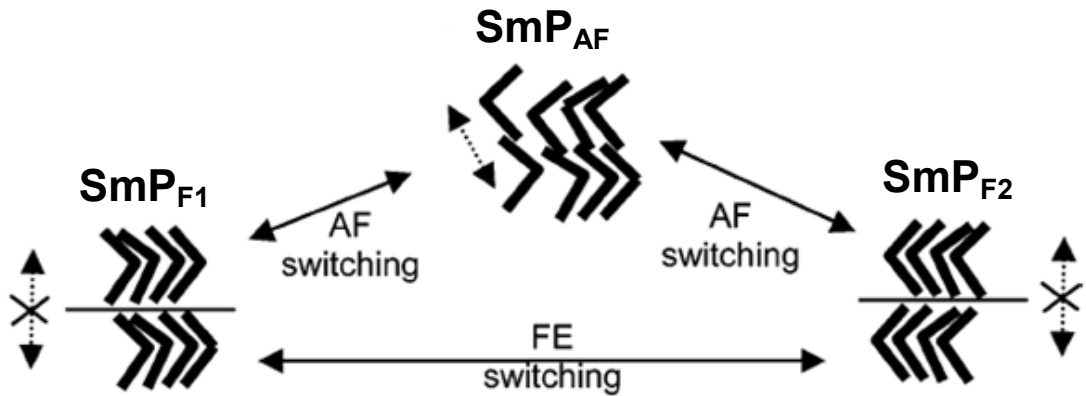
Figure 1.14. The definitions of polar switching behaviors of ferroelectric and anti-ferroelectric behaviors.

In general, those polar switching behaviors have been determined by using a triangular wave method (see Figure 1.15).[22] As shown in Figure 1.16, two current

peaks per half-period of an applied triangular voltage were obtained in the switching current response curves. Here, the characteristic behavior of a sequential electric response was due to a ferroelectric state switches into an antiferroelectric ground state and back to the opposite ferroelectric state, which was confirmed the SmCP$_{AF}$ structure of the B$_2$ phase. Single current peak per half-period of an applied triangular voltage was acquired in switching current response curves, indicating that a sequential electric response was due to a ferroelectric state switches into the opposite ferroelectric state, which confirms the SmCP$_{FE}$ structure of the B$_2$ phase. In addition, the AF/FE behaviors have been further proved by an applying modified triangular wave as well.[23] The switching current peaks of AF behavior would be separated to two peaks, which situate at the start and the end locations of zero potential. However, only one switching current peak of FE behavior was displayed at the start or end locations of zero potential. This method can be applied to confirm the too fast switching of unobvious AF state clearly and avoid the erroneous judgment of fake FE behavior (AF behavior with a hidden AF state in normal triangular wave supplying).
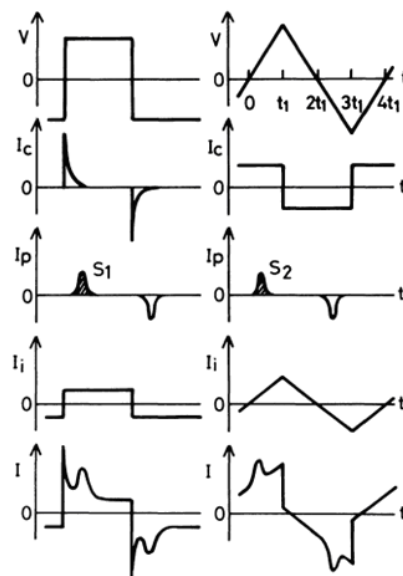
Figure 1.15. The identifications of spontaneous polarization behaviors of triangular wave method. [22]
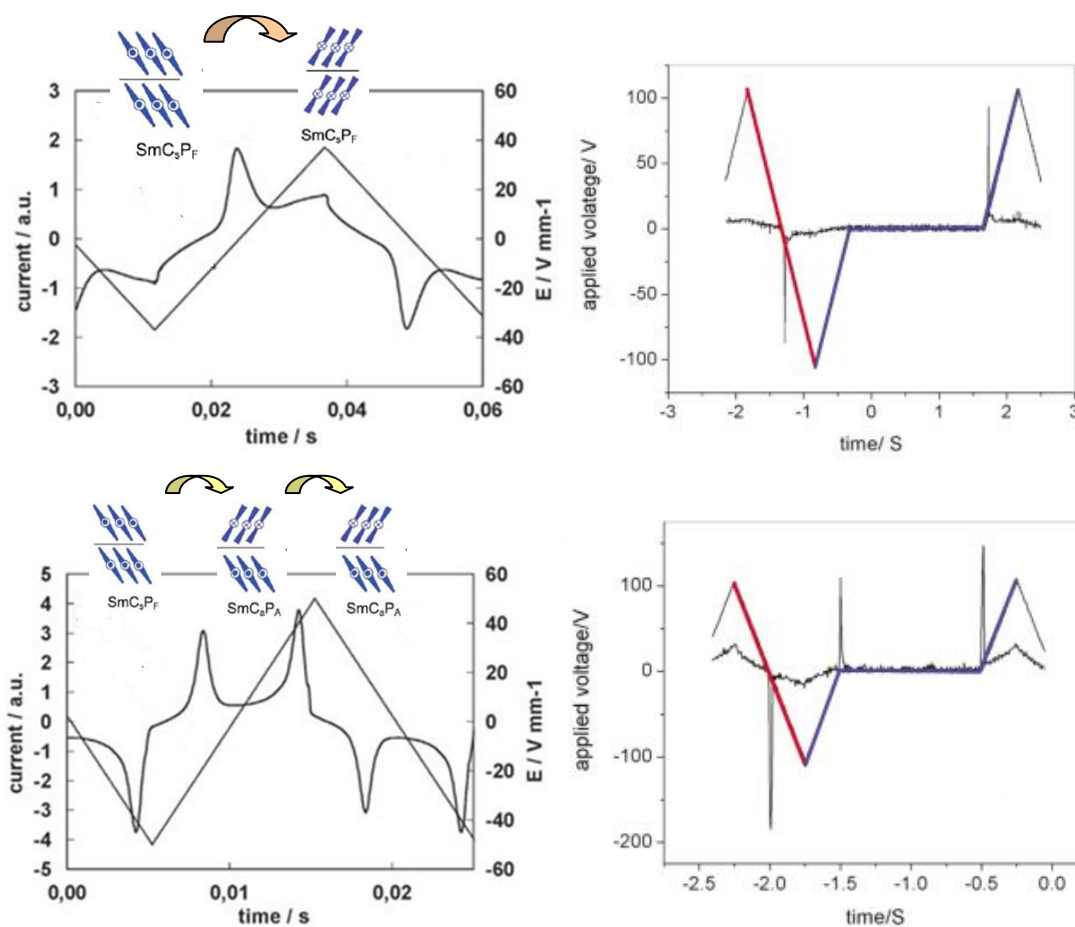
Figure 1.16. The ferroelectric and anti-ferroelectric response switching current behaviors under normal and modified triangular waves. [25b]

1.4. Identifications of Racemic/Homochiral Chirality of B_2 Phase

The exhibition of chirality in achiral bent-core structures is due to the molecular tilted directions and the polar directions as shown in Figure 1.3. Besides triangular wave method, a switching process could also be checked through the rotation of the extinction crosses by applying (or after removing) opposite d.c. electric fields, where the layer structures were arrangement corresponding to the domain models proposed by Link et al.[24] Depending on the polar directions and molecular tilted directions in neighboring layers, four kinds of different molecular architectures denoted as SmC_AP_A, SmC_SP_A, SmC_AP_F, and SmC_SP_F were categorized to homochiral (SmC_AP_A

17

and SmC_SP_F) and racemic (SmC_SP_A and SmC_AP_F) conditions, respectively. In previous studies, four chirality switching behaviors between the described fundamental molecular architectures of B_2 phase were collated: the switching of (i) SmC_AP_A ground state to SmC_SP_F excited state, (ii) SmC_SP_F state to opposite SmC_SP_F state, (iii) SmC_SP_A ground state to SmC_AP_F excited state, and (iv) SmC_AP_F state to opposite SmC_AP_F state. The rotated phenomena of extinction crosses in four chirality switching behaviors were shown in Figure 1.17.[25] In addition, the homochiral behavior could also be determined by the rotating of polarizer. As shown in Figure 1.18, the regions of dark and bright domains were revealed by rotating one of the polarizer, and these two domains would be exchanged by opposite rotating of the polarizer.[25d]

1.5. Classifications of Bent-Core Structural Configurations

Up to now, many kinds of bent-shaped configurations have been reported which are established by five-ring resorcinol derivatives. The structural variations of achiral molecular designs, such as the central parts, lateral substitutes, linking groups, terminal chains, and the number of rings, would affect their physical properties to different extents in small molecular systems. Recently, poly-molecular systems, i.e., dimeric, polymeric, and dendritic frameworks, were also developed to investigate the influence of molecular configurations on mesomorphic and electro-optical properties. Moreover, some novel supramolecular bent-core interactions or their nanocomposite architectures have been integrated into organic or inorganic parts to display special electro-optical characteristics, for instance, bent-core derivatives embedded with nanoparticles, bent-core H-bonded supramolecules, and bent-core structures with silyl and siloxyl linkages. In this session, the reported examples of bent-core molecules with structural varieties are collated.
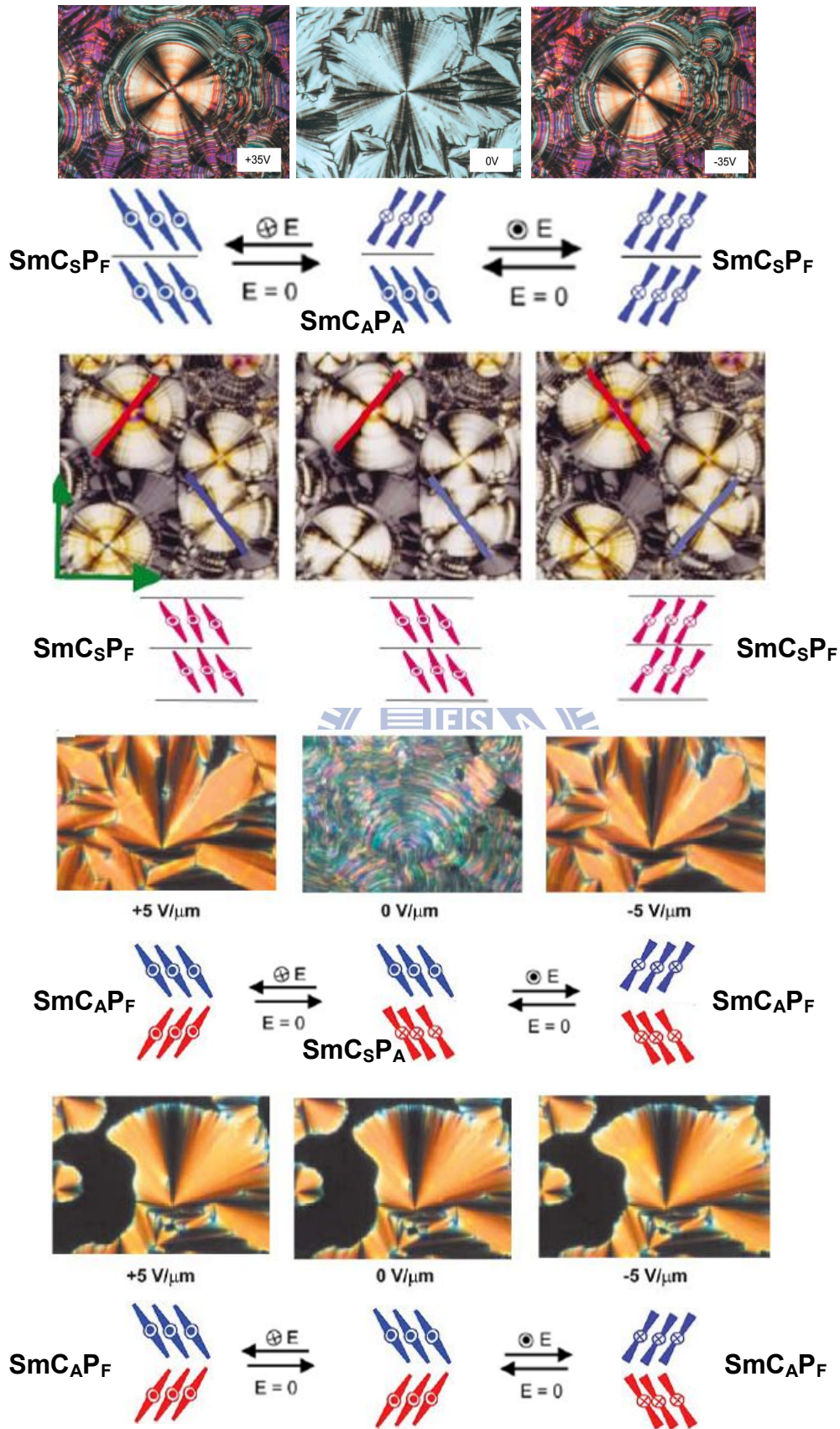
Figure 1.17. The identifications of Racemic/Homochiral Chirality: SmC_AP_A, SmC_SP_A, SmC_AP_F, and SmC_SP_F. [25]
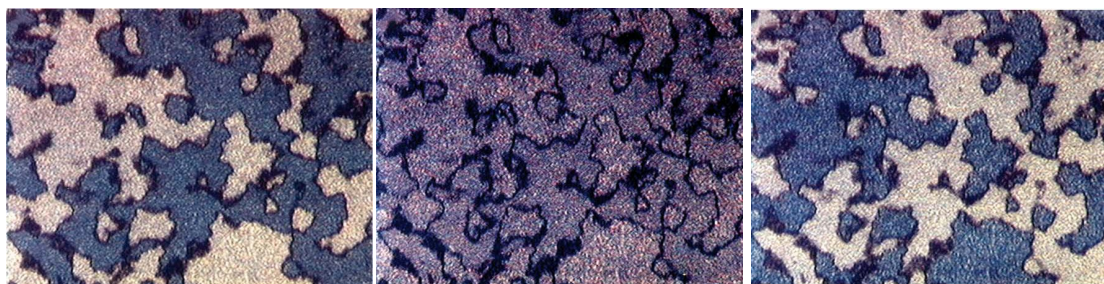
Figure 1.18. The identifications of homochiral chirality by the rotating of polarizer. [25d]

Compound	BU	Phase transitions/°C
5a[93a]	Ph	Cr 105 SmCP$_A$ 119 I
6a (OC$_{16}$H$_{33}$)[111]	Naph	Cr 122 SmCP$_A$[*] 173 I
7a[93a]	Biph	Cr 85 SmCP$_A$ 162 I
8[93a]	Terph	Cr 158 SmCP$_A$ 202 I
9[93a]	Tol$_1$	Cr 137 Col$_r$ 208 I
10[93a]	Tol$_2$	Cr 136 Col$_r$ 204 I
11[136]	PhSPh[b]	Cr 150 Col$_r$ 156 I
12[225]	PhCH$_2$Ph	Cr 110 SmCP$_A$[*]162 I

[a] Abbreviations: Cr = crystalline solid, SmCP$_A$ = AF switching polar SmC phase, SmCP$_A$[*] = AF switching polar SmC phase with chiral superstructure, Col$_r$ = non-switchable rectangular columnar mesophase, I = isotropic liquid. [b] Temperatures obtained on cooling.

Figure 1.19. The configuration effects of bent-core structures by different central parts on mesophasic varieties. [5,7,26]

1.5.1. Central ring part

In the central ring parts of bent-core structures, basic central structures i.e., 1,3-disubstituted benzene unit, 2,6-disubstituted pyridine ring, 2,7-disubstituted naphthalene unit, 1,3-disubstituted biphenyl unit, terphenyl units, and oxadiazole derivative were often used (see Figure 1.19).[7,26] Based on the discussions of Reddy's and Tschierke's article,[5] for instance, the SmCP phase was observable in compounds with phenyl, naphthenyl, biphenyl, and terphenyl centers, but the non-switchable smectic and nematic phases were occurred in oxadiazole derivatives due to the larger bending angles. However the central-part configuration effects by in bent-core structures on the mesomorphic properties have been enthusiastically considered. Novel mesomorphic phenomena depending on the varieties of bent-shaped structures should be displayed in the future.

1.5.2. linking group

The types and polar directions of linking groups are the important factor to decide the mesophasic classifications. C=N, COO, N=N, N=N(O), COS, and C=C linking, have been used to connect the rigid wings. As shown in Figure 1.20, B_2 to B_4 phases were obtained in structures with C=N and COO linkages. The SmCP of B_2 phase was achieved in structures with COS, single N=N, and N=N(O) linkages. Furthermore, the Col_{ob}, Col_r, SmC, $SmCP_A$, and $SmCP_F$ were obtained in the five-ring bent-core structures connecting by fully ester linking group with various polar linking directions.[7,15b,27] According to the described linking group effects on mesomorphic properties, they were strongly indicated linking groups displayed the critical role to change such as polar order, molecular size, and inter-molecular stacking in the bent-core structures. We also consider that the influence of linkages should be the one of important factor even in the future studies.

Compound	Y, Y'	Phase transitions/°C
1a[143]	N=CH, CH=N	Cr ? B4 139 B3 152 SmCP$_A$ I
5b[93]	COO, OOC	Cr 106 SmCP$_A$ 117 I
16[94]	COS, SOC	Cr 109 SmCP$_A$ 114 I
17a[87]	CH=CH, CH=CH	Cr 183 LC 200 dec.

[a] B3, B4 = higher ordered mesophases or soft crystalline ph
LC = unknown LC phase
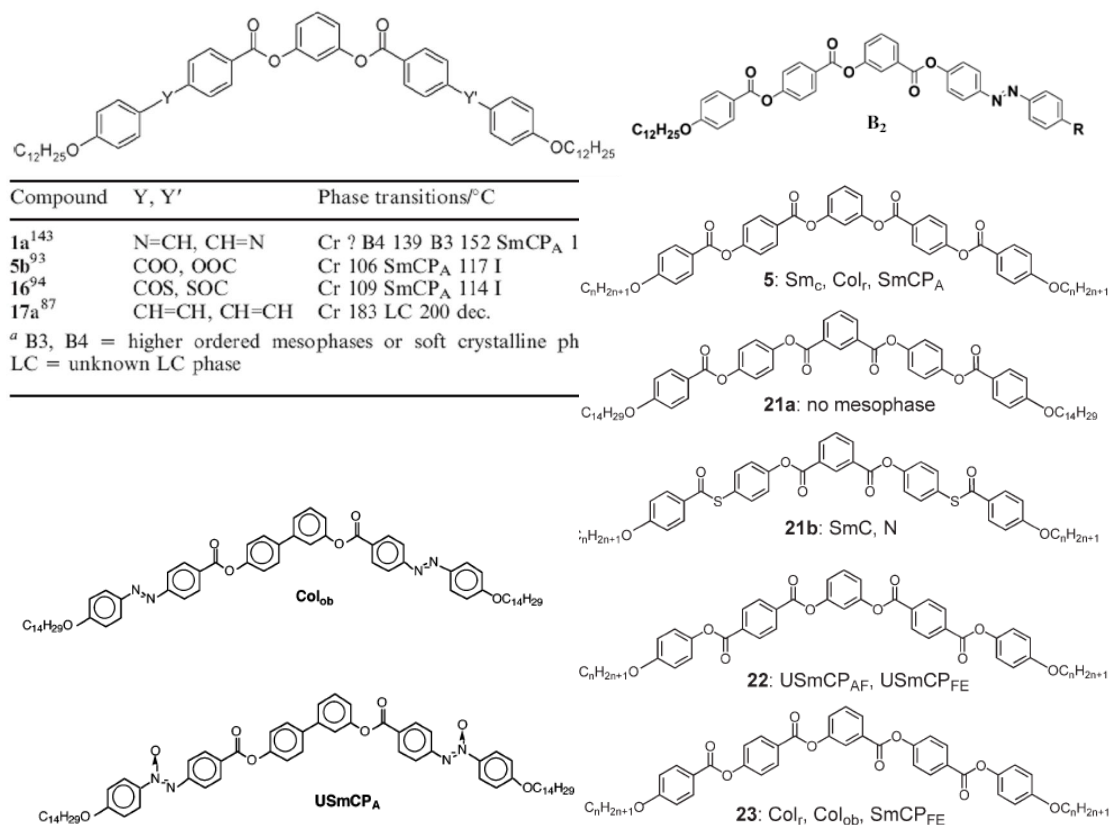
Figure 1.20. The configuration effects of bent-core structures by different linking groups on mesophasic varieties.[5,7,15b,27]

1.5.3. Lateral substitute

Lateral substitutes can be utilized to change the mesophasic types of bent-core structures. The common lateral substitutes like CH$_3$, Cl, F, Br, I, NO$_2$, CN, and OCH$_3$ groups are often used. Based on the discussions of Reddy's and Tschierke's article,[5] four kinds of analogous bent-core structures were approximately chosen to compare the influence of lateral substitute effect on the varieties of mesophasic types (see Figure 1.21-1.23). The F substitute effect at different positions of bent-core structures with 1,3-disubstituted benzene and 2,7-disubstituted naphthalene units was shown in Figure 1.21.[28] In general, non-switching smectic, polar smectic, column rectangular, and column oblique phases were obtained in these structures with single or double F substitutes at different positions of bent-core. As shown in Figure 1.22, the Schiff's

base derivative bent-core structures with NO_2, CN, and F substitutes displayed the influence of lateral substitute effect on mesophasic varities[16-18,29] The B_7 phase was revealed in the structures with NO_2 and CN substitutes at the internal position of central ring. The B_5 phase was exhibited in the structures with F substitutes at the external position of central and terminal rings. Otherwise, B_4 and SmCP phases were observable in other kinds of Schiff's base derived bent-core structures. Many kinds of bent-core molecules such as those compounds shown in Figure 1.23 revealed that mesophases and mesophasic range could be modified depending on lateral substitutes and their positions.[7,25a,30] According the comparison of the forgoing comparisons of lateral substituted effect in bent-core structures, those are clearly indicated that the influence of the substitutes strongly depends on the position of the bent-core molecule.

Figure 1.21. The lateral substitute effects of bent-core structures with phenyl and naphthenyl central rings on mesophasic varieties. [5,28]

Compound	C, D	Phase transitions/°C
34a[104b] (OC8H17)	H, H	Cr 150 SmCP_A 180 I
34b[104b]	F, H	Cr 140 SmCP_A 142 I
34c[104,178]	H, F	Cr 112 B5_FE 123 B5_A 128 SmCP_A 157 I
34d[199]	H, Cl	Cr 59 B7_FE[*] 114 SmCP_A[*] 137 I

Compound	n	C, D	Phase transitions/°C
35a	12	H, H	Cr 88 B7 173 I
35b	12	F, H	Cr 88 B7 156 I
35c	12	H, F	Cr ? B7 168 I
35d	8	H, Cl	Cr 117 B7 148 I

Compound	n	C, D	Phase transitions/°C
1a[104b]	12	H, H	Cr ? B4[*] 139 B3 152 SmCP_A 174 I
32a[104b]	12	F, H	Cr 118 SmCP_A 144 I
32b[72c,112,114]	12	F, H	Cr 120 (B4[*] 98) SmCP_A[*] 132 U^mSmC_sP_F[*a] 160 I
32c[112,113]	8	H, Cl	Cr 56 X 65 U^mSmC_sP_F 132 I

[a] Smectic phase with domains of opposite chirality helical filaments were also observed during the growth, at first this phase was assigned to SmCG,[72c] but later assigned to U^mSmC_sP_F[*], a B7-subtype (modulated-undulated SmC_sP_F phase).[112]

Compound	C, D	Phase transitions/°C
33a	H, H	Cr 115 SmCP_A 151 I
33b	F, H	Cr 100 SmCP_A 130 I
33c	H, F	Cr 111 SmCP_FE (B7') 157 I
33d	F, F	Cr 136 SmCP_FE/AF (B7')[b] 163 I

[a] Abbreviations: B7' = B7-like, mesophase showing helical filaments during the growth. [b] Depending on the strength of the applied voltage either FE or AF switching is observed.

36: Cr 160 °C B7 192 °C I

Figure 1.22. The lateral substitute effect for series of bent-core structures bearing different directions of C=N and COO linking groups on varieties of mesophases. [16-18,29]

Compound	D	D'	Phase transitions/°C
40a[87]	NO_2	NO_2	Cr 142 Col_r 150 SmC 151 I
40b[123]	NO_2	OCH_3	Cr 99 SmCP_A(X) 106 SmAP_R 118 I
40c[123]	NO_2	Cl	Cr 122 SmCP_A(X) 128 SmAP_R 138 I
40d[123]	NO_2	I	Cr 89 Col_obP_AF 113 SmAP_R 126 I
40e[63]	F	F	Cr 152 (SmC_sP_A 145) I
40f[63]	I	I	Cr 106 I
40g[123]	Cl	F	Cr 136 SmCP_A(Y) 142 I
40h[123]	Cl	I	Cr 127 (SmCP_A(Y)115) I

[a] Abbreviations: SmCP_A(X), SmCP_A(Y) = structure is different from conventional SmCP_A phases, but not clear yet. SmAP_R = FE polar switching smectic A phase with non-correlated layers.

Compound	D	D'	Phase transitions/°C
39a[122]	H	H	Cr 183 LC 200 dec.
39b[63]	F	F	Cr 137 SmCP_A[*] 164 I
39c[122]	Cl	Cl	Cr 116 SmCP_A (B7') 144 I
39d[122]	Br	Br	Cr 118 SmCP_A (B7') 131 I
39e[63]	I	I	Cr 114 B7 123 I
39f[122]	OCH_3	OCH_3	Cr 127 I
39g[87]	NO_2	NO_2	Cr 142 Col_r 150 Sm_c 151 I
39h[123]	NO_2	F	Cr 128 B_XP 157 I
39i[123]	NO_2	Cl	Cr 114 Col_obP_AF 147 I
39j[123]	NO_2	I	Cr 113 Col_r 135 I

[a] Abbreviations: Col_obP_AF = AF polar switching columnar phase with an oblique cell; B_XP mesophase with unknown structure.

7a: A = H: Cr 85 °C SmCP_A 162 °C I
41a: A = OH: Cr 42 °C SmCP_A 135 °C I

29: (a - f = H or F): Col_r, SmCP_A

Figure 1.23. The lateral substitute effects of five-ring bent-core structures with C=C and COO linking groups and six-ring bent-core structures on mesophasic varieties. [7,25a,30]

1.5.4. Bent-core dimer

The first example of bent-core dimer was published by Tschierske et al, which are the structures with two bent-core units linking by the siloxyl spacer in the central part (see Figure 1.24).[31a] Few kinds of bent-core dimers have been developed and polar switchable SmCP and columnar phases were also enhanced.[31] Up to now, this kinds of reported literatures are very limited. The influence of bent-shaped configuration effects are not studied thoroughly yet.

1 (n = 1): Cr 64 [27.7] SmCP$_F$* 132 [41.2] Iso
2 (n = 2): Cr 92 [16.6] SmCP$_A$ 132 [41.8] Iso
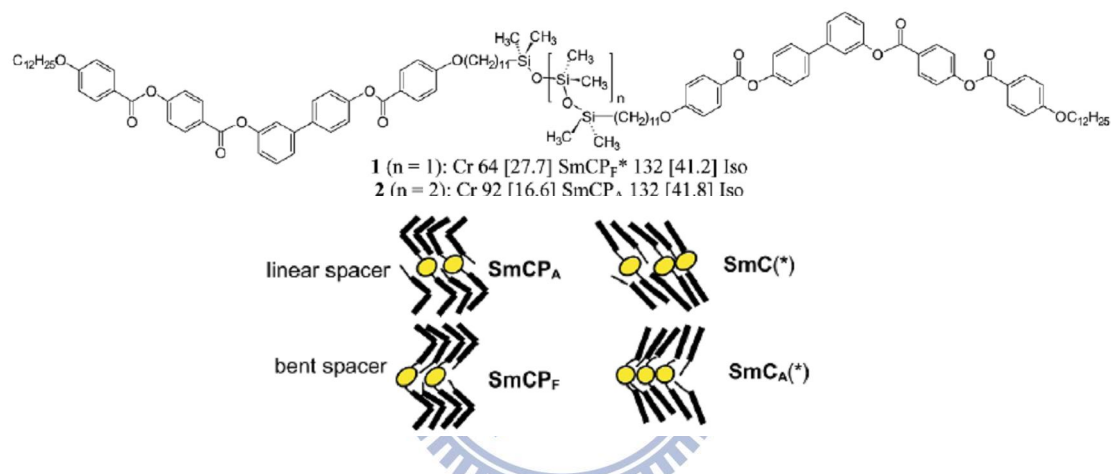
Figure 1.24. The example of bent-core dimers. [31a]

1.5.5. Bent-core main-chain polymer

The researches of bent-core main-chain polymer are still few. As the polymeric molecule shown in Figure 1.25, which was reported by Serrano et al,[32d] SmCP phase was obtained and its fundamental mesophasic studies were demonstrated. Concerning the fully covalent-bonded bent-core polymers, since the example of the bent-core main-chain polymer with a polar smectic mesophase was synthesized, the polar switching behavior has been declared to exist in the polymeric framework.[32c]
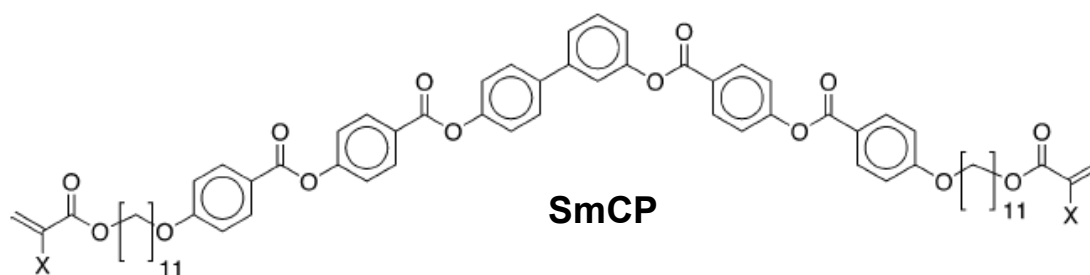
Figure 1.25. The example of bent-core main-chain polymer. [32d]

1.5.6. Bent-core side-chain polymer

Up to now, the first case of the bent-core side-chain polymer, where the bent-core units were connected by siloxyl spacers, displayed clear ferroelectric switching properties (see Figure 1.26).[33a] Interestingly, the switching current behavior of the SmCP phase in the monomeric units was sustained and the ferro-electricity could be modified by the polymer structural design of dimethylsiloxane diluted polysiloxane side-chain copolymer frameworks. However, just only scarce cases of bent-core side-chain polymers were achieved with barely detectable polar switching properties (see Figure 1.26).[33] To retain the electro-optical switching behavior in the bent-core structures is constantly the important assignment in the field of banana-shaped LC research. Even if many kinds of bent-core small molecular systems displayed particular polar switching current behaviors, duo to the higher viscosities and larger inter-/intra-molecular interactions in polymers, such switching current behaviors were not easy to be obtained (or detected) in analogous bent-core polymer derivatives.

1.5.7. Bent-core dendrimer

The first example of bent-core dendrimer based on carbosilyl core was reported with polar switchable mesophases by Tschierske et al. (see Figure 1.27). Later, the related dendrimers based on POSS and DAB dedritic core were also synthesized. However, the published articles in this field are still limited.[34]

26

Poly-1: Cr 67 (g 29) SmCP$_F$ 119 Iso

R=H, m=12, PAC12

R=CH$_3$, m=6, PMAC6

R=CH$_3$, m=12, PMAC12
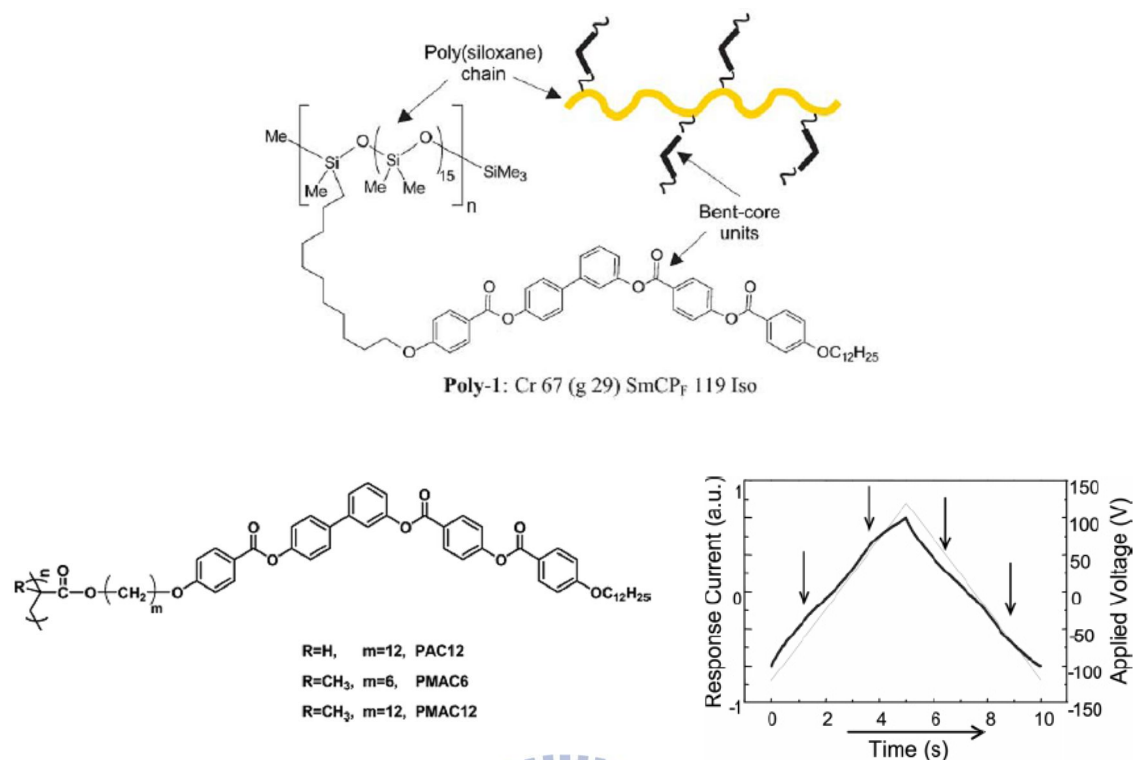
Figure 1.26. The example of bent-core side-chain polymers. [33]

1a (X = CH$_2$)
1b (X = O)
1b: Cr 92 (SmCP$_A$ 74) Iso

Den-3H:
R = H

Den-1H:
R = H

BC =

Den-1 (4 x R, R = BC): Cr 73 SmCP$_A$[*] 111 Iso

Den-3 (1 x OMe, 15 x R, R = BC): Cr 79 SmCP$_A$[*] 113 Iso
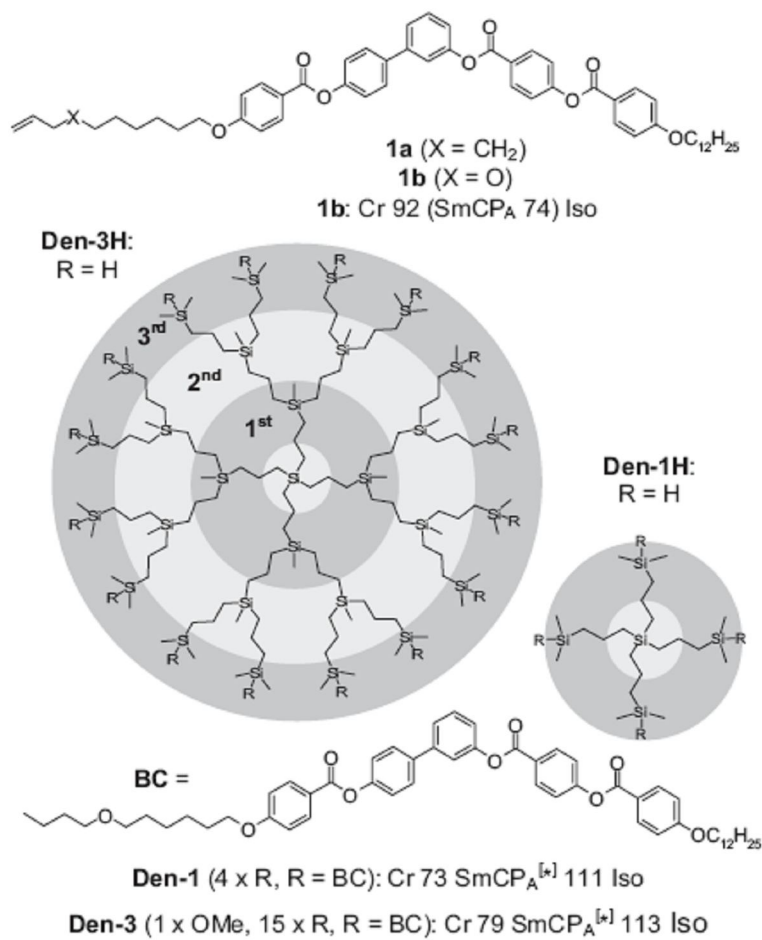
Firgure 1.27. The example of bent-core dendrimers. [34b]

27

Figure 1.28. The mesophasic varieties of siloxyl terminal subsituted bent-core structures depending on various siloxyl terminal linkages and various positions of F lateral substitutes.[35]

1.5.8. Bent-core structures with silyl and siloxyl linkages

The silyl and siloxyl linkages are the useful functions to decrease and extend the mesophasic transition temperatures and ranges, respectively. Up to now, this research field has been developed thoroughly, which was mainly studied by Tschierske et al. In addition, the lateral substituted effect in bent-core structures with silyl or siloxyl linkages was also investigated.[35] As shown in Figure 1.28, The FE and AF switching behaviors could be modified by the turning of siloxyl number, and SmC_SP_F phase was mainly obtained in bent-core structures bearing more than two siloxyl terminal linkages. Regarding the lateral substituted effect of bent-core structures with siloxyl terminal linkages on mesophasic varieties, AF/FE SmCP and $Col_{ob}P_A$ phases were observable in those bent-core structures. Interestingly, lower mesophasic transition

temperatures were achieved in almost silyl and siloxyl substituted bent-core structures. For instance, the six-ring bent-core molecule with three siloxyl members, where the C and D positions bear F substitutes, possessed the lowest mesophasic transition temperature (41°-125°).

1.5.9. Bent-core metallo structures

As shown in Figure 1.29, the examples of bent-core metallo structures were performed.[36] However, the polar switchable mesophase was not received in this case. It was suggested that the metallo insertion would destroy the bent-shaped molecular stacking and the polar order duo to the influence of stronger electron field, which is contributed from metal factor. Up to now, these kind of published articles are still lacking.

$[Ln(L11)(NO_3)_3]$ (9-13) : R = $C_{12}H_{25}$

$[Ln(L11)(CF_3CO_2)_3(H_2O)]$ (14) : R = $C_{12}H_{25}$
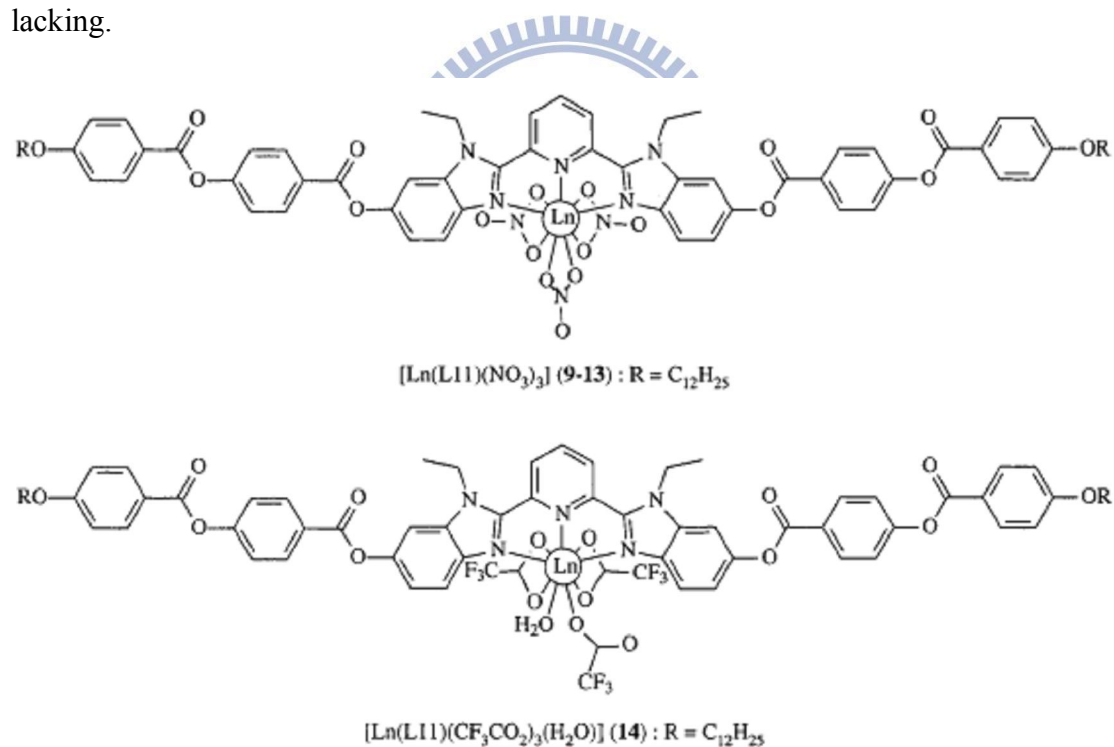
Figure 1.29. The examples of bent-core metallo structures. [36]

1.5.10. Bent-core nanocomposite architectures

The bent-core supra-structure, which connected with nanoparticle, was firstly reported by Hegmann et al. However the pure bent-core nanocomposite architecture

did not exhibited any mesophase. It was used to be an organic-inorganic guest dopant in five-ring fully covalent-bonded bent-core molecular host by very less doping ratios. The mesophasic varieties were studies and their surface arrangements were also investigated by High-resolution TEM instrument (see Figure 1.30).[37]
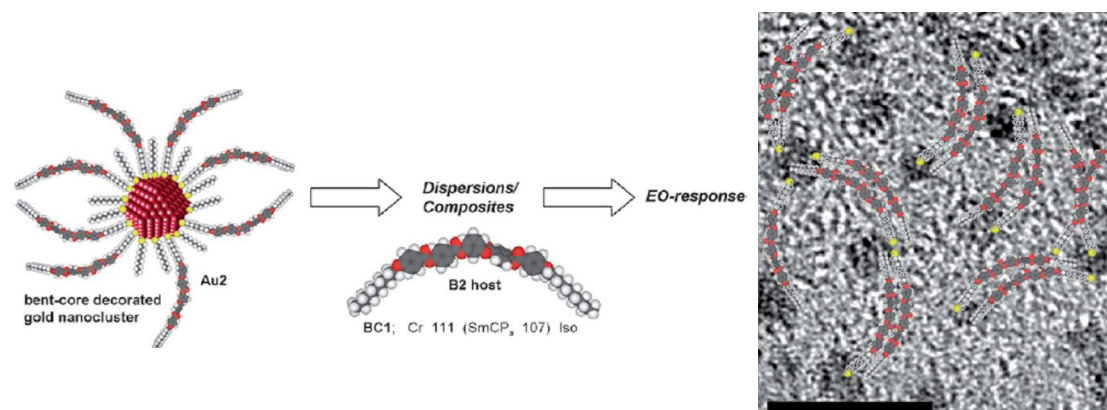
Figure 1.30. The example of the bent-core anocomposited structures/mixtures and there TEM image. [37]

1.5.11. Bent-core H-bonded supramolecules

Hydrogen bond (H-bond) can be seen a kind of linkage, which is often used to form a novel molecular configuration by connecting with two structural parts. In recent years, this smart linking method has been utilized in bent-core molecular designs. As shown in Figure 1.31, the first example of bent-core H-bonded structure was published by Serrano et al, which revealed the polar switchable SmCP phase. Later, several kinds of bent-core H-bonded molecular configurations were also developed.[38] However, the polar switching behavior seems only to be demonstrated in single H-bonded bent-core structures. Based on our researches in this dissertation, H-bond would destroy the intra-molecular dipole moment to cause the less contribution in double H-bonded bent-shaped molecules.[39] The detailed discussions will be further described later.
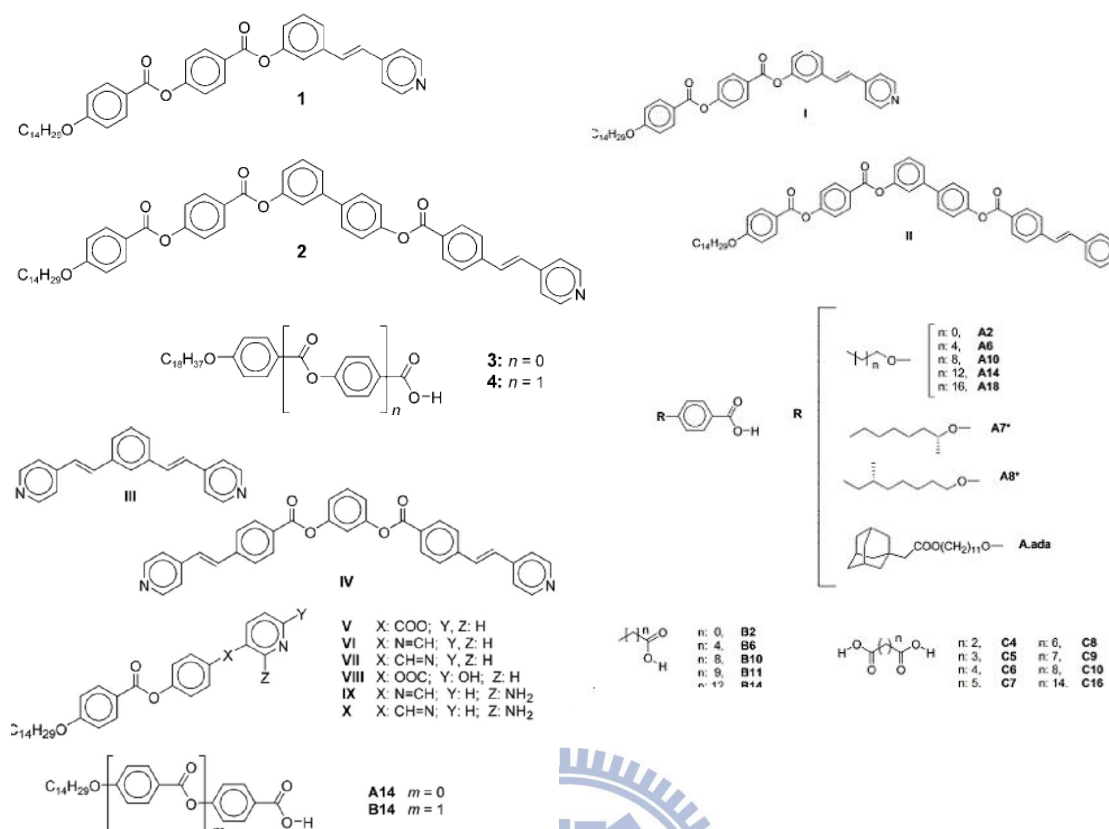
Figure 1.31. The examples of bent-core H-bonded structures.[38]

1.6. Research Motive

Supramolecular conception bearing noncovalent bond segments, e.g. hydrogen-bonds (H-bonds), was investigated and developed because of its functional properties and extensive availabilities by the molecular design of inter- or intra-molecular configurations. Self-assembed phenomena through molecular recognition between complementary constituents have been explored in various areas, such as biomaterials, liquid crystalline (LC) materials and materials for electro-optical applications. Interestingly, supramolecular approaches have been employed ripely in mesomorphic studies to establish self-assembled molecules, such as H-bonded mesogens.

In recent years, the supramolecular bent-core model in which two complementary segments were linked through H-bonds was referred. So far, few

31

records regarding H-bonded banana-shaped liquid crystals with given fundamental electric and optical behavior were reported, and their analogous side-chain polymers were developed by Serrano's group. However, the comprehensive influences of the number and site of H-bonds on the spontaneous polarization and switching current behavior of banana-shaped liquid crystalline supramolecules were lacking. In addition, the influence of H-bonds on the threshold voltages of (anti)ferroelectric switching phenomena and the investigations of dipole moment and bent angle effects on polar switching behaviors in bent-core H-bonded supramolecules were still not reported. Moreover, to retain the electro-optical switching behavior in the bent-core structures is constantly the important assignment in the field of banana-shaped LC research. However, even if many kinds of bent-core H-bonded small molecular systems displayed particular polar switching current behaviors, duo to the higher viscosities and larger inter-/intra-molecular interactions in polymers, such switching current behaviors were not easy to be obtained (or detected) in analogous pure bent-core H-bonded polymer derivatives.

Hence, we will focus the purpose on bent-core H-bonded researches, which are containing five topics: (i) H-bonded banana-shaped supramolecules with single and double H-bonded linkages, (ii) H-bonded banana-shaped liquid crystalline dimeric complexes and main-chain Polymers, (iii) H-bonded supramolecular side-chain banana-shaped liquid crystalline polymers/copolymers, (iv) bent-core covalent- and H-bonded polymeric/small-molecular dopants, and (v) bent-core covalent- and H-bonded small-molecular dopants. The variations of mesomorphic and electro-optical properties influenced by H-bonded number and position effects in small-molecules, main-chain polymers, side-chain copolymers, small-molecular dopants, and polymeric/small-molecular dopants will be mainly investigated and further described at the next chapters (Chapter 2-6).

Capter 2

Configuration Effects of H-Bonded Sites and Rigid Core Lengths on H-Bonded Banana-Shaped Liquid Crystalline Supramolecules Consisting of Symmetric Trimers and Asymmetric Hetero-Dimers

2.1. Introduction

Supramolecular conception bearing noncovalent bond segments, e.g. hydrogen-bonds (H-bonds), was investigated and developed because of its functional properties and extensive availabilities by the molecular design of inter- or intra-molecular configurations. Self-assembed phenomena through molecular recognition between complementary constituents have been explored in various areas, such as biomaterials, liquid crystalline (LC) materials and materials for electro-optical applications.[40] Interestingly, supramolecular approaches have been employed ripely in mesomorphic studies to establish self-assembled molecules, such as H-bonded mesogens.[41] Ferroelectric and anti-ferroelectric liquid crystals (FLCs and AFLCs) become more important due to their fast response of electro-optical properties by applying external electric fields.[42] At early stages, the molecular design of FLCs was only confined to molecular structures having chiral centers. However, since the first example of the achiral bent-core (banana-shaped) mesogen possessing switchable behavior has been explored,[1a,12a] many kinds of bent-core liquid crystals were synthesized to examine the mesomorphic and electro-optical properties. Regarding the single bent-core molecules with low molecular weights, the configuration effects, such as various rigid core shapes, flexible chain lengths, and substituents at different

positions of rigid cores, were studied as well.[26,43,25a,28c,35a,] Furthermore, the bent-core molecules with rod-like rigid units attached to one end of the terminal flexible chains[44] and the special bent-core structures connnected with silicon groups at the centers or the termini of the flexible chains[45,25b] were inspected. In addition, polymeric,[32d,33] dimeric,[31,45a,46] and dendritic bent-core molecules[34] also have been developed. Hence, detailed studies of banana-shaped molecules with bent-core structures connected by normal covalent bonds have been surveyed thoroughly. In recent years, the supramolecular bent-core model in which two complementary segments were linked through H-bonds was referred.[5,47] One H-bonded bent-core system formed by oxadiazole mesogens was developed and only the SmA phase without switching behavior was exhibited.[48] So far, few records regarding H-bonded banana-shaped liquid crystals with given fundamental electric and optical behavior were reported, and their analogous side-chain polymers were developed by Serrano's group.[38] However, the comprehensive influences of the number and site of H-bonds on the spontaneous polarization and switching current behavior of banana-shaped liquid crystalline supramolecules were lacking. In addition, the influence of H-bonds on the threshold voltages of (anti)ferroelectric switching phenomena and the investigations of dipole moment and bent angle effects on polar switching behaviors in H-bonded bent-core supramolecules were still not reported.

Herein, in order to investigate the influence of H-bonded configurations (H-bonded linking positions, the aromatic ring numbers, and the chain lengths) in molecular skeletons on mesomorphic and electro-optical properties of bent-core structures, several series of novel banana-shaped supramolecules consisting of H-bonded symmetric trimers (with two H-bonds) and asymmetric hetero-dimers (with one H-bond) were self-assembled by appropriate molar ratios of proton donors (H-donors) and acceptors (H-acceptors). Three kinds of acidic H-donors (**Am**, **Bm**, and **Cm**) and
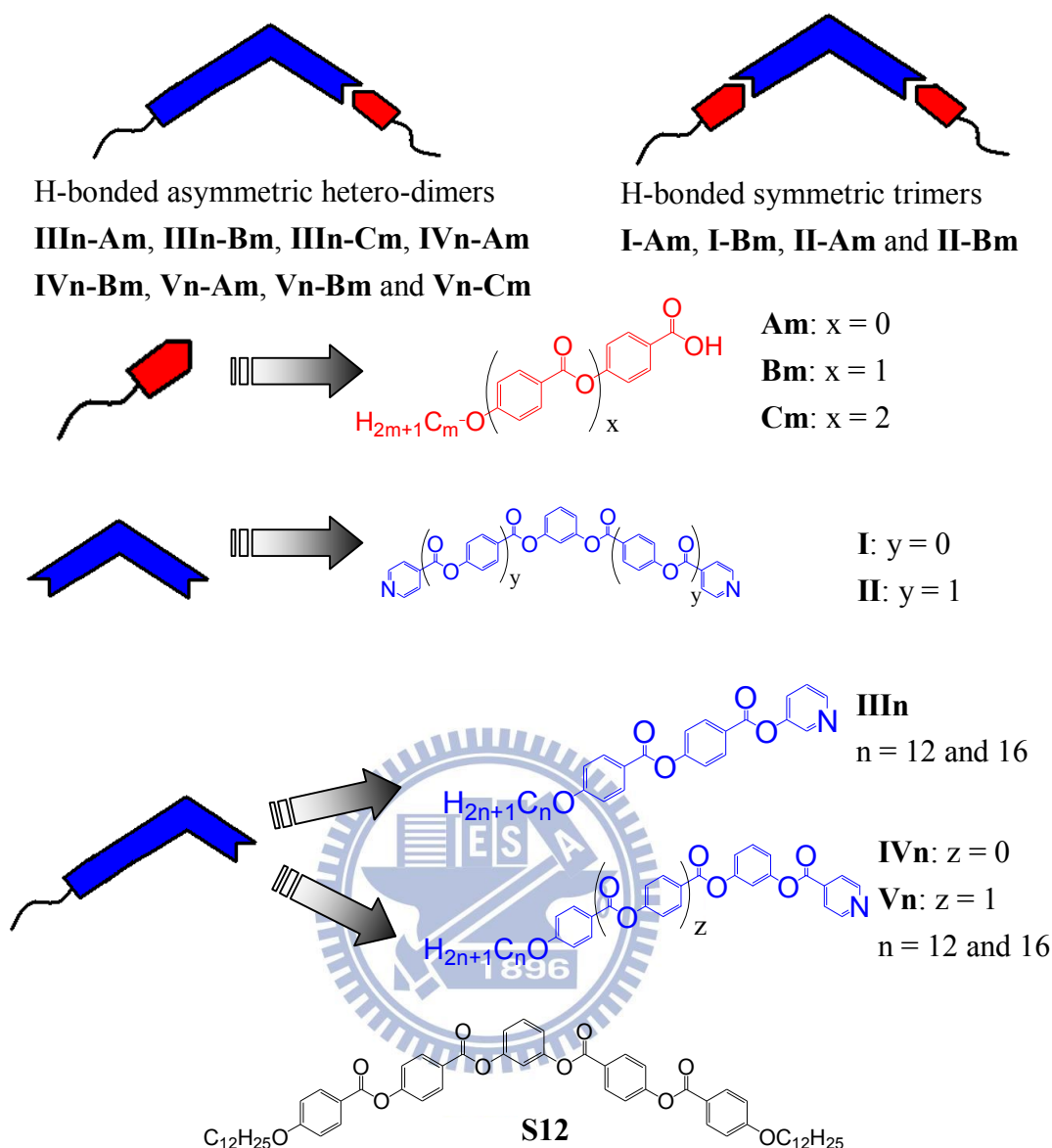
Figure 2.1. Chemical structures of fully covalent-bonded five-ring bent-core molecule **S12**, H-bonded bent-core symmetric trimers (with two H-bonds), and asymmetric dimers (with one H-bond) containing acidic H-donors (**Am**, **Bm**, and **Cm**) and pyridyl H-acceptors (**I-II** and **IIIn-Vn**).

five kinds of bent-core H-acceptors (**I-II** and **IIIn-Vn**, bearing double and single terminal pyridyl groups, respectively) were synthesized and displayed in Figure 2.1. H-bonded symmetric supramolecules were self-assembled by bis-pyridyl H-acceptors (**I-II**) with acidic H-donors (**Am** and **Bm**) to form trimers (with two H-bonds), where acidic H-donor **Cm** was not used due to the super-high transition temperatures of their

supramolecules consisting of **Cm** and H-acceptors (**I-II**). H-bonded asymmetric supramolecules were self-assembled by single-pyridyl H-acceptors (**IIIn-Vn**) with acidic H-donors (**Am**, **Bm**, and **Cm**) to form hetero-dimers (with one H-bond). In contrast to the fully covalent-bonded structures, the H-bonded effects of H-bonded symmetric trimers (with two H-bonds) and asymmetric hetero-dimers (with one H-bond) with analogous H-bonded configurations on mesomorphic and electro-optical properties were investigated. The mesomorphic and electro-optical properties of all H-bonded complexes were examined and surveyed by polarizing optical microscopy (POM), differential scanning calorimetry (DSC), powder X-ray diffraction (XRD) measurements and electro-optical (EO) switching experiments. The variation of polar switching behavior for H-bonded symmetric trimers (with two H-bonds) and asymmetric hetero-dimers (with one H-bond) were evaluated by the theoretical calculation of electron cloud dispersions, dipole moments, and bent angles.
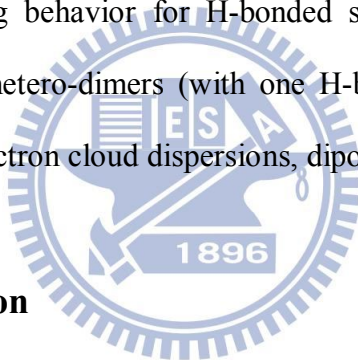
2.2 Experimental Section

2.2.1. Characterization methods

^{1}H NMR spectra were recorded on a Varian Unity 300 MHz spectrometer using DMSO-d_6 and CDCl$_3$ as solvents. Mass data were measured by a Micromass TRIO-2000 GC-MS. Elemental analyses (EA) were performed on a Heraeus CHN-OS RAPID elemental analyzer. Mesophasic textures were characterized by polarizing optical microscopy (POM) using a Leica DMLP equipped with a hot stage. Infrared (IR) spectra were investigated by Perk-Elmer Spectrum 100 instrument. Temperatures and enthalpies of phase transitions were determined by differential scanning calorimetry (DSC, model: Perkin Elmer Pyris 7) under N$_2$ at a heating and cooling rate of 5 °Cmin^{-1}. Synchrotron powder X-ray diffraction (XRD) measurements were performed at beamline BL17A of the National Synchrotron Radiation Research

Center (NSRRC), Taiwan, where the wavelength of X-ray was 1.334431 Å. The XRD data were collected using imaging plates (IP, of an area = 2 × 40 cm^2 and a pixel resolution of 100) curved with a radius equivalent to a sample-to-image plate distance of 280 mm, and the diffraction signals were accumulated for 3 min. The powder samples were packed into a capillary tube and heated by a heat gun, where the temperature controller is programmable by a PC with a PID feedback system. The scattering angle theta was calibrated by a mixture of silver behenate and silicon. The electro-optical properties were determined in commercially available ITO cells (from Mesostate Corp., thickness = 4.25 μm, active area = 1 cm^2) with rubbed polyimide alignment coatings (parallel rubbing direction). A digital oscilloscope (Tektronix TDS-3012B) was used in these measurements, and a high power amplifier connected to a function generator (GW Model GFG-813) with a d.c. power supply (Keithley 2400) was utilized in the d.c. field experiments. During electro-optical measurements, the modulations of textures by applying electric fields were observed by POM. The dielectric permittivity studies were investigated by a impedance/gain-phase analyzer (HP4194A) in non-rubbing cells with a cell gap of 9 μm at a frequency of 5 kHz and various cooling temperatures.

2.2.2. Computational method

Sets of low energy structures were obtained from systematic pseudo Monte Carlo search using MacroModel V 9.5 with an all-atom amber* force-field in gas phase on each bent-core structures of **S1**, **I-A1**, **IV1-A1**, and **III1-B1.**[49] 5000 structures were sampled (with an energy window of 5 kcal/mol) for each search and they were minimized using PR conjugated gradient method to obtain the lowest energy structure in each simulation. Unique conformations within 1 kcal/mol of the global minimum were used in full geometry optimization using Gaussian03 at B3LYP level with 6-31G(d) basis set.[50]

2.2.3. Synthesis

All synthetic processes were followed according to five routes shown in Scheme S1 (see Supporting Information). The esterification reactions were carried out via two procedures (i.e., steps i and iii) to acquire related products. Protecting reactions were proceeded by step iv. De-protecting actions were executed by two procedures (i.e., steps ii and v) to eliminate protecting groups. In addition, the starting compounds **Am** (**m** = 12 and 16) were prepared according to the literature procedures,[16] and all synthetic details were described in the Supporting Information.

2.2.4. Sample preparation

All H-bonded complexes were constructed by mixing appropriate molar ratios of proton donors (H-donors) and acceptors (H-acceptors) in the solutions of chloroform/THF (ca. 1:1 vol.), which were self-assembled into supramolecules by evaporating solvents slowly. Several series of H-bonded bent-core structures with 4-8 aromatic rings were formed in two types of configurations: (i) asymmetric hetero-dimers (with one H-bond) consisting of single-pyridyl H-acceptors (**IIIn-Vn**, where **n** = 12 and 16) with acidic H-donors (**Am**, **Bm**, and **Cm**, where **m** = 12 and 16); (ii) H-bonded symmetric trimers (with two H-bonds) consisting of bis-pyridyl H-acceptors (**I-II**) with acidic H-donors (**Am** and **Bm**, where **m** = 12 and 16).

2.3. Results and Discussion

2.3.1. Mesophasic and thermal properties of H-bonded asymmetric hetero-dimers (with one H-bond):

2.3.1.1. Four- and five-ring systems (IIIn-Am, IIIn-Bm, and IVn-Am). In order to understand the influence of H-bonded sites (at the rigid cores) on mesomorphic, molecular stacking, and thermal properties, H-bonded four- and five-ring asymmetric hetero-dimers, i.e., **IIIn-Am**, **IIIn-Bm**, and **IVn-Am** (**n**, **m** = 12 and 16), were
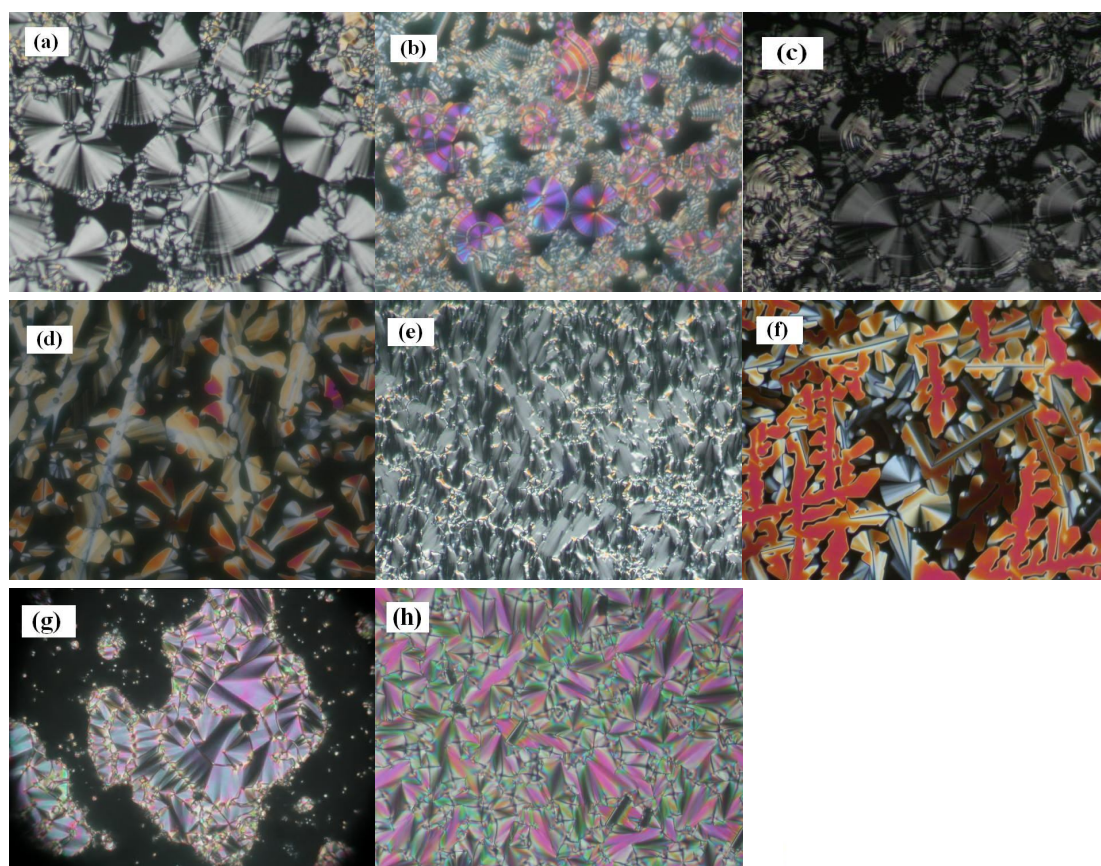
Figure 2.2. POM textures at the cooling process: (a) the polar smectic phase with the spherulite texture of complex **IV12-A12** at 96 °C; (b) the polar smectic phase with spherulite and non-specific grainy textures of complex **IV12-B16** at 100 °C; (c) the polar smectic phase with spherulite and stripe textures of complex **V12-A12** at 100 °C; (d) the Col$_r$ phase with dendritic- and mosaic-like textures of complex **V12-B12** at 120 °C; (e) the polar smectic phase with the fan-like texture of complex **V16-B16** at 140 °C; (f) the Col$_r$ phase with dendritic- and mosaic-like textures of complex **V12-C12** at 130 °C; (g) the smectic A phase with the fan-like texture of complex **III16-B16** at 110 °C. (h) the smectic A phase with the fan-like texture of complex **III16-A16** at 95 °.

investigated by POM and DSC measurements. In addition, an analogous fully covalent-bonded structure **S12** (**n** = 12) with five rings (see Figure 2.1), which has been reported by Pelzl et al,[2,4] was compared as well. Furthermore, their mesophasic textures, phase transition temperatures, enthalpy values are shown in Figure 2.2 (a, g, and h), Figure 2.3a, and Table 2.1. All complexes **IIIn-Am** and **IIIn-Bm** (**n**, **m** = 12

and 16) possessed the smectic A (SmA) phase, which were verified by POM to show the enantiotropic fan-like texture. For instance, the fan-like texture of complexes **III16-A16** and **III16-B16** are demonstrated in Figs. 2h and 2g, respectively. However, complexes **IVn-Am** revealed a polar smectic (B2 or SmCP) phase[11,27a,52] in both heating and cooling processes, and the POM texture of complex **IV12-A12** is shown in Figure 2.2a.

Regarding H-bonded four- and five-ring asymmetric hetero-dimers **IIIn-Am** and **IIIn-Bm** with different bent-core lengths (4 and 5 rings) but the same near-central H-bonded sites at the rigid cores, complexes **IIIn-Bm** bearing longer bent-core lengths (5 rings) possessed higher phase transition temperatures and broader SmA phase ranges than analogous complexes **IIIn-Am** (4 rings). To compare the mesophasic type of five-ring complexes **IIIn-Bm** and **IVn-Am** with different H-bonded sites at the rigid cores, the SmCP and SmA mesophases were achieved for supramolecular mesogens with far- and near-central H-bonded sites, respectively. This phenomenon suggested that the polar smectic phase would be preferred if the H-bonded site was far away from the bent-core center in supramolecular design, which means the higher stability of the SmCP phase was induced by longer covalent-bonded bent cores of **IVn** in complexes **IVn-Am**. Moreover, the isotropization temperatures of complexes **IIIn-Bm** are higher than those of complexes **IVn-Am** due to the relatively higher isotropization temperatures of H-donors **Bm** with longer rigid cores in analogous **Am** and **Bm** (**m** = 12 and 16). In comparison with analogous compound **S12**, complexes **IVn-Am** show lower phase transition temperatures and similar mesophasic ranges.

Table 2.1. Phase Transition Temperatures and Enthalpies of H-Bonded Four- and Five-Ring Asymmetric Hetero-Dimers (with One H-Bond)

IIIn-Am (x = 1)

IIIn-Bm (x = 2)

IVn-Am

Complex	n	m	x		Phase transition temperature/^{o}C [Enthalpy/kJ/g]			
III12-A12	12	12	1	**I**	114.3 [20.5]	**SmA**	71.2 [69.8]	**K**
III12-A16	12	16	1	**I**	105.0 [14.0]	**SmA**	70.4 [152.1]	**K**
III16-A12	16	12	1	**I**	114.6 [25.0]	**SmA**	69.1 [49.3]	**K**
III16-A16	16	16	1	**I**	103.9 [14.3]	**SmA**	80.6 [146.5]	**K**
III12-B12	12	12	2	**I**	149.0 [7.5]	**SmA**	99.0 [161.2]	**K**
III12-B16	12	16	2	**I**	149.1 [9.6]	**SmA**	96.3 [169.8]	**K**
III16-B12	16	12	2	**I**	128.0 [10.8]	**SmA**	91.2 [135.0]	**K**
III16-B16	16	16	2	**I**	128.1 [8.2]	**SmA**	96.2 [157.2]	**K**
IV12-A12	12	12	—	**I**	99.2 [27.1]	**SmCP**	91.7 [22.3]	**K**
IV12-A16	12	16	—	**I**	96.5 [21.3]	**SmCP**	86.9 [30.1]	**K**
IV16-A12	16	12	—	**I**	88.2 [17.2]	**SmCP**	75.0 [33.4]	**K**
IV16-A16	16	16	—	**I**	119.0 [20.7]	**SmCP**	103.7 [54.1]	**K**

I = isoptropic state; SmA = smectic phase with no (or less) tilt angle arrangements; SmCP = polar tilt smectic phase; K = crystalline state. The phase transitions were measured by DSC at the 2nd cooling scan with a cooling rate of 5 °C/min. Phase transitions of compound **S12** were obtained as **I** 119.0 [22.5] **CmCP** 109.0 [41.9] **K**.

2.3.1.2. Six-ring systems (IIIn-Cm, IVn-Bm, and Vn-Am). Three series of comparable six-ring asymmetric hetero-dimers, i.e., **IIIn-Cm**, **IVn-Bm**, and **Vn-Am** (**n**, **m** = 12 and 16), were investigated for the influence of different H-bonded sites (at the rigid cores) on their mesophasic types and phase transition temperatures as shown

Table 2.2. Phase Transition Temperatures and Enthalpies of H-Bonded Six-Ring Asymmetric Hetero-Dimers (with One H-Bond)

Complex	n	m	Phase transition temperature/°C [Enthalpy/kJ/g]				
III12-C12	12	12	**I**	147.2 [20.3]	**N**	120.1 [2.7]	**K**
III12-C16	12	16	**I**	142.6 [25.0]	**N**	121.8 [2.3]	**K**
III16-C12	16	12	**I**	156.7 [17.8]	**N**	119.1 [3.6]	**K**
III16-C16	16	16	**I**	142.9 [11.9]	**N**	127.7 [3.1]	**K**
IV12-B12	12	12	**I**	113.8 [32.7]	**SmCP**	103.4 [64.1]	**K**
IV12-B16	12	16	**I**	111.3 [20.0]	**SmCP**	98.4 [50.7]	**K**
IV16-B12	16	12	**I**	114.4 [34.4]	**SmCP**	97.2 [82.6]	**K**
IV16-B16	16	16	**I**	116.5 [30.7]	**SmCP**	100.4 [98.2]	**K**
V12-A12	12	12	**I**	110.0 [19.6]	**SmCP**	91.4 [43.6]	**K**
V12-A16	12	16	**I**	113.7 [27.1]	**SmCP**	92.8 [39.4]	**K**
V16-A12	16	12	**I**	112.4 [22.8]	**SmCP**	93.6 [59.9]	**K**
V16-A16	16	16	**I**	115.5 [28.5]	**SmCP**	96.6[72.3]	**K**

I = isotropic state; N = nematic phase; SmCP = polar tilt smectic phase; K = crystalline state. The phase transitions were measured by DSC at the 2nd cooling scan with a cooling rate of 5 °C/min.

in Table 2.2 and Figure 2.3b. With respect to the mesophasic types, the enantiotropic nematic phase was obtained in complexes **IIIn-Cm** (**n, m** = 12 and 16) with near-central H-bonded sites (at the rigid cores) to indicate their loose molecular stackings, but analogous complexes **IVn-Bm** and **Vn-Am** (**n, m** = 12 and 16) exhibited SmCP phases owing to their far-central H-bonded sites, whose trends are

the same as five-ring asymmetric hetero-dimers **IVn-Am** with H-bonded sites far away from the bent-core centers. The mesophasic textures were examined by POM experiments, for instance, complex **IV12-B16** revealed spherulite and non-specific grainy textures in Figure 2.2b, and complex **IV12-A12** exhibited spherulite and stripe textures in Figure 2.2c, which suggested the polar smectic (SmCP) phase.

Comparing the phase transition temperatures of six-ring asymmetric hetero-dimers **IIIn-Cm**, **IVn-Bm**, and **Vn-Am** (Figure 2.3b), complexes **IIIn-Cm** revealed the highest isotropization temperatures due to the relatively much higher isotropization temperatures of ingredients in H-donors **Cm** with the longest rigid cores (see Supporting Information Figure S2.1 and Table S2.1) in analogous **Am**, **Bm**, and **Cm** (**m** = 12 and 16). Similar phenomena were also displayed in isotropization temperatures of five-ring complexes **IIIn-Bm** and **IVn-An**. Meanwhile, the SmCP phase ranges of **Vn-Am** are slightly wider than those of **IVn-Bm**, which might be due to the higher stability of the SmCP phase caused by longer covalent-bonded bent cores of **Vn** in complexes **Vn-Am**.

2.3.1.3. Seven- and eight-ring systems (IVn-Cm, Vn-Bm, and Vn-Cm). Three series of H-bonded seven- and eight-ring asymmetric hetero-dimers, i.e., **IVn-Cm**, **Vn-Bm**, and **Vn-Cm** (**n**, **m** = 12 and 16), were investigated for the influence of different H-bonded sites (at the rigid cores) and ring numbers on their mesophasic types and phase transition temperatures as shown in Table 2.3 and Figure 2.3c. Due to the large variation of solubilities in H-donors **Cm** and H-acceptors **IVn**, phase separation occurred in the preparation of complexes **IVn-Cm**, so these complexes could not be compared in this study. In regard to the mesophasic types, the nematic phase was observed in both series of complexes **Vn-Bm** and **Vn-Cm**. Besides, the rectangular columnar (Col$_r$ or B1) and SmCP phases were obtained in complexes **Vn-Bm** (**n, m** = 12 and 16) with seven rings (at

Table 2.3. Phase Transition Temperatures and Enthalpies of H-Bonded Seven- and Eight-Ring Asymmetric Hetero-Dimers (with One H-Bond)

IVn-Cm (x = 1, y = 2)
Vn-Bm (x = 2, y = 1)
Vn-Cm (x = 2, y = 2)

Complex	n	m	Phase transition temperature/^{o}C [Enthalpy/kJ/g]						
IV12-C12	12	12	Phase separation						
IV12-C16	12	16	Phase separation						
IV16-C12	16	12	Phase separation						
IV16-C16	16	16	Phase separation						
V12-B12	12	12	**I**	152.6 [1.9]	**N**	142.1 [28.5]	**Col$_r$**	107.0 [86.7]	**K**
V12-B16	12	16	**I**	156.9 [1.6]	**N**	148.2 [36.9]	**SmCP**	110.4 [92.2]	**K**
V16-B12	16	12	**I**	158.6 [2.0]	**N**	149.4 [38.8]	**SmCP**	101.9 [78.6]	**K**
V16-B16	16	16	**I**	155.4 [0.7]	**N**	152.5 [37.7]	**SmCP**	114.5 [96.5]	**K**
V12-C12	12	12	**I**	156.1 [31.1]	**N**	133.8 [2.0]	**Col$_r$**	92.2 [24.5]	**K**
V12-C16	12	16	**I**	159.0 [21.6]	**N**	147.3 [7.9]	**Col$_r$**	119.9 [50.1]	**K**
V16-C12	16	12	**I**	159.8 [12.3]	**N**	138.9 [4.4]	**Col$_r$**	104.7 [33.7]	**K**
V16-C16	16	16	**I**	158.4 [15.5]	**N**	147.9 [7.3]	**Col$_r$**	111.0 [48.4]	**K**

I = isoptropic state; N = nematic phase; Col$_r$ = column rectangular (Col$_r$) phase; SmCP = polar tilt smectic phase; K = crystalline state. The phase transitions were measured by DSC at the 2nd cooling scan with a cooling rate of 5 °C/min.

the rigid cores), where complex **V12-B12** demonstrated the Col$_r$ phase due to its shorter flexible chain length (**n, m** = 12). However, analogous complexes **Vn-Cm** (**n, m** = 12 and 16) with eight rings (at the rigid cores) exhibited only the Col$_r$ phase owing to their longer rigid cores in contrast to complexes **Vn-Bm** (with 7 rings). The mesophasic textures were evidenced by POM experiments, for example, complex **V16-B16** displayed the fan-like texture in Figure 2.2e as the evidence of the polar smectic (SmCP) phase, and complexes **V12-B12** and **V12-C12** exhibited dendritic-like and mosaic-like textures in Figures 2.2d and 2.2f, which were the

symbolic textures of the Col$_r$ phase. In general, complexes **Vn-Cm** (with 8 rings) had higher transition temperatures and wider nematic phase ranges than **Vn-Bm** (with 7 rings), where the wider nematic phase ranges in complexes **Vn-Cm** is due to their higher length ratios of rigid cores (with 8 rings) to flexible chains.

Overall, comparing all H-bonded asymmetric hetero-dimers (with one H-bond), complexes **IVn-Am**, **IVn-Bm**, **Vn-Am**, and **Vn-Bm** (**n, m** = 12 and 16, except **V12-B12**) possessed the SmCP phase. Furthermore, complexes **Vn-Bm** (**n, m** = 12 and 16, except **V12-B12**) had the highest transition temperatures and the widest ranges of the SmCP phase.
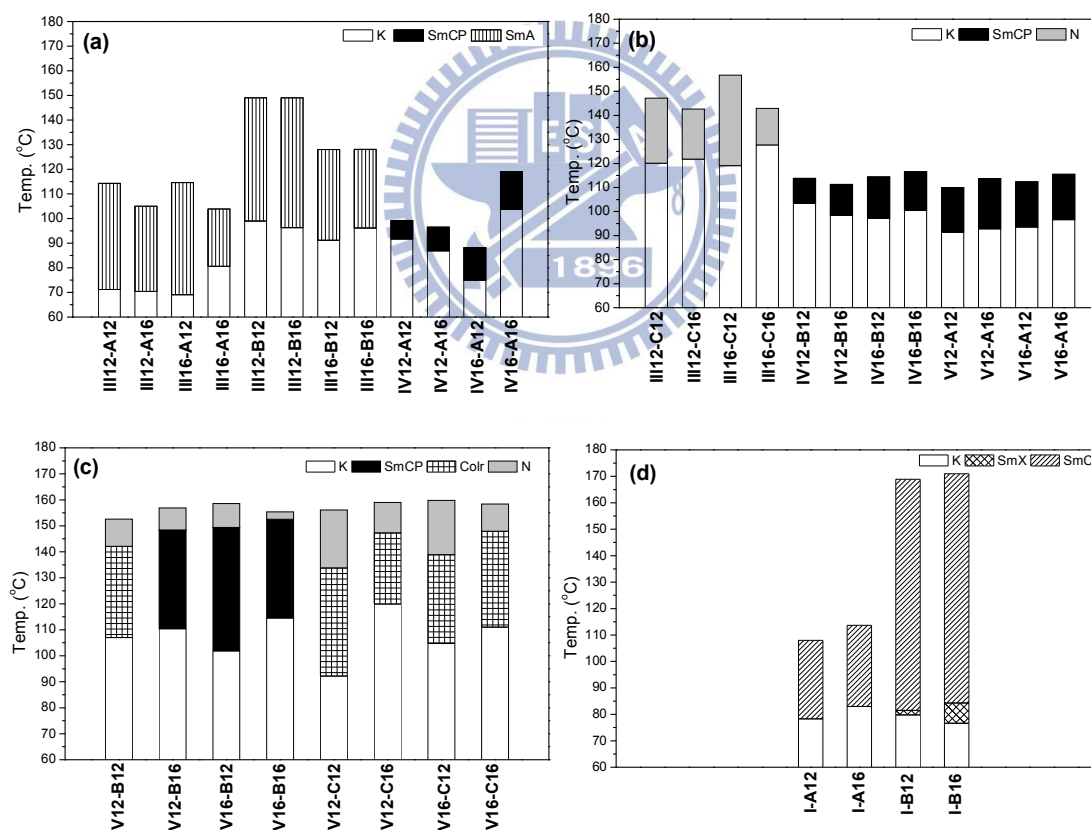
Figure 2.3. Phase diagrams (upon 2nd cooling) of asymmetric hetero-dimers: (a) four- and five-ring systems (**IIIn-Am, IIIn-Bm,** and **IVn-Am**); (b) six-ring systems (**IIIn-Cm, IVn-Bm,** and **Vn-Am**); (c) seven- and eight-ring systems (**Vn-Bm** and **Vn-Cm**), and symmetric trimers: (d) five- and seven-ring systems (**I-Am** and **II-Am**).

2.3.2. Mesophasic and thermal properties of H-bonded symmetric trimers (I-Am, I-Bm, II-Am, and II-Bm with two H-bonds)
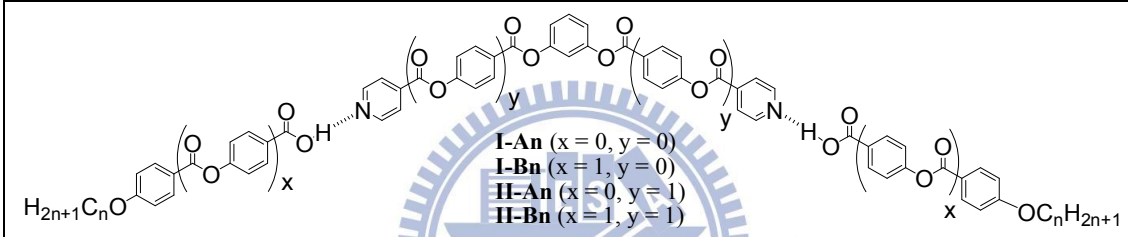
Four series of analogous symmetric trimers, i.e., **I-Am**, **I-Bm**, **II-Am**, and **II-Bm** (m = 12 and 16) with 5, 7, and 9 rings, were investigated for the influence of different ring numbers and H-bonded sites (at the rigid cores) on their mesophasic types and phase transition temperatures as shown in Table 2.4 and Figure 2.3d. Due to the large variation of solubilities in H-donors **Am**, **Bm**, and H-acceptor **II**, phase separation occurred in the preparation of complexes **II-Am** and **II-Bm**, so these complexes could not be compared in this study. Regarding the mesophasic types, a tilt smectic phase was observed in both series of complexes **I-Am** and **I-Bm** (**m** = 12 and 16), where a SmX phase was obtained in complexes **I-Bm** with seven rings (at the rigid cores). The mesophasic textures were observed by POM experiments, for instance, complex **I-A12** revealed the tilt smectic phase with spherulite and schlieren textures in Figure 2.4a, and complex **I-B12** exhibited the tilt smectic (SmC) phase with the fan-like texture in Figure 2.4b, which were the evidence of the tilt smectic (SmC) phase. Besides, complex **I-B12** demonstrated the undefined smectic phase with the arced fan-like texture in Figure 2.4c.
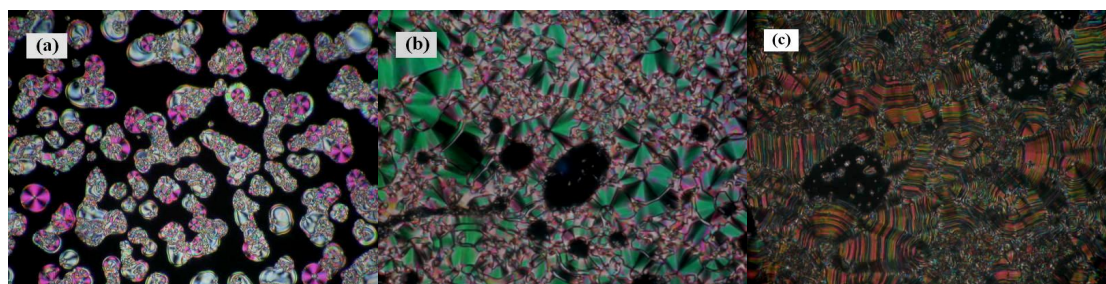
Figure 2.4. POM textures at the cooling process: (a) the till smectic phase with spherulite and schlieren texture of complex **I-A12** at 100 °C; (b) the till smectic phase with the fan-like texture of complex **I-B12** at 130 °C; (c) the undefined smectic phase with the arced fan-like texture of complex **I-B12** at 80 °C.

To compare the phase transition temperatures of symmetric trimers **I-Bm** and **I-Am** (**m** = 12 and 16) (Figure 2.3c), complexes **I-Bm** (with 7 rings) possessed higher isotropization temperatures and wider SmC phase ranges than complexes **I-Am** (with 5 rings) due to the longer rigid core of **I-Bm**. Overall, in contrast to H-bonded asymmetric hetero-dimers (with one H-bond), all H-bonded symmetric trimers (**I-Am** and **I-Bm** with two H-bonds) do not show the SmCP phase due to higher flexibilities of two H-bonds in the supramolecular complexes.

Table 2.4. Phase Transition Temperatures and Enthalpies of H-Bonded Symmetric Trimers (with Two H-Bonds)

I-An (x = 0, y = 0)
I-Bn (x = 1, y = 0)
II-An (x = 0, y = 1)
II-Bn (x = 1, y = 1)

Complex	m	Phase transition temperature/^{o}C [Enthalpy/kJ/g]					
I-A12	12	I	108.0 [4.4]	**SmC**	78.3 [46.8]	**K**	
I-A16	16	I	113.7 [11.8]	**SmC**	83.0 [53.3]	**K**	
I-B12	12	I	168.9 [14.6]	**SmC**	81.5 [31.9]	**SmX**	79.8[a]	**K**
I-B16	16	I	171.0 [14.1]	**SmC**	84.3 [29.6]	**SmX**	76.6 [18.3]	**K**
II-A12	12	Phase separation					
II-A16	16	Phase separation					
II-B12	12	Phase separation					
II-B16	16	Phase separation					

I = isotropic state; SmC = normal tilt smectic phase without polar switching behavior; B1 = column rectangular (Col$_r$) phase; SmX = undefinded smectic phase; K = crystalline state. [a] means the temperature data is observed in POM only. The phase transitions were measured by DSC at the 2nd cooling scan with a cooling rate of 5 °C/min.

2.3.3. IR characterization

In order to prove the formation of supramolecules, (compared with the transition temperatures of individual components in Figure S2.1 and Table S2.1 of the Supporting Information) new transition temperatures and homogeneous phase transitions of H-bonded complexes would be observed in DSC and POM measurements, respectively. In addition, the existence of H-bonds in these H-bonded complexes can be characterized by IR spectra at various temperatures. Therefore, two examples of asymmetric and symmetric H-bonded complexes are demonstrated as follows:

The IR spectra of H-bonded asymmetric complex **V16-B16** (with one H-bond) and its constituents **V16** (H-acceptor) and **B16** (H-donor) were compared in Figure 5 to examine the H-bonds in crystalline and mesophasic states. In contrast to the O-H band of pure **B16** (self-H-bonded dimeric acids) at 2546 cm^{-1}, and the weaker O-H bands observed at 2506 and 1920 cm^{-1} in the H-bonded complex **V16-B16** were indicative of hydrogen bonding between the pyridyl group of H-acceptor **V16** and acidic group of H-donor **B16**. On the other hand, a C=O stretching vibration appeared at 1742 cm^{-1} in complex **V16-B16**, which showed that the carbonyl group is in a less associated state than that in pure **B16** with weaker C=O stretching vibration appeared at 1729 cm^{-1} either in crystalline phase or mesophases (Figures 2.5a and 2.5b).[53] Both results suggested that H-bonds formed between **B16** and **V16** in both solid and mesophasic states of complex **V16-B16**.

In addition, similar IR analysis of H-bonds in symmetric H-bonded complex **I-B16** (with one H-bond) was inspected at various temperatures. With the IR evidence of weak O-H band at 2516 and 1914 cm^{-1} and less association of C=O stretching vibration at 1740 cm^{-1} as shown in Figs. 5c and 5d, it revealed the successful supramolecular framework of H-bonded complex **I-B16** by complexation of H-donor

48

B16 and H-acceptor **I** in 2:1 molar ratio.
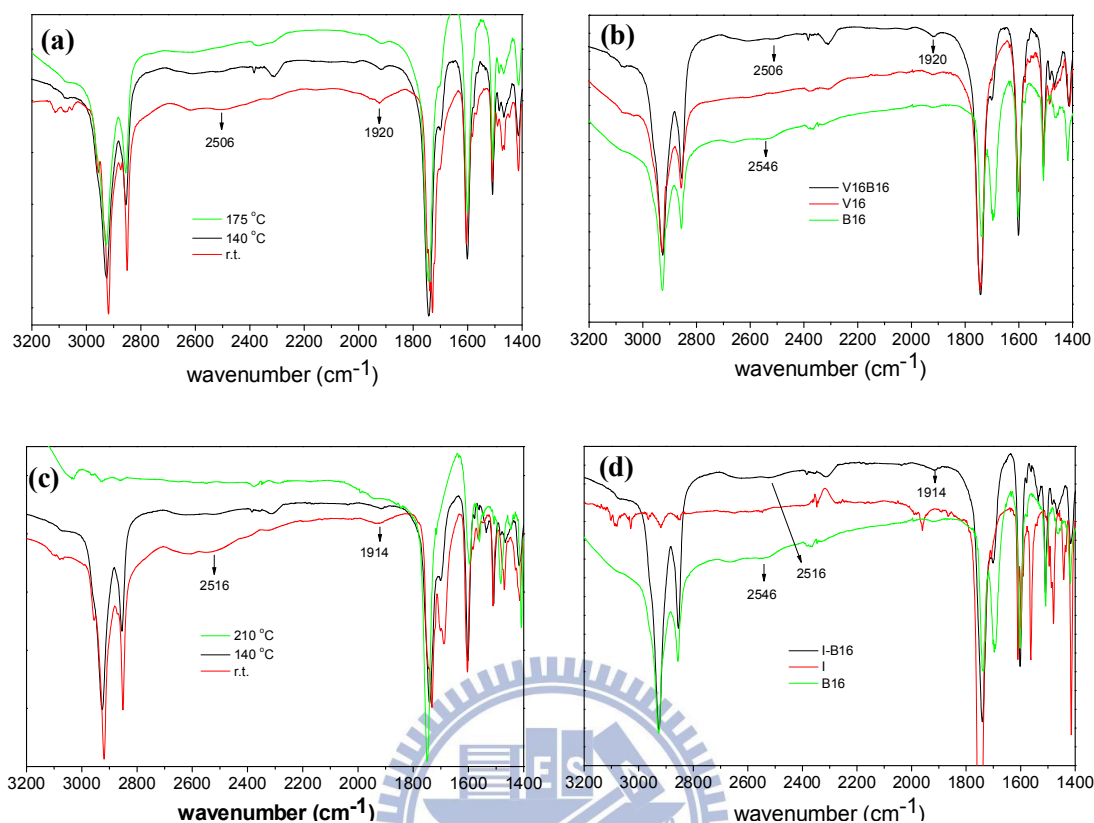
Figure 2.5. IR spectra of H-bonded asymmetric hetero-dimeric complex **V16-B16** (a) at variable temperatures and (b) its composed moieties (at room temperature); H-bonded symmetric trimeric complex **I-B16** (c) at variable temperatures and (d) its composed moieties (at room temperature).

2.3.4. Powder XRD analyses of H-bonded asymmetric hetero-dimers (with one H-bond):

2.3.4.1. Four- and five-ring systems (IIIn-Am, IIIn-Bm, and IVn-Am). The H-bonded molecular organizations of four- and five-ring asymmetric complexes in different mesophases (smectic phases) were investigated by XRD measurements (see Table 2.5). Wide angle diffuse peaks corresponding to a d-spacing value of 4.6 Å indicated that similar liquid-like in-plane orders with average intermolecular distances were prevalent inside the smectic layers of all H-bonded complexes. In addition, sharp

XRD peaks indexed as (001) were observed at the corresponding d-spacing values of d_1 = 42.5, 46.1, 46.6, and 49.5 Å in small angle regions of **III12-A12**, **III12-A16**, **III16-A12**, and **III16-A16**, respectively. The tilt angle values (between the molecular axis and the layer normal) were calculated from the values of d-spacing (d_1) and molecular length (L), where L is the theoretical coplanar molecular length from the molecular modelling. Almost equal values of d-spacing and calculated molecular length (L) were obtained in all complexes **IIIn-Am** (**n, m** = 12 and 16), which revealed that LC molecules were nearly perpendicular to the plane surface. Hence, the XRD data supported the existence of the SmA phase, which was also verified by POM experiments to observe the fan-like and homeotropic textures. The analogous XRD results also suggested the SmA phase for all complexes **IIIn-Bm**, which exhibited a single sharp reflection peak in small angle region with a d-spacing value (d_1) corresponding to the calculated molecular length (L) to prove the SmA phase, and the detailed XRD data are illustrated in Table 2.5.

With respect to complexes **IVn-Am**, sharp peaks indexed as (001) in the small angle region were obtained at the associated d-spacing values of d_1 = 42.2 Å, 47.6 Å, 46.3 Å, and 50.6 Å in **IV12-A12**, **IV12-A16**, **IV16-A12**, and **IV16-A16**, respectively. The tilt angles (θ) calculated from the values of d-spacing (d_1) and molecular length (L) were around in 35 - 39°, and the tilt angles were normally larger than those of the SmC phase (without polar switching behavior), which have also been confirmed in previous reports.[54] It is an indication that tilt lamellar arrangements existed in the mesophasic range of all complexes **IVn-An**. Therefore, the two-dimensional structures of the SmCP phase in complexes **IVn-An** were further confirmed by the XRD results.

Table 2.5. XRD Data of H-Bonded Four- and Five-Ring Asymmetric Hetero-Dimers (with One H-Hond)

Complex	Measured spacing (d)/Å	Miller index	Theoretical length (L)/Å	Tilt angle
III12-A12	42.5	(100)	L = 43.4	11.7°
III12-A16	46.1	(100)	L = 46.5	7.5°
III16-A12	46.6	(100)	L = 46.7	3.8°
III16-A16	49.5	(100)	L = 49.7	5.1°
III12-B12	51.9	(100)	L = 52.1	5.9°
III12-B16	55.4	(100)	L = 55.6	4.9°
III16-B12	54.6	(100)	L = 55.5	10.3°
III16-B16	59.2	(100)	L = 59.8	8.2°
IV12-A12	42.2	(100)	L = 54.5	39.2°
IV12-A16	47.6	(100)	L = 58.3	35.2°
IV16-A12	46.3	(100)	L = 58.2	37.2°
IV16-A16	50.6	(100)	L = 61.8	35.0°

Table 2.6. XRD Data of H-Bonded Six-Ring Asymmetric Hetero-Dimers (with One H-Bond)

Complex	Measured spacing (d)/Å	Miller index	Theoretical length (L)/Å	Tilt angle
IV12-B12	42.3	(100)	L = 57.5	42.6°
IV12-B16	49.0	(100)	L = 60.9	36.4°
IV16-B12	50.3	(100)	L = 60.7	34.1°
IV16-B16	52.7	(100)	L = 64.0	34.6°
V12-A12	46.6	(100)	L = 54.1	31.0°
V12-A16	48.7 24.4	(100) (200)	L = 59.2	34.9°
V16-A12	49.0 24.3	(100) (200)	L = 59.3	34.3°
V16-A16	51.3	(100)	L = 61.7	33.9°

2.3.4.2. Six-ring systems (IIIn-Cm, IVn-Bm, and Vn-Am). The structural arrangements of six-ring asymmetric complexes **IVn-Bm** and **Vn-Am** investigated by XRD measurements are shown in Table 2.6. Only broad peaks of complexes

IIIn-Cm in small and wide angle regions were obtained in the mesophasic ranges, which ruled out the presence of the smectic phase and thus suggested the existence of the nematic phase. However, one set of sharp peaks indexed as (001) with lamellar orders in complexes **IVn-Bm** and **Vn-Am** were observed at the related d-spacing (d_1) values of 42 – 52 Å, which implied the polar smectic (SmCP) phase with the tilt angles of 31 – 42°.

Table 2.7. XRD Data of H-Bonded Seven- and Eight-Ring Asymmetric Hetero-Dimers (with One H-Bond)

Complex	Measured spacing (d)/Å	Miller index	Theoretical length (L)/Å	Tilt angle or lattice parameters
V12-B12	44.9 32.4	(110) (200)	L = 64.8	a = 64.8 Å b = 62.3 Å
V12-B16	51.3 25.8	(100) (200)	L = 69.4	42.3°
V16-B12	52.4 26.2	(100) (200)	L = 69.6	41.2°
V16-B16	54.2 27.6 17.9	(100) (200) (300)	L = 72.9	41.9°
V12-C12	40.0 32.6	(110) (200)	L = 66.9	a = 65.2 Å b = 50.6 Å
V12-C16	42.2 32.9	(110) (200)	L = 70.5	a = 65.8 Å b = 55.0 Å
V16-C12	41.1 33.1	(110) (200)	L = 69.7	a = 66.2 Å b = 52.4 Å
V16-C16	46.3 33.6	(110) (200)	L = 73.1	a = 67.2 Å b = 60.5 Å

2.3.4.3. Seven- and eight-ring systems (Vn-Bm and Vn-Cm). The structural arrangements of seven- and eight-ring asymmetric complexes **Vn-Bm** and **Vn-Cm** investigated by XRD measurements are shown in Table 2.7. Regarding the

complexes **Vn-Bm**, the tilt smectic arrangements were demonstrated in **V12-B16**, **V16-B12**, and **V16-B16**. For example, sharp layer reflection peaks (up to the third order diffraction as shown in Figure 2.6a) were observed at the associated d-spacing values of $d_1 = 54.2$ Å, $d_2 = 27.6$ Å, and $d_3 = 17.9$ Å with tilt angles c.a. 42° in complex **V16-B16** as the evidence of the tilt lamellar arrangements. However, two sharp reflection peaks indexed as (011) and (002) were observed at the corresponding d-spacing values of $d_1 = 44.9$ Å and $d_2 = 32.4$ Å in complex **V12-B12** to reveal the rectangular columnar (Col$_r$) arrangement.[4,6] The analogous XRD results also suggested the Col$_r$ phase for all complexes **Vn-Cm**. For instance, two sharp reflection peaks indexed as (011) and (002) indicated the rectangular columnar arrangement as the example of one- and two-dimensional XRD patterns in complex **V16-C16** (see Figure 2.6b). The two-dimensional lattice parameters could be calculated as $a = 67.2$ Å and $b = 60.5$ Å as shown in the inserted pattern of Figure 2.5b. All centre-rectangular lattices with two-dimensional lattice parameters were identified as a Col$_r$ phase as revealed in Table 2.7.

2.3.5. Powder XRD analyses of H-bonded symmetric trimers (I-Am and I-Bm, with two H-bonds)

Two series of analogous symmetric trimers with mesomorphic properties, i.e., **I-Am** and **I-Bm** (**m** = 12 and 16) containing 5 and 7 rings, were investigated by XRD measurements to evaluate the influence of different ring numbers (at the rigid cores) on their layer spacing values as shown in Table 2.7. The tilt lamellar arrangements with various tilt angles (as shown in Table 2.8) were confirmed by XRD measurements in the mesophasic ranges of complexes **I-Am** and **I-Bm** (**m** = 12 and 16) according to the observation of sharp and broad diffuse XRD diffraction peaks in small and wide angle regions, respectively. Generally, the tilt angles of complexes **I-Bm** (containing 7 rings) are larger than those of complexes

53

I-Am (containing 5 rings).
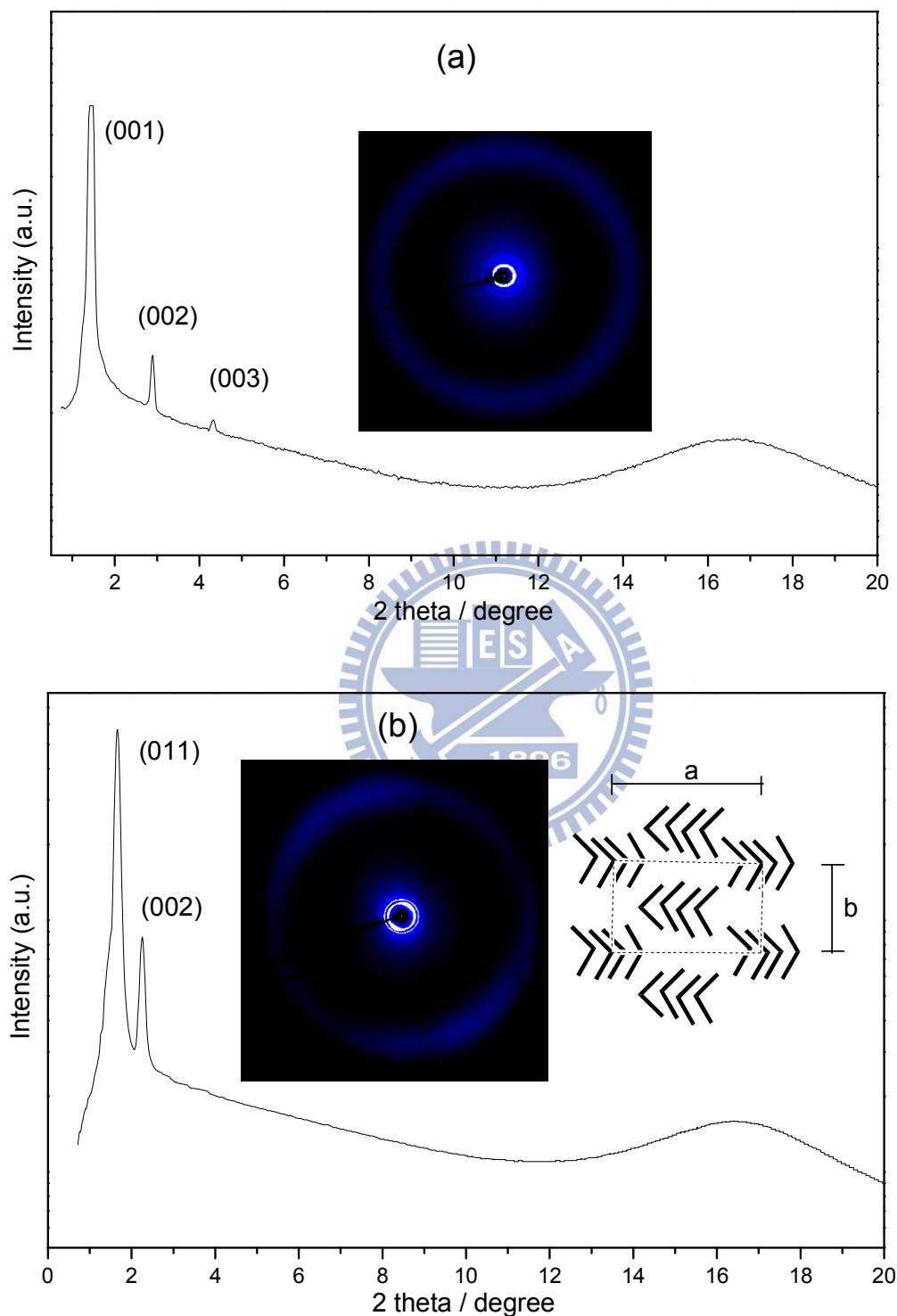
Figure 2.6. Powder X-ray diffraction intensity against angle profiles obtained upon cooling from the isotropic phase: (a) in the polar smectic phase of complex **V16-B16**; (b) in the Col$_r$ phase of complex **V16-C16**.

Table 2.8. XRD Data of H-Bonded Symmetric Trimers (with Two H-Bonds)

Complex	Measured spacing (d)/Å	Miller index	Theoretical length (L)/Å	Tilt angle
I-A12	32.5	(001)	L = 46.2	45.3°
I-A16	40.9	(001)	L = 50.9	36.5°
I-B12	33.5	(001)	L = 61.1	56.7°
I-B16	37.6	(001)	L = 66.6	55.6°

2.3.6. Spontaneous polarization (Ps) behaviour and dielectric analysis of H-bonded complexes

In order to prove the polar switching properties in symmetric trimer and asymmetric hetero-dimer complexes, the triangular wave method[22] was applied to measure the switching current behaviour (i.e., the spontaneous polarization) under 4.25 μm thick parallel rubbing cells. Two current peaks per half-period of an applied triangular voltage were obtained in the switching current response curves of all SmCP phase in the asymmetric hetero-dimeric complexes **IVn-Am**, **IVn-Bm**, **Vn-Am**, and **Vn-Bm** (**n** and **m** = 12 and 16, except **V12-B12)**. For instance, the two-peak switching current response curves of complexes **IV12-A12** and **V16-B16** are shown in Figure 2.7. Here, the characteristic behavior of a sequential electric response was due to a ferroelectric state switched into an antiferroelectric ground state and back to the opposite ferroelectric state, which confirmed the $SmCP_A$ (A = anti-ferroelectric behavior) structure of the B2 phase in these asymmetric hetero-dimeric complexes.[55] The Ps values (the saturated values at high voltages) could be calculated in the ranges of 200-240, 135-140, 140-145, and 115-125 nC/cm^2 for complexes **Vn-Bn**, **Vn-An**, **IVn-Bn,** and **IVn-An**, respectively. The Ps values were higher in complexes with longer rigid-core rings, but were not influenced by the H-bonded sites and flexible chain lengths. As shown in Figure 2.8, the spontaneous polarization values vs. applied electric fields were surveyed in the SmCP phase of the H-bonded asymmetric

hetero-dimers (**Vn-Bn**, **Vn-An, IVn-Bn**, and **IVn-An**), where the maximum applied voltages were Vpp = 600 V – 650 V and the saturated Ps values were reached at voltages above Vpp = 200-230 V. On the contrary, the saturated Ps value of 500 nC/cm^{-2} in compound **S12** was obtained at a much higher voltage above Vpp = 320 V in our study (as shown in Figure S2.2 of the Supporting Information). Hence, the H-bonded substitution for the covalent-bonded ester groups in the bent-core systems would not only decrease the phase transition temperatures but also reduce the voltages of the saturated Ps values due to the softer rigid-core configurations in the H-bonded complexes.
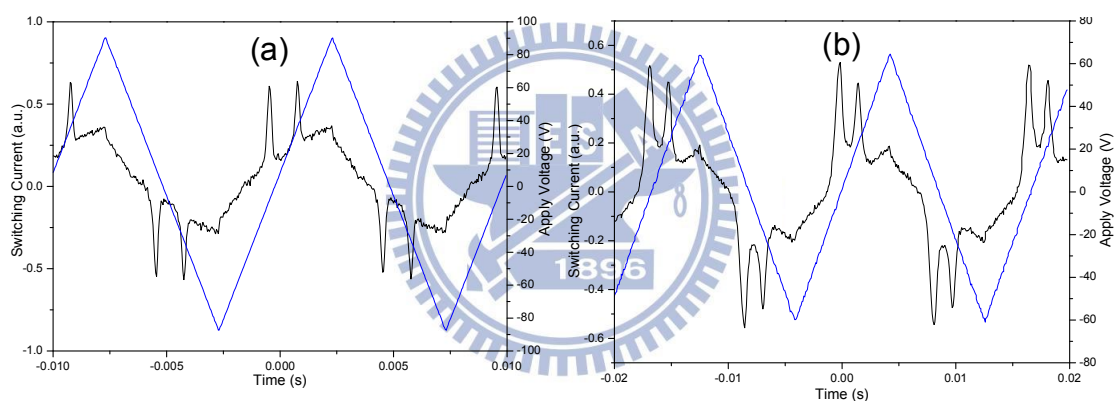
Figure 2.7. Switching current responses of H-bonded asymmetric hetero-dimers (a) **IV12-A12** at 95 °C (as Vpp = 180 V, f = 60 Hz) and (b) **V16-B16** at 130 °C (as Vpp = 120 V and f = 100 Hz) by applying a triangular wave (in parallel rubbing cells with 4.25 μm thickness).

However, since the B1$_{rev}$ and B1$_{rev,tilt}$ phases have the switching phenomena by applying electric fields,[34a,56] the Col$_r$ (B1) phase in complexes **V12-B12** and **Vn-Cm** (**n, m** = 12 and 16) was confirmed considering no switching current behaviour observed. Moreover, the Col$_r$ phase was further verified in view of no texture variation (in 4.25 μm thick parallel rubbing cells) under polarizing optical microscopy by applying electric fields up to 400Vpp (peak to peak). Regarding the electro-optical

properties of the SmC phase in symmetric trimers **I-Am** and **I-Bm** (**m** = 12 and 16, with two H-bonds), it was proven by that no switching current responses were observed under AC fields. As the applied electric field was raised to 200 Vpp, the fan-like domain was broken into the grainy domain, which suggested the unstable H-bonds were arisen due to the symmetric bent-core structures with two H-bonds.
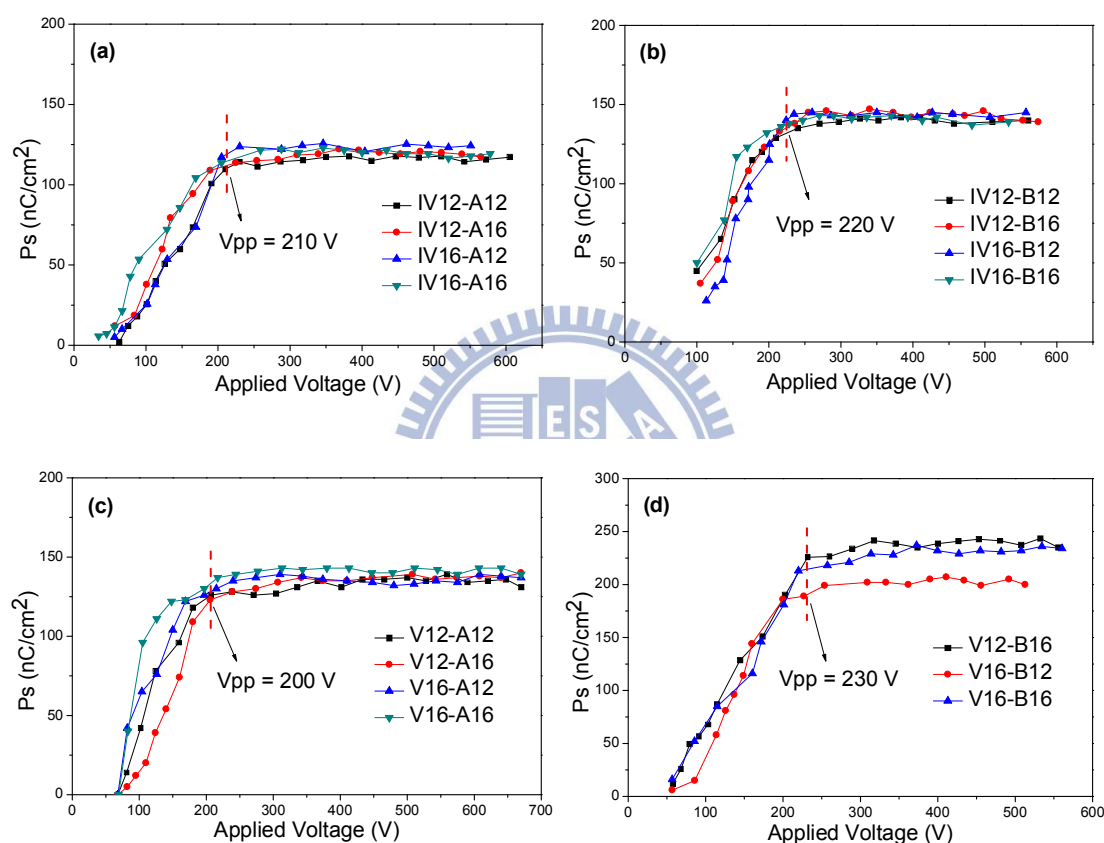
Figure 2.8. Ps values as a function of applied voltages (at the SmCP phase as f = 60Hz) for (a) complexes **IVn-Am**, (b) complexes **IVn-Bm**, (c) complexes **Vn-Am**, and (d) complexes **Vn-Bm**.

The antiferroelectricity was also further evidenced by the dielectric permittivity studies, and compound **S12**, H-bonded complexes **IV12-A12**, **V16-B16**, and **I-A12** were investigated under their cooling processes at a frequency of 5 kHz in non-rubbing cells (9um cell gap) as shown in Figure 2.9. Higher permittivity values (ε

~ 32) of the SmCP phase were observed than those of the isotropic, nematic and crystalline states in complex **V16-B16** to indicate the antiferroelectric polar smectic phase.[57] Similar higher permittivity values ($\varepsilon \sim 10\text{-}15$) of the SmCP phase in compound **S12** and H-bonded complex **IV12-A12** were also obtained. However, no higher permittivity values were achieved in the SmC phase of complex **I-A12** to further prove that the tilt smectic phase without polar switching behavior.
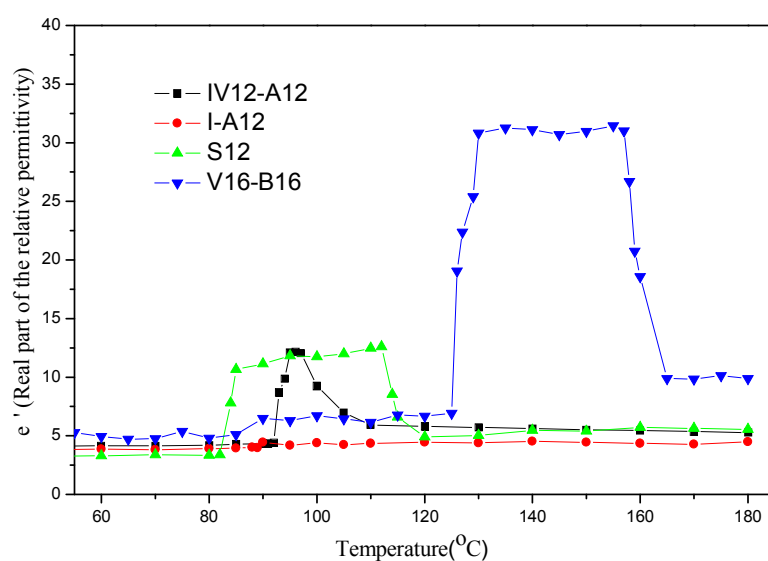
Figure 2.9. Dielectric permittivity studies of compound **S12** and H-bonded complexes **IV12-A12**, **I-A12**, and **V16-B16** in the cooling processes.

2.3.7. Chirality investigation

Besides triangular wave method, a switching process could also be checked through the rotation of the extinction crosses (Figure 2.10) by applying (or after removing) opposite d.c. electric fields in the bent-core H-bonded complexes with the SmCP phase. For instance, circular domains of complex **IV16-A16** were formed in the SmCP mesophasic range, in which the smectic layers were circularly arranged around the centers of the domains. The layer structures were arrangement corresponding to the domain models proposed by Link et al.[8,24] As shown in Figure 2.10, the rotation of the extinction crosses during the switched on and off
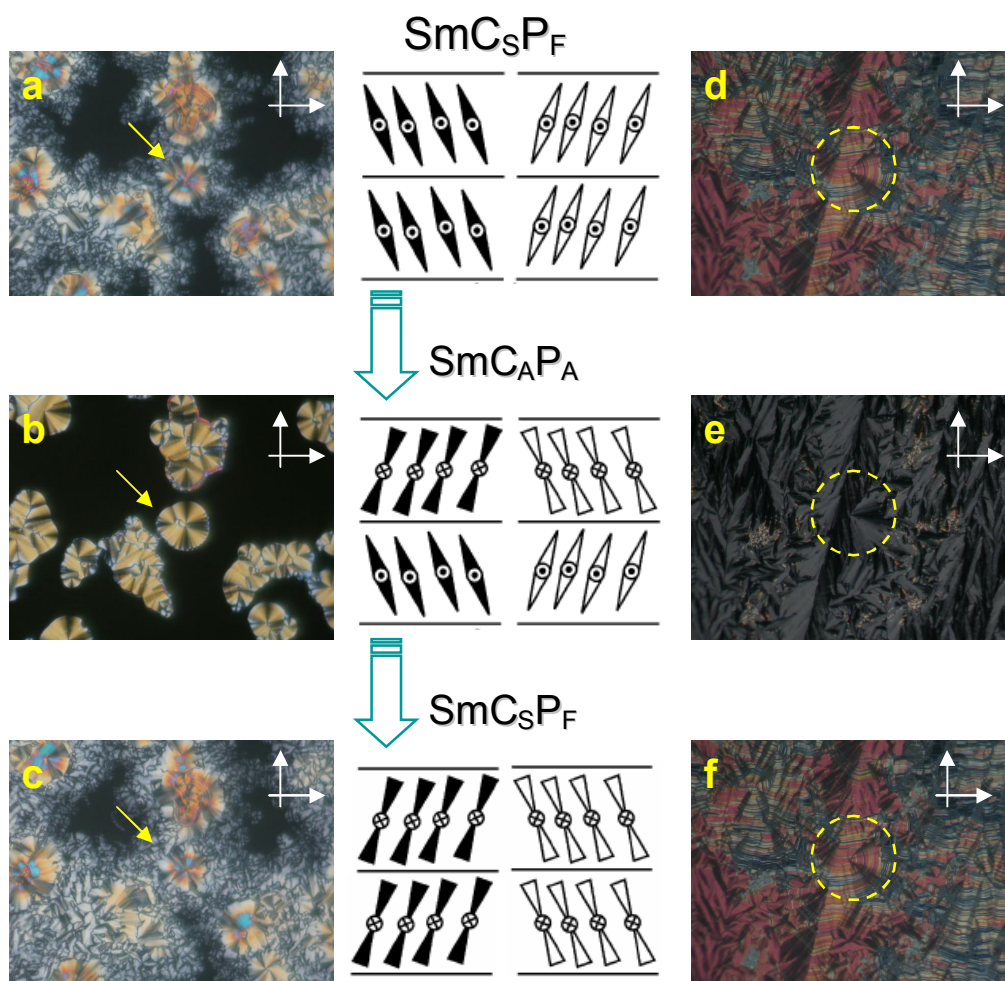
Figure 2.10. POM textures of the anti-ferroelectric SmC$_A$P$_A$ chiral domain (in a parallel rubbing cell with a cell gap of 4.25 μm) in five-ring complex **IV16-A16** by applying d.c. electric fields from (a) -50 V → (b) 0 V → (c) +50 V; in seven-ring complex **V16-B16** by applying d.c. electric fields from (d) -50 V → (e) 0 V → (f) +50 V. (White arrows are the directions of polarizers and analyzers.)
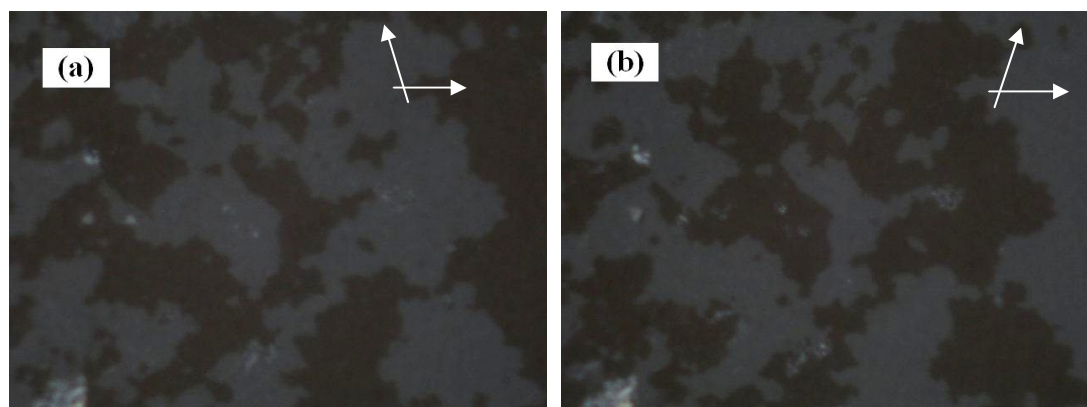
Figure 2.11. Chiral domain textures for complex **V16-B16**. (Arrows are the directions of polarizers and analyzers.)

states in complexes **IV16-A16** and **V16-B16** demonstrated the chiral domain behavior.[7] In view of Figure 2.10a and 2.10c, by applying d.c. electric fields (with reverse polarities), the extinction crosses rotated either counterclockwise or clockwise (i.e., rotated oppositely with positive and negative fields), indicating a synclinic tilt in the ferroelectric state (SmC_SP_F). By removing electric fields (off state), the extinction crosses were reoriented back to the crossed polarizer directions (see Figure 2.10b), indicating an anticlinic tilt in the antiferroelectric ground state (SmC_AP_A). Similarly, complex **V16-B16** yielded the synclinic and ferroelectric SmC_SP_F state by applying opposite d.c. electric fields (see Figures 2.10d and 2.10f), and the SmC_AP_A state after removing electric fields (see Figure 2.10e).

The chiral domain behavior could also be proven by the method of rotating the polarizer without applying electric fields. For example, the polarizer was rotated clockwise by a small angle of 10° from the crossed position in complex **V16-B16**, then the dark and bright domains become clearly distinguishable (see Figure 2.11a). On rotating the polarizer counterclockwise by the same angle (10°) from the crossed position, the previously observed dark domains turned to bright domains, and vice versa (see Figure 2.11b). This observation was also indicative of the occurrence of chiral domains with opposite handednesses.

2.3.8. Theoretical analyses of dipole moments and bent angles in H-bonded complexes

In order to analyze the variation of the polarities by insertion of single and double H-bonds in H-bonded complexes, the supramolecular dipole moments, electron cloud distributions, and bent angles were calculated by the molecular modelling, which would influence the polar switching behavior in covalent- and H-bonded bent-core structures with suitable bent-cores and flexible chains. Four simplified bent-core
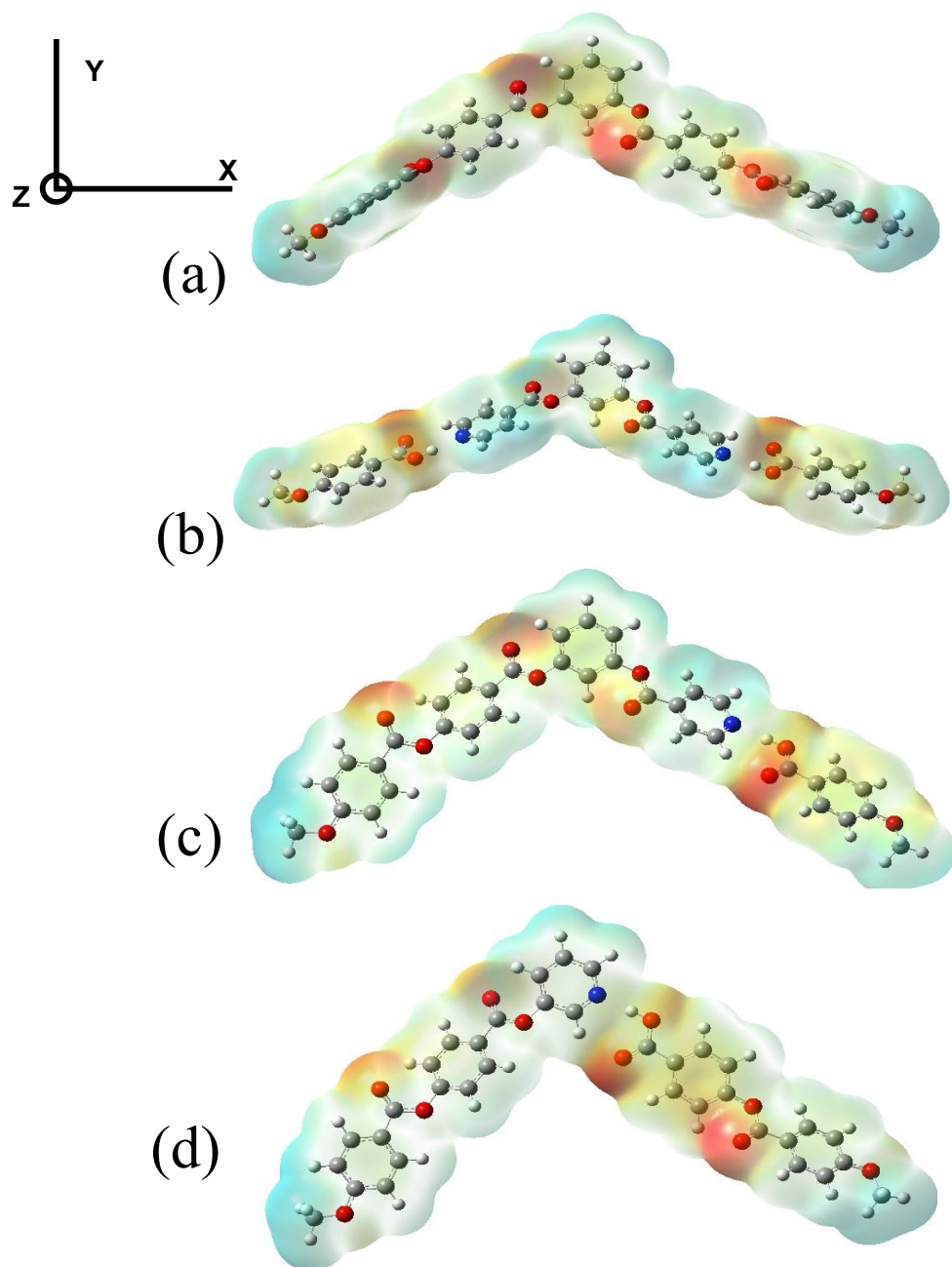
Figure 2.12. Molecular electrostatic potential mapped on the electron density isosurface of 0.0004 au of the lowest energy structure for the four bent-core structures (a) **S1**, (b) **I-A1**, (c) **IV1-A1**, and (d) **III1-B1**.

structures, including H-bonded complexes **I-A1**, **III1-B1**, and **IV1-A1**, and covalent-bonded compound **S1**, bearing methoxyl groups at their terminuses were designed as shown in Figure 2.12, where the electron cloud distributions of these model structures are demonstrated. Due to the H-bonds, the polarities and dipoles of

complexes **I-A1**, **III1-B1**, and **IV1-A1** were reduced by the non-covalent aggregation of H-bonded electrons at benzoic acid positions. As shown in Table 2.9, the theoretical calculations of molecular modeling for covalent- and H-bonded bent-core structures with lowest energies (see supporting information) were simulated by Gaussian03 at B3LYP level with 6-31G(d) basis set. Regarding covalent-bonded compound **S1**, the projective low values of dipole moments along X and Z directions were equal to 1.394 and 0.172 Debyes, which were mutually offset due to the symmetric structure. However, a large value of -4.123 Debyes in direction Y was evaluated to contribute to the total dipole moment in the molecular polar direction. Because of the symmetric skeleton in H-bonded complex **I-A1**, the similar results of the projective low values of dipole moments in X and Z dimensions were eliminated to 1.041 and -0.090 Debyes, and a very small value of 1.126 Debye was acquired in Y dimension due to the non-covalent electron aggregation of H-bonded sites. Hence, a much smaller total dipole moment of 1.53 Debye (along with the smallest polarity) was obtained in the simplified H-bonded complex **I-A1**, and thus to speculate the non-polar switching behavior for H-bonded symmetric trimers **I-Am** (with two H-bonds). In contrast to complex **I-A1**, the polar destruction was also obtained in Y direction (-2.971 Debyes) for complex **IV1-A1** due to the non-covalent electron aggregation of H-bonded sites. However, the projective dipole contribution along X and Z directions (-3.418 and -0.022 Debyes, respectively) were revealed as a result of the asymmetric structure in complex **IV1-A1**. Therefore, the total dipole moment of 4.53 Debyes in complex **IV1-A1** was achieved to suggest the polar switching behavior for H-bonded asymmetric dimers **IVn-Am** (with one H-bond). Comparing complexes **I-A1** and **IV1-A1**, the polar switching behavior of H-bonded asymmetric dimers **IVn-Am** can be expected according to the visualization of the simplified model complex **IV1-A1** with larger total dipole moments.

Table 2.9. Calculated Dipole Moments and Bent Angles of Optimized Covalent- and H-Bonded Bent-Core Structures at the B3LYP/6-31G(d) Level

Compound	Bent angle (°)[a]	Axial	Dipole moment (Debye)
S1	120.0	X	1.394
		Y	-4.123
		Z	0.172
		Total	4.35
I-A1	131.2	X	1.041
		Y	1.126
		Z	-0.090
		Total	1.53
IV1-A1	113.7	X	-3.418
		Y	-2.971
		Z	-0.022
		Total	4.53
III1-B1	99.6	X	-1.385
		Y	-3.837
		Z	-0.457
		Total	4.10

Sets of unique conformations within 1 kcal/mol of the global minimum from conformational search using molecular mechanics force-field were used for full geometry optimization at the B3LYP/6-31G(d) level. [a] Bent angle (°) measured as the angle between the first, central and final benzene rings' centers of the bent-core structures. The dipole moments of the lowest energy structure are given, and the calculated dipoles are in the range of 4.00-8.85 (S1), 0.21-1.94 (I-A1), 4.53-6.69 (IV1-A1), and 4.10-7.24 (III-B1) (see supporting information).

In the investigation of bent angle effect on the polar switching behavior of bent-core liquid crystals, the suitable bent angle for bent-core molecular configuartion is better close to 120° (or in the range of 110° to 130°).[3,29a,43d,58] Usually, calamitic LC materials possessing bent-core configurations with bent angles larger than 130° or less than 110° will reveal normal mesophases without polar switching behavior, such as the smecitc C, smecitc A, and nematic phases. In our theoretical molecular modelling, almost 120° and 114° bent angles were

obtained in molecules **S1** and **IV1-A1**, respectively, to support the existence of spontaneous polarization. However, the lower bent angle values (less than c.a. 100°) were achieved in complex **III1-B1** due to the near central-site H-bonds, even if the sufficient total dipole moment values (c.a. 4.10 Debyes) were acquired. It would be speculated that the deficiency of polar switching behavior in H-bonded asymmetric dimers with single near-central H-bonded sites, such as complexes **IIIn-Bm** and **IIIn-Cm**, was owing to their small bent angles (less than c.a. 100°). Overall, the asymmetric H-bonded molecular design as well as the suitable molecular bent angle is useful to enhance the total dipole moments and polarities in accordance with the theoretical analyses of molecular modelling, and the spontaneous polarization and switching behavior can not only be experimentally proven but also theoretically predicted in our study.

2.4. Conclusions

In summary, several series of novel banana-shaped liquid crystalline supramolecules consisting of H-bonded symmetric trimers (with two H-bonds) and asymmetric hetero-dimers (with one H-bond) were self-assembled by appropriate molar ratios of proton donors (H-donors) and acceptors (H-acceptors). The influences of H-bonded linking positions and aromatic ring numbers (in the rigid cores) as well as the chain lengths (in the flexible parts) on the mesomorphism and the switching behavior of the bent-core supramolecules were reported. Moreover, the voltage-dependent switching properties of spontaneous polarization (Ps) in the polar smectic C phase of the banana-shaped H-bonded complexes were observed. In the normal field-off state, except for the supramolecular structures with longer rigid cores or shorter flexible chains possessing the rectangular columnar (Col$_r$ or B1) phase, the SmC$_A$P$_A$ phase was revealed in most supramolecular asymmetric hetero-dimers (with

one H-bond), which was switched to the SmC_SP_F phase by applying electric fields. In addition, the SmA and nematic phases were observed in H-bonded asymmetric dimers with H-bonded sites close to the core center, but the polar smectic C phase was dominated for those with H-bonded sites apart from the core center. Compared with the fully covalent-bonded analogue, lower transition temperatures and lower threshold voltages were developed in H-bonded asymmetric dimers with the polar smectic C phase. The existence of polar switching behavior in the polar smectic C phase of asymmetric hetero-dimers (with one H-bond) related to the molecular configurations with higher dipole moments as well as the suitable bent angle was further demonstrated by the theoretical calculations of molecular modeling. Besides, the lack of polar switching behavior in supramolecular symmetric trimers (with two H-bonds), which exhibited the regular SmC phase with weak electrical stabilities, might be related to their configurations with smaller dipole moments. Finally, due to the low electrical stabilities of the H-bonded symmetric trimers (with two H-bonds), their supramolecular architectures with the polar smectic C phase may be preserved or created by the stabilization H-bonded structures through further auxiliary techniques (such as copolymerization and blending with covalent-bonded analogues) in the future studies. Finally, the spontaneous polarization and switching behavior of H-bonded banana-shaped LC materials are the first time experimentally proven and theoretically predicted in our study.

2.5. Electronic Supplementary Information

2.5.1. Synthesis

The synthetic procedures of all H-donors and H-accepters were proceeded according to scheme S2.1.

2.5.1.1 Synthesis of Am (m = 12 and 16). Compounds **Am** (m = 12 and 16)

were prepared by following the literature procedures.[13] **A12**: Yield: 92%, ^{1}H NMR (300 MHz, DMSO-d$_6$): δ 12.59 (s, 1H, COOH), 7.85 (d, J = 8.7 Hz, 2H, Ar-H), 6.98 (d, J = 8.7 Hz, 2H, Ar-H), 4.01 (t, J = 6.3 Hz, 2H, OC$\underline{H}_2$), 1.74-1.66 (m, 2H, OCH$_2$C$\underline{H}_2$), 1.34-1.16 (m, 18H, C$\underline{H}_2$), 0.84 (t, J = 6.3 Hz, 3H, C$\underline{H}_3$); EIMS: m/e 306; C$_{19}$H$_{30}$O$_3$ requires m/e 306.44; EA: Calcd for C$_{19}$H$_{30}$O$_3$: C, 74.47; H, 9.87;. Found: C, 74.44; H, 9.52. **A16**: Yield: 95%, ^{1}H NMR (300 MHz, DMSO-d$_6$): δ 12.59 (s, 1H, COOH), 7.85 (d, J = 8.7 Hz, 2H, Ar-H), 6.98 (d, J = 8.7 Hz, 2H, Ar-H), 4.01 (t, J = 6.3 Hz, 2H, OC$\underline{H}_2$), 1.72-1.65 (m, 2H, OCH$_2$C$\underline{H}_2$), 1.39-1.15 (m, 28H, C$\underline{H}_2$), 0.84 (t, J = 6.0 Hz, 3H, C$\underline{H}_3$); EIMS: m/e 363; C$_{23}$H$_{38}$O$_3$ requires m/e 362.55; EA: Calcd for C$_{23}$H$_{38}$O$_3$: C, 75.41; H, 10.25;. Found: C, 75.72; H, 10.37.

2.5.1.2. Synthesis of compound I. A mixture of resorcinol (1 eq.), isonicotinoyl chloride hydrochloride (1.1 eq.) and triethylamine was dissolved in dry dichloromethane (DCM) under nitrogen for 8 h at room temperature. After work up, the solvent was extracted with water/DCM and organic liquid layer was dried over anhydrous magnesium sulphate. After removal of the solvent by evaporation under reduced pressure, the residue was purified by column chromatography and recrystallized from THF/hexane to give a white solid. **I :** Yield: 74%, ^{1}H NMR (300 MHz, DMSO-d$_6$): δ 8.88 (d, J = 6.0 Hz, 2H, Ar-H), 8.01 (d, J = 6.0 Hz, 2H, Ar-H), 7.60 (t, J = 7.8 Hz, 1H, Ar-H), 7.44 (s, 1H, Ar-H), 7.34 (d, J = 8.7 Hz, 2H, Ar-H); EIMS: m/e 320; C$_{18}$H$_{12}$N$_2$O$_4$ requires m/e 320.30; EA: Calcd for C$_{18}$H$_{12}$N$_2$O$_4$: N, 8.75 C, 67.50; H,3.78;. Found: N, 8.54 C, 67.43; H, 3.74.

2.5.1.3. Synthesis of compound 8. Resorcinol (1 eq.)**,** benzyl bromide (1 eq.), K$_2$CO$_3$ (1 eq.) and acetone were mixed and stirred for 15h at reflux temperature. After reaction, acetone was removed by evaporation under reduced pressure, and the residue was extracted with water/DCM and the organic liquid layer was dried over anhydrous magnesium sulphate. After removal of the solvent by evaporation under

reduced pressure, the crude product was purified by column chromatography to get a waxed solid. Yield: 49%, ^{1}H NMR (300 MHz, CDCl$_3$): δ 7.43-7.30 (m, 5H, Ar-H), 7.12 (t, J = 7.8 Hz, 1H, Ar-H), 6.56 (d, J = 7.8 Hz, 1H, Ar-H), 6.48 (s, 1H, Ar-H), 6.42 (d, J = 7.8 Hz, 1H, Ar-H), 5.02 (s, 1H, -OH), 4.95 (s, 2H, OC$\underline{H}_2$).

2.5.1.4. Synthesis of compound 1 (n = 12 and 16). Am, compound **7**, N,N-dicyclohexylcarbodiimide (DCC) (1.2 eq) and a catalytic amount of 4-(N,N-dimethylamino) pyridine (DMAP) was dissolved in dry dichloromethane (DCM) under nitrogen for 15 h at room temperature. The precipitated dicyclohexylurea (DCU) was filtered off and washed with an excess of DCM (20 ml). The filtrate was extracted with water/DCM and the organic liquid layer was dried over anhydrous magnesium sulphate. After removal of the solvent by evaporation under reduced pressure, the residue was recrystallized from ethanol to give a white solid. **1/12**: Yield: 71%, ^{1}H NMR (300 MHz, CDCl$_3$): δ 8.20-8.15 (m, 4H, Ar-H), 7.51 (d, J = 8.7 Hz, 2H, Ar-H), 7.46-7.37 (m, 5H, Ar-H), 7.04 (d, J = 9.0 Hz, 2H, Ar-H), 6.95-6.82 (m, 3H, Ar-H), 5.07 (s, 2H, -OC$\underline{H}_2$-), 4.10 (t, J = 6.3 Hz, 2H, OC$\underline{H}_2$), 1.80 (m, 2H, OCH$_2$C$\underline{H}_2$), 1.28 (m, 18H, C$\underline{H}_2$), 0.88 (s, 3H, -CH$_3$). **1/16**: Yield: 73%, ^{1}H NMR (300 MHz, CDCl$_3$): δ 8.18 (d, J = 9.0 Hz, 2H, Ar-H), 8.15 (d, J = 8.4 Hz, 2H, Ar-H), 7.52 (d, J = 8.4 Hz, 2H, Ar-H), 7.45-7.36 (m, 5H, Ar-H), 7.08 (d, J = 9.0 Hz, 2H, Ar-H), 5.40 (s, 2H, -OC$\underline{H}_2$-), 4.10 (t, J = 6.3 Hz, 2H, OC$\underline{H}_2$), 1.86-1.81 (m, 2H, OCH$_2$C$\underline{H}_2$), 1.51-1.31 (m, 28H, C$\underline{H}_2$), 0.92 (t, J = 6.3 Hz, 3H, C$\underline{H}_3$).

2.5.1.5. Synthesis of compound Bm (m = 12 and 16). Compound **1** and Pd/C catalyst were stirred in THF under hydrogen at room temperature. The catalyst was removed by filtration through Celite and washed with THF. The solvent was removed by evaporation under reduced pressure and the crude product was recrystallized by THF/hexane to give a white solid. **B12**: Yield: 92%, ^{1}H NMR (300 MHz, CDCl$_3$): δ 13.05 (s, 1H, COOH), 8.17 (d, J = 8.4 Hz, 2H, Ar-H), 8.12 (d, J = 8.7 Hz, 2H, Ar-H),

7.31 (d, J = 8.4 Hz, 2H, Ar-H), 6.96 (d, J = 8.7 Hz, 2H, Ar-H), 4.07 (t, J = 6.6 Hz, 2H, O$\underline{CH_2}$), 1.78-1.68 (m, 2H, OCH$_2\underline{CH_2}$), 1.38-1.26 (m, 18H, $\underline{CH_2}$), 0.85 (t, J = 6.6 Hz, 3H, $\underline{CH_3}$); EIMS: m/e 426; $C_{26}H_{34}O_3$ requires m/e 426.55; EA: Calcd for $C_{26}H_{34}O_3$: C, 73.21; H, 8.03;. Found: C, 73.21; H, 8.06. **B16**: Yield: 90%, ^{1}H NMR (300 MHz, DMSO-d$_6$): δ 13.02 (s, 1H, COOH), 8.06 (d, J = 8.7 Hz, 2H, Ar-H) 8.01 (d, J = 9.0 Hz, 2H, Ar-H) 7.38 (d, J = 8.7 Hz, 2H, Ar-H), 7.10 (d, J = 9.0 Hz, 2H, Ar-H), 4.07 (t, J = 6.3 Hz, 2H, O$\underline{CH_2}$), 1.75-1.70 (m, 2H, OCH$_2\underline{CH_2}$), 1.41-1.22 (m, 28H, $\underline{CH_2}$), 0.83 (t, J = 5.7 Hz, 3H, $\underline{CH_3}$); FABMS: m/e 484; $C_{30}H_{42}O_3$ requires m/e 482.65; EA: Calcd for $C_{30}H_{42}O_3$: C, 74.65; H, 8.77. Found: C, 74.71; H, 8.80.

2.5.1.6. Synthesis of compound 2 (n = 12 and 16). By following the similar esterification procedure of compound **1**, compounds **Bm** (1 eq.) and compound **8** (1.2 eq.) were reacted to obtain a white solid. **2/12**: Yield: 72% ^{1}H NMR (300 MHz, DMSO-d$_6$); δ 8.16 (d, J = 8.7 Hz, 2H, Ar-H), 8.08 (d, J = 8.7 Hz, 2H, Ar-H), 7.49 (d, J = 8.7 Hz, 2H, Ar-H), 7.46-7.32 (m, 6H, Ar-H), 7.11 (d, J = 8.7 Hz, 2H, Ar-H), 7.01 (s, 1H, Ar-H), 6.96 (d, J = 8.1 Hz, 1H, Ar-H), 6.88 (d, J = 8.1 Hz, 1H, Ar-H), 5.11 (s, 2H, O$\underline{CH_2}$), 4.08 (t, J = 6.6 Hz, 2H, O$\underline{CH_2}$), 1.73 (t, J = 6.3 Hz, 2H, OCH$_2\underline{CH_2}$), 1.41-1.23 (m, 18H, $\underline{CH_2}$), 0.92 (t, J = 6.6 Hz, 3H, $\underline{CH_3}$). **2/16**: Yield: 79% ^{1}H NMR (300 MHz, CDCl$_3$); δ 8.25 (d, J = 8.7 Hz, 2H, Ar-H), 8.13 (d, J = 9.0 Hz, 2H, Ar-H), 7.42-7.29 (m, 8H, Ar-H), 6.94 (d, J = 9.0 Hz, 2H, Ar-H), 6.90-6.81 (m, 3H, Ar-H), 5.06 (s, 2H, O$\underline{CH_2}$), 4.04 (t, J = 6.6 Hz, 2H, O$\underline{CH_2}$), 1.81 (t, J = 6.6 Hz, 2H, OCH$_2\underline{CH_2}$), 1.45-1.24 (m, 28H, $\underline{CH_2}$), 0.86 (t, J = 6.3 Hz, 3H, $\underline{CH_3}$).

2.5.1.7. Synthesis of compound 3 (n = 12 and 16). By following the similar deprotection procedure of compounds **Bm**, compound **2** were reacted Pd/C catalyst to yield a white solid. **3/12**: Yield: 95%, ^{1}H NMR (300 MHz, DMSO-d$_6$): δ 8.25 (d, J = 8.7 Hz, 2H, Ar-H), 8.14 (d, J = 9.0 Hz, 2H, Ar-H), 7.40 (d, J = 8.7 Hz, 2H, Ar-H), 7.22 (t, J = 8.1 Hz, 1H, Ar-H), 7.03 (d, J = 9.0 Hz, 2H, Ar-H), 6.71-6.66 (m, 3H,

Ar-H), 4.06 (t, J = 6.6 Hz, 2H, O$\underline{CH_2}$), 1.80 (m, 2H, OCH$_2$$\underline{CH_2}$), 1.47-1.28 (m, 18H, $\underline{CH_2}$), 0.88 (t, J = 6.3 Hz, 3H, $\underline{CH_3}$). **3/16**: Yield: 98%, [1]H NMR (300 MHz, CDCl$_3$): δ 8.24 (d, J = 8.7 Hz, 2H, Ar-H), 8.12 (d, J = 9.0 Hz, 2H, Ar-H), 7.34 (d, J = 8.7 Hz, 2H, Ar-H), 7.26 (t, J = 8.4 Hz, 1H, Ar-H), 6.96 (d, J = 9.0 Hz, 2H, Ar-H), 6.79-6.71 (m, 3H, Ar-H), 4.04 (t, J = 6.6 Hz, 2H, O$\underline{CH_2}$), 1.81 (t, J = 6.6 Hz, 2H, OCH$_2$$\underline{CH_2}$), 1.46-1.25 (m, 28H, $\underline{CH_2}$), 0.86 (t, J = 6.6 Hz, 3H, $\underline{CH_3}$).   ;

2.5.1.8. Synthesis of compound IVn (n = 12 and 16). Compound **3** (1 eq.), isonicotinoyl chloride hydrochloride (1.1 eq.) and triethylamine were reacted according to the similar esterification procedure of compound **I** to get a white solid. **IV12 :** Yield: 95%, ^{1}H NMR (300 MHz, DMSO-d$_6$): δ 8.89 (d, J = 4.2 Hz, 2H, Ar-H), 8.22 (d, J = 8.7 Hz, 2H, Ar-H), 8.08(d, J = 8.7 Hz, 2H, Ar-H), 8.01 (d, J = 4.2 Hz, 2H, Ar-H), 7.59 (t, J = 8.1 Hz, 1H, Ar-H), 7.51 (d, J = 9.0 Hz, 2H, Ar-H), 7.41 (s, 1H, Ar-H), 7.32 (br, 2H, Ar-H), 7.10 (d, J = 9.0 Hz, 2H, Ar-H); 4.07 (t, J = 6.3 Hz, 2H, O$\underline{CH_2}$), 1.74 (br, 2H, OCH$_2$$\underline{CH_2}$), 1.23 (br, 18H, $\underline{CH_2}$), 0.84 (t, J = 6.3 Hz, 3H, $\underline{CH_3}$); FABMS: m/e 624; C$_{38}$H$_{41}$NO$_7$ requires m/e 623.73; EA: Calcd for C$_{38}$H$_{41}$NO$_7$: N, 2.25 C, 73.17; H, 6.63;. Found: N, 2.44 C, 73.25; H, 6.75. **IV16 :** Yield: 89%, [1]H NMR (300 MHz, DMSO-d$_6$): δ 8.81 (d, J = 6.0 Hz, 2H, Ar-H), 8.25 (d, J = 9.0 Hz, 2H, Ar-H), 8.10 (d, J = 9.0 Hz, 2H, Ar-H), 7.98 (d, J = 6.0 Hz, 2H, Ar-H), 7.49 (t, J = 8.1 Hz, 1H, Ar-H), 7.38 (d, J = 9.0 Hz, 2H, Ar-H), 7.27 (s, 1H, Ar-H), 7.22-7.17 (m, 2H, Ar-H), 7.01 (d, J = 9.0 Hz, 2H, Ar-H); 4.03 (t, J = 6.6 Hz, 2H, O$\underline{CH_2}$), 1.79-1.75 (m, 2H, OCH$_2$$\underline{CH_2}$), 1.45-1.24 (m, 28H, $\underline{CH_2}$), 0.84 (t, J = 6.6 Hz, 3H, $\underline{CH_3}$); FABMS: m/e 681; C$_{38}$H$_{41}$NO$_7$ requires m/e 679.84; EA: Calcd for C$_{42}$H$_{49}$NO$_7$: N, 2.06 C, 74.20; H, 7.26. Found: N, 2.17 C, 74.24; H, 7.18.

2.5.1.9. Synthesis of compound 4 (n = 12 and 16). Compounds **Bm** (1 eq.) and compound **7** (1.2 eq.) were reacted by following the esterification procedure of compound **1** to produce a white solid. **4/12**: Yield: 64%, ^{1}H NMR (300 MHz, CDCl$_3$)

δ 8.27 (d, J = 8.7 Hz, 2H, Ar-H), 8.17 (d, J = 9.0 Hz, 2H, Ar-H), 8.15 (d, J = 9.0 Hz, 2H, Ar-H), 7.47-7.35 (m, 7H, Ar-H), 7.31 (d, J = 9.0 Hz, 2H, Ar-H), 7.00 (d, J = 9.0 Hz, 2H, Ar-H), 5.38 (s, 2H, -O$\underline{C}H_2$-), 4.05 (t, J = 6.0 Hz, 2H, O$\underline{C}H_2$), 1.87-1.80 (m, 2H, OCH$_2\underline{C}H_2$), 1.48-1.27 (m, 18H, $\underline{C}H_2$), 0.88 (t, J = 5.4 Hz, 3H, -CH_3).; **4/16**: Yield: 73%, ^{1}H NMR (300 MHz, CDCl$_3$) δ 8.21 (d, J = 8.7 Hz, 2H, Ar-H), 8.13 (d, J = 8.7 Hz, 2H, Ar-H), 8.10 (d, J = 9.0 Hz, 2H, Ar-H), 7.42-7.30 (m, 7H, Ar-H), 7.24 (d, J = 8.7 Hz, 2H, Ar-H), 6.95 (d, J = 9.0 Hz, 2H, Ar-H), 5.43 (s, 2H, -O$\underline{C}H_2$-), 4.03 (t, J = 6.0 Hz, 2H, O$\underline{C}H_2$), 1.81-1.72 (m, 2H, OCH$_2\underline{C}H_2$), 1.44-1.23 (m, 28H, $\underline{C}H_2$), 0.86 (s, 3H, -CH_3).

2.5.1.10. Synthesis of compound Cm (m = 12 and 16). By following the similar deprotection procedure of compounds **Bm**, compound **4** were reacted Pd/C catalyst to yield a white solid. **C12**: Yield: 94%, ^{1}H NMR (300 MHz, DMSO-d$_6$) δ 8.32 (d, J = 8.7 Hz, 2H, Ar-H), 8.18 (d, J = 8.7 Hz, 2H, Ar-H), 8.14 (d, J = 8.7 Hz, 2H, Ar-H), 7.47 (d, J = 8.7 Hz, 2H, Ar-H), 7.41 (d, J = 8.7 Hz, 2H, Ar-H), 7.10 (d, J = 8.7 Hz, 2H, Ar-H), 4.11 (t, J = 6.3 Hz, 2H, O$\underline{C}H_2$), 1.82 (m, 2H, OCH$_2\underline{C}H_2$), 1.46-1.25 (m, 18H, $\underline{C}H_2$), 0.92 (t, J = 4.8 Hz, 3H, $\underline{C}H_3$).; FBMS: m/e 547; $C_{33}H_{38}O_7$ requires m/e 546.65; EA: Calcd for $C_{33}H_{38}O_7$: C, 72.51; H, 7.1. Found: C, 72.11; H, 6.99. **C16**: Yield: 98%, ^{1}H NMR (300 MHz, DMSO-d$_6$) δ 8.25 (d, J = 8.7 Hz, 2H, Ar-H), 8.10 (d, J = 8.1 Hz, 2H, Ar-H), 8.07 (d, J = 8.4 Hz, 2H, Ar-H), 7.39 (d, J = 8.7 Hz, 2H, Ar-H), 7.32 (d, J = 8.1 Hz, 2H, Ar-H), 7.01 (d, J = 8.4 Hz, 2H, Ar-H), 4.03 (t, J = 6.3 Hz, 2H, O$\underline{C}H_2$), 1.76 (br, 2H, OCH$_2\underline{C}H_2$), 1.43-1.24 (m, 28H, $\underline{C}H_2$), 0.84 (t, J = 4.8 Hz, 3H, $\underline{C}H_3$).; FBMS: m/e 603; $C_{37}H_{46}O_7$ requires m/e 602.76; EA: Calcd for $C_{37}H_{46}O_7$: C, 73.73; H, 7.69. Found: C, 73.86; H, 7.72.

2.5.1.11. Synthesis of compound 5 (n = 12 and 16). Compounds **Cm** (1 eq.) and compound **8** (1.2 eq.) were reacted by following the esterification procedure of compound **1** to acquire a white solid. **5/12**: Yield: 73%, ^{1}H NMR (300 MHz, DMSO)

8.25 (d, J = 9.0 Hz, 2H, Ar-H), 8.23 (d, J = 8.7 Hz, 2H, Ar-H), 8.10 (d, J = 8.4 Hz, 2H, Ar-H), 7.56 (d, J = 9.0 Hz, 2H, Ar-H), 7.53 (d, J = 8.7 Hz, 2H, Ar-H), 7.47 (s, 1H, Ar-H), 7.45-7.33 (m, 5H, Ar-H), 7.12 (d, J = 8.4 Hz, 2H, Ar-H), 7.03 (t, J = 8.1Hz, 1H, Ar-H), 6.98 (d, J = 8.1Hz, 1H, Ar-H), 6.90 (d, J = 8.1 Hz, 1H, Ar-H), 5.12 (s, 2H, O$\underline{CH_2}$), 4.09 (t, J = 6.3 Hz, 3H, O$\underline{CH_2}$), 1.74 (br, 2H, OCH$_2$$\underline{CH_2}$), 1.40-1.23 (m, 18H, $\underline{CH_2}$), 0.84 (t, J = 5.7 Hz, 3H, $\underline{CH_3}$). **5/16**: Yield: 81%, [1]H NMR (300 MHz, DMSO) 8.26 (d, J = 9.6 Hz, 2H, Ar-H), 8.23 (d, J = 8.7 Hz, 2H, Ar-H), 8.10 (d, J = 8.7 Hz, 2H, Ar-H), 7.56 (d, J = 9.6 Hz, 2H, Ar-H), 7.53 (d, J = 8.7 Hz, 2H, Ar-H), 7.47 (s, 1H, Ar-H), 7.45-7.33 (m, 5H, Ar-H), 7.13 (d, J = 8.7 Hz, 2H, Ar-H), 7.02 (t, J = 7.5Hz, 1H, Ar-H), 6.97 (d, J = 7.5Hz, 1H, Ar-H), 6.89 (d, J = 7.5 Hz, 1H, Ar-H), 5.13 (s, 2H, O$\underline{CH_2}$), 4.10 (t, J = 6.3 Hz, 3H, O$\underline{CH_2}$), 1.73 (br, 2H, OCH$_2$$\underline{CH_2}$), 1.43-1.23 (m, 28H, $\underline{CH_2}$), 0.83 (t, J = 5.7 Hz, 3H, $\underline{CH_3}$).

2.5.1.12. Synthesis of compound 6 (n = 12 and 16). By following the similar deprotection procedure of compounds **Bm**, compound **5** were reacted Pd/C catalyst to yield a white solid. **6/12**: Yield: 95%, ^{1}H NMR (300 MHz, DMSO-d$_6$); δ 8.26 (d, J = 8.7 Hz, 4H, Ar-H), 8.14 (d, J = 8.1 Hz, 2H, Ar-H), 7.45 (d, J = 8.4 Hz, 4H, Ar-H), 7.25 (t, J = 8.1 Hz, 1H, Ar-H), 7.07 (d, J = 8.4 Hz, 2H, Ar-H), 6.71-6.69 (m, 3H, Ar-H), 4.10 (t, J = 6.3 Hz, 2H, O$\underline{CH_2}$), 1.82 (t, J = 6.6 Hz, 2H, OCH$_2$$\underline{CH_2}$), 1.43-1.22 (m, 18H, $\underline{CH_2}$), 0.86 (t, J = 6.6 Hz, 3H, $\underline{CH_3}$). **6/16**: Yield: 91%, [1]H NMR (300 MHz, DMSO-d$_6$) δ 8.25 (d, J = 9.0 Hz, 4H, Ar-H), 8.11 (d, J = 8.4 Hz, 2H, Ar-H), 7.41 (d, J = 8.4 Hz, 4H, Ar-H), 7.19 (t, J = 8.4 Hz, 1H, Ar-H), 7.02 (d, J = 8.4 Hz, 2H, Ar-H), 6.69-6.64 (m, 3H, Ar-H), 4.04 (t, J = 6.6 Hz, 2H, O$\underline{CH_2}$), 1.78 (t, J = 6.9 Hz, 2H, OCH$_2$$\underline{CH_2}$), 1.45-1.23 (m, 28H, $\underline{CH_2}$), 0.85 (t, J = 6.6 Hz, 3H, $\underline{CH_3}$).

2.5.1.13. Synthesis of compound Vn (n = 12 and 16). Compound **6** (1 eq.), isonicotinoyl chloride hydrochloride (1.1 eq.) and triethylamine were reacted according to the similar esterification procedure of compound **I** to get a white solid.

V12: Yield: 95%, ^{1}H NMR (300 MHz, DMSO-d$_6$) δ 8.89 (d, J = 5.4 Hz, 2H, Ar-H), 8.25 (d, J = 8.7 Hz, 4H, Ar-H), 8.10 (d, J = 8.7 Hz, 2H, Ar-H), 8.02 (d, J = 5.4 Hz, 2H, Ar-H), 7.27-7.52 (m, 5H, Ar-H), 7.42 (s, 1H, Ar-H), 7.34 (d, J = 8.7 Hz, 2H, Ar-H), 7.12 (d, J = 8.7 Hz, 2H, Ar-H). 4.09 (t, J = 6.6 Hz, 2H, OC$\underline{H_2}$), 1.74 (t, J = 6.3 Hz, 2H, OCH$_2$C$\underline{H_2}$), 1.42-1.24 (m, 18H, $\underline{CH_2}$), 0.84 (t, J = 6.6 Hz, 3H, $\underline{CH_3}$).; EIMS: m/e 744; C$_{45}$H$_{45}$NO$_9$ requires m/e 743.84; EA: Calcd for C$_{45}$H$_{45}$NO$_9$: N, 1.88; C, 72.66; H, 6.10. Found: N, 1.98; C, 72.69; H, 5.98. **V16**: Yield: 91%, ^{1}H NMR (300 MHz, DMSO-d$_6$) δ 8.81 (d, J = 4.8 Hz, 2H, Ar-H), 8.27 (d, J = 9.0 Hz, 4H, Ar-H), 8.11 (d, J = 9.0 Hz, 2H, Ar-H), 8.02 (d, J = 4.8 Hz, 2H, Ar-H), 7.50 (t, J = 8.1 Hz, 1H, Ar-H), 7.44 (d, J = 8.7 Hz, 2H, Ar-H), 7.42 (d, J = 8.4 Hz, 2H, Ar-H), 7.27 (s, 1H, Ar-H), 7.23-7.18 (m, 2H, Ar-H), 7.02 (d, J = 9.0 Hz, 2H, Ar-H), 4.04 (t, J = 6.3 Hz, 2H, OC$\underline{H_2}$), 1.77 (t, J = 6.6 Hz, 2H, OCH$_2$C$\underline{H_2}$), 1.45-1.28 (m, 28H, $\underline{CH_2}$), 0.85 (t, J = 5.4 Hz, 3H, $\underline{CH_3}$).; EIMS: m/e 801; C$_{49}$H$_{53}$NO$_9$ requires m/e 799.95; EA: Calcd for C$_{49}$H$_{53}$NO$_9$: N, 1.75; C, 73.57; H, 6.68;. Found: N, 1.94; C, 73.69; H, 6.49.

2.5.1.14. Synthesis of compound 10. Methyl 4-hydroxybenzoate (1eq.), benzyl bromide (1.1eq.), and K$_2$CO$_3$ (1.5eq.) were reacted in acetone at reflux temperature for 10h. After removing acetone at reduced pressure, the precipitate was produced immediately by adding water. The crude product was recrystallized from acetone/hexane to give a white solid. **10**: Yield: 97%, ^{1}H NMR (300 MHz, CDCl$_3$) δ 7.03 (d, J = 9.0 Hz, 2H, Ar-H), 6.63-6.50 (m, 5H, Ar-H), 6.35 (d, J = 9.0 Hz, Ar-H), 4.38 (s, 2H, OC$\underline{H_2}$), 2.49 (s, 3H, OC$\underline{H_3}$).

2.5.1.15. Synthesis of compound 11. Compound **10** (1eq.) and KOH (4eq.) were reacted in ethanol at reflux temperature for 10h. Water was added to produce the precipitate, and the crude product was recrystallized from THF/hexane to give a white solid. **11**: Yield: 98%, ^{1}H NMR (300 MHz, DMSO) δ 7.87 (d, J = 9.0 Hz, 2H, Ar-H), 7.46-7.33 (m, 5H, Ar-H), 7.07 (d, J = 9.0 Hz. 2H, Ar-H), 5.17 (s, 2H, OC$\underline{H_2}$).

2.5.1.16. Synthesis of compound 12. Compound **11** (2.2 eq.) and compound **9** (1 eq.) were reacted by following the esterification procedure of compound **1** to acquire a white solid. **12**: Yield: 75%, ^{1}H NMR (300 MHz, CDCl$_3$) δ 8.15 (d, J = 9.0 Hz. 4H, Ar-H), 7.48-7.33 (m, 11H, Ar-H), 7.13 (d, J = 9.0 Hz. 2H, Ar-H), 7.12 (s, 1H, Ar-H), 7.05 (d, J = 9.0 Hz. 4H, Ar-H), 5.16 (s, 4H, OC$\underline{H}_2$).

2.5.1.17. Synthesis of compound 13. By following the similar deprotection procedure of compounds **Bm**, compound **12** were reacted Pd/C catalyst to yield a white solid. **13**: Yield: 95%, ^{1}H NMR (300 MHz, CDCl$_3$) δ 7.98 (d, J = 9.0 Hz. 4H, Ar-H), 7.51 (t, J = 7.5 Hz. 1H, Ar-H), 7.06 (d, J = 7.5 Hz. 2H, Ar-H), 7.03 (s, 1H, Ar-H), 6.92 (d, J = 9.0 Hz. 4H, Ar-H).

2.5.1.18. Synthesis of compound II. Compound **13** (1 eq.), isonicotinoyl chloride hydrochloride (2.4 eq.) and triethylamine were reacted according to the similar esterification procedure of compound **I** to get a white solid. **II**: Yield: 84%, ^{1}H NMR (300 MHz, DMSO-d$_6$) δ 8.92 (d, J = 5.4 Hz, 4H, Ar-H), 8.38 (d, J = 8.4 Hz, 4H, Ar-H), 8.10 (d, J = 5.4 Hz, 4H, Ar-H), 7.60 (t, J = 7.8 Hz, 1H, Ar-H), 7.55 (d, J = 8.4 Hz, 4H, Ar-H), 7.34-7.28 (m, 3H, Ar-H).; FBMS: m/e 562; C$_{32}$H$_{20}$N$_2$O$_8$ requires m/e 560.51; EA: Calcd for C$_{32}$H$_{20}$N$_2$O$_8$: N, 5.00; C, 68.57; H, 3.60;. Found: N, 5.07; C, 68.43; H, 3.84.

2.5.1.19. Synthesis of compound IIIn. Compounds **Bm** (1 eq.) and compound **14** (1 eq.) were reacted by following the esterification procedure of compound **1** to acquire a white solid. **III12**: Yield: 86%, ^{1}H NMR (300 MHz, DMSO-d$_6$) δ 8.61 (s, 1H, Ar-H), 8.30 (d, J = 6.0 Hz, 1H, Ar-H), 8.25 (d, J = 8.7 Hz, 2H, Ar-H), 8.10 (d, J = 8.7 Hz, 2H, Ar-H), 7.85-7.82 (m, 1H, Ar-H), 7.57 (m. 1H, Ar-H), 7.53 (d, J = 8.7 Hz, 2H, Ar-H), 7.12 (d, J = 8.7 Hz, 2H, Ar-H), 4.09 (t, J = 6.3 Hz, 2H, OC$\underline{H}_2$), 1.73 (m, 2H, OCH$_2$C$\underline{H}_2$), 1.49-1.24 (m, 18H, C$\underline{H}_2$), 0.84 (t, J = 6.3 Hz, 3H, C$\underline{H}_3$).; EIMS: m/e 504; C$_{31}$H$_{37}$NO$_5$ requires m/e 504; EA: Calcd for C$_{31}$H$_{37}$NO$_5$: N, 2.78; C, 73.93; H,

73

7.41. Found: N, 2.81; C, 73.67; H, 7.35. **III16**: Yield: 82%, ^{1}H NMR (300 MHz, DMSO-d_6) δ 8.51 (s, 1H, Ar-H), 8.46 (d, J = 4.5 Hz, 1H, Ar-H), 8.26 (d, J = 8.7 Hz, 2H, Ar-H), 8.11 (d, J = 8.7 Hz, 2H, Ar-H), 7.63-7.62 (m, 1H, Ar-H), 7.42 (s. 1H, Ar-H), 7.39 (d, J = 8.7 Hz, 2H, Ar-H), 7.02 (d, J = 8.7 Hz, 2H, Ar-H), 4.03 (t, J = 6.3 Hz, 2H, O$\underline{CH_2}$), 1.77 (t, J = 6.6 Hz, 2H, OCH$_2\underline{CH_2}$), 1.44-1.24 (m, 28H, $\underline{CH_2}$), 0.84 (t, J = 5.4 Hz, 3H, $\underline{CH_3}$).; EIMS: m/e 559; $C_{35}H_{45}NO_5$ requires m/e 559; EA: Calcd for $C_{35}H_{45}NO_5$: N, 2.50; C, 75.10; H, 8.10. Found: N, 2.85; C, 74.95; H, 8.11.
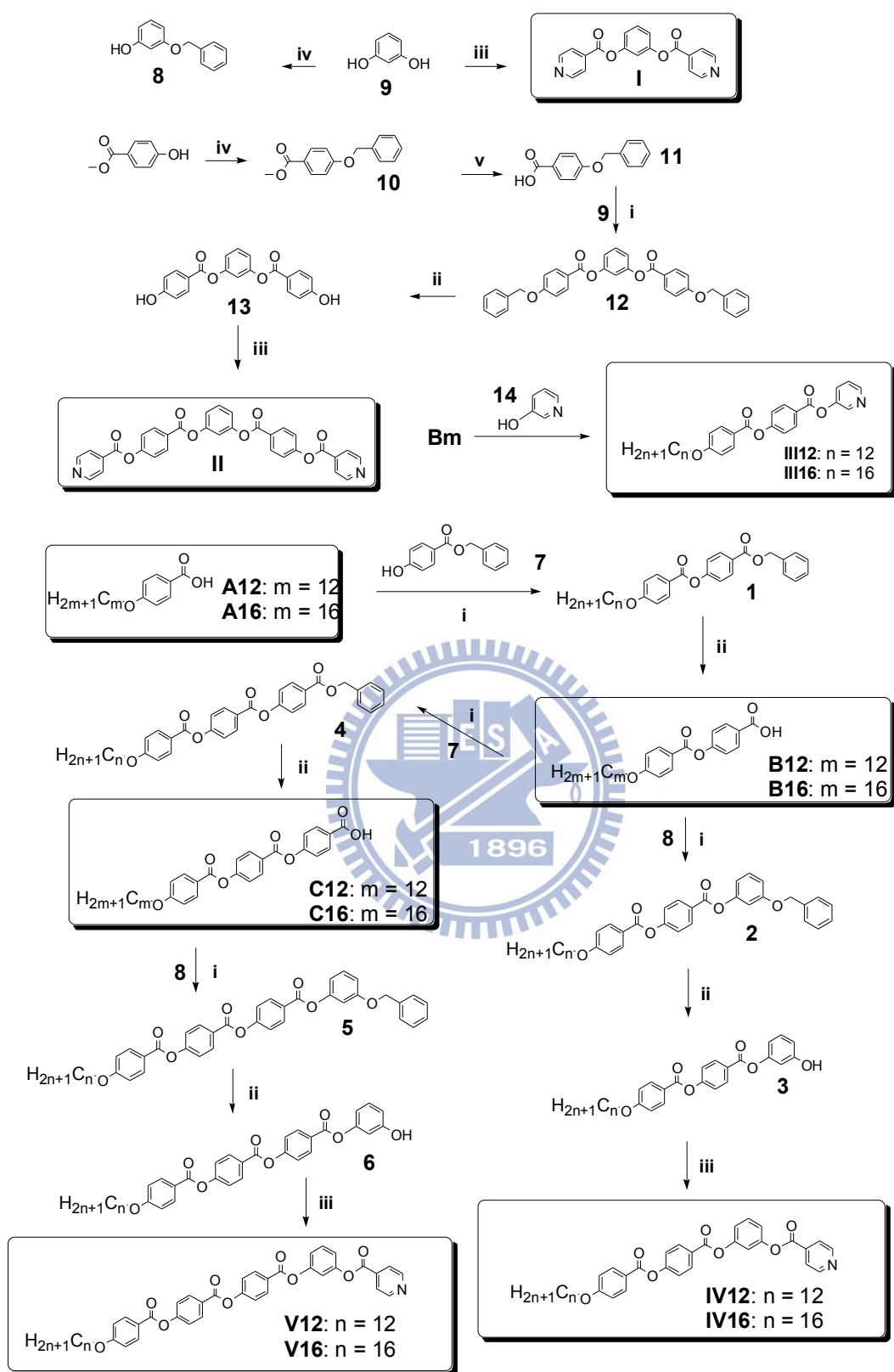
Scheme S2.1. Synthetic procedures of H-donors and H-acceptors **Am**, **Bm**, **Cm**, **I**, **II**, **IIIn**, **IVn**, and **Vn** (**n** and **m** = 12, 16). (i): DCC, DMAP, DCM; (ii): Pd/C, H$_2$, THF; (iii): isonicotinoyl chloride hydrochloride, Et$_3$N, DCM; (iv): benzyl bromide, K$_2$CO$_3$, Acetone; (v): KOH, EtOH.
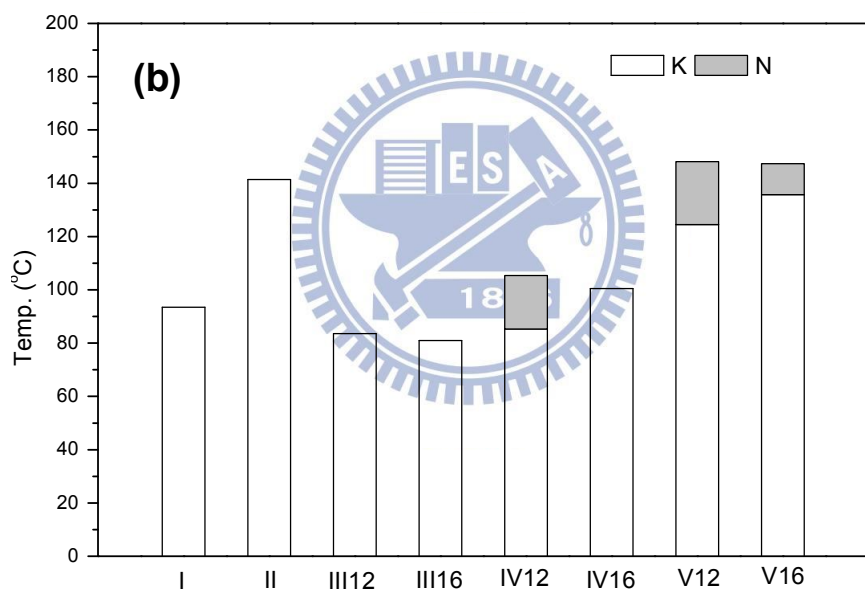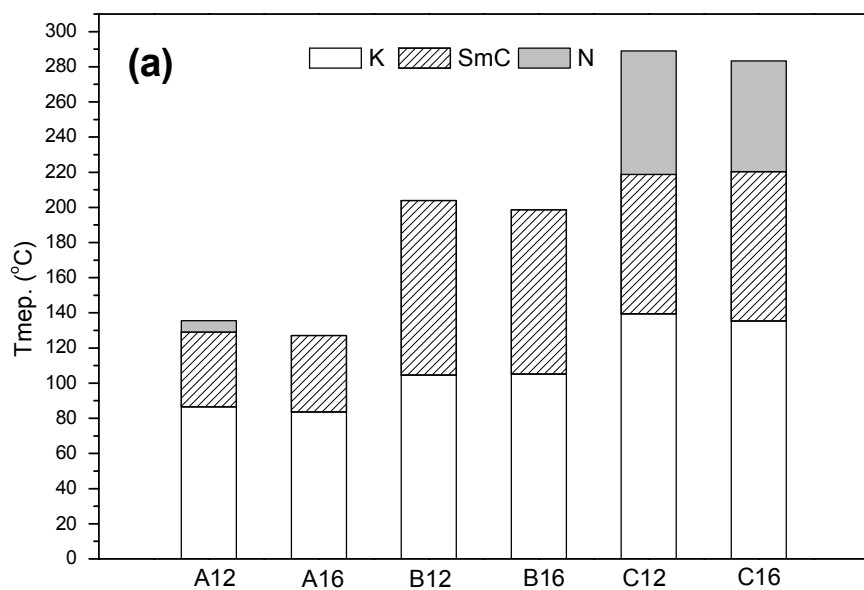
Figure S2.1. Phase diagram of (a) H-acceptors (**Am**, **Bm**, and **Cm**) and (b) H-donors (**I**, **II**, **IIIn**, **IV**n, and **Vn**).
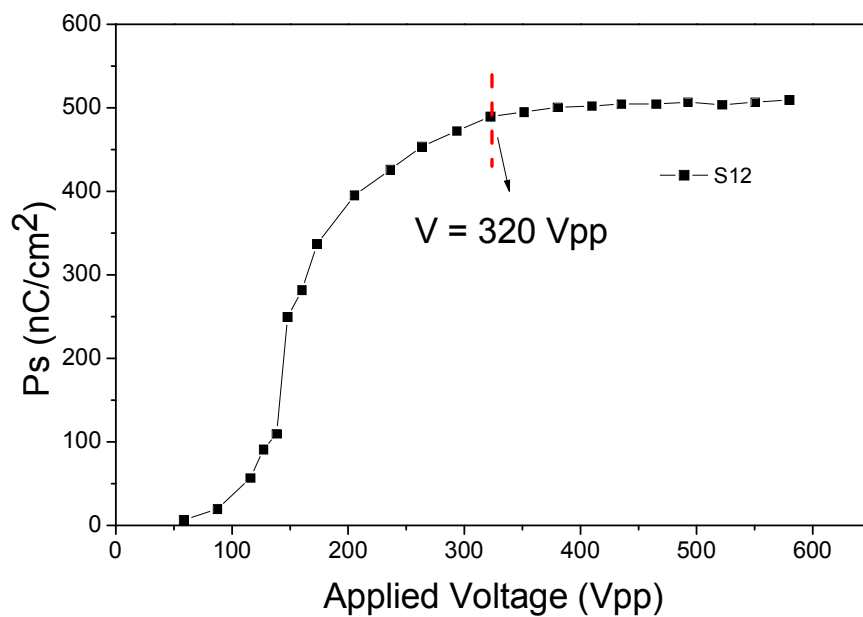
Figure S2.2. Ps values vs. applied voltages for compound **S12**.
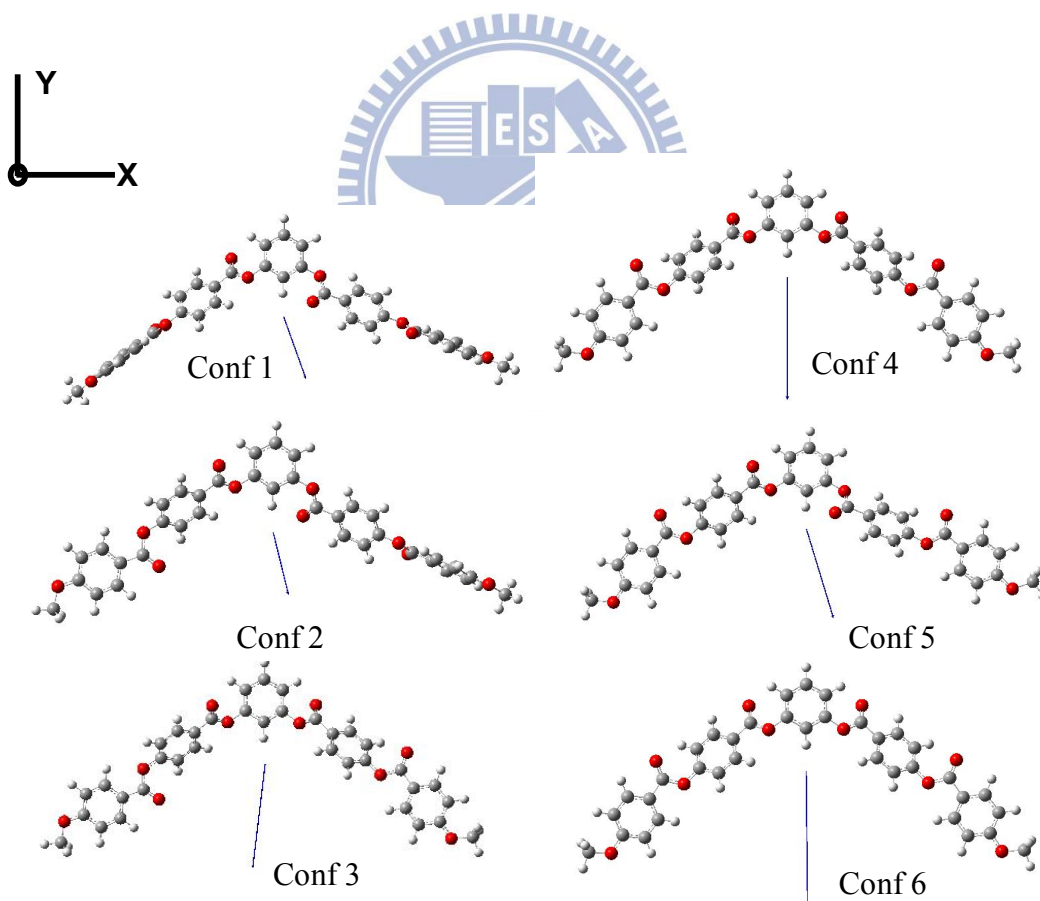
Figure S2.3. Low energy structures of **S1** optimized at B3LYP/6-31G(d).
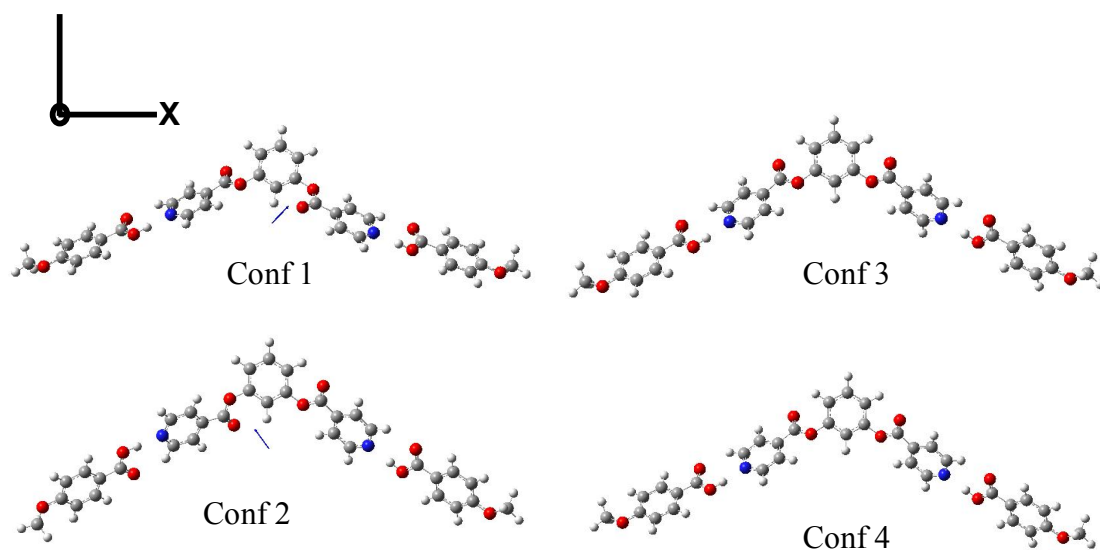
Figure S2.4. Low energy structures of **I-A1** optimized at B3LYP/6-31G(d).
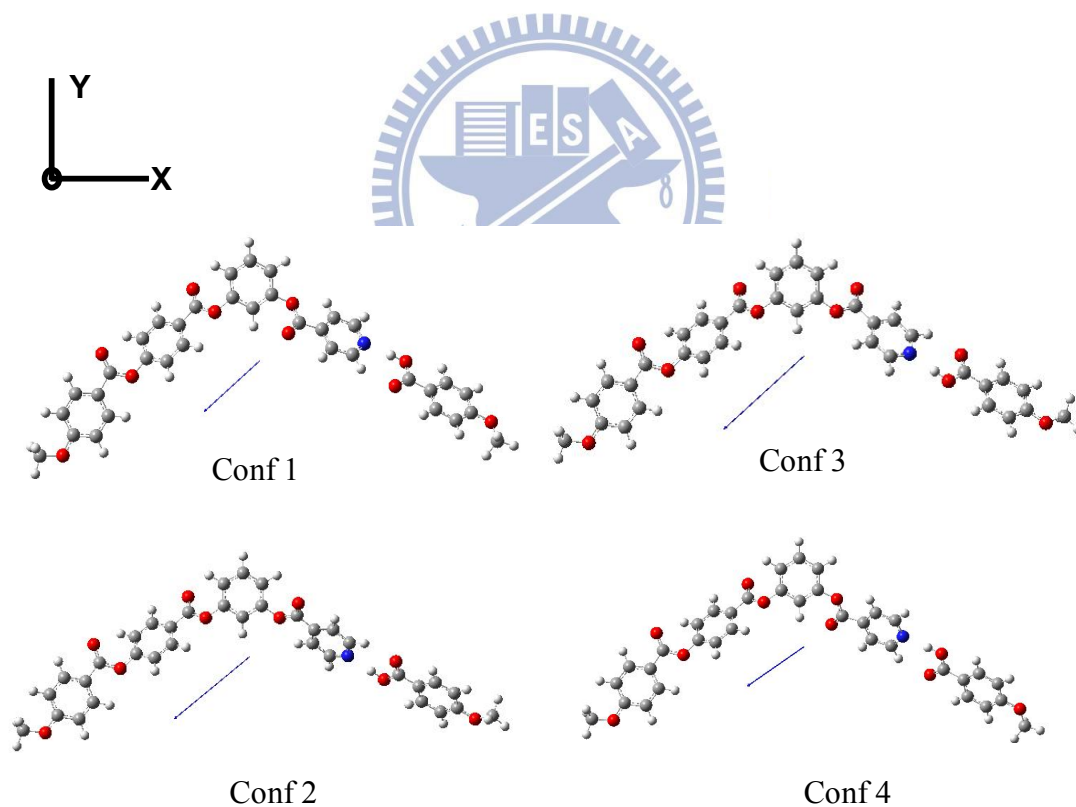
Figure S2.5. Low energy structures of **IV1-A1** optimized at B3LYP/6-31G(d).
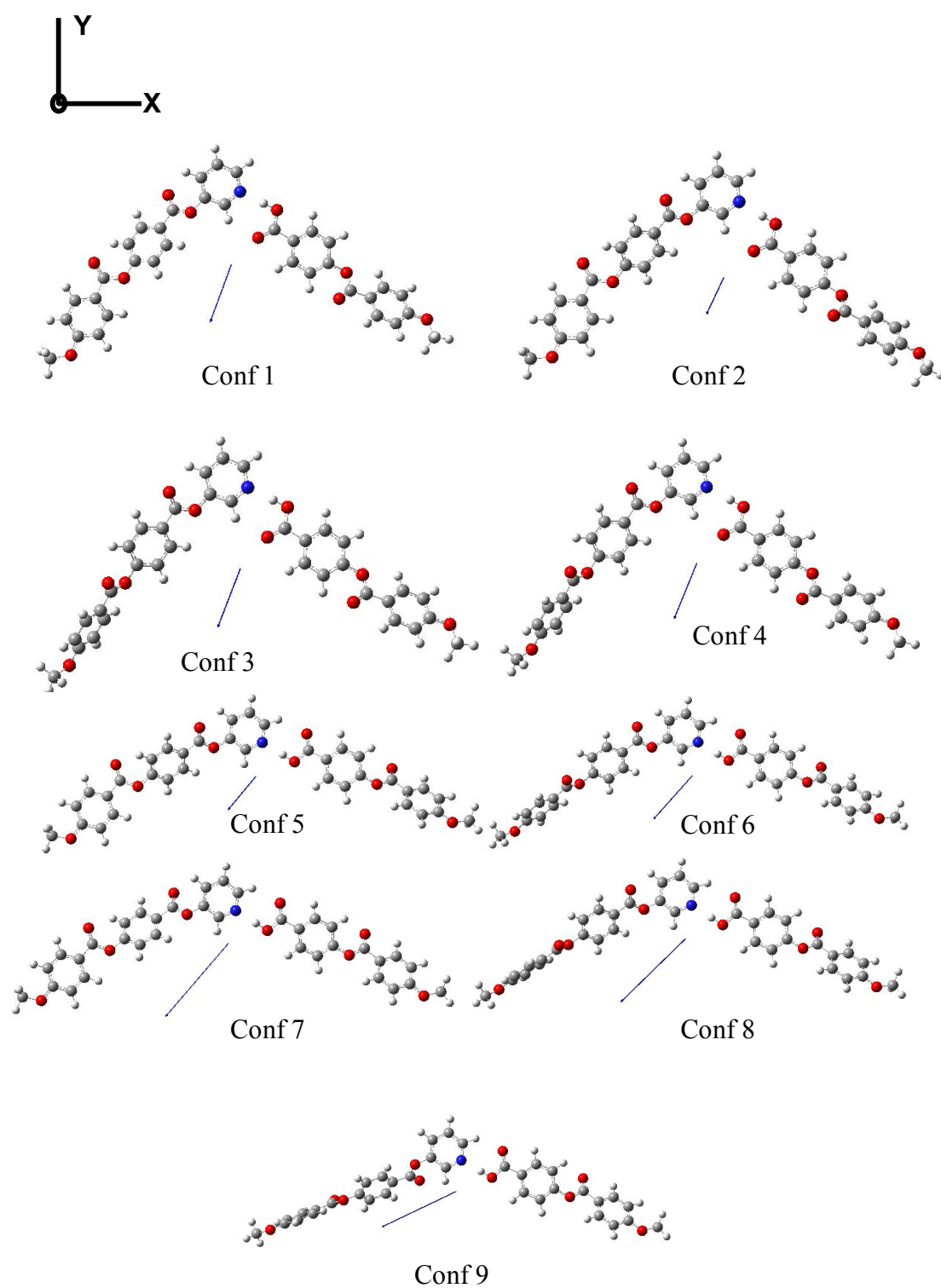
Figure S2.6. Low energy structures of **III1-B1** optimized at B3LYP/6-31G(d).

Table S2.1. Phase Transition Temperatures and Enthalpies of H-Donors (**Am**, **Bm**, and **Cm**) and H-Acceptors (**I**, **II**, **IIIn**, **IVn**, and **Vn**)

Compd.	Phase transition temperature/^{o}C [Enthalpy/kJ/g]					
A12	**I**	135.5 [8.09]	**N**	129.2 [6.3]	**SmC**	86.5 [40.2]	**K**
A16	**I**	127.1 [25.8]	**SmC**	83.7 [71.5]	**K**		
B12	**I**	203.9 [7.7]	**SmC**	104.7 [46.2]	**K**		
B16	**I**	198.6 [8.5]	**SmC**	105.3 [40.3]	**K**		
C12	**I**	289[a]	**N**	218.8 [2.9]	**SmC**	139.5 [13.6]	**K**
C16	**I**	283[a]	**N**	220.3 [1.7]	**SmC**	135.4 [15.9]	**K**
I	**I**	93.5 [104.8]	**K**				
II	**I**	141.4 [89.5]	**K**				
III12	**I**	83.6 [99.4]	**K**				
III16	**I**	81.0 [106.8]	**K**				
IV12	**I**	105.4 [2.5]	**N**	85.3 [48.2]	**K**		
IV16	**I**	100.5 [93.9]	**K**				
V12	**I**	148.1 [4.9]	**N**	124.5 [64.4]	**K**		
V16	**I**	147.4 [4.4]	**N**	135.7 [66.6]	**K**		

I = isoptropic state; N = nematic phase; SmC = normal tilt smectic phase; K = crystalline state. [a] means the temperature data is observed in POM only. The phase transitions were measured by DSC at the 2nd cooling scan with a cooling rate of 5°Cmin^{-1}.

Table S2.2. Sets of Low Energy Structures Calculated at B3LYP/6-31G(d) of the
Bent-Core Structures of **S1**, **I-A1**, **IV1-A1**, and **III1-B1**

	conform ation	ΔE kcal/mol	Energy/au	dipole (Debye)	axial (x, y, z)	Bent angle[a]
S1	1	0	-2139.766923	4.35	1.3938, -4.1232, 0.1724	120.0
	2	0.01	-2139.766901	3.99	1.0048, -3.7895, 0.7715	118.7
	3	0.01	-2139.766905	6.84	0.8859, -6.7903, -0.0177	114.1
	4	0.07	-2139.766804	7.64	0.0004, -7.6426, -0.0069	117.1
	5	0.10	-2139.766771	6.42	1.7294,-5.7808, -2.2023	121.5
	6	0.24	-2139.766545	8.54	0, -8.4013, -1.5619	114.1
1-A1	1	0.00	-2174.281484	1.53	1.0407, 1.1258, -0.0896	131.2
	2	0.11	-2174.281306	1.57	-0.9194, 1.2815, -0.0478	119.8
	3	0.26	-2174.281069	0.21	-0.0001, -0.2131, 0	125.5
	4	0.40	-2174.280849	1.94	0, -0.1646, -1.9337	124.7
IV1-A1	1	0.00	-2157.024320	4.53	-3.4182, -2.9711, -0.0225	113.7
	2	0.07	-2157.024213	6.19	-4.7331, -3.9889, -0.2286	121.4
	3	0.14	-2157.023980	6.69	-4.805, -4.2353, -1.9228	120.2
	4	0.17	-2157.024055	5.05	-3.6149, -2.7624, -2.1964	115.6
III1-B1	1	0.00	-2157.028836	4.10	-1.3853, -3.8368, -0.4568	99.6
	2	0.04	-2157.028772	4.52	-1.4495, -3.9812, -1.5770	99.1
	3	0.07	-2157.028654	4.49	-1.4595, -3.6807, -2.1111	97.4
	4	0.11	-2157.028654	4.48	-1.2277, -3.6898, -2.085	97.3
	5	0.18	-2157.028489	7.06	-4.5694, -5.3715, -0.3763	130.9
	6	0.21	-2157.028438	7.03	-4.7317, -5.0783, -1.1274	129.7
	7	0.25	-2157.028443	7.24	-4.6038, -5.4708, -1.1317	131.5
	8	0.27	-2157.028407	6.91	-4.8768, -4.7492, -1.2033	130.5
	9	0.68	-2157.027754	6.95	-5.9565, -2.5551, -2.5049	135.6

[a] Bent angle (°) measured as the angle between the first, central and final benzene
rings' centers of the bent-core structures.

Chapter 3

H-Bonded Banana-Shaped Liquid Crystalline Dimeric Complexes and Main-Chain Polymers Containing Bent-Core Pyridyl Acceptors and Siloxane Diacid Donors

3.1. Introduction

Supramolecular design has been displayed the intelligent approach to create exquisite architectures during inter- and intra-molecular non-covalent linking groups such as the popular useful tool, e.g. hydrogen-bonds (H-bonds).[41] Many classified investigations (including liquid crystal research) spread out excellent achievements on the judicious way between hydrogen-acceptor (H-acceptor) and -donor (H-donor) parts to emerge various attractive mesogenic properties, especially their electro-optical characteristic under electric fields. For instance, ferroelectric and anti-ferroelectric liquid crystals (FLCs and AFLCs) became more important due to their fast responses of electro-optical properties by applying external electric fields.[42] It is because that the chiral center insertion was disposed in the rod molecular configuration to induce the chirality and spontaneous polarization properties.

However, since the novel formation building by bent-shaped structures without any chiral elements revealed ferroelectric and anti-ferroelectric effects,[1] more bent-shaped derivatives, so called banana-shaped or bent-core mesogens were presented and conferred their fascinating optical and electrical studies. Naturally, their particular mesophases, including column stacking, tilt smectic phases, and three dimension structures, named as B1 to B7 were developed and identified. Traditionally, electro-optical switching behavior was observed in the smectic B1, B2, B5, and B7 phases. Among these phases with switching properties, the B2 phase was the most

frequently investigated. The B2 (SmCP) phase depends on the polar direction and molecular tilt direction in neighboring layers. Ferroelectric (F) and antiferroelectric (A) states are performed duo to the identical and inverse polarization between layer to layer, respectively, and synclinic (S) and anticlinic (A) status are executed cause of the alike and opposite molecular tilt aspect between layer to layer, respectively. Hence, four kinds of different supramolecular architectures denoted SmC_AP_A, SmC_SP_A, SmC_AP_F, and SmC_SP_F are carried out to recognize homochiral (SmC_AP_A and SmC_SP_F) and racemic (SmC_SP_A and SmC_AP_F) conditions individually. However, it is the most important and interesting assignment to perform the lamellar organization with electric-optical switching properties and chirality.

In common studies, more recently, different parts of achiral molecular structures, such as the central parts, lateral substituents, linking groups, terminal chains, and the number of rings, have been varied to study their influences of molecular designs on the mesomorphic behavior. Moreover, more molecular systems with bent-core configurations were investigated, including not only molecules with low molecular weights comprising many kinds of substituents at different positions of rigid cores and flexible chains,[4,25a-b,28c,35a,43d-e,] but also polymeric,[33] dimeric[31,46] and dendritic molecules.[34] Particularly, some special supramolecular structures constructed with silicon groups are also investigated by Tschierske et al.[25a,45] In previous reports, several kinds of molecular architectures were also developed and showed that materials with special segregation contributed by silyl and siloxyl groups displayed a novel way for the switching of ferroelectricity. Simultaneously, lower phase transition temperatures could be procured by different number of silyl units. The fascinating characteristics of silyl and siloxyl insertions have become a useful approach to modify the flexible spacers. Even though some successful cases of covalent bent shaped dimeric and main-chain polymeric molecules[25a] have been reported, very limit

illustrations of non-covalent, i.e. H-bonds bent-core mesogenic structures with polar smectic phase and antierroelectric switching properties were observed in previous literatures, [38] not to mention the H-bonded main-chain polymers which had no case to report. It is because that the suppression of polar switching behaviors for main-chain bent polymers was taken place constantly due to intermolecular micro-segregation based on the serious rigid core and shower flexible spacer which both established on main chain framework.
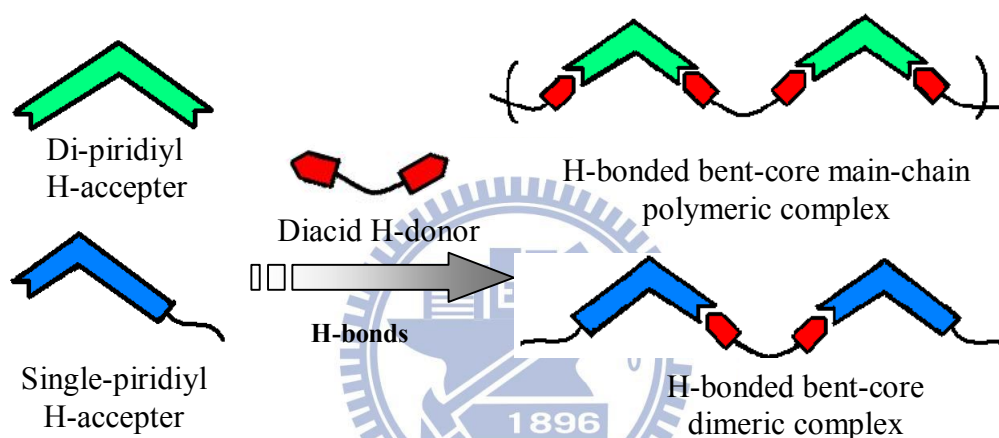
Fig. 3.1. The bent-shaped supramolecular frameworks of H-bonded bent-core dimeric and main-chain polymeric (MCP) complexes.

Accordingly, in fundamental molecular designs of H-bonded bent-core dimeric and main-chain polymeric complexes, siloxyl derivative inserted at middle part of flexible chain is necessary in bent configuration to maintain intermolecular organization and induce their electro-optical and chiral properties. Therefore, in order to elucidate the effects of various structural configurations (H-bonded injections, various siloxyl numbers, and different core shapes) on mesomorphic, electro-optical and chiral properties of H-bonded bent-core dimeric and main-chain polymeric (MCP) supramolecules, several kinds of H-bonded bent-core dimers and MC polymers were self-assembled by appropriate molar
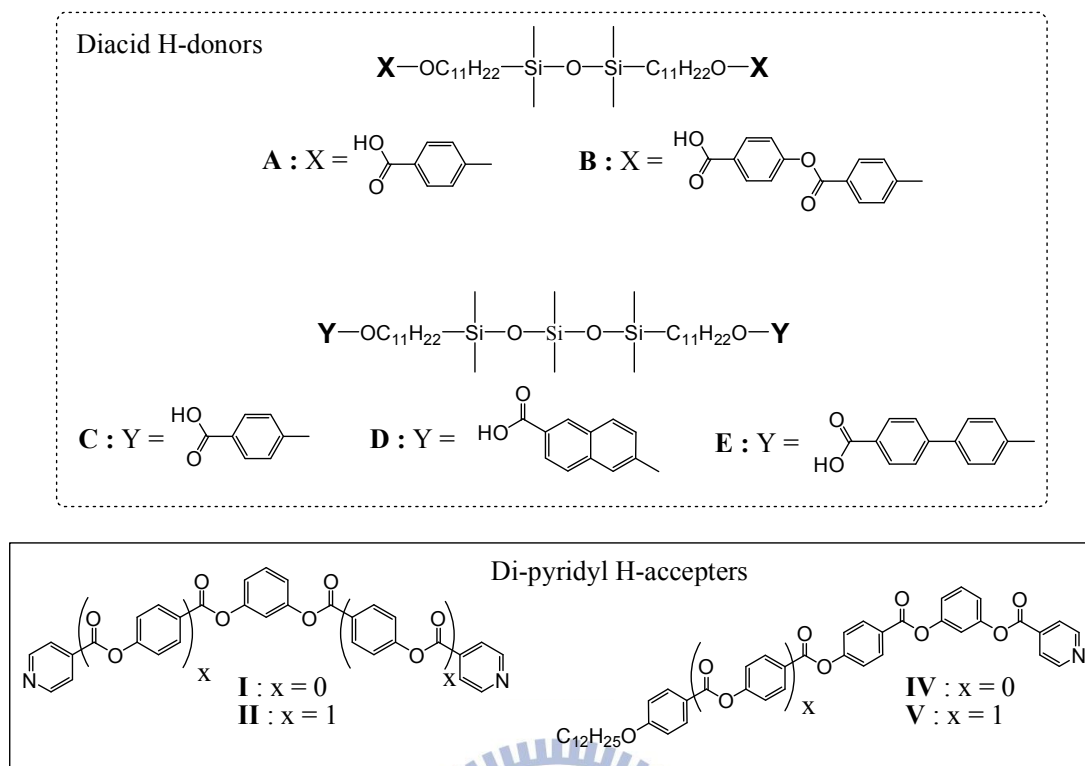
Figure 3.2. The chemical structures of five diacid H-donors and four pyridyl H-accepters.

ratios of proton donors (H-donors) and acceptors (H-acceptors) as shown in Figure 3.1. Five kinds of acidic H-donors with two or three siloxyl units (**A**, **B**, **C**, **D**, and **E,** bearing two terminal acidic groups) and four kinds of bent-core H-acceptors (**I-II** and **IV-V**, bearing double and single terminal pyridyl groups, respectively) were synthesized and displayed in Figure 3.2. H-bonded dimeric supramolecules **IV-N** and **V-N** (N = **A**, **B**, **C**, **D**, and **E**) were self-assembled by single-pyridyl H-acceptors (**IV** and **V**) with all acidic H-donors (**A**, **B**, **C**, **D**, and **E**) as shown in Figure 3.3, and H-bonded MCP supramolecules **I-N** and **II-N** (N = **A**, **B**, **C**, **D**, and **E**) were self-assembled by bis-pyridyl H-acceptors (**I-II**) with all acidic H-donors (**A**, **B**, **C**, **D**, and **E)** as shown in Figure 3.4. The configuration effects of H-bonded bent-core dimeric and MCP complexes on mesomorphic, electro-optical, and chiral properties were investigated, and the polar switching behavior depended on

85

applied electric fields was also examined. The mesomorphic, electro-optical, and chiral properties of all H-bonded complexes were surveyed by polarizing optical microscopy (POM), differential scanning calorimetry (DSC), powder X-ray diffraction (XRD) measurements, and electro-optical (EO) switching experiments.

IV-A: x = 1, y = 1, N = A:
IV-B: x = 1, y = 1, N = B:
IV-C: x = 1, y = 2, N = C:
IV-D: x = 1, y = 2, N = D:
IV-E: x = 1, y = 2, N = E:

V-A: x = 2, y = 1, N = A:
V-B: x = 2, y = 1, N = B:
V-C: x = 2, y = 2, N = C:
V-D: x = 2, y = 2, N = D:
V-E: x = 2, y = 2, N = E:
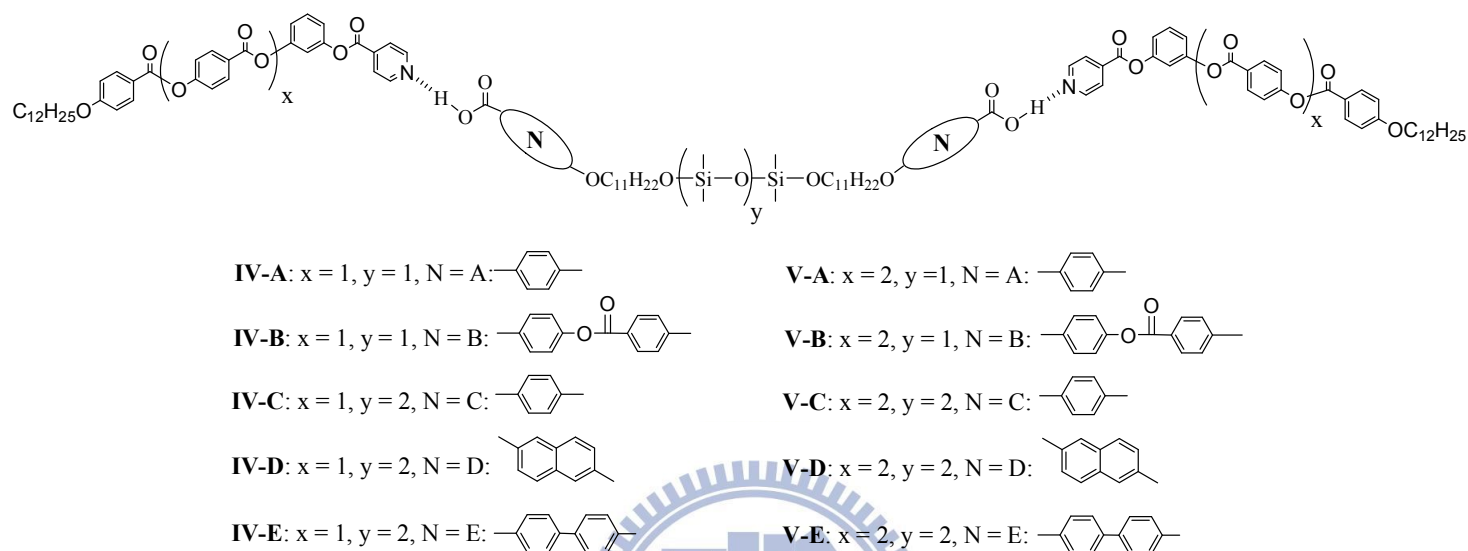
Figure 3.3. H-bonded bent-core dimeric complexes **IV-N** and **V-N** (**N** = **A**, **B**, **C**, **D** and **E**).

I-A: x = 0, y = 1, N = A:
I-B: x = 0, y = 1, N = B:
I-C: x = 0, y = 2, N = C:
I-D: x = 0, y = 2, N = D:
I-E: x = 0, y = 2, N = E:

II-A: x = 1, y = 1, N = A:
II-B: x = 1, y = 1, N = B:
II-C: x = 1, y = 2, N = C:
II-D: x = 1, y = 2, N = D:
II-E: x = 1, y = 2, N = E:
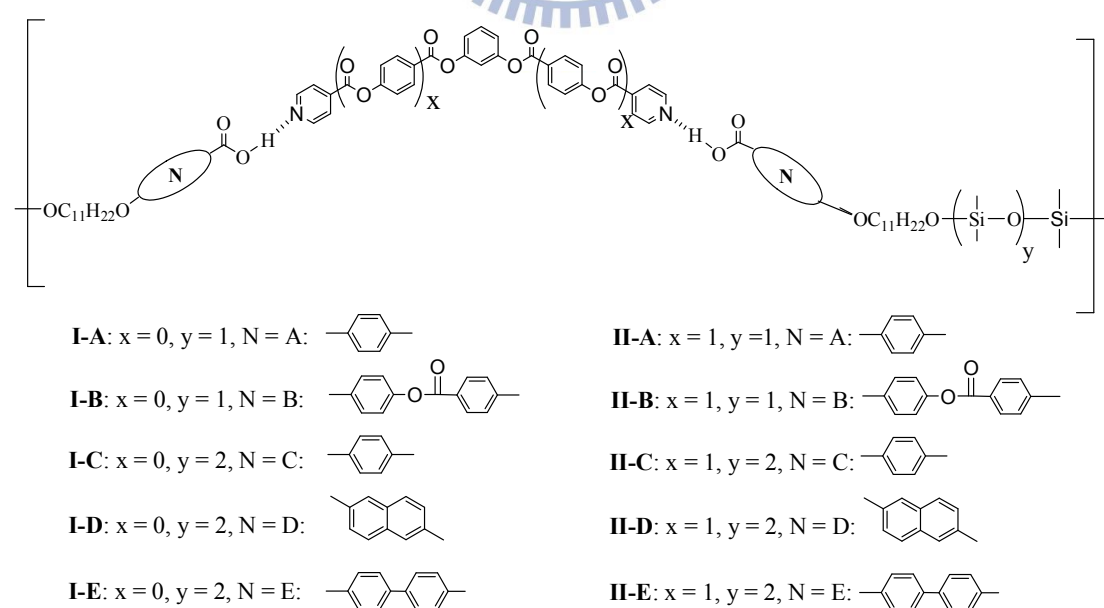
Figure 3.4. H-bonded bent-core main-chain polymeric (MCP) complexes **I-N** and **II-N** (**N** = **A**, **B**, **C**, **D** and **E**).

3.2. Experimental

3.2.1. Characterization methods

^{1}H NMR spectra were recorded on a Varian Unity 300 MHz spectrometer using DMSO-d_6, CDCl$_3$ and D-THF as solvents. Elemental analyses (EA) were performed on a Heraeus CHN-OS RAPID elemental analyzer. Mesomorphic textures were characterized by polarizing optical microscopy (POM) using a Leica DMLP equipped with a hot stage. Infrared (IR) spectra were investigated by Perk-Elmer Spectrum 100 instrument. Temperatures and enthalpies of phase transitions were determined by differential scanning calorimetry (DSC, model: Perkin Elmer Pyris 7) under N$_2$ at a heating and cooling rate of 5 °Cmin^{-1}. Synchrotron powder X-ray diffraction (XRD) measurements were performed at beamline BL17A of the National Synchrotron Radiation Research Center (NSRRC), Taiwan, where the wavelength of X-ray was 1.33336 Å. The powder samples were packed into a capillary tube and heated by a heat gun, whose temperature controller is programmable by a PC with a PID feedback system. The scattering angle theta was calibrated by a mixture of silver behenate and silicon. The electro-optical properties were determined in commercially available ITO cells (from Mesostate Corp., thickness = 4.25 μm, active area = 1 cm^2) with rubbed polyimide alignment coatings (parallel rubbing direction). A digital oscilloscope (Tektronix TDS-3012B) was used in these measurements, and a high power amplifier connected to a function generator (GW Model GFG-813) with a d.c. power supply (Keithley 2400) was utilized in the d.c. field experiments. During electro-optical measurements, the modulations of textures by applying electric fields were observed by POM.

3.2.2. Synthesis

All synthesized processes of H-donors and H-acceptors were shown in Scheme S3.1 and S3.2 (see Supporting Information). Regarding preparations of acidic

compositions (**A**, **B**, **C**, **D**, and **E)**, their synthesized ways were following according to five fundamental methods shown in Scheme S3.1. The benzoic acidic derivatives were protected by benzyl bromide (i.e., steps i), and combinded with alkene chain by triphenyl phosphine (PPH3), diethyl azodicarboxylate (DEAD) in tetrahydrofuran (THF) solvent (i.e., steps ii). The dimeric conformations were established via siloxyl linking part using platinum(0)-1,3-divinyl-1,1,3,3-tetramethyldisiloxane complex, solution in xylenes,(~2% Pt) (i.e., steps iii), and the esterification reactions were carried out by N,N-dicyclohexylcarbodiimide (DCC) and 4-(N,Ndimethylamino) pyridine (DMAP) in dichloromethane (DCM) solvent to acquire related products (i.e., steps iv). De-protecting actions were executed by Pd/C catalyst and hydrogen gas (N_2) in THF solvent as the procedure (i.e., steps v) to eliminate protecting groups.

All the synthesized processes of pyridyl-core compositions (**I**, **II**, **IV**, and **V**) were realized according to five routes shown in scheme S3.2. The esterification reactions were carried out via two procedures (i.e., steps i and iii) to acquire related products. Protecting reactions were proceeded by step iv. De-protecting actions were executed by two procedures (i.e., steps ii and v) to eliminate protecting groups. In addition, the starting compound **14** were prepared according to the literature procedures,[51] and all synthesized details were described in the Supporting Information.

3.2.3. Sample preparation

All H-bonded complexes were constructed by mixing appropriate molar ratios of proton donors (H-donors) and acceptors (H-acceptors) in the solutions of chloroform/THF (ca. 2:1 vol.), which were self-assembled into supramolecules by evaporating solvents slowly. Hence, ten H-bonded bent-core dimers **IV-N** and **V-N** (with single site of H-bond in each bent-core unit) consisting of single-pyridyl H-acceptors (**IV** and **V**) with diacid H-donors (**A**, **B**, **C**, **D**, and **E**) and ten H-bonded

bent-core MC polymers **I-N** and **II-N** (with two sites of H-bonds in each bent-core unit) consisting of bis-pyridyl H-acceptors (**I** and **II**) with diacid H-donors (**A**, **B**, **C**, **D**, and **E**) were achieved by H-bonded force.

3.3. Result and Disscussion

3.3.1. Identification of H-bonds existence

In order to prove the formation of supramolecules, (compared with the transition temperatures of individual components in Figure S3.1 and Table S3.1 of the Supporting Information) new transition temperatures and homogeneous phase transitions of H-bonded complexes would be observed in DSC and POM measurements, respectively. In addition, the stability of H-bonding in all polymeric and dimeric complexes **IV-N**, **V-N**, **IV-N**, and **V-N** was characterized by IR spectra at various temperatures. Therefore, two examples of H-bonded dimeric and polymeric complexes are demonstrated and compared with their components (pyridyl and acidic derivatives) as shown in Figure 3.5.

For instance, the IR spectra of H-bonded bent-core dimeric complex **V-A** and its constituents **V** (H-acceptor) and **A** (H-donor) were compared in Figure 3.5 to examine the H-bonds in crystalline and mesophasic states. In contrast to the O-H band of pure **A** at 2560 cm^{-1}, and the weaker O-H band observed at 2500 and 1920 cm^{-1} in the H-bonded complex **V-A** were indicative of hydrogen bonding between the pyridyl group of **V** and acidic group of **A**. On the other hand, a C=O stretching vibration appeared at 1740 cm^{-1} in complex **V-A**, which showed that the carbonyl group is in a less associated state than in pure **A** with weaker C=O stretching vibration appeared at 1680 cm^{-1} either in crystalline phase or mesophase (Figure 3.5a and 3.5b).[53] Both results suggest that H-bonds are formed between **A** and **V** in solid and mesophasic states of the H-bonded complex **V-A**. In addition, similar

IR analysis of H-bonds in H-bonded bent-core polymeric complex **II-A** was inspected at various temperatures. With the IR evidence of weak O-H band at 2500 and 1920 cm^{-1} and less association of C=O stretching vibration at 1730 cm^{-1} as shown in Figurs. 3.5a and 3.5c, it revealed the successful supramolecular framework of H-bonded complex **II-A** by complexation of H-donor **A** and H-acceptor **II** in 1:1 molar ratio.
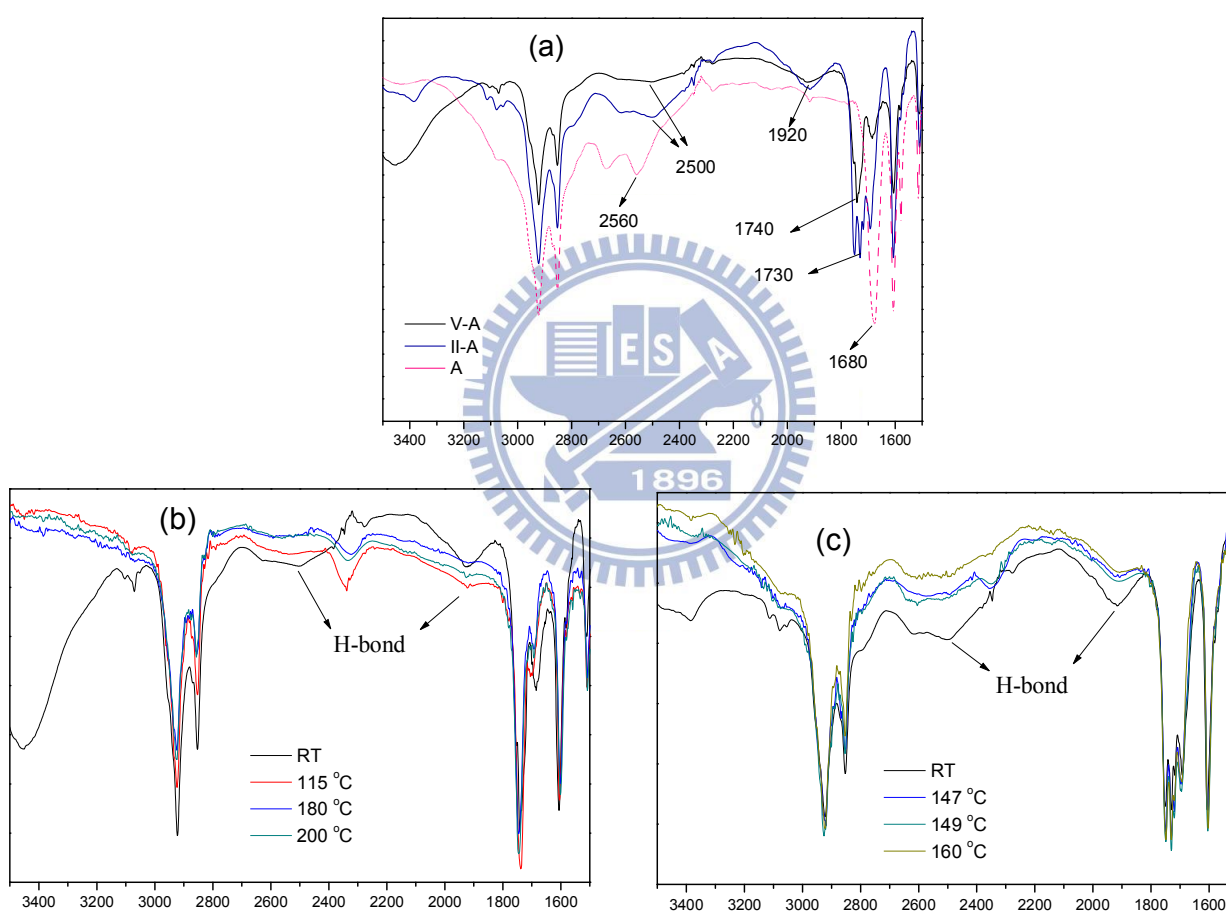
Figure 3.5. IR spectra of (a) complexes **II-A**, **V-A** and their composed moieties **A**; (b) complex **V-A** at variable temperatures; (c) complex **II-A** at variable temperatures.

3.3.2. Mesophasic and thermal properties of H-bonded bent-core dimeric complexes

In order to understand the influence of various bent-core configurations (different chain lengths, rigid cores, and H-bonded sites effect) on mesophasic and thermal properties, ten H-bonded bent-core dimers were identified by POM and DSC measurements as shown in Table 1, Figures 3.6 and 3.7a. All dimeric complexes (except **IV-B**) possessed the polar tilt smectic phase (SmCP), so called B2 phase, which were confirmed by POM to show the spherulite and grainy textures.[11,27a,52] For instance, the spherulite and grainy small spherulite textures are demonstrated in dimeric complexes **IV-A** and **V-D**, respectively (see Figures 3.6a and 3.6b). Furthermore, another kind of spherulite texture was verified in dimeric complex **IV-B** as shown in Figure 3.6c to display the tilt smectic phase with chiral behavior but without polar switching property.

Comparing the phase transition temperatures of dimeric complexes **V-A**, **V-B** and **V-C**, higher isotropization temperature was revealed in complex **V-B** duo to the relatively much higher isotropization temperature of ingredient in H-donor **B** with the longest rigid cores (see Supporting Information Figure S3.1 and Table S3.1). Meanwhile, complex **V-C** showed the lower isotropization temperature and the wide enantiotropic SmCP phase than complexes **V-A** and **V-B** duo to the more bulky siloxyl units (tri-siloxyl unit) of acidic linking spacer to reduce the molecular stacking and provide the higher stability of the SmCP phase (more expansive mesophasic range). The phenomenon of wide enantiotropic mesophasic ranges were also observed in dimeric complexes **V-D** and **V-E**. Regarding the phase transition temperatures of complexes **V-C**, **V-D**, and **V-E** as shown in Figure 3.7a and Table 3.1, the most extensive SmCP phase range was executed in complex **V-E** (bearing biphenyl acidic H-donor) to suggest that more rigid design at terminal core such as the biphenyl acidic H-donor is helpful to stabilize mesophasic exhibition.

Table 3.1. Phase transition temperatures (°C) and enthalpies (kJ/g) of H-bonded bent-core dimeric complexes

Complex	Mesophase transition: heating(up) and cooling(down)
IV-A	**K** 120.5(85.2) **I** **I** 104.5(-35.7) **SmC$_A$P$_A$** 101.2(-47.6) **K**
IV-B	**K** 123.1(35.0) **SmC*** 162.8(11.0) **I** **I** 127.0(-8.1) **SmC*** 100.0(-29.2) **K**
IV-C	**K** 106.8(28.00) **I** **I** 97.5(-26.7) **SmC$_S$P$_A$** 77[a] **K**
IV-D	**K** 118.1(39.0) **SmC$_S$P$_A$** 124.6(17.6) **I** **I** 112.2(-15.6) **SmC$_S$P$_A$** 93.6 (-29.6) **K**
IV-E	**K** 117.0(30.4) **SmC$_S$P$_A$** 152.4(7.9) **I** **I** 131.9(-6.4) **SmC$_S$P$_A$** 87(-24.8) **K**
V-A	**K** 149.6 (49.0) **I** **I** 127.0(-23.4) **SmC$_A$P$_A$** 95.7(-18.9) **K**
V-B	**K** 140.1(21.0) **SmC$_A$P$_A$*** 159.5(15.4) **I** **I** 154.7(-17.2) **SmC$_A$P$_A$*** 131.6(-19.0) **K**
V-C	**K** 102.0(23.8) **SmC$_S$P$_A$** 139.2(18.4) **I** **I** 121.2(-21.8) **SmC$_S$P$_A$** 83.2(-12.9) **K**
V-D	**K** 115.0(31.0) **SmC$_S$P$_A$** 129.3(20.7) **I** **I** 112.7(-19.8) **SmC$_S$P$_A$** 84.1(-32.4) **K**
V-E	**K** 121.9(27.4) **SmC$_S$P$_A$** 140.3(16.2) **I** **I** 125.9(-19.1) **SmC$_S$P$_A$** 78.6(-17.0) **K**

I = isoptropic state; SmCP = polar tilt smectic phase; SmC = normal tilt smectic phase without polar switching behavior; K = crystalline state; [a] means that the phase change can be observed by POM only; * means that chiral domain can be determined by POM.
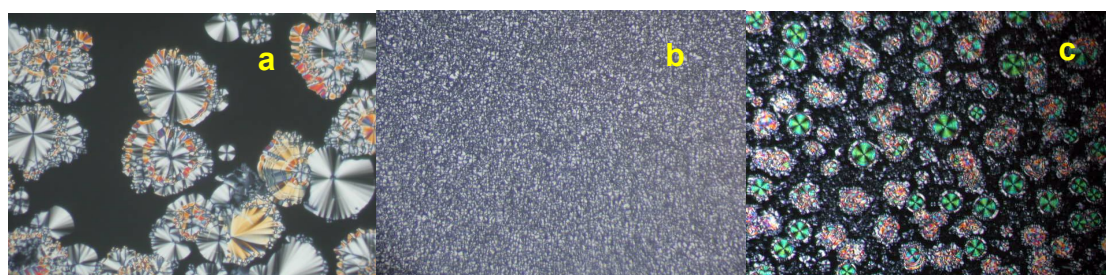
Figure 3.6. POM textures at cooling approach: (a) the polar smectic phase with spherulite domain of dimeric complex **IV-A** at 103 °C; (b) the polar smectic phase with grainy and small spherulite domains of dimeric complex **V-D** at 105 °C; (c) the tilt smectic phase with spherulite domain of dimeric complex **IV-B** at 110 °C.
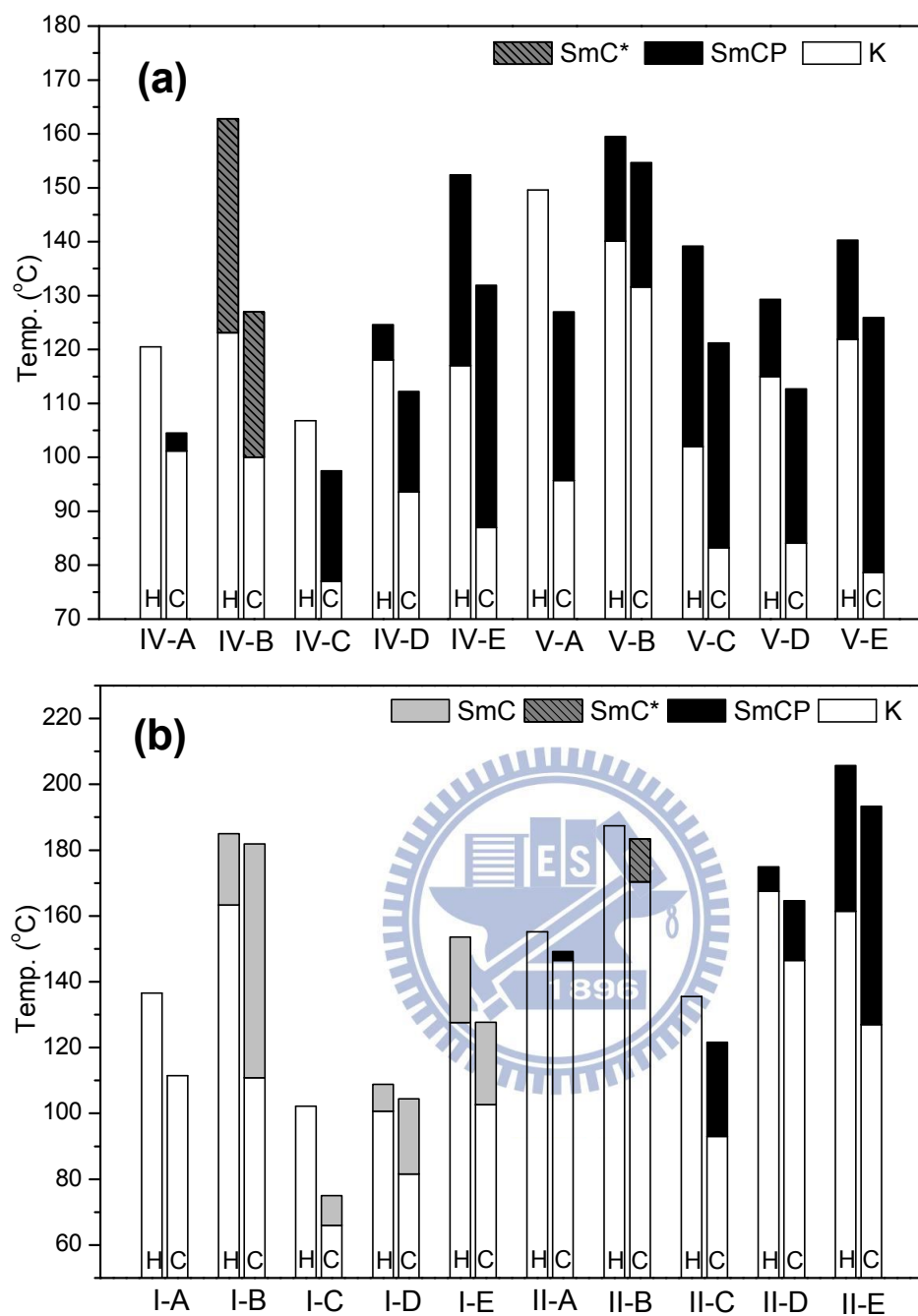
Figure 3.7. Phase diagrams of H-bonded bent-core (a) dimeric and (b) MCP complexes during 2nd heating (H) and cooling (C) conditions.

The analogous phase transition tendencies such as series of complexes **V-N** were acquired in series of dimeric complexes **IV-N** (**N** = **A**, **B**, **C**, **D**, and **E**), where the highest and lowest isotropization temperatures were obtained in complexes **IV-B** and **IV-C**, respectively duo to the relatively ingredient in H-donor and the bulky siloxyl units. The most extensive and narrow SmCP phase ranges were achieved in complexes

IV-E and **IV-A**, respectively to indicate again that the mesophasic stability would be performed in mesogenic designs with the rigid core (as biphenyl acidic H-donor) and the bulky siloxane diacidic H-donors (tri-siloxyl unit). In addition, almost dimeric complexes **V-N** exhibited wider SmCP phase than those of dimeric complexes **IV-N** owning to their longer length of rigid cores, and the SmCP phase was induced in complex **V-B**.

3.3.3. Mesophasic and thermal properties of H-bonded bent-core main-chain polymeric complexes

Two series of analogous MCP complexes, i.e., **I-N**, and **II-N** (N = **A**, **B**, **C**, **D**, and **E**) were investigated for the influence of H-bonded sites, rigid-core, and flexible chain variations on their mesophasic types and phase transition temperatures as shown in Figure 3.8, Figure 3.7b and Table 3.2. In regard to the mesophasic types, the tilt smectic phase without polar switching and chiral properties was examined in MCP complexes **I-N**, except complex **I-A**, which presented only crystalline state. With respect to MCP complexes **II-N**, the tilt smectic with chiral behavior was revealed in complex **II-B**, and polar smectic phase were demonstrated in complexes **II-C**, **II-D**, and **II-E**. The mesophasic textures were evidenced by POM experiments, for example, complex **I-B** displayed the spherulite domain in Figure 3.8a, and complex **II-A** exhibited the other kind of spherulite domain in Figure 3.8b as the evidence of the polar smectic (SmCP) phase. In addition, the evidence of SmCP phase was also performed as the schlieren texture in complex **II-D** (see Figure 3.8c).
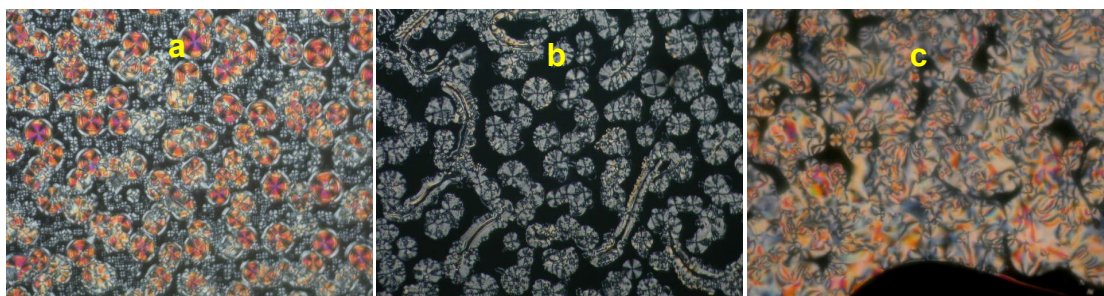
Figure 3.8. POM textures at cooling approach: (a) the tilt smectic phase with spherulite domain of MCP complex **I-B** at 170 °C; (b) the polar smectic phase with spherulite domain of MCP complex **II-A** at 147 °C; (c) the polar smectic phase with schlieren texture of MCP complex **II-E** at 150 °C.

Table 3.2. Phase transition temperatures (^{o}C) and enthalpies (kJ/g) of H-bonded bent-core main-chain polymeric complexes

Complex	Mesophase transition: heating(up) and cooling(down)
I-A	**K** 84.2(4.6) **K'** 120.6[b] **K"** 136.6 (61.3)[b] **I** **I** 111.46(28.0) **K"** 79.6(8.2) **K'** 71.1 (11.7) **K**
I-B	**K** 129.2(20.4) **K'** 163.3(22.8) **SmC** 185[a] **I** **I** 181.9(3.3) **SmC** 110.8(17.4) **K'** 91.5(22.7) **K**
I-C	**K** 78.0 (3.8) **K'** 102.2 (35.5) **I** **I** 75.0(-38.3) **SmC** 66[a] **K**
I-D	**K** 100.7(20.7) **SmC** 110.9(8.1) **I** **I** 104.4(-11.9) **SmC** 81.6 (-21.3) **K**
I-E	**K** 127.6(15.6) **SmC** 153.6(11.0) **I** **I** 129.7 (-10.7) **SmC** 102.7 (-14.3) **K**
II-A	**K** 155.2(108.0) **I** **I** 149.3[b] **SmC$_A$P$_A$** 146.5(-91.7)[b] **K**
II-B	**K** 187.4(35.5) **I** **I** 183.4 (10.3) **SmC*** 170.4(26.5) **K**
II-C	**K** 73.46(11.2) **K'** 135.51(29.1) **I** **I** 121.61(22.9) **SmC$_A$P$_F$** 93[a] **K'** 43.58 (11.5) **K**
II-D	**K** 167.5(23.6) **SmC$_A$P$_F$** 174.9(34.4) **I** **I** 164.6(-31.8) **SmC$_A$P$_F$** 146.5 (-24.7) **K**
II-E	**K** 155.4(11.8) **K'** 161.4 (2.8) **SmC$_A$P$_F$** 204.7 (33.0) **I** **I** 193.3(27.5) **SmC$_A$P$_F$** 127.0(1.9) **K'** 105.9 (9.6) **K**

I = isoptropic state; SmCP = polar tilt smectic phase; SmC = normal tilt smectic phase without polar switching behavior; K = crystalline state; [a] means that the phase change can be observed by POM only; [b] means the enthalpy values of two cover transition peaks; * means that chiral domain can be determined by POM.

With respect to the phase transition temperatures of CMP complexes **I-N** (**N** = **A**, **B**, **C**, **D**, and **E**), the highest isotropization temperature was obtained in complexes **I-B** due to much higher isotropization temperature of ingredient in H-donor **B** with the longest rigid cores, and the lowest isotropization temperature was received in complex **I-C** due to the bulky siloxane spacer of diacidic H-donor. To compare the phase transition temperatures of complexes **I-C**, **I-D**, and **I-E**, the higher and more extensive range of enantiotropic tilt smectic phase was obtained in complex **I-E**, oppositely, the narrow range of monotropic tilt smectic phase was acquired in complex **I-C** (see Figure 3.7 and Table 3.2). Regarding the phase transition temperatures of MCP complexes **II-N** (**N** = **A**, **B**, **C**, **D**, and **E**), the analogues phase transition tendencies and extensive mesophasic ranges than those of CMP complexes **I-N** were obtained, where lower phase transition temperature and wide enantiotropic mesophasic range were observed in complexes **II-C** and **II-E**, respectively. It would be suggested that higher mesophasic stability can provided by the rigid terminal core designs as well as the bulky siloxane spacer. To compare the Phase transition temperatures of H-bonded bent-core dimers and MC polymers, almost MCP complexes exhibited higher mesophasic transitons, and dimeric complexes displayed wider mesophasic ranges. In addition, SmCP phases were more stable in dimeric complexes.

3.3.4. Powder XRD analyses of H-bonded bent-core dimeric complexes

The H-bonded molecular organizations of H-bonded bent-core dimeric complexes **IV-N** and **V-N** (**N** = **A**, **B**, **C**, **D**, and **E**) in different mesophases (smectic phases) were investigated by XRD measurements (see Table 3). Duo to the too narrow mesophasic range of complex **IV-N**, its XRD analyses was limited to determinate. However, the tilt smectic arrangements were demonstrated in complexes **IV-N**. For

example, sharp layer reflection peaks (up to the second order diffraction as shown in Figure 3.9a) were observed at the associated d-spacing values of $d_1 = 38.0$ Å and $d_2 = 19.0$ Å indexed as (001) and (002), respectively with tilt angles (between the molecular axis and the layer normal) c.a. 46.4°in complex **IV-E** (see Table 3.3) as the evidence of the tilt lamellar arrangements. Furthermore, wide angle diffuse peaks corresponding to a d-spacing value of 4.6 Å indicated that similar liquid-like in-plane orders with average intermolecular distances were prevalent inside the smectic layers. [54]

With respect to dimeric complexes **V-N** (**N** = **A**, **B**, **C**, **D**, and **E**), for instance, complex **V-D** displayed sharp layer reflection peaks (up to the third order diffraction as shown in Figure 3.9b), which were acquired at the associated d-spacing values of $d_1 = 50.9$ Å, $d_2 = 25.5$ Å, and $d_3 = 17.0$ Å with tilt angles c.a. 41° (see Table 3.3) to indicate the tilt smectic organization. The analogues XRD investigations of other dimeric complexes **V-N** were obtained in their mesophasic ranges to confirm the tilt smectic behaviors.[54]

3.3.5. Powder XRD analyses of H-bonded bent-core main-chain polymeric complexes

In powder XRD studies of two series H-bonded bent-core main-chain polymers **I-N** and **II-N**, the collative data was displayed in Table 3.4, and two XRD patterns of molecules **I-B** and **II-D** were procured in Figure 3.10. The broad peak situated in spacing value of 4.6 Å and sharp reflection peak were obtained at (001) index of $d_1 = 36.2$ Å in MCP complex **I-B** (see Figure 3.10a), and all the MCP complex **I-N** (**N** = **A**, **B**, **C**, **D**, and **E**) exhibited the similar XRD investigations, where the longest d-spacing and tilt angle values were calculated in ranges of 33.2 – 38.2 Å and 44° – 58°, respectively to suggest the lamellar order exists (see Table 3.4). Regarding the series of MCP complexes **II-N** (**N** = **A**, **B**, **C**, **D**, and **E**), for example, complex **II-E**

revealed the sharp and broad peaks at corresponding d-spacing values of 52.7 Å and 4.6 Å, respectively in the mesophasic range as shown in Figure 3.10b. The tilt angle value of 44° was acquired. The XRD results of complex **II-E** was indicated the lamellar order exists. Others H-bonded MCP complexes **II-A**, **II-B**, **II-C** and **II-D** displayed the lamellar molecular arrangements duo to their d-spacing and tilt angle values in ranges of 52.7 – 58.7 Å and 33° – 48°, respectively.

Table 3.3. Powder XRD data of H-bonded bent-core dimeric complexes

Complex	Phase	D-Spacing D(Å)	Miller index (a b c)	Molecular length L(Å)	Tilt angle Ø(degree)
IV-A	SmCP	—	—	51.1	—
IV-B	SmC*	35.2 17.7	(001) (002)	64.8	57.1
IV-C	SmCP	38.2 19.5	(001) (002)	52.0	42.7
IV-D	SmCP	36.2	(001)	53.3	47.2
IV-E	SmCP	38.0 19.0	(001) (002)	55.2	46.4
V-A	SmCP	39.8	(001)	64.8	52.1
V-B	SmCP*	51.1 25.8	(001) (002)	68.0	41.2
V-C	SmCP	50.0	(001)	65.7	40.5
V-D	SmCP	50.9 25.5 17.0	(001) (002) (003)	66.9	40.5
V-E	SmCP	39.4 26.5	(001) (002)	68.8	55.0

Figure 3.9. Powder X-ray diffraction pattern intensity against angle profiles obtained upon cooling from the isotropic phase: (a) in the SmCP phase of dimeric complex **IV-E**; (b) in the SmCP phase of dimeric complex **V-D**.

Table 3.4. Powder XRD data of H-bonded bent-core main-chain polymeric complexes

Complex	Phase	D-Spacing D(Å)	Miller index (a b c)	Molecular length L(Å)	Tilt angle Ø(degree)
I-B	SmC	36.2	(001)	67.9	57.8
I-C	SmC	38.2 19.1	(001) (002)	53.0	43.9
I-D	SmC	35.9 17.9	(001) (002)	57.3	54.8
I-E	SmC	33.2 16.6	(001) (002)	61.1	57.0
II-A	SmCP	52.7	(001)	68.0	39.2
II-B	SmC*	53.4 27.1 18.2	(001) (002) (003)	80.2	48.2
II-C	SmCP	58.7	(001)	69.9	32.8
II-D	SmCP	54.6 27.5 18.5	(001) (002) (003)	74.2	42.6
II-E	SmCP	55.7	(001)	77.9	44.4
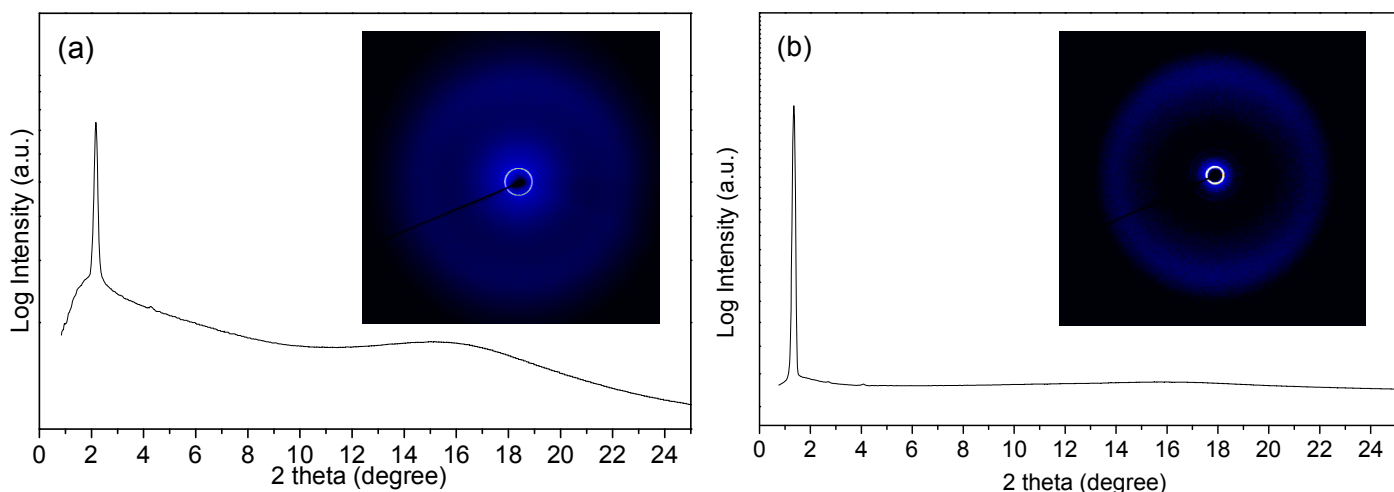
Figure 3.10. Powder X-ray diffraction pattern intensity against angle profiles obtained upon cooling from the isotropic phase: (a) in the tilt SmC phase of MCP complex **I-B**; (b) in the SmCP phase of MCP complex **II-D**.

3.3.6. Spontaneous polarization (Ps) behavior of H-bonded bent-core dimeric complexes

In order to verify the polar switching properties in H-bonded bnet-core dimeric structures, the triangular wave method[22] was applied to measure the switching current behavior (i.e., the spontaneous polarization) under 4.25 μm thick parallel rubbing cells. The current peaks per half-period of an applied triangular voltage were obtained in the switching current response curves of all SmCP phase in almost H-bonded bent-core dimeric complexes **IV-N** and **V-N** (except complex **IV-B**). Regarding the H-bonded bent-core dimeric complexes **IV-N** and **V-N** (N = **A** and **B** with di-siloxyl units), antiferroelectric behavior was clearly examined in complexes **IV-A**, **V-A** and **V-B** according to the two-peak switching current response. For example, the two-peak switching current response curves of complex **IV-A** was shown in Figure 3.11a. Here, the characteristic behavior of a sequential electric response was due to a ferroelectric state switched into an antiferroelectric ground state and back to the opposite ferroelectric state, which confirmed the SmCP$_A$ (A =

anti-ferroelectric behavior) structure of the B2 phase in complex **IV-A**.[55] Furthermore, the POM texture of **IV-A** (see Figure 3.11b) under applied electric field was compared with POM texture of **IV-A** without voltage applying as shown figure 6a. The extinction crosses of spherulite domain paralleled with polarizer indicated antiferroelectric state, and the extinction cross of switching domain was rotating to mean ferroelectric state. The analogues results were also provided in complexes **V-A** and **V-B** (with di-siloxyl unit).

With respect to the dimeric complexes **IV-N** and **V-N** (**N** = **C**, **D** and **E** with tri-siloxyl unit), for instance, the single like current peak of dimeric complex **V-D** was observed under triangular wave applying at low (30 – 60 Hz) or high frequencies (200 – 500 Hz) as shown in Figure 3.11c. However, when the modified triangular wave[25a] was applied (Figure 3.11e), the current response was separated into two peaks at both offset of voltage arrearage. It was also indicated that the SmCP$_A$ state is existed and hidden under triangular wave measurement cause of the quick exchange of SmCP$_F$ → SmCP$_A$ → SmCP$_F$. The POM texture of switched-on state (SmCP$_F$) was shown in Figure 3.11d to compare the POM texture (see Figure 3.6b) of switched-off ground state (SmCP$_A$). The similar results were also preformed in other dimeric complexes **IV-N** and **V-N** (**N** = **C**, **D** and **E** with tri-siloxyl units) to mean the antiferroelectric behavior. In addition, The Ps values of series **IV-N** and **V-N** (except complex **IV-B**) were calculated in the ranges of 40 – 224 nC/cm^2 and 303 – 361 nC/cm^2, respectively. It was indicated that more stable polar switching behavior is achieved caused by longer covalent-bonded bent-core design of H-acceptor **V** in complexes **V-N**.
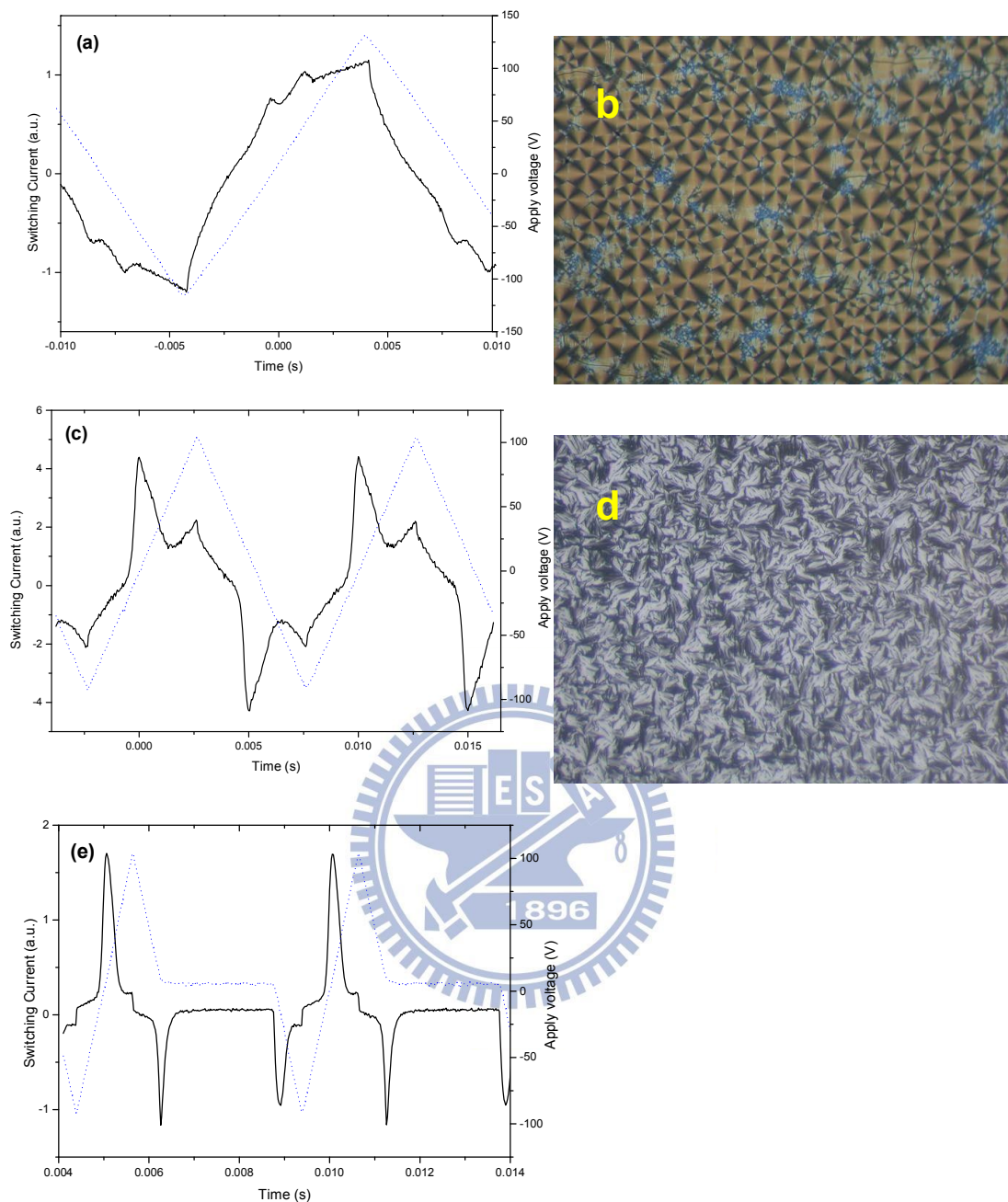
Figure 3.11. Switching current response of H-bonded bent-core dimeric complexes (a) **IV-A** at 104 °C (as Vpp = 231 V, f = 60 Hz) by applying a triangular wave and (b) its POM texture under the corresponding electric field; (c) **V-D** at 120 °C (as Vpp = 197 V, f = 200 Hz) by applying a triangular wave, and (d) its POM texture under the corresponding electric field; (e) **V-D** at 120 °C (as Vpp = 197 V, f = 200 Hz) under a modified triangular wave. (in parallel rubbing cells with 4.25 μm thickness).

3.3.7. Spontaneous polarization behaviors of H-bonded bent-core main-chain polymeric complexes

To investigate the polar switching behavior of H-bonded MCP complexes of **I-N** and **II-N** (N = **A**, **B**, **C**, **D**, and **E**), their smectic phases of MCP complexes **I-N** and **II-N** were examined by triangular and modified triangular waves in applied electric field (up to 300Vpp) under 4.25 μm thick parallel rubbing cells. The tilt smectic phase of complexes **I-N** was confirmed considering no switching current behaviour observed, however, the first example of novel bent-core main-chain polymers constructed on H-bonded design with spontaneous polarization behaviors were achieved in series **II-N** (N = **A**, **C**, **D**, and **E**, except for complex **II-B**).

The current response of polar switching behaviors were determined in of MCP complexes **II-N** (N = **A**, **C**, **D**, and **E**). Regarding complex **II-A**, two current peaks were obtained at 147 °C (as Vpp = 264 V, f = 200 Hz) to mean the antiferroelectric behavior as shown in Figure 3.12a. In addiction, the POM texture of complex **II-A** (inserted in Figure 3.12a) under electric field was compared with the POM texture of **II-A** without voltage applying as shown Figure 3.8b. The antiferroelectric and ferroelectric states were verified duo to the extinction crosses of spherulite domains paralleled with polarizer (Figure 3.8b) and the rotating extinction cross of switching domain (the orange part in the inserted texture of Figure 3.12a), respectively. However, a single current peak indicative the ferroelectric behavior, which confirmed the $SmCP_F$ (F = ferroelectric behavior) structure of the B2 phase was observed in MCP complexes **II-N** (N = **C**, **D**, and **E**). For instance, the polar smectic phase of complex **II-E** exhibited the single current response peak, which prove the molecular rotation around a cone, in both triangular (Figure 3.12b) and modified triangular waves (Figure 3.12c) to mean the ferroelectric state switched into the opposite ferroelectric state ($SmCP_F$ → $SmCP_F$).[35a] Hence the bistable switching of

ferroelectricity and the range of Ps values (27 – 144 nC/cm²) were obtained in MCP complexes **II-C**, **II-D** and **II-E** (with tri-siloxyl unit).
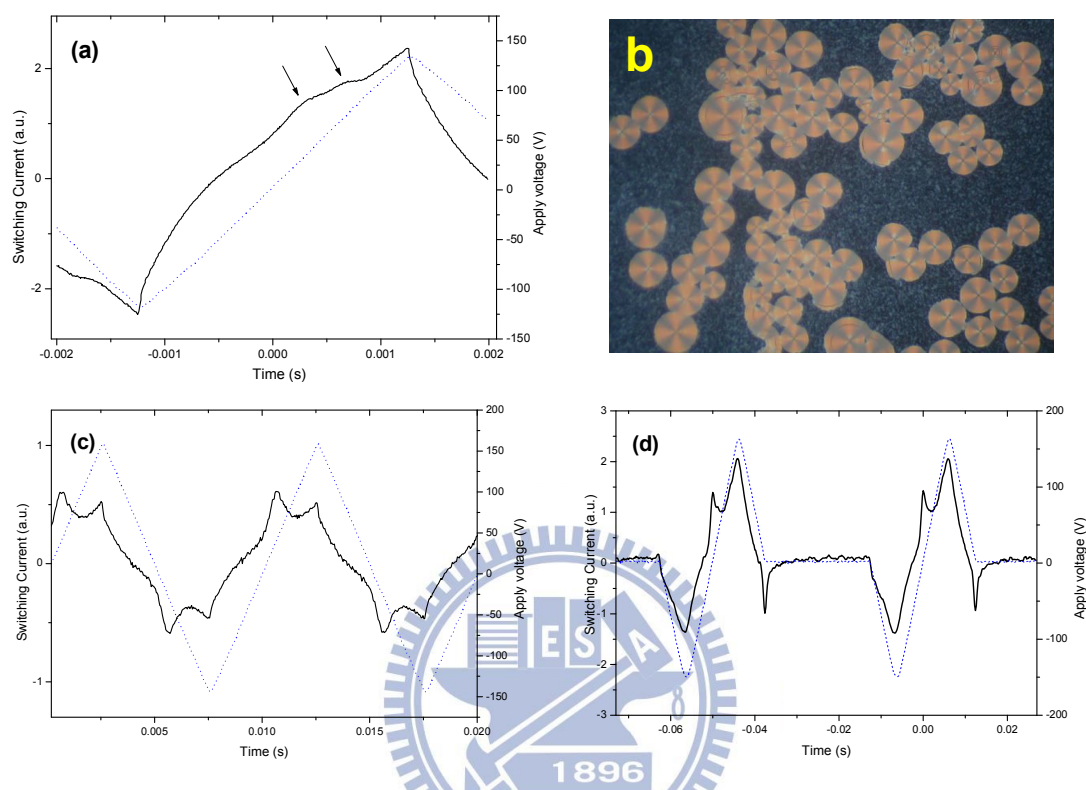
Figure 3.12. Switching current response of H-bonded bent-core MCP complexes (a) **II-A** at 147 °C (as Vpp = 264 V, f = 200 Hz) by applying a triangular wave and (b) its POM texture under the corresponding electric field; (c) **II-E** at 120 °C (as Vpp = 327 V and f = 100 Hz) by applying a triangular wave and (c) **II-E** at 120 °C (as Vpp = 327 V and f = 30 Hz) under a modified triangular wave (in parallel rubbing cells with 4.25 μm thickness).

Table 3.5. Ps values and operating conditions of switching behavior

Complex	Ps (nC/cm²)	phase	Complex	Ps (nC/cm²)	phase	Complex	Ps (nC/cm²)	phase
II-A	27	AF	**IV-A**	40	AF	**V-A**	313	AF
II-B	—	—	**IV-B**	—	—	**V-B**	363	AF
II-C	85	FE	**IV-C**	84	AF	**V-C**	303	AF
II-D	144	FE	**IV-D**	224	AF	**V-D**	351	AF
II-E	114	FE	**IV-E**	123	AF	**V-E**	309	AF

Overall, to compare the ferroelectricity of H-bonded bent-core dimeric and MCP complexes, only the antiferroelectric behavior was revealed in dimeric complexes **IV-N** and **V-N** with SmCP phase. However, the ferroelectricity of MCP complexes **II-N** was dependent on the siloxyl unit of H-donors, where antiferroelectric and ferroelectric behaviors were displayed according to their corresponding di-siloxyl and tri-siloxyl H-donors, respectively. The Ps values of all H-bonded bent-core dimeric and MCP complexes (with SmCP phase) were shown in Table 3.5. To compare the SmCP phase range and Ps values of each series of H-bonded bent-core complexes, wider ranges of SmCP phases were occurred in series of complexes with H-donor **E** (complexes **IV-E**, **V-E** and **II-E**). However the higher Ps values were observed in almost series of complexes with H-donor **D** (complexes **IV-D** and **II-D**), but not including series of complexes **V-N**, which the highest Ps value was obtained in complex **V-B** duo to its most rigid of molecular stacking.

3.3.8. Voltage- and temperature-dependent spontaneous polarization behaviors of H-bonded bent-core dimeric and main-chain polymeric complexes

In theory, the spontaneous polarization behaviors were demonstrated in H-bonded bent-shaped dimers and main-chain polymers if the suitable electric field, frequency, and temperature were given. In order to identify the influence of H-bonds as well as the applied electric fields and temperatures on spontaneous polarization behaviors, two series of complexes **V-N** and **II-N** (not including complex **II-B)** with SmCP phases (represented the H-bonded bent-core dimers and MCP polymers, respectively) were examined in various electric fields and temperatures, and their correlative data were shown in Figures 3.13 and 3.14.

To consider the temperature-dependent spontaneous polarization studies of series of complexes **V-N**, their Ps values were raised gradually and diminished substantially during the cooling process of isotropic to mesophasic states and mesophasic to

crystalline states, respectively (see Figure 3.13a). The observations of Ps value vs. temperature were corresponded with DSC measurements to indicate that the Ps behavior is certainly contributed from polar smectic arrangement. The similar results in series of complexes **II-N** were also accomplished as shown in Figure 3.13b.
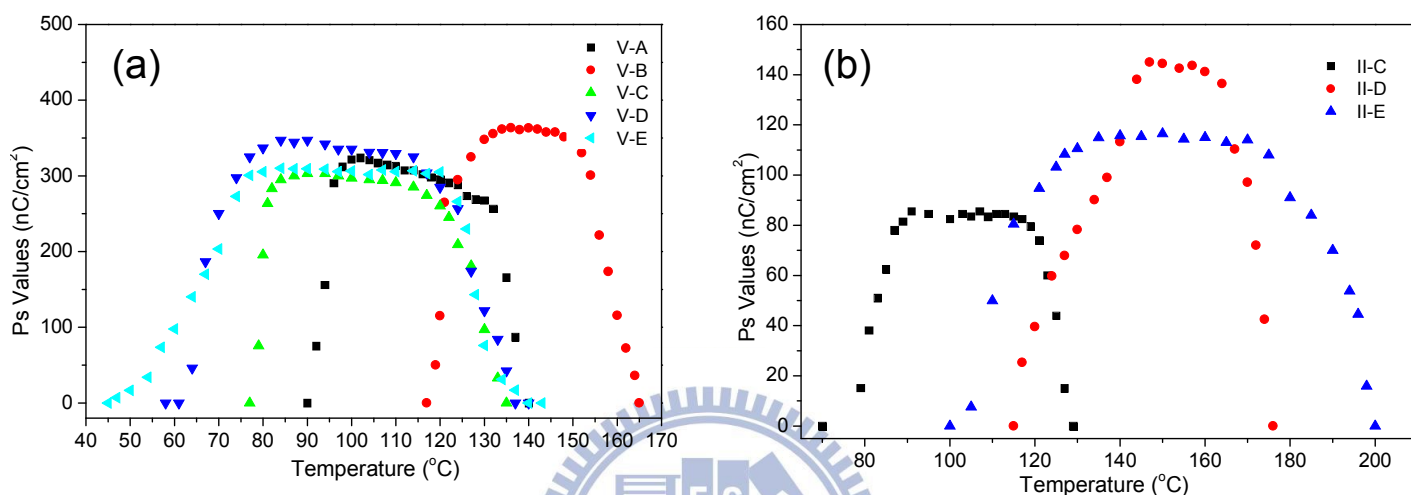
Figure 3.13. Ps values of (a) dimeric complexes **V-N** (**N** = **A**, **B**, **C**, **D** and **E**) and (b) MCP complexes **II-N** (**N** = **C**, **D** and **E**) as a function of cooling temperatures (as f = 200Hz and Vpp = 250 V).
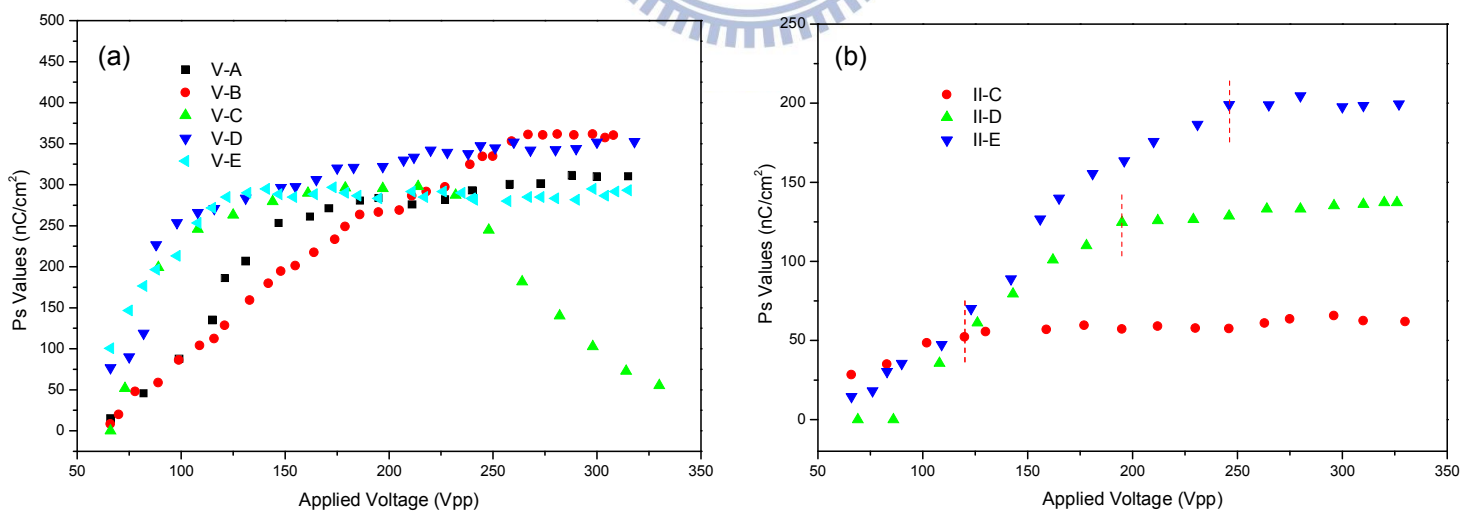
Figure 3.14. Ps values of (a) dimeric complexes **V-N** (**N** = **A**, **B**, **C**, **D** and **E**) and (b) MCP complexes **II-N** (**N** = **C**, **D** and **E**) as a function of applied voltage (as f = 200Hz and (Tc - T) = 10 ^{o}C).

To inspect the voltage-dependent effect of spontaneous polarization behaviors, the tendencies of Ps value vs. applied electric field were surveyed in the SmCP phases of complexes **V-N** and **II-N** (not including complex **II-B**) as shown in Figure 3.14. Regarding the series of dimeric complexes **V-N** (**N** = **A**, **B**, **D**, and **E**), Ps values were increased and saturated via the increasing of applied voltage, where the maximum applied voltages were Vpp = 325 V and the saturated Ps values were reached at voltages above Vpp = 125 – 260 V. With respect to series of MCP complexes **II-N** (**N** = **C**, **D**, and **E**), their saturated Ps values of complexes **II-C**, **II-D** and **II-E** were attained in voltages above 120 Vpp, 195 Vpp and 246 Vpp, respectively (see Figure 3.14b). Higher voltages were necessary to switch the relatively spontaneous polarization behaviors of complexes with higher isotropization temperatures duo to the tighter molecular stacking. This phenomenon was also revealed obviously in series of dimeric complex **V-N**, where the minimum required voltage of dimeric complex **V-B** (above Vpp = 260 V) were higher than those of other dimeric complexes **V-A**, **V-C**, **V-D** and **V-E** duo to its high isotropization temperature.

Almost H-bonded bent-core dimeric and MCP complexes would exhibit the stable spontaneous polarization behaviors under high applied electric fields, but not completely. For instance, as shown in Figure 3.14a, the Ps values of complex **V-C** were decreased when applied voltage was higher than 230 Vpp cause of the broken hydrogen bond force. In order to demonstrate this condition, the further clear apparent case of complex **II-A** was inspected by POM observations, which its Ps vs. Voltage data was lose collected imprecisely because that non-clear current response peak and very less Ps value were demonstrated under lower (Vpp $<$ 240 V) and higher (Vpp $<$ 270 V) voltage applying duo to the voltage sensitive effect. In general, the SmC_AP_A ground state would be transformed to polar switching domain (SmC_SP_F, as the orange circular domain shown in inserted POM texture of Figure 3.15a) to

107

contribute Ps property by the increasing of applied electric field. Nevertheless, the polar circular domain was disappeared and changed gradually to gray grainy domain to form the non polar switching domain as shown in Figure 3.15b and 3.15c. Afterwards, the fan-like domain indicative the SmC_AP_A state (see Figure 3.15d) would return by the removing of electric field. It was indicated that the H-bond of complex **II-A** would become weak and unstable easily under large electric field applied to restrain the arising of spontaneous polarization behavior. Consequently, a voltage applied dependent material is established.
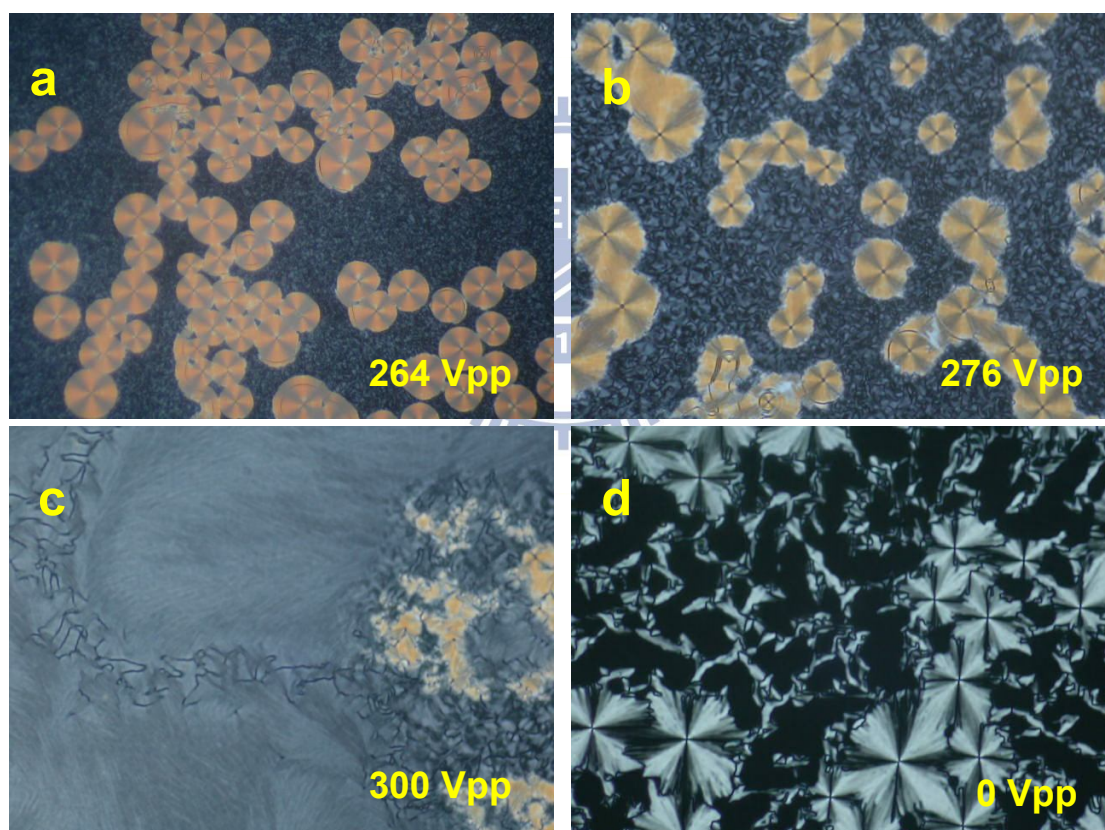
Figure 3.15. POM textures of MCP complex **II-A** under the applied triangular wave electric field as (a) Vpp = 264 V, (b) Vpp = 276 V, (c) vpp = 300 V and (d) Vpp = 0 V (electric field removing).
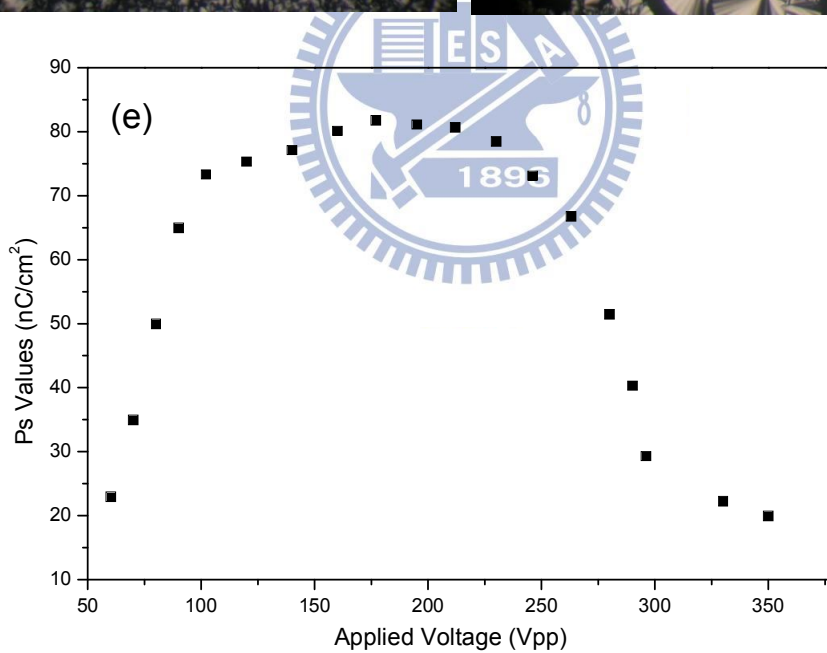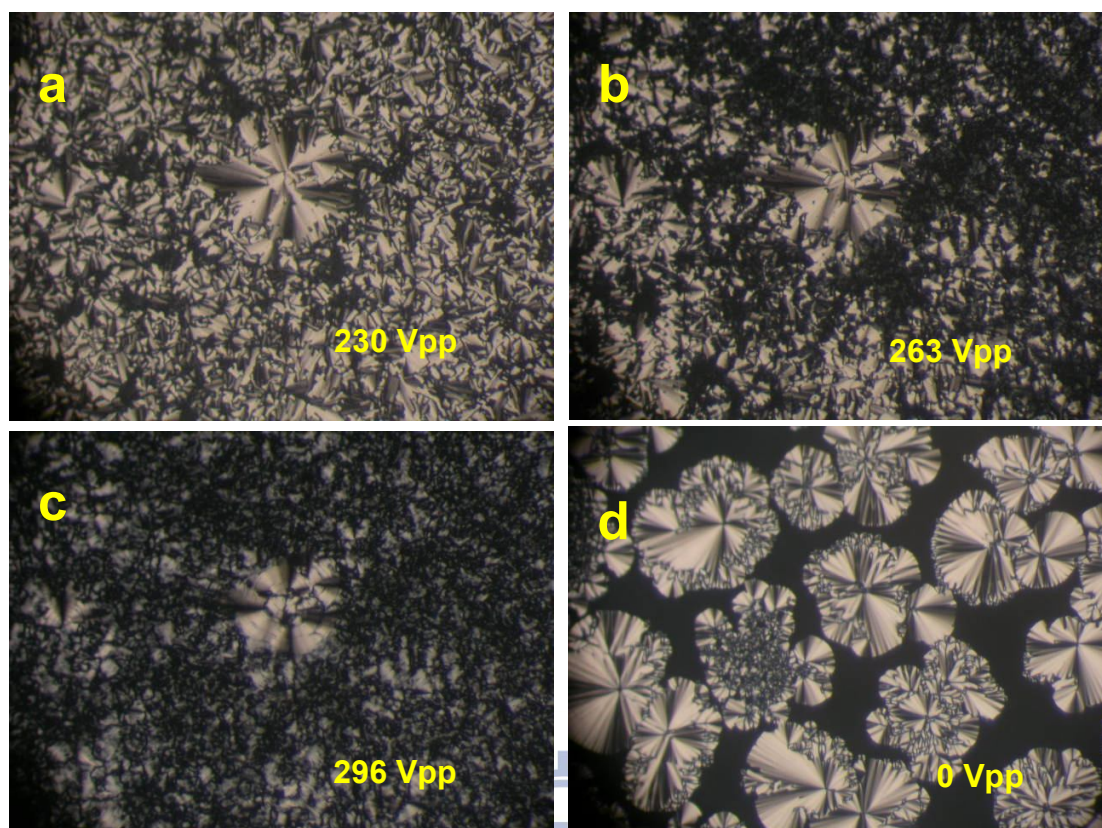
Figure 3.16. POM textures of dimeric complex **IV-C** under the applied triangular wave electric field as (a) Vpp = 230 V, (b) Vpp = 263 V, (c) Vpp = 296 V and (d) Vpp = 0 V (voltage removing and heating and cooling again); (e) Ps values of dimeric complex **IV-C** as a function of applied voltage (as f = 200Hz and (Tc - T) = 10 ^{o}C).

109

In addition, the voltage-dependent condition was also demonstrated in complex **IV-C** to record its tendency of Ps value completely in Figure 3.16e. The saturated Ps values were obtained by the increasing of electric field up to V = 102 Vpp, and Ps values were decreased when the applied electric field was more than 246 Vpp. The circular and broken-fan domains indicative the polar switching behavior was shown in Figure 3.16a at 230 Vpp. However when the voltage was higher than 246 Vpp, the circular and broken-fan domains were dispersed into the dark grainy domain as shown in Figure 3.16b and 3.16c. Finally, the circular and fan-like domains (Figure 3.16d) were reversible by voltage removing, heating and cooling again. It was a typical case to show the voltage-sensitive polar switching behavior of bent-core material duo to the collapsible and reversible weak H-bonded force.

3.3.9. Chirality investigation

In principle, the chirality of SmCP phase was depended on molecular polar direction and molecular tilt direction in neighboring layers. The polar direction was determined based on the current response under triangular wave electric field applying to show opposite or identical directions between neighboring layers. In addition, a switching process of molecular tilt direction could be determined through the rotation and retention of the extinction crosses. In order to understand the chirality of all H-bonded bent-core dimeric and MCP complexes with SmCP phases, their optical investigations were observed by applying (or after removing) triangular wave (TAW), square wave (SW) and opposite direct current (d.c.) electric fields in H-bonded bent-core complexes with polar smectic phase.

In investigation the antiferroelectric characteristic of the H-bonded bent-core complexes with H-donors **A** and **B** (owning di-siloxyl unit), circular domains were formed in the SmCP phase, where the smectic layers are circularly arranged around the centers of the domains. The layer structure arrangement corresponds to the
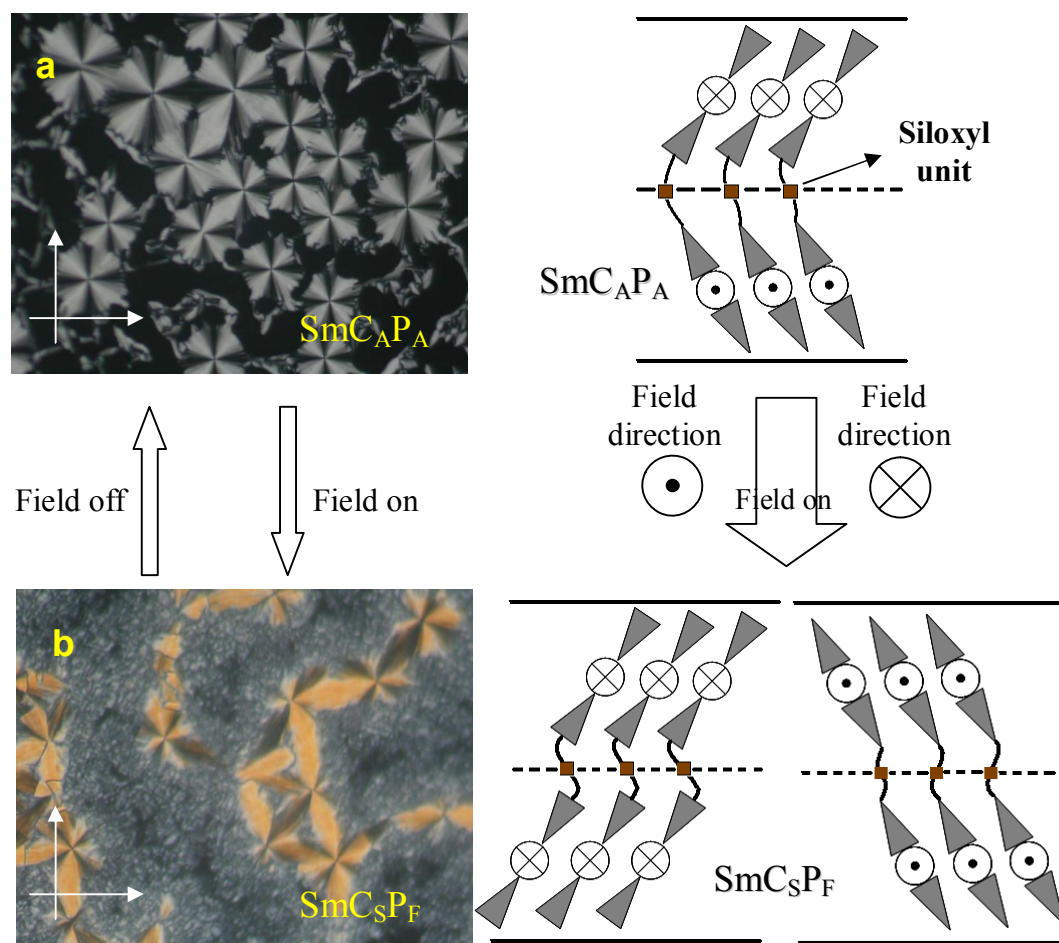
Figure 3.17. The POM textures of chiral domain switching in MCP complex **II-A** between (a) SmC_AP_A ground state with 0 V (without electric field) and (b) SmC_SP_F state with ±30 V of applied d.c. electric field in a parallel rubbing cell with a cell gap of 4.25 μm. (White arrows are the directions of polarizers and analyzers.)

domain models was proposed by Link et al.[8,24] As shown in Figure 3.17, the rotation of the extinction crosses during the switched on and off states in complex **II-A** demonstrated the chiral domain behavior.[7] Without the electric fields (off state), the extinction crosses were reoriented to the crossed polarizer directions (see Figure 3.17a), indicating an anticlinic tilt in the antiferroelectric ground state (SmC_AP_A). In view of Figure 3.17b, by applying d.c. electric fields (with reverse polarities), the extinction crosses rotated either counterclockwise or clockwise (i.e., rotated oppositely with positive and negative fields), indicating a synclinic tilt in the ferroelectric state (SmC_SP_F). The chiral domain switching between SmC_SP_F and

111

SmC$_A$P$_A$ states was also observed by triangular wave method as shown in Figure 3.8 and Figure 3.12b. Meanwhile, all H-bonded bent-core complexes with SmCP phase bearing H-donors **A** and **B** (owning di-siloxyl unit) like **IV-A**, **V-A** and **V-B** exhibited the similar chirlity investigation with complex **II-A** to show the chiral domain of anticlinic tilt in the antiferroelectric ground state (SmC$_A$P$_A$).
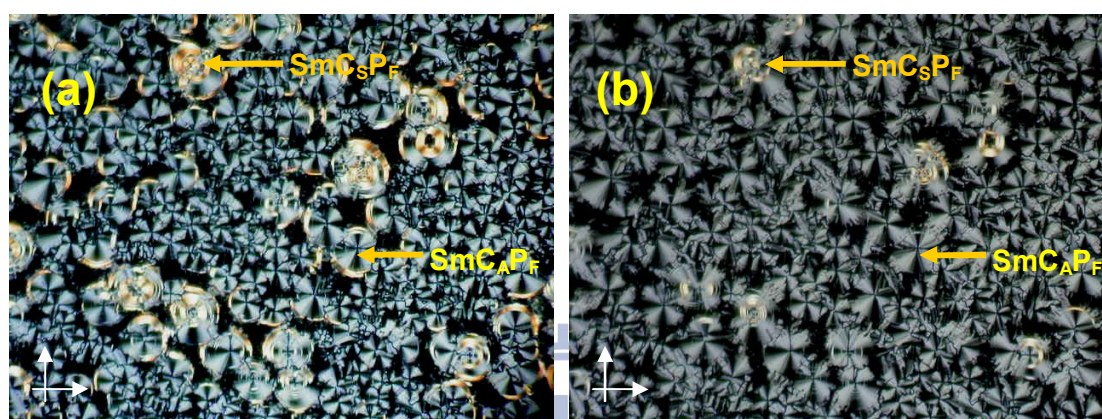
Figure 3.18. The co-existence of chiral (SmC$_S$P$_F$) and racemic (SmC$_A$P$_F$) domains under (a) the first time of the d.c. electric field applying and (b) second time of d.c. electric field applying (opposite polarities). (White arrows are the directions of polarizers and analyzers.)

In chirality investigation of H-bonded bent-core dimeric complexes with H-donors **C**, **D** and **E** (owning tri-siloxyl unit), the chirality switching processes were determined in the complex **V-C** by applying the triangular wave, square wave and direction current (d.c.) electric fields. When the first time of d.c electric field was applied, two different circular domains were exhibited. As shown in Figure 3.18a, the extinction crosses of circular domain oriented to crossed polarizer directions was indicated the SmC$_A$P$_F$ state, and the rotated extinction crosses of circular domains (orange region) was meant the SmC$_S$P$_F$ state (see the red arrows in Figure 3.18a). This phenomenon was described the co-existence of chiral (SmC$_S$P$_F$) and racemic (SmC$_A$P$_F$) domains under the first time of the d.c. electric field applying. The similar

observation was obtained in the applied triangular wave field as well. However, the SmC$_S$P$_F$ domains became smaller or disappeared to switch into the SmC$_A$P$_F$ domains under the second time of opposite d.c. electric field applying as shown in Figure 3.18b. In order to understand chirality switching processes, the optical investigation of the switching behavior of complex **V-C** were performed by the processes of applied SW (±35 V, 0.05 Hz) and TAW (140 Vpp, 100Hz) electric fields as shown in Figure 3.19. When the SW electric field started to apply, The retented extension crosses of racemic domain (SmC$_A$P$_F$ state) and few rotating extension crosses of chiral domain (SmC$_S$P$_F$ state), which were pointed out by the red arrows as shown in Figures 3.19b and 3.20b, were received form the ground states (SmC$_S$P$_A$ and SmC$_A$P$_A$, see Figures 3.19a and 3.20a). The area of rotating extension cross were diminished obviously and oriented to crossed polarizer directions with the applied times of SW electric field (Figures 19c, 3.19d and 3.20c) to mean the changing chirality from chiral (SmC$_S$P$_F$) to racemic (SmC$_A$P$_F$) domains. When the SW electric field was removed, the SmC$_A$P$_F$ state was switched into SmC$_S$P$_A$ ground state as shown in Figures 3.19e and 3.20d, and then, even if the TAW or SW fields were applied, only the transfer of racemic domain (SmC$_S$P$_A$ → SmC$_A$P$_F$) could be examined under switched off- (Figures 3.19f and 3.20d) and on-states (Figure 3.19g and 3.20c) of electric fields, suggesting the racemic behavior with no reversible of chiral behavior under electric field applying. However, the co-existence of chiral (SmC$_S$P$_F$) and racemic (SmC$_A$P$_F$) domains could be achieved by heating to isotropic state and cooling to mesophasic state again.

Regarding the chirality of H-bonded bent-core MCP complexes with H-donors **C**, **D** and **E** (owning tri-siloxyl unit), the racemic domain of SmC$_A$P$_F$ ground state was identified. In optical inspection of MCP complex **II-D**, the extension crosses were oriented to the crossed polarizer directions with no d.c. electric field applying to mean the racemic domain of SmC$_A$P$_F$ ground state (see Figure 3.21a). However, the

extension crosses were retained without rotating phenomenon under d.c. (Figure 3.21b) and TAW (Figure 3.21c) electric fields applying simultaneously, suggesting the opposite racemic domain of SmC_AP_F state.[25c] This kind of characteristic was performed in H-bonded bent-core MCP complexes **II-C**, **II-D** and **II-E** with H-donors **C**, **D** and **E** to reveal the racemic behavior.

The chiral domain behavior could also be proven by the method of rotating the polarizer without applying electric fields.[2,4] For example, the polarizer was rotated clockwise by a small angle of 10° from the crossed position in complex **II-B**, and then the dark and bright domains become clearly distinguishable (see Figure 3.22a). On rotating the polarizer counterclockwise by the same angle (10°) from the crossed position, the previously observed dark domains turned to bright domains, and vice versa (see Figure 3.22b). This observation was also indicative of the occurrence of chiral domains with opposite handednesses. The phenomenon could also be displayed in complexes **IV-B** and **V-B**. It means even if the complexes **II-B**, **IV-B** and **V-B** (with H-donor **B**) exhibited no spontaneous polarization behaviors, the opposite handednesses of chiral domain were still maintained (see Figure 3.22c to 3.22f).

Overall, the chirality of H-bonded bent-core dimeric complexes were depended on the siloxyl unit of H-donors, where the chiral domain of SmC_AP_A ground state and opposite handednesses was revealed in dimeric complexes with di-siloxyl H-donors **A** and **B**, and racemic domain of SmC_SP_A ground state was demonstrated in the dimeric complexes with tri-siloxyl H-donors **C**, **D** and **E**, respectively. However, the chiral domain was demonstrated in MCP complexes, in which SmC_AP_A ground state and opposite handednesses were displayed in MCP complexes with di-siloxyl H-donors **A** and **B**, and SmC_SP_F ground state was exhibited in MCP complexes with tri-siloxyl H-donors **C**, **D** and **E**, respectively.
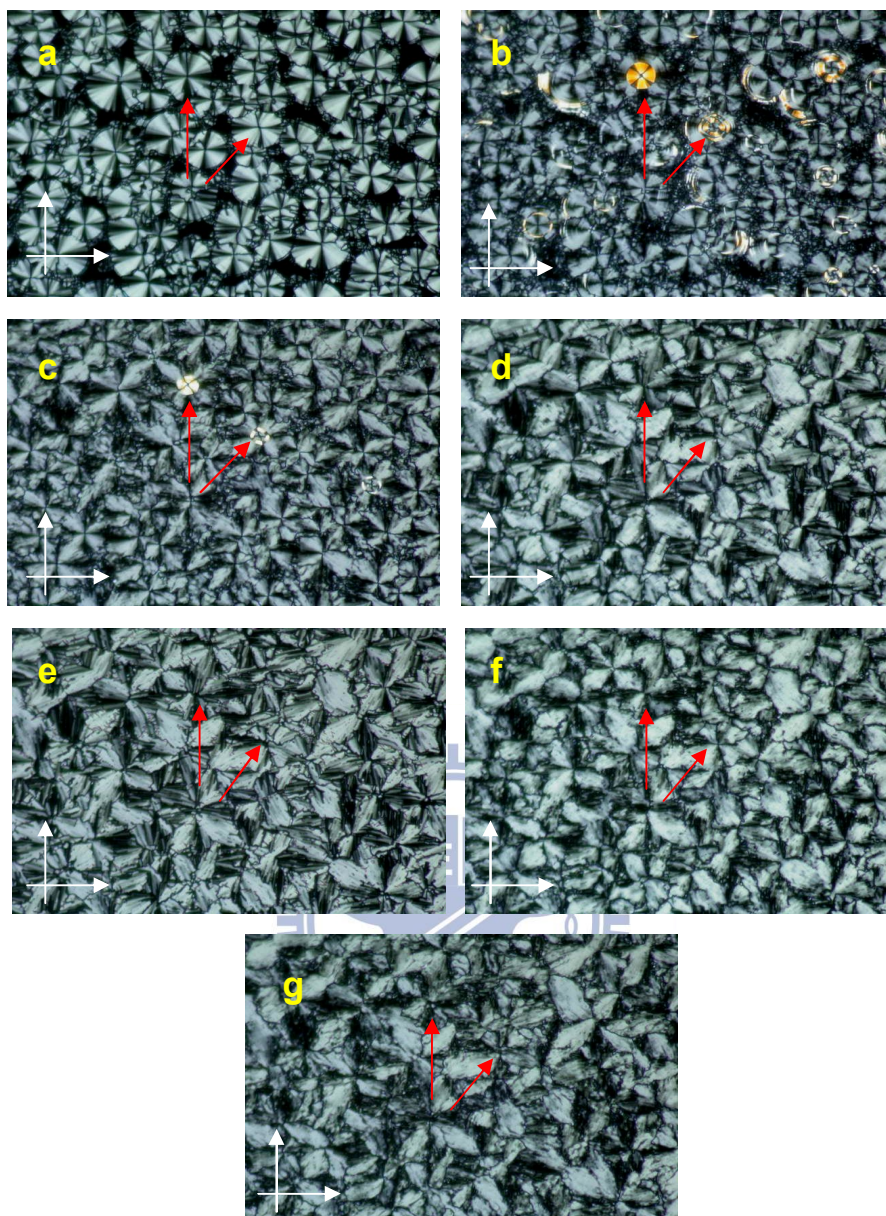
Figure 3.19. The spherulite domains of dimeric complex **V-C**: (a) the co-existence of chiral (SmC_AP_A) and racemic (SmC_SP_A) domains without electric field applying; (b) the co-existence of chiral (SmC_SP_F) and racemic (SmC_AP_F) domains under the first time of square wave electric field applying; (c) The decreasing of chiral (SmC_SP_F) domains, which transferred to racemic (SmC_AP_F) domains partially under third time of square wave electric field applying; (d) The racemic (SmC_AP_F) domains with the disappearance of chiral (SmC_SP_F) domains under fifth time of square wave electric field applying; (e) the racemic (SmC_SP_A) domains without electric field applying; (f) the racemic (SmC_AP_F) domains under triangular wave electric field applying; (g) the racemic (SmC_AP_F) domains after the removing of triangular wave electric field applying. (White arrows are the directions of polarizers and analyzers, and red arrows are the indicators of chiral (SmC_AP_A or SmC_SP_F) domains.)
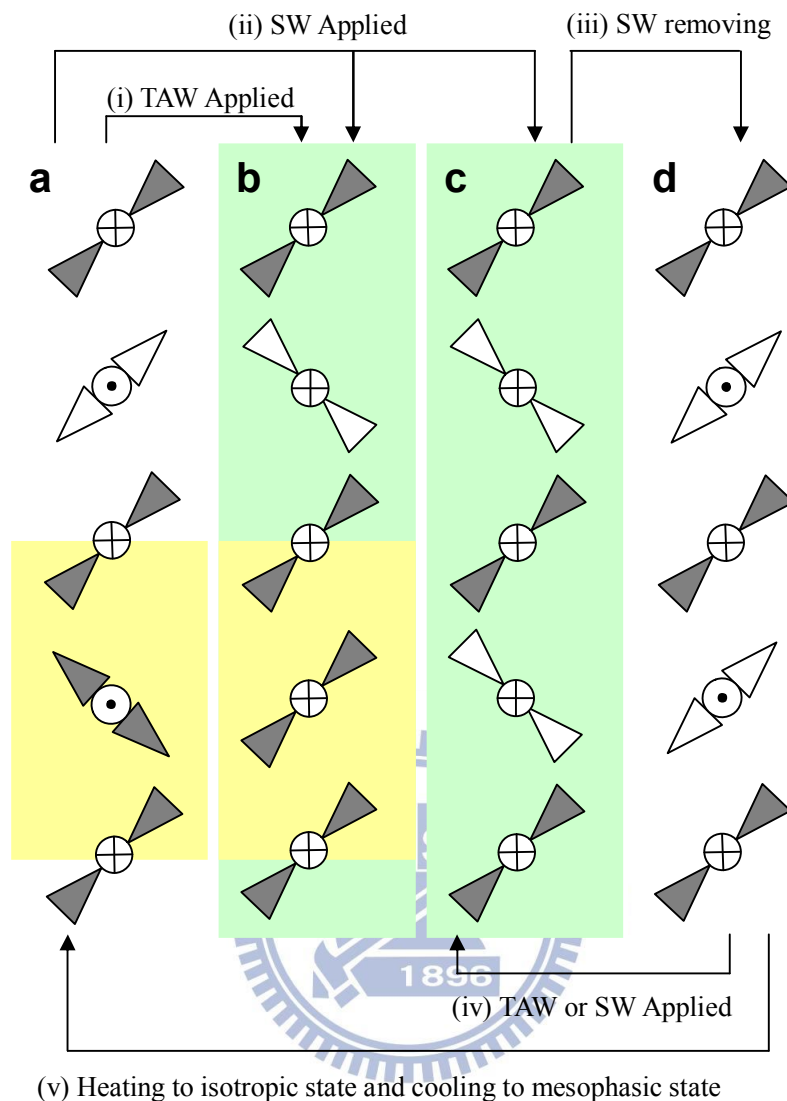
Figure 20. The layer structural models of chirality switching behavior in dimeric complex **V-C** by five executed switching processes: (a) the initial state with co-existence of SmC_SP_A and SmC_AP_A mixed domains was transferred into (b) the field-on state of SmC_AP_F and SmC_SP_F mixed domains, where the SmC_SP_F domains were retained under triangular wave electric fields (i.e., steps i) but decreased gradually under square wave electric fields (i.e., steps ii). (c) The fully SmC_AP_F domains (field-on state) were achieved by applying square wave electric field several times (i.e., steps ii), and switched into (d) SmC_SP_A domains (field-off state) were transferred after the electric field removing (i.e., steps iii). Afterwards, the inconvertibly chirality switching of racemic behavior (SmC_SP_A and SmC_AP_F) was established even if the triangular or square wave electric fields were applied (i.e., steps iv). However, the co-existence of SmC_SP_A and SmC_AP_A mixed domains were occurred by heating to isotropic state and cooling to mesophasic state again (i.e., steps v).
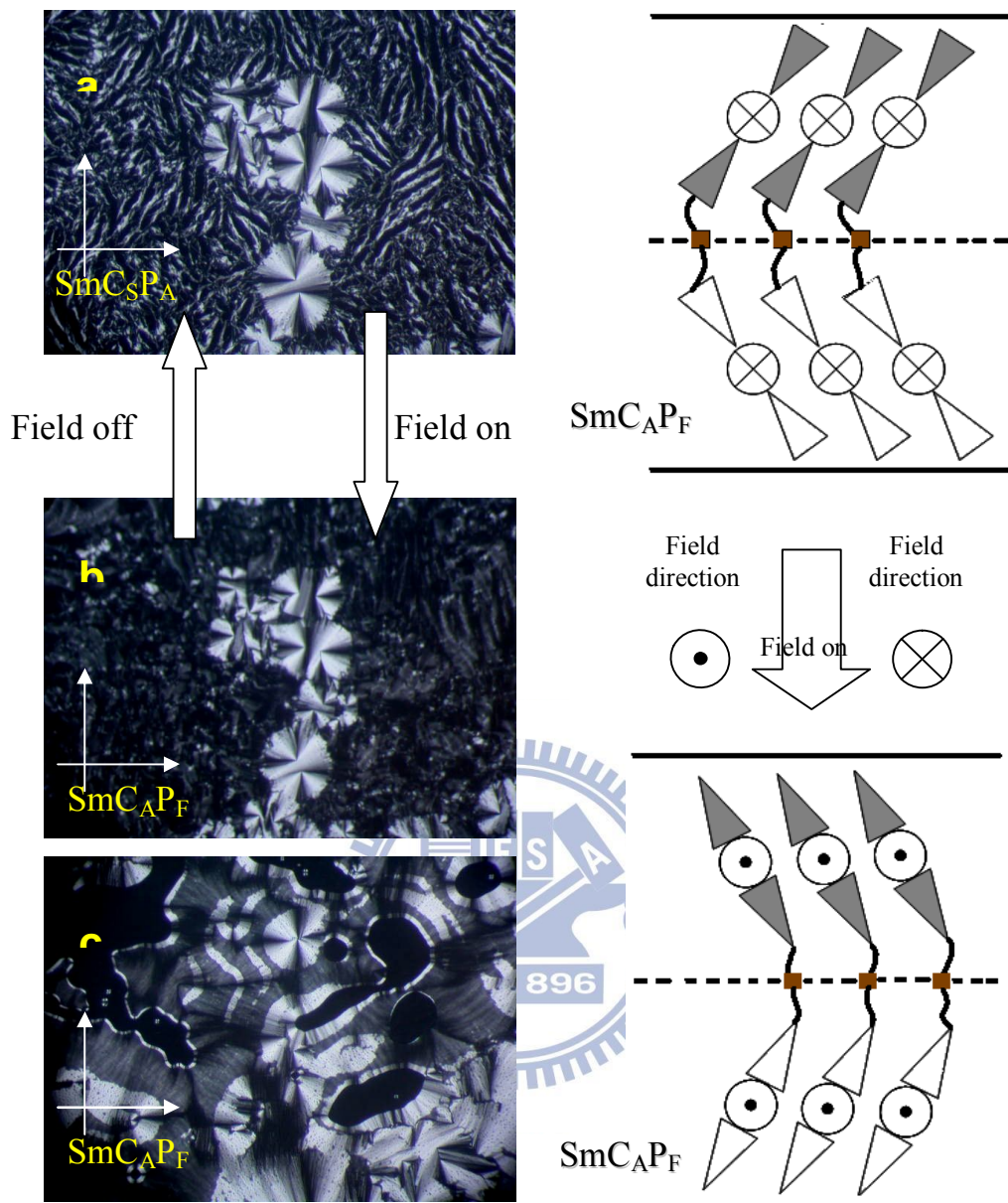
Figure 3.21. The POM textures of racemic domain switching in MCP complex **II-D**: (a) SmC_AP_F ground state under 0 V d.c. electric field; (b) SmC_AP_F state under ± 50 V d.c. electric field; (c) SmC_AP_F state under triangular wave electric field as Vpp = 140 V in a parallel rubbing cell with a cell gap of 4.25 μm. (White arrows are the directions of polarizers and analyzers.)
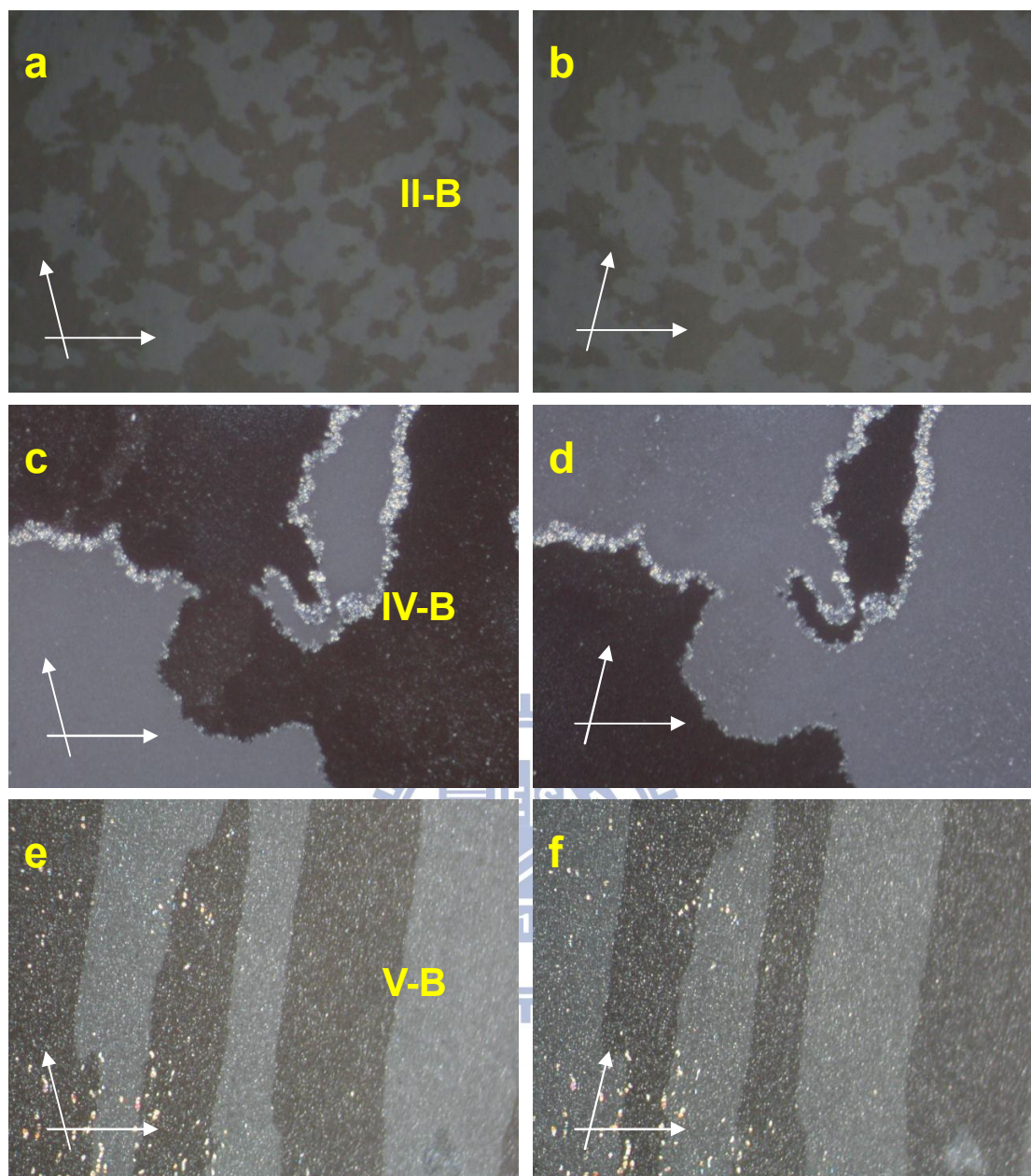
Figure 3.22. Chiral domain textures of exchange of dark and bright areas in (a) and (b) complex **II-B**; (c) and (d) complex **IV-B**; (e) and (f) complex **V-B**. (White arrows are the directions of polarizers and analyzers.)

3.4. Conclusion

In conclusion, the novel example of H-bonded bent-core main-chain polymers and their corresponding dimers with polar switching behaviors were developed by self-assembling via H-bonded force of bent-core pyridyl H-accepters and siloxane diacid H-donors. Their mesoporphism, polar switching behaviors and chirality

influenced by molecular configuration effects such as H-bonded injection, siloxyl units and rigid cores were reported. Almost H-bonded bent-core dimeric and MCP supramolecules exhibited the SmCP phases expect for the series of five-ring main-chain polymers and some complexes with diacid H-donors **B**. In addiction, the most extensive SmCP phase ranges and highest Ps values were achieved in H-bonded bent-core complexes composited with the biphenyl and naphthyl diacid H-donors **E** and **D**, respectively duo to the rigid terminal core designs as well as the bulky siloxane spacer. The SmC_AP_A ground state was observed in H-bonded bent-core dimeric and MCP complexes with di-siloxyl linking spacer of H-donor **A** to identify the chiral domain behavior, and SmC_SP_A ground state were investigated in H-bonded bent-core MCP complexes with tri-siloxyl linking spacer of H-donors to recognize the racemic domain behavior. However, a co-existence of SmC_AP_A and SmC_SP_A ground states were examined in H-bonded bent-core dimers with tri-siloxyl linking spacer of H-donors, and the unstable SmC_AP_A state would retain under triangular wave electric field, but exchange inconvertibly to the SmC_SP_A state under applying then removing the d.c. or square wave electric fields. Simultaneously, the voltage-dependent switching behavior of spontaneous polarization in H-bonded bent-core supramolecules were established by reorganized H-bonded design to be the voltage sensitive removable and reassemble (anti)ferroelectric materials.

3.5. Electronic Supplementary Information

3.5.1. Synthesis

The synthetic procedures of all diacid H-donors and pyridyl H-acceptors were proceeded according to scheme S1 and S2, respectively.

3.5.1.1. Synthesis of NP0 and BP0. In preparation of compound **NP0**, 6-hydroxy-2-naphthoic acid (1 eq.), benzyl bromide (1.2 eq.) and potassium carbonate (K_2CO_3) (1.5 eq.) were mixed in N,N-Dimethyl formamide (DMF) solvent

for 8 hours (h) under reflux temperature. After that, reacted solution was extracted with water and Ethyl acetate (EA), and organic liquid layer was dried over anhydrous magnesium sulphate. After removal of the solvent, the residue was purified by column chromatography by EA and hexane to give a white solid. Identically, compound **BP0** were reacted according to the similar protecting procedure of compound **NP0** to get a white solid. Yield of **NP0**: 88%. ^{1}H NMR (300 MHz, CDCl$_3$) δ (ppm) : 8.56 (s, 1H, Ar-H), 8.06 (d, 1H, J = 9.3 Hz, Ar-H), 7.86 (d, 1H, J = 6.0 Hz, Ar-H), 7.71 (d, 1H, J = 9.0 Hz, Ar-H), 7.51-7.32 (m, 5H, Ar-H), 7.16 (d, 1H, J = 9.0 Hz, Ar-H), 7.13 (s, 1H, Ar-H), 5.41 (s, 2H, -OCH$_2$-). Yield of **BP0**: 90%. ^{1}H NMR (300 MHz, CDCl$_3$) δ (ppm) : 8.12 (d, 2H, J = 6.0 Hz, Ar-H), 7.62 (d, 2H, J = 6.0 Hz, Ar-H), 7.53 (d, 2H, J = 6.0 Hz, Ar-H), 7.49-7.35 (m, 5H, Ar-H), 6.94 (d, 2H, J = 6.0 Hz, Ar-H), 5.38 (s, 2H, -OCH$_2$-).

3.5.1.2. Synthesis of PH1, BP1 and NP1. In preparation of compound **PH1**, Benzyl-4-hydroxy benzoate (1 eq.), w-undecylenyl alcohol (1.1 eq.) and triphenyl phosphine (1.1 eq.) were mixed in THF solvent under nitrogen for 10 min at room temperature (RT), and DEAD (40 % in toluene) (1.1 eq.) was added into solution for 24 h. After that, reacted solution was extracted with water and DCM, and organic liquid layer was dried over anhydrous magnesium sulphate. After removal of the solvent, the residue was purified by column chromatography by DCM and hexane to give a liquid product. Identically, compounds **BP1** and **NP1** were reacted according to the similar procedure of compound **PH1** to get products. Yield of **PH1**: 92%. ^{1}H NMR (300 MHz, CDCl$_3$) δ (ppm) : 8.02 (d, 2H, J = 9.0 Hz, Ar-H), 7.45-7.29 (m, 5H, Ar-H), 6.92 (d, 2H, J = 9.0 Hz, Ar-H), 5.88-5.74 (m, 1H, -CH=CH$_2$-), 5.33(s, 2H, Ar-CH$_2$-), 5.03-4.91(m, 2H, -CH=CH$_2$-), 3.98 (t, J = 6.3 Hz, 2H, OCH$_2$), 2.08-2.01 (m, 2H, CH$_2$), 1.83-1.71 (m, 2H, CH$_2$), 1.47-1.27 (m, 12H, CH$_2$-CH$_3$). Yield of **NP1**: 85%. ^{1}H NMR (300 MHz, CDCl$_3$) δ (ppm) : 8.47 (s, 1H, Ar-H), 8.02 (d, 2H, J = 9.0

Hz, Ar-H), 7.66 (d, 2H, J = 9.0 Hz, Ar-H), 7.60 (d, 2H, J = 9.0 Hz, Ar-H), 7.41-7.24 (m, 5H, Ar-H), 7.10 (d, 1H, J = 9.0 Hz, Ar-H), 6.97 (s, 1H, Ar-H), 5.82-5.70 (m, 1H, -C<u>H</u>=CH$_2$-), 5.32 (s, 2H, Ar-C<u>H$_2$</u>-), 5.02-4.90 (m, 2H, -CH=C<u>H$_2$</u>), 3.86 (t, J = 6.0 Hz, 2H, OC<u>H$_2$</u>), 2.03-1.96 (m, 2H, C<u>H$_2$</u>), 1.73-1.66 (m, 2H, C<u>H$_2$</u>), 1.39-1.23 (m, 12H, C<u>H$_2$</u>-C<u>H$_3$</u>). Yield of **BP1**: 82%. ^{1}H NMR (300 MHz, CDCl$_3$) δ (ppm) : 8.13 (d, 2H, J = 9.0 Hz, Ar-H), 7.62 (d, 2H, J = 9.0 Hz, Ar-H), 7.56 (d, 2H, J = 9.0 Hz, Ar-H), 7.48-7.32 (m, 5H, Ar-H), 7.00 (d, 2H, J = 9.0 Hz, Ar-H), 5.88-5.74 (m, 1H, C<u>H</u>=CH$_2$-), 5.39 (s, 2H, Ar-C<u>H$_2$</u>-), 5.03-4.91 (m, 2H, -CH=C<u>H$_2$</u>-), 4.01 (t, J = 6.0 Hz, 2H, OC<u>H$_2$</u>), 2.05-2.00 (m, 2H, C<u>H$_2$</u>), 1.85-1.75 (m, 2H, C<u>H$_2$</u>), 1.51-1.25 (m, 12H, C<u>H$_2$</u>-C<u>H$_3$</u>).

3.5.1.3. Synthesis of PH2-1, PH2-2, BP2 and NP2. In preparation of compound **PH2-1**, reactant **PH2** (2 eq.), 1,1,3,3-tetramethyldisiloxane (1 eq.) and Platinum(0)-1,3-divinyl-1,1,3,3-tetramethyldisiloxane complex, solution in xylenes,(~2% Pt) (0.03 eq.) were mixed in toluene for 24 h at RT. The reacted solution was extracted with water and DCM, and organic liquid layer was dried over anhydrous magnesium sulphate. After removal of the solvent, the residue was purified by column chromatography by DCM and hexane to give a white solid. Identically, compounds **PH2-2, BP2** and **NP2** were reacted according to the similar procedure of compound **PH2-1** to get products. Yield of **PH2-1**: 87%. ^{1}H NMR (300 MHz, CDCl$_3$) δ (ppm) : 8.01 (d, 4H, J = 9.0 Hz, Ar-H), 7.43-7.31 (m, 10H, Ar-H), 6.89 (d, 4H, J = 9.0 Hz, Ar-H), 5.32 (s, 4H, Ar-C<u>H$_2$</u>-), 3.97 (t, 4H, J = 6.3 Hz, OC<u>H$_2$</u>), 1.83-1.71 (m, 4H, C<u>H$_2$</u>), 1.47-1.26 (m, 36H, C<u>H$_2$</u>-C<u>H$_3$</u>), 0.04-0.02 (s, 12H, Si-OC<u>H$_3$</u>). Yield of **PH2-2**: 90%. ^{1}H NMR (300 MHz, CDCl$_3$) δ (ppm) : 8.04 (d, 4H, J = 9.0 Hz, Ar-H), 7.46-7.33 (m, 10H, Ar-H), 6.90 (d, 4H, J = 9.0 Hz, Ar-H), 5.34 (s, 4H, Ar-C<u>H$_2$</u>-), 3.99 (t, 4H, J = 6.3 Hz, OC<u>H$_2$</u>), 1.83-1.75 (m, 4H, C<u>H$_2$</u>), 1.67-1.28 (m, 36H, C<u>H$_2$</u>-C<u>H$_3$</u>), 0.06 (s, 12H, Si-OC<u>H$_3$</u>), 0.02 (s, 6H, Si-OC<u>H$_3$</u>). Yield of **NP2**: 86%. ^{1}H NMR (300 MHz, CDCl$_3$) δ

(ppm) : 8.56 (s, 2H, Ar-H), 8.08 (d, 2H, J = 9.0 Hz, Ar-H), 7.84 (d, 2H, J = 9.0 Hz, Ar-H), 7.74 (d, 2H, J = 9.0 Hz, Ar-H), 7.52-7.33 (m, 10H, Ar-H), 7.21 (d, 2H, J = 9.0 Hz, Ar-H), 7.13(s, 2H, Ar-H), 5.42 (s, 4H, Ar-$\underline{CH_2}$-), 4.07 (t, 4H, J = 6.0 Hz, O$\underline{CH_2}$), 1.90-1.81 (m, 4H, $\underline{CH_2}$), 1.51- 1.27 (m, 36H, $\underline{CH_2}$-$\underline{CH_3}$), 0.08 (s, 12H, Si-O$\underline{CH_3}$), 0.05 (s, 6H, Si-O$\underline{CH_3}$). Yield of **BP2**: 83%. ^{1}H NMR (300 MHz, CDCl$_3$) δ (ppm) : 8.12 (d, 4H, J = 8.4 Hz, Ar-H), 7.65 (d, 4H, J = 8.4 Hz, Ar-H), 7.60 (d, 4H, J = 9.0 Hz, Ar-H), 7.48-7.26 (m, 10H, Ar-H), 6.98 (d, 4H, J = 9.0 Hz, Ar-H), 5.40 (s, 4H, Ar-$\underline{CH_2}$-), 3.99 (t, 4H, J = 6.0 Hz, O$\underline{CH_2}$), 1.84-1.75 (m, 4H, $\underline{CH_2}$), 1.51-1.28 (m, 36H, $\underline{CH_2}$-$\underline{CH_3}$), 0.056 (s, 12H, Si-O$\underline{CH_3}$), 0.026 (s, 6H, Si-O$\underline{CH_3}$).

3.5.1.4. Synthesis of A, C, D and E. Diacid structure of **A** was synthesized by de-protecting procedure. **PH2-1** (1 eq.) and Pd/C powder (3 wt%) were mixed in THF under hydrogen gas for 24 h at RT. The catalyst powder was filtered, and the organic solvent was removed to form white powder. The purification was recrystallized by THF and hexane to give a white solid, and compounds **C**, **D** and **E** were reacted according to the similar procedure of compound **A**. Yield of **A**: 85%. ^{1}H NMR (300 MHz, D-THF) δ (ppm): 7.93 (d, 4H, J = 9.0 Hz, Ar-H), 6.91 (d, 4H, J = 9.0 Hz, Ar-H), 4.00(t, 4H, J = 6.0 Hz, O$\underline{CH_2}$), 1.83-1.71 (m, 4H, $\underline{CH_2}$), 1.47-1.31 (m, 36H, $\underline{CH_2}$-$\underline{CH_3}$), 0.03 (s, 12H, Si-O$\underline{CH_3}$). ^{13}C NMR (300 MHz, D-THF) δ (ppm): 167.197, 163.57, 132.18, 123.82, 114.42, 68.59, 34.24, 30.43, 30.38, 30.18, 30.16, 29.94, 26.77, 24.05, 18.99, 0.24. EA: Calcd for $C_{40}H_{66}O_7Si_2$: C, 67.18, H, 9.30; Found: C, 66.74; H, 9.33. Yield of **C**: 86%. ^{1}H NMR (300 MHz, DMSO) δ (ppm) : 7.87 (d, 4H, J = 9.0 Hz, Ar-H), 6.98 (d, 4H, J = 9.0 Hz, Ar-H), 3.99 (t, 4H, J = 6.3 Hz, O$\underline{CH_2}$), 1.73-1.64 (m, 4H, $\underline{CH_2}$), 1.37-1.22 (m, 36H, $\underline{CH_2}$-$\underline{CH_3}$), 0.02 (s, 12H, Si-O$\underline{CH_3}$), -0.02 (s, 6H, Si-O$\underline{CH_3}$). ^{13}C NMR (300 MHz, DMSO) δ (ppm) : 166.74, 162.17, 131.23, 122.91, 113.83, 67.57, 32.95, 29.27, 29.18, 29.03, 28.98, 28.71, 25.57, 22.76, 17.75, 0.99, -0.06. EA: Calcd for $C_{42}H_{72}O_8Si_3$: C, 63.91, H, 9.19; Found: C, 63.83; H, 9.34. Yield

of **D**: 78%. ^{1}H NMR (300 MHz, CDCl$_3$) δ (ppm) : 8.57(s, 2H, Ar-H), 8.05 (d, 2H, J = 8.7 Hz, Ar-H), 7.84 (d, 2H, J = 8.7 Hz, Ar-H), 7.73 (d, 2H, J = 8.7 Hz, Ar-H), 7.16 (d, 2H, J = 8.7 Hz, Ar-H), 7.10 (s, 2H, Ar-H), 4.05 (t, 4H, J = 6.6 Hz, O<u>CH$_2$</u>), 1.86-1.79 (m, 4H, <u>CH$_2$</u>), 1.49-1.29 (m, 36H, <u>CH$_2$</u>-<u>CH$_3$</u>), 0.06 (s, 12H, Si-O<u>CH$_3$</u>), 0.02 (s, 6H, Si-O<u>CH$_3$</u>). ^{13}C NMR (300 MHz, CDCl$_3$) δ (ppm) : 172.43, 159.37, 137.69, 131.87, 130.99, 127.68, 126.83, 126.02, 124.10, 119.97, 106.31, 68.16, 33.49, 29.67, 29.62, 29.43, 29.17, 26.09, 23.24, 18.30, 1.30, 0.21. EA: Calcd for C$_{50}$H$_{76}$O$_8$Si$_3$: C, 67.52, H, 8.61; Found: C, 67.81; H, 8.72. Yield of **E**: 88%. ^{1}H NMR (300 MHz, D-THF) δ (ppm) : 8.04 (d, 4H, J = 9.0 Hz, Ar-H), 7.67 (d, 4H, J = 9.0 Hz, Ar-H), 7.62 (d, 4H, J = 9.0 Hz, Ar-H), 6.99 (d, 4H, J = 9.0 Hz, Ar-H), 3.99 (t, 4H, J = 6.0 Hz, O<u>CH$_2$</u>), 1.80-1.74 (m, 4H, <u>CH$_2$</u>), 1.48-1.27 (m, 36H, <u>CH$_2$</u>-<u>CH$_3$</u>), 0.07 (s, 12H, Si-O<u>CH$_3$</u>), 0.02 (s, 6H, Si-O<u>CH$_3$</u>). ^{13}C NMR (300 MHz, D-THF) δ (ppm) : 167.35, 160.34, 145.51, 132.73, 130.80, 129.73, 128.70, 126.62, 115.55, 115.25, 68.43, 33.49, 30.43, 30.20, 18.91, 0.515, -0.099. EA: Calcd for C$_{54}$H$_{80}$O$_8$Si$_3$: C, 68.89, H, 8.56; Found: C, 68.56; H, 8.37.

3.5.1.5. Synthesis of PH3. compound **A** (1 eq.), N,N-dicyclohexylcarbodiimide (DCC) (1.2 eq) and a catalytic amount of 4-(N,Ndimethylamino) Pyridine (DMAP) was dissolved in dry dichloromethane (DCM) under nitrogen for 15 h at room temperature. The precipitated dicyclohexylurea (DCU) was filtered off and washed with an excess of DCM (20 ml). The filtrate was extracted with water/DCM and organic liquid layer was dried over anhydrous magnesium sulphate. After removal of the solvent by evaporation under reduced pressure, the residue was recrystallized from ethanol to give a white solid. Yield of **PH3**: 80%. ^{1}H NMR (300 MHz, CDCl$_3$) δ (ppm) : 8.16 (q,8H, Ar-H), 7.47-7.31 (m, 10H, Ar-H), 7.29 (d, 4H, J = 9.0 Hz, Ar-H), 6.95 (d, 4H, J = 9.0 Hz, Ar-H), 5.37 (s, 4H, Ar-<u>CH$_2$</u>-), 4.03 (t, 4H, J = 6.6 Hz, O<u>CH$_2$</u>), 1.83-1.71 (m, 4H, <u>CH$_2$</u>), 1.49-1.32 (m, 36H, <u>CH$_2$</u>-<u>CH$_3$</u>), 0.048 (s, 12H, Si-O<u>CH$_3$</u>).

3.5.1.6. Synthesis of B. By following the similar deprotecting procedure of compound **A**, compound **PH3** (1 eq.) and Pd/C powder (3 wt%) were reacted to obtain a white solid. Yield of **B**: 75%. ^{1}H NMR (300 MHz, D-THF) δ (ppm) : 8.11 (m, 8H, Ar-H), 7.32 (d, 4H, J = 9.0 Hz, Ar-H), 7.04 (d, 4H, J = 9.0 Hz, Ar-H), 4.06 (t, 4H, 6.3Hz, O$\underline{CH}_2$), 1.83-1.71 (m, 4H, $\underline{CH}_2$), 1.47-1.26 (m, 36H, $\underline{CH}_2$-$\underline{CH}_3$), 0.04 (s, 12H, Si-O$\underline{CH}_3$). ^{13}C NMR (300 MHz, D-THF) δ (ppm) : 166.757, 164.560, 164.219, 155.612, 132.71, 131.65, 128.977, 122.30, 122.106, 114.955, 68.863, 34.255, 30.442, 30.38, 30.17, 29.90, 26.75, 24.065, 18.998, 0.335. EA: Calcd for $C_{54}H_{74}O_{11}Si_2$: C, 67.89, H, 7.81; Found: C, 67.75; H, 8.09.
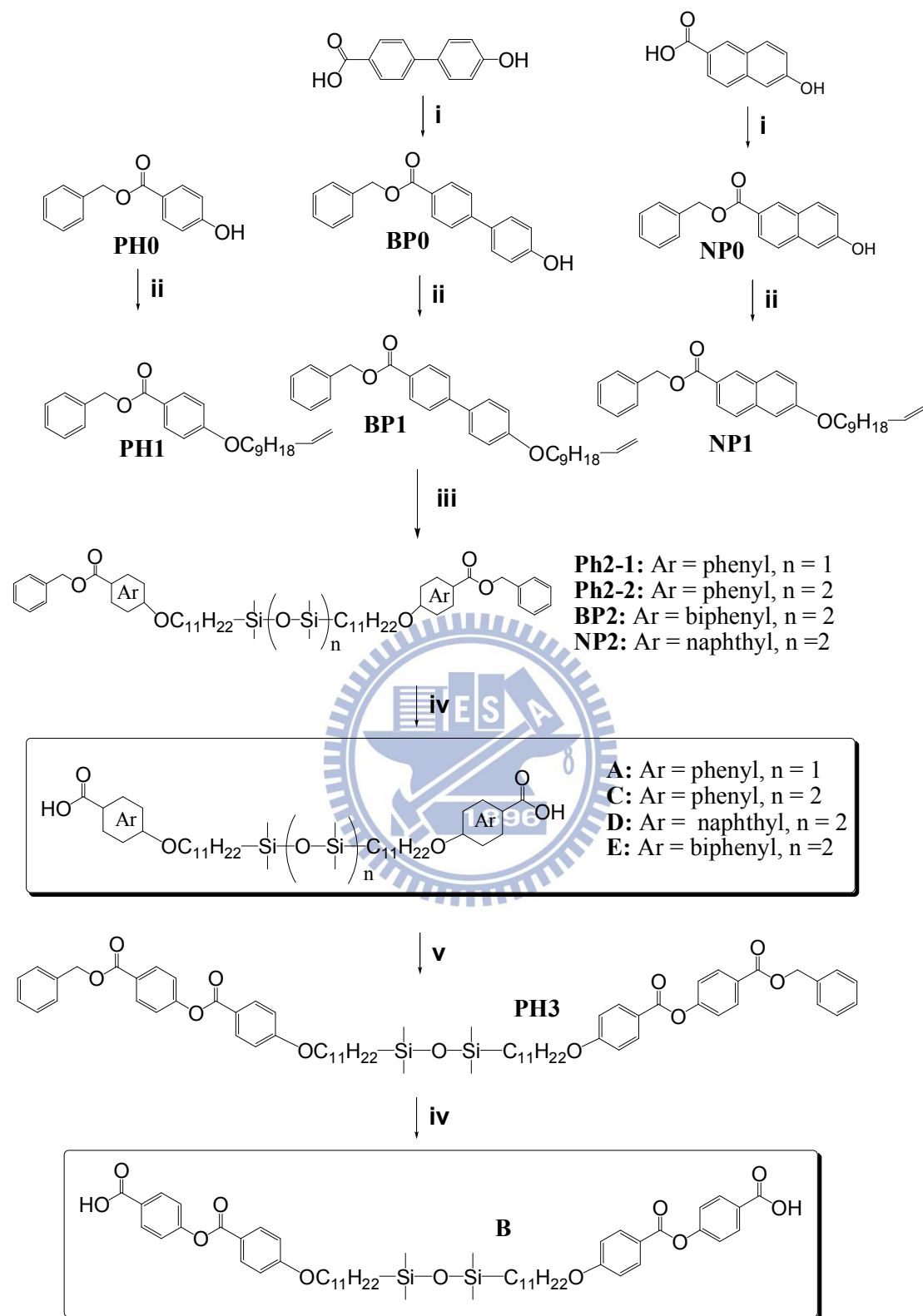
Scheme S3.1. Synthetic procedures of diacid H-donors **A**, **B**, **C**, **D** and **E**. (i): benzyl bromide, K$_2$CO$_3$, DMF; (ii): PPh3, DEAD, THF; (iii): pt(0), siloxyl derivatives; (iv): Pd/C, H$_2$, THF; (v): DCC, DMAP, DCM.
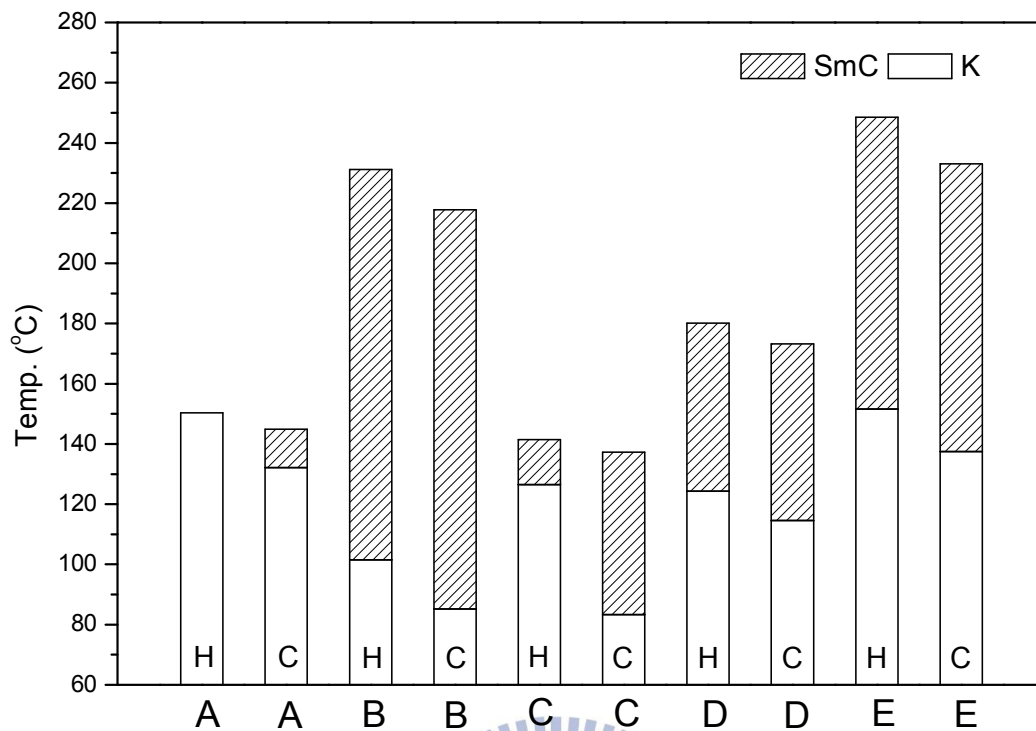
Figure S3.1. Phase diagram of diacid H-donors **A**, **B**, **C**, **D** and **E**.
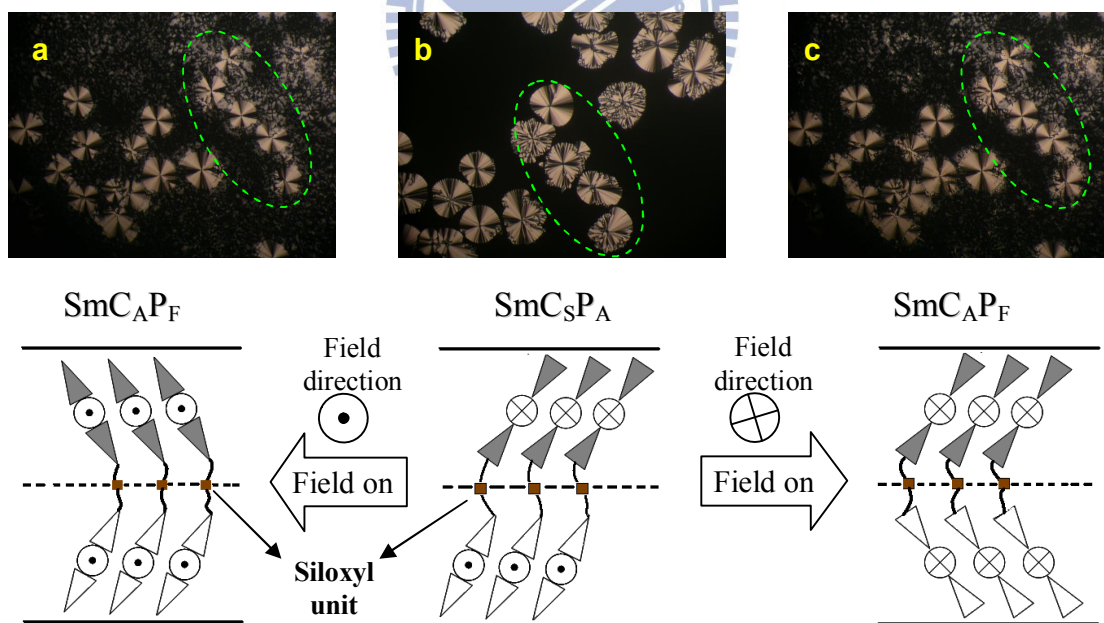
Figure S3.2. The POM patterns under various direct current (D.C.) electric field applying: (a) $+100$ V; (b) 0 V (voltage removing); (c) -100 V for complex **IV-C** with antiferroelectric switching property to show racemic domain (exchanging between SmC_SP_A and SmC_AP_F).

Chapter 4

Novel Supramolecular Side-Chain Banana-Shaped Liquid Crystalline Polymers Containing Covalent- and Hydrogen-Bonded Bent-Cores

4.1. Introduction

Liquid crystalline (LC) materials bearing bent-shaped mesogens become interesting topics duo to their special electro-optical properties, such as spontaneous polarized capabilities and nonlinear optics.[42] Since the first example of bent-core molecules, which possessed achiral configurations but with chiral characteristics, was published and revealed antiferroelectric effects, bent-shaped LC derivatives with banana-shaped (or bent-core) mesogens were developed and conferred fascinating optical and electrical properties.[11] Consequently, their particular mesophases, including columnar stacking, tilted smectic phases, and three dimensional structures, named as B1 to B7 phases were explored and identified. The most prevailingly investigated B2 phase revealed ferroelectric (F)/antiferroelectric (A) properties, which possessed identical/inverse polarizations, and synclinic (S)/anticlinic (A) arrangements with alike/opposite molecular tilted aspects between layer to layer, respectively.[43g] Hence, depending on the polar directions and molecular tilted directions in neighboring layers, four kinds of different molecular architectures denoted as SmC_AP_A, SmC_SP_A, SmC_AP_F, and SmC_SP_F were categorized to homochiral (SmC_AP_A and SmC_SP_F) and racemic (SmC_SP_A and SmC_AP_F) conditions, respectively.

In general, bent-core mesogenic configurations consist of a central core and two rigid wing segments linking through polar functional groups with a suitable bent angle

where appropriate lengths of flexible chains are attached linking groups. The structural variations of achiral molecular designs, such as the central parts, lateral substituents, linking groups, terminal chains, and the number of rings, would affect their physical properties to different extents in small molecular systems. Recently, poly-molecular systems, i.e., dimeric,[31,45a,46] polymeric,[32d,33,59] and dendritic[34] frameworks, were also developed to investigate the influence of molecular configurations on mesomorphic and electro-optical properties. However, the most important and interesting issue of bent-core molecule is to retain the lamellar organization with spontaneous polarization and electric-optical switching properties which need to be further realized duo to their possible applications of fast responsive LCD devices. Moreover, some novel supramolecular bent-core interactions or their nanocomposite architectures have been integrated into organic or inorganic parts to display special electro-optical characteristics, for instance, bent-core derivatives embedded with nanoparticles,[37] H-bonded bent-core supramolecules,[5,38,47,48] and bent-core structures with silyl and siloxyl linkages.[25b,45b-c]

Concerning the fully covalent-bonded bent-core polymers, since the example of the bent-core main-chain polymer with a polar smectic mesophase was synthesized,[32d] the polar switching behavior has been declared to exist in the polymeric framework. Up to now, even if the first case of the bent-core side-chain polymer, where the bent-core units were connected by siloxyl spacers, displayed clear ferroelectric switching properties,[33a] just only scarce cases of bent-core side-chain polymers were achieved with barely detectable polar switching properties.[33b] With regard to H-bonded bent-core structures, different molecular designs in terms of small molecules and polymers (side-chain polymers)[38,48] have been developed and reported, but very few H-bonded bent-core structures with ferroelectric or anti-ferroelectric properties have been measured and analyzed. Therefore, more detailed researches of

H-bonded bent-core molecules (as well as polymers) with special ferroelectric or anti-ferroelectric properties may be beneficial for the electro-optical applications of supramolecular materials.
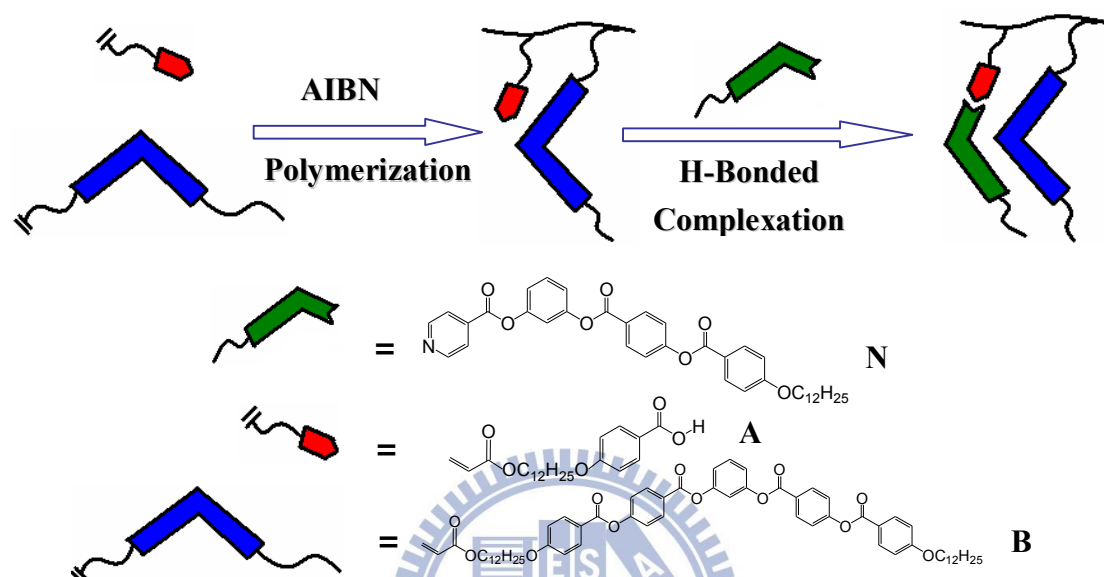
Figure 4.1. The chemical structures and formation procedures of bent-core side-chain polymer complexes (**AmBn-N**) with covalent- and H-bonded components (**B** and **A-N** units, respectively).

In our previous studies, the singly H-bonded five-ring banana-shaped supramolecule (complex **H12**)[39] showed lower mesophasic transition temperatures and enthalpies than those of the fully covalent-bonded five-ring banana-shaped analogue (compound **S12**)[55] as shown in Figure S4.1 of the Supporting Information, which suggested that the H-bonded framework exhibited a softer mesogenic arrangement than the covalent-bonded architecture. On the other hand, the H-bonded rod-like (or banana-shaped) molecules may be stabilized by the fully covalent-bonded counterparts (or as dopants) to have more steady electro-optical properties. Considering both merits of covalent- and H-bonded molecular designs, there might be some intermediate or even premium properties can be achieved by blending or

copolymerizing two types of covalent- and H-bonded analogues.[60] Therefore, H-bonded bent-core units would behave as softer skeletons to tune the suitable molecular arrangements in harmony with the fully bent-core covalent-bonded units in polymeric side-chain structures. Hence, we would prefer the molecular designs of bent-core covalent-bonded moieties to be incorporated with bent-core H-bonded moieties with various molar ratios in the bent-core side-chain polymers (see Scheme 4.2) to modulate the molecular organization and optimize the polar switching behavior.

According to our previous conception, H-donor and bent-core covalent-bonded monomers with acrylate terminal groups were designed and synthesized. The bent-core covalent-bonded five-ring monomer was connected by polar ester groups, and its H-bonded analogue was established as a five-ring supramolecule by blending two complementary components of an acidic proton donor (H-donor with a terminal acrylate) and bent-core proton acceptor (H-acceptor with a terminal pyridine). Then, the H-donor monomer (**A**) and bent-core covalent-bonded monomer (**B**) with different molar ratios were copolymerized to obtain H-donor side-chain copolymers/homopolymers **AmBn** (where **m** and **n** are repeating units of **A** = H-donor structure and **B** = covalent-bonded bent-core structure, respectively), and then they were blended with pyridyl H-acceptor **N** to form H-bonded bent-core polymer complexes **AmBn-N**. Therefore, H-donor side-chain copolymers/homopolymers **AmBn** with various molar ratios of **A** and **B** units were synthesized, where **m**/**n** molar ratios are 1/0, 16/1, 10/1, 4/1, 1/2, 1/5, 1/13, and 0/1 as shown in Figure 4.1 and Table 4.1. In addition, the bent-core side-chain LC copolymers bearing both bent-core covalent- and H-bonded components were developed in this study via their corresponding H-bonded polymer complexes **AmBn-N**, which consisted of H-Donor side-chain copolymers/homopolymers (**AmBn**)

and pyridyl H-Acceptor (**N**). The variations of mesomorphic and electro-optical properties influenced by the molar ratios of bent-core covalent- and H-bonded structures in bent-core side-chain polymer and H-bonded polymer complexes were mainly investigated, and their mesomorphic and electro-optical properties were examined and characterized by polarizing optical microscopy (POM), differential scanning calorimetry (DSC), powder X-ray diffraction (XRD), and electro-optical (EO) switching current experiments.
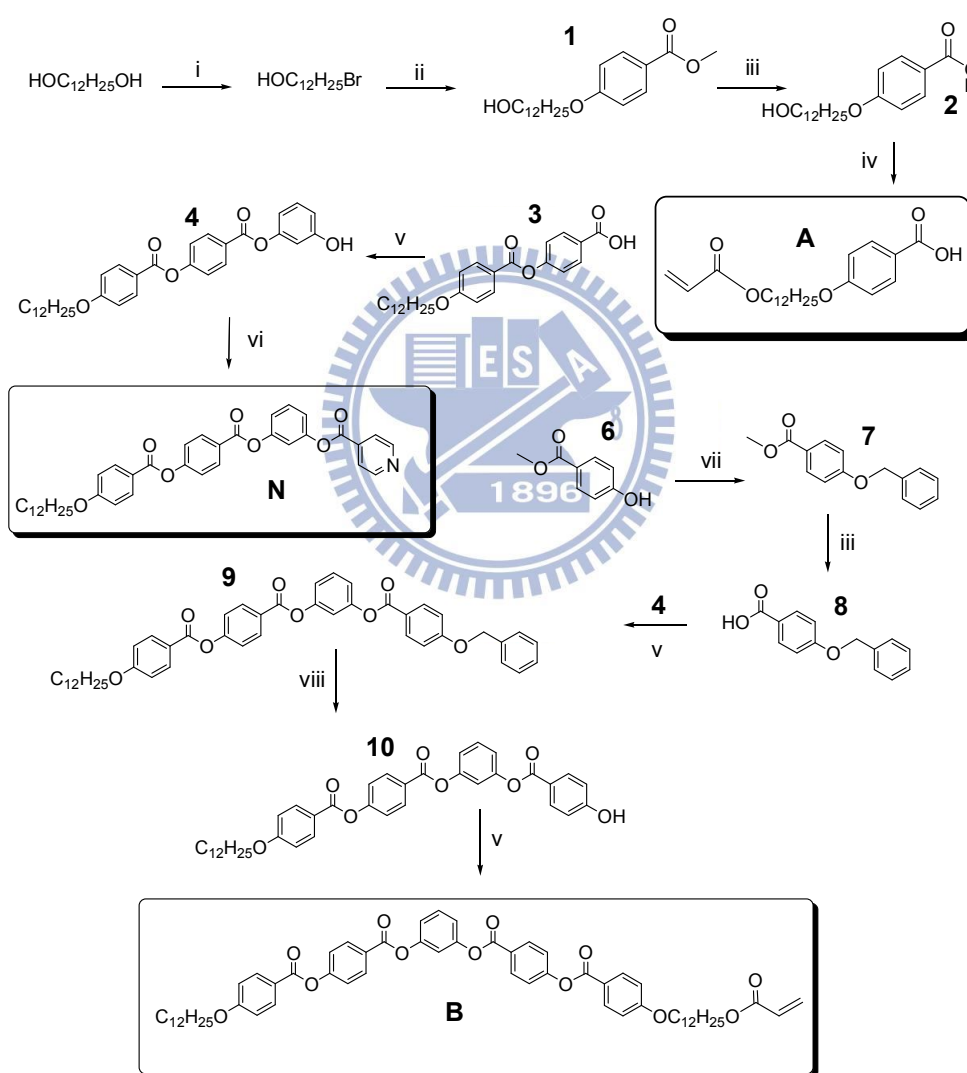
Scheme 4.1. Synthetic routes of monomers **A** and **B** along with pyridyl H-acceptor **N**. (i): HBr, toluene, (ii): methyl 4-hydroxybenzoate, K_2CO_3, acetone; (iii) KOH, ethanol; (iv) acryloyloxy chloride, DMA, 1,4-dioxane; (v) DCC, DMAP, DCM; (vi) isonicotinoyl chloride hydrochloride, triethylamine, DCM; (vii) benzyl bromide, K_2CO_3, acetone; (viii) Pd/C, H_2, THF.

4.2. Experimental Section

4.2.1. Characterization Methods

^{1}H NMR spectra were recorded on a Varian Unity 300 MHz spectrometer using d_6-dioxane and $CDCl_3$ as solvents and mass measurements were determined on a Micromass TRIO-2000 GC-MS. Elemental analyses (EA) were performed on a Heraeus CHN-OS RAPID elemental analyzer. Gel permeation chromatography (GPC) analyses were conducted on a Waters 1515 separation module using polystyrene as a standard and THF as an eluant. Mesophasic textures were characterized by polarizing optical microscopy (POM) using a Leica DMLP equipped with a hot stage. Infrared (IR) spectra were investigated by Perk-Elmer Spectrum 100 instrument. Temperatures and enthalpies of phase transitions were determined by differential scanning calorimetry (DSC, model: Perkin Elmer Pyris 7) under N_2 at a heating and cooling rate of 10 °Cmin^{-1}. Synchrotron powder X-ray diffraction (XRD) measurements were performed at beamline BL17A of the National Synchrotron Radiation Research Center (NSRRC), Taiwan, where the wavelength of X-ray was 1.33366 Å. The powder samples were packed into capillary tubes and heated by a heat gun, whose temperature controller was programmable by a PC with a PID feedback system. The scattering angle theta was calibrated by a mixture of silver behenate and silicon. The electro-optical properties were determined in commercially available ITO cells (from Mesostate Corp., thickness = 4.25 μm, active area = 1 cm^2) with rubbed polyimide alignment coatings (parallel rubbing direction). A digital oscilloscope (Tektronix TDS-3012B) was used in these measurements.

4.2.2. Synthesis

4.2.2.1. Synthesis of Monomers. All synthetic procedures of monomers **A** (H-donor monomer) and **B** (bent-core covalent-bonded monomer) as well as H-acceptor **N** were demonstrated in Scheme 4.1. The synthetic details of all

compounds in Scheme 4.1 are shown in the following descriptions.

4.2.2.2. 12-Bromododecanol (1). Doecan 1,12-diol (1e.q) and HBr (1e.q.) were dissolved in toluene solvent to react at 60 °C for 24 hours, and side product H_2O could be removed by dean stark installation. After then, the reacted solution was extracted by ethyl acetate (EA) and water, and the organic liquid layer was purified by column chromatography to give a liquid product. Yield: 56%. ^{1}H NMR (300 MHz, CDCl$_3$) δ (ppm) : 3.57 (t, J = 6.6 Hz, 2H, -OC$\underline{H}_2$-), 3.39 (t, J = 6.9 Hz , 2H, Br-C$\underline{H}_2$-), 3.19 (s, 1H, -O$\underline{H}$), 2.04-1.80 (m, 2H, Br-CH$_2$C$\underline{H}_2$-), 1.56-1.49 (m, 2H, HO-CH$_2$C$\underline{H}_2$-), 1.44-1.21 (m, 16H, -C$\underline{H}_2$-).

4.2.2.3. Compound (cpd) 2. 12-bromododecanol (**1**) (1.1 e.q), methyl 4-hydroxybenzoate and potassium carbonate (K_2CO_3) (1.5 eq.) were dissolved in acetone solvent to react at reflux temperature for 20 hours. After that, water was added to dissolve the inorganic salt and a white precipitation was produced. Subsequently, the white powder was washed by hexane to get a pure product. Yield: 91 %. ^{1}H NMR (300 MHz, CDCl$_3$) δ (ppm): 7.95 (d, J = 9.0 Hz, 2H, Ar-H), 6.87 (d, J = 9.0 Hz, 2H, Ar-H), 3.97 (t, J = 6.3 Hz, 2H, -OC$\underline{H}_2$-), 3.85 (s, 3H, -OC$\underline{H}_3$), 3.61 (m, 2H, -C$\underline{H}_2$OH), 1.79 (s, 1H, -O$\underline{H}$), 1.26(m, 20H, -C$\underline{H}_2$-).

4.2.2.4. Compound (cpd) 3. Cpd **2** (1 e.q.) and potassium hydroxide (KOH) (4 e.q.) were dissolved in ethanol solvent to reflux and react for 16 hours. After cooling reacted liquid to room temperature, HCl (10 vol% in water) solution was added to react 30 minutes. The precipitation was filtered and a white powder was formed. The powder was recrystallized by ethanol and hexane (1:3 vol) to collect a pure white product. Yield: 95 %. ^{1}H NMR (300 MHz, CDCl$_3$) δ (ppm): 7.92 (d, J = 8.7 Hz, 2H, Ar-H), 6.92 (d, J = 8.7 Hz, 2H, Ar-H), 4.00 (t, J = 6.6 Hz, 2H, -OC$\underline{H}_2$-), 3.45 (t, J = 6.3 Hz, 2H, -C$\underline{H}_2$OH), 2.06(s, 1H, -O$\underline{H}$), 1.78 (m, 2H, -CH$_2$C$\underline{H}_2$OH), 1.29 (m, 18H, -C$\underline{H}_2$-).

4.2.2.5. H-Donor Monomer (A). The addition of terminal acryl group on cpd **2** was proceeded by the reaction of acryloyloxy chloride (1.5 e.q.) and cpd **2** (1 e.q.) in 1,4-dioxane solvent with an organic base of dimethylaniline (DMA) (1.1 e.q.) under nitrogen to react at room temperature for 24 hours. When the reaction was finished, a dilute HCl solution (10 vol% in water) was added to the reacted solution to form a white powder. The product was purified by column chromatography to give a white product. Yield: 55 %. ^{1}H NMR (300 MHz, CDCl$_3$) δ (ppm): 8.03 (d, J = 9.0 Hz, 2H, Ar-H), 6.91 (d, J = 9.0 Hz, 2H, Ar-H), 6.41 (d, J = 18 Hz, 1H, -CH=C$\underline{H}_2$), 6.35 (m, 1H, =C$\underline{H}$-), 6.07 (d, J = 9.0 Hz, 1H, -CH=C$\underline{H}_2$), 4.13 (t, J = 6.6 Hz, 2H, Ar-OC$\underline{H}_2$-), 4.00 (t, J = 6.3 Hz, 2H, C=C-OC$\underline{H}_2$-), 1.79 (m, 2H, Ar-OCH$_2$C$\underline{H}_2$-), 1.63 (m, 2H, C=C-OCH$_2$C$\underline{H}_2$-), 1.26 (m, 16H, -C$\underline{H}_2$-). MS (EI): m/z [M+] 377; calcd m/z [M+] 376.5. EA: Calcd for C$_{22}$H$_{32}$O$_5$: C, 70.18; H, 8,57. Found: C, 70.33; H, 8.52.

4.2.2.6. Compound (cpd) 5. Cpd **4** (1 e.q.), resorcinol (1 e.q.), N,N-dicyclohexylcarbodiimide (DCC) (1.1 eq), and a catalytic amount of 4-(N,N-dimethylamino) Pyridine (DMAP) were dissolved in dry dichloromethane (DCM) under nitrogen to react at room temperature for 15 hours, where the starting reactant **4** was a well known structure and was synthesized by following the literature procedure.[51] The precipitated dicyclohexylurea (DCU) was filtered off and washed with an excess of DCM (20 ml). The filtrate was extracted with water and DCM, and the organic liquid layer was dried over anhydrous magnesium sulphate. After removal of the solvent by evaporation under reduced pressure, the residue was recrystallized from ethanol to give a white solid. Yield: 44 %. ^{1}H NMR (300 MHz, CDCl$_3$) δ (ppm) : 8.25 (d, J = 8.7 Hz, 2H, Ar-H), 8.14 (d, J = 9.0 Hz, 2H, Ar-H), 7.40 (d, J = 8.7 Hz, 2H, Ar-H), 7.22 (t, J = 8.1 Hz, 1H, Ar-H), 7.03 (d, J = 9.0 Hz, 2H, Ar-H), 6.71-6.66 (m, 3H, Ar-H), 4.06 (t, J = 6.6 Hz, 2H, OC$\underline{H}_2$), 1.80 (m, 2H, OCH$_2$C$\underline{H}_2$), 1.47-1.28 (m, 18H, C$\underline{H}_2$), 0.88 (t, J = 6.3 Hz, 3H, C$\underline{H}_3$).

4.2.2.7. Pyridyl H-Acceptor (N). A mixture of cpd **5** (1 e.q.), isonicotinoyl chloride hydrochloride (1.1 e.q.), and triethylamine (1.2 e.q.) were dissolved in dry DCM under nitrogen to react at room temperature for 8 hours. After work up, the solvent was extracted with water and DCM, and organic liquid layer was dried over anhydrous magnesium sulphate. After removal of the solvent by evaporation under reduced pressure, the residue was purified by column chromatography and recrystallized by DCM and hexane (1:4 vol) to give a white solid. Yield: 95 %, ^{1}H NMR (300 MHz, CDCl$_3$): δ 8.89 (d, J = 4.2 Hz, 2H, Ar-H), 8.22 (d, J = 8.7 Hz, 2H, Ar-H), 8.08(d, J = 8.7 Hz, 2H, Ar-H), 8.01 (d, J = 4.2 Hz, 2H, Ar-H), 7.59 (t, J = 8.1 Hz, 1H, Ar-H), 7.51 (d, J = 9.0 Hz, 2H, Ar-H), 7.41 (s, 1H, Ar-H), 7.32 (br, 2H, Ar-H), 7.10 (d, J = 9.0 Hz, 2H, Ar-H); 4.07 (t, J = 6.3 Hz, 2H, O$\underline{CH_2}$), 1.74 (br, 2H, OCH$_2$$\underline{CH_2}$), 1.23 (br, 18H, $\underline{CH_2}$), 0.84 (t, J = 6.3 Hz, 3H, $\underline{CH_3}$). MS (EI): m/z [M+] 624; calcd m/z [M+] 623.7. EA: Calcd for C$_{38}$H$_{41}$NO$_7$: N, 2.25 C, 73.17; H, 6.63;. Found: N, 2.44 C, 73.25; H, 6.75.

4.2.2.8. Compound (cpd) 7. Methyl 4-hydroxybenzoate (cpd **6**) (1eq.), benzyl bromide (1.1eq.), and K$_2$CO$_3$ (1.5eq.) were dissolved in acetone solvent and reacted at reflux temperature for 10 hours. After removing acetone at reduced pressure, water was added and a precipitate was produced immediately. The crude product was recrystallized by acetone and hexane (1:4 vol) to give a white solid. Yield: 97%, ^{1}H NMR (300 MHz, CDCl$_3$) δ 7.03 (d, J = 9.0 Hz, 2H, Ar-H), 6.63-6.50 (m, 5H, Ar-H), 6.35 (d, J = 9.0 Hz, Ar-H), 4.38 (s, 2H, O$\underline{CH_2}$), 2.49 (s, 3H, O$\underline{CH_3}$).

4.2.2.9. Compound (cpd) 8. Cpd **7** (1eq.) and KOH (4eq.) were dissolved in ethanol and reacted at reflux temperature for 10 hours. HCl solution (10 vol% in water) was added to produce a precipitate, and the crude product was recrystallized by THF and hexane (1:10 vol) to give a white solid. Yield: 98 %, ^{1}H NMR (300 MHz, DMSO) δ 7.87 (d, J = 9.0 Hz, 2H, Ar-H), 7.46-7.33 (m, 5H, Ar-H), 7.07 (d, J = 9.0 Hz,

2H, Ar-H), 5.17 (s, 2H, OCH$_2$).

4.2.2.10. Compound (cpd) 9. Cpd **8** (1.1 e.q.) and cpd **4** (1 e.q.) were dissolved in dry DCM solvent and reacted with a catalytic amount of DMAP (0.2 e.q.) and DCC (1.1 eq) under nitrogen for 24 hours. The organic solution was extracted by DCM and water (1:1 vol) and recrystallized by DCM and ethanol (1:10 vol) to yield a white solid. Yield: 57%. ^{1}H NMR (300 MHz, d-dioxane) δ (ppm) : 8.26 (d, J = 9.0 Hz, 2H, Ar-H), 8.13 (d, J = 9.0 Hz, 2H, Ar-H), 7.44-7.29 (m, 10H, Ar-H), 6.97 (d, J = 9.0 Hz, 2H, Ar-H)，6.91-6.81 (m, 7H, Ar-H), 5.06(s, 1H, -Ar-O-CH$_2$-Ar), 4.04(t, J = 6.6 Hz, 2H, OCH$_2$), 1.81(t, J = 6.3 Hz, 2H, OCH$_2$CH$_2$)，1.46-1.25(m, 18H, -CH$_2$-), 0.86 (t, J = 6.3 Hz, 3H, CH$_3$).

4.2.2.11. Compound (cpd) 10. Cpd **9** and Pd/C catalyst were mixed in THF solvent under hydrogen to react at room temperature for 20 hours. The catalyst was removed by filtration through Celite and washed with THF. The solvent was removed by evaporation under reduced pressure, and the crude product was recrystallized by THF and hexane (1:10 vol) to produce a white solid. Yield: 80 %. ^{1}H NMR (300 MHz, d-dioxane): δ(ppm) : 8.28 (d, J = 9.0 Hz, 2H, Ar-H), 8.13 (d, J = 9.0 Hz, 2H, Ar-H), 8.05 (d, J = 8.7 Hz, 2H, Ar-H), 7.47 (t, J = 8.1 Hz, 1H, Ar-H), 7.41 (d, J = 8.7 Hz, 2H, Ar-H), 7.22 (s, 1H, Ar-H), 7.19-7.14 (m, 4H, Ar-H), 7.03 (d, J = 9.0 Hz, 2H, Ar-H), 6.86 (d, J = 8.7 Hz, 2H, Ar-H), 4.05 (t, J = 6.3 Hz, 2H, -OCH$_2$-)，1.80(m, 2H, -OCH$_2$CH$_2$-)，1.28(m, 18H, -CH$_2$-)，0.88(t, J = 6.3 Hz, 3H, -CH$_3$).

4.2.2.12. Bent-Core Covalent-Bonded Monomer (B). Cpd **A** (1.1 e.q.), cpd **10** (1 e.q.), DCC (1.1 e.q.), and DMAP (0.2 e.q.) were dissolved in THF solvent under nitrogen to react at room temperature for 24 hours. The solution was extracted by DCM and water, and purified by column chromatography to acquire a white solid. Yield: 60 %. ^{1}H NMR (300 MHz, d-dioxane) δ (ppm) : 8.25 (d, J = 9.0 Hz, 2H, Ar-H), 8.10 (d, J = 8.7 Hz, 2H, Ar-H), 7.48 (t, J = 8.1 Hz, 1H, Ar-H), 7.38 (d, J = 9.0 Hz, 2H,

Ar-H), 7.25(s, 1H, Ar-H), 7.17 (d, J = 8.1 Hz, 1H, Ar-H), 7.01 (d, J = 8.7 Hz, 2H, Ar-H), 6.29 (d, J = 17.1 Hz, 1H, -CH=<u>CH$_2$</u>), 6.08(m, 1H, -<u>CH</u>=)，5.77 (d, J = 10.2 Hz, 1H, -CH=<u>CH$_2$</u>), 4.08-4.00 (m, 6H, -O<u>CH$_2$</u>-)，1.78-1.71(m, 4H, -OCH$_2$<u>CH$_2$</u>-)，1.59-1.56(m, 2H, -OCH$_2$<u>CH$_2$</u>-), 1.43-1.26 (m, 34H, -<u>CH$_2$</u>-), 0.84 (t, J = 6.3 Hz, 3H, -CH$_3$). MS (EI): m/z [M+] 998; calcd m/z [M+] 997.2. EA: Calcd for C$_{61}$H$_{72}$O$_{12}$: C, 73.47; H, 7.28;. Found: C, 73.82; H, 6.95.

4.2.3. Polymerization

As shown in Scheme 4.2, the polymerizations of side-chain polymers **AmBn** with various molar ratios were carried out by free radical reactions in dry THF via different input molar ratios (see Table 4.1) of monomers **A** and **B** with 2,2'-azobis-isobutyronitrile (AIBN) as an initiator. All reactions were performed under N$_2$ at reflux temperature for 24 hours. The produced organic liquids were dropped into fast stirring diethyl ether (EA) solvent to precipitate products, and purified again by THF and EA (1:10 vol) to obtain white solids. According to similar manufactured procedures, a series of side-chain polymers **AmBn** (**m/n** = 1/0, 16/1, 10/1, 4/1, 1/2, 1/4, 1/13, 0/1) were prepared by various input molar ratios of monomers **A** and **B**, Furthermore, the extent of polymerization and output molar ratios (**m/n**) of polymer products were determined by ^{1}H NMR spectra.

4.2.4. Preparation of Polymer Complexes

All bent-core side-chain polymer complexes **AmBn-N** were constructed by mixing appropriate molar ratios of H-donor polymers (**AmBn**, excluding **A0B1**) and pyridyl H-Acceptor (**N**) in the solutions of chloroform/THF (ca. 1:1 vol.), which were self-assembled into supramolecules by evaporating solvents slowly, and seven polymer complexes **A1B0-N, A16B1-N**, **A10B1-N**, **A4B1-N**, **A1B2-N**, **A1B5-N**, and **A1B13-N** were formed.
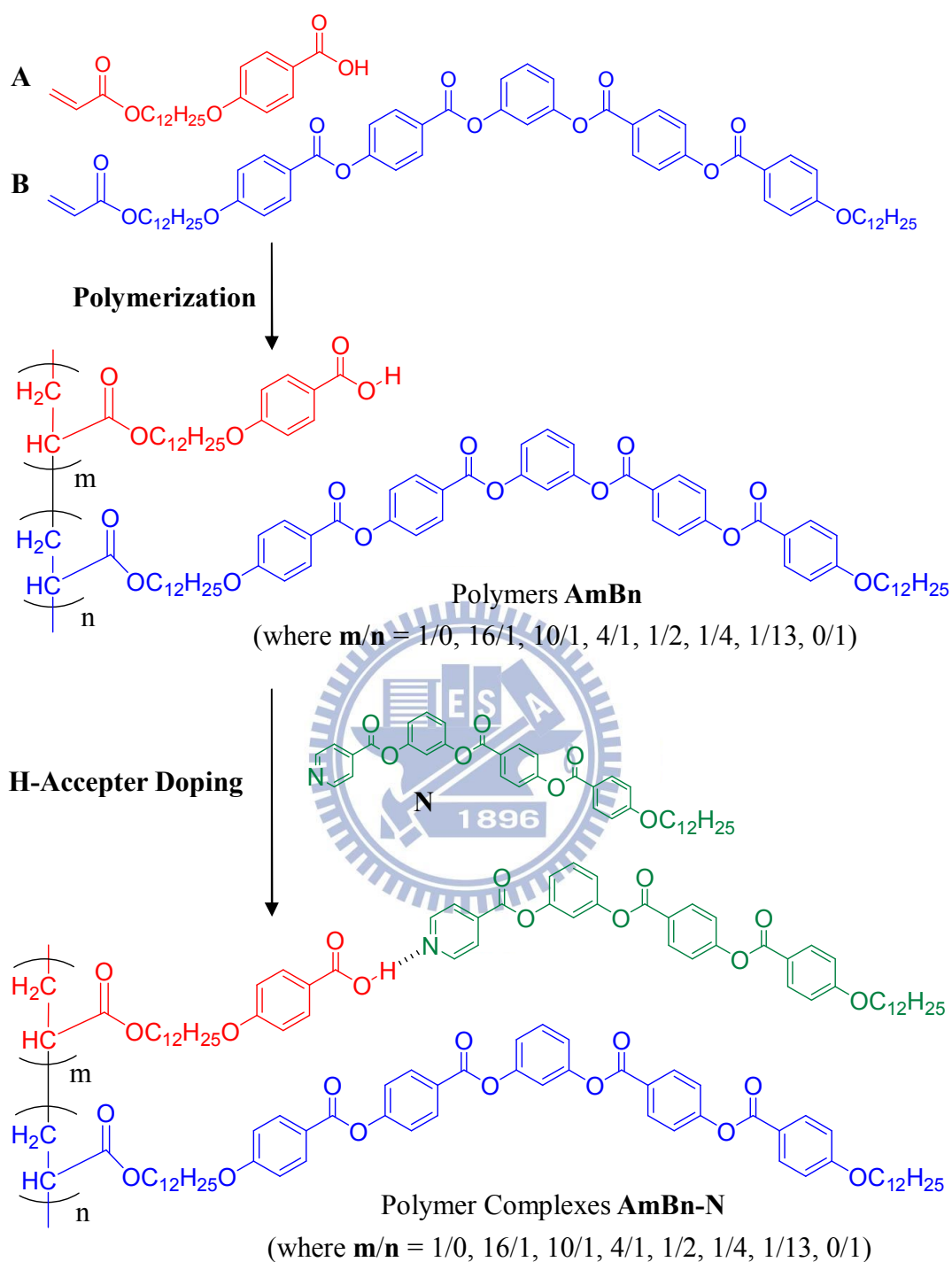
Scheme 4.2. Synthetic approaches of side-chain polymers **AmBn** (homopolymers/copolymers) and their corresponding bent-core side-chain polymer complexes **AmBn-N**

Table 4.1. Chemical Compositions and Molecular Weights of Side-Chain Polymers

polymer	input molar ratio A : B	output molar ratio A : B (m:n)	Mn (×10³)	PDI
A1B0	1 : 0	1 : 0	5.1	1.13
A16B1	15 : 1	16 : 1	5.8	1.29
A10B1	10 : 1	10 : 1	7.2	1.25
A4B1	5 : 1	4 : 1	7.1	1.26
A1B2	1 : 1	1 : 2	10.5	1.20
A1B5	1 : 5	1 : 5	9.1	1.21
A1B13	1 : 10	1 : 13	12.7	1.17
A0B1	0 : 1	0 : 1	12.1	1.16

4.3. Results and Discussion

4.3.1. Synthesis and Characterization of Polymers

In order to identify the polymers (or copolymers) and the molar ratio of copolymers, all side-chain polymers **AmBn** and monomers **A** and **B** were investigated by ^{1}H NMR measurements. As shown in Figure 4.2, both monomers **A** and **B** possessed the resonant peaks in the chemical shift range of 5.7 – 6.4 ppm belonging to the signal of acryl groups, which disappeared in the corresponding homopolymers **A1B0** and **A0B1** (see Figure 4.3). Meanwhile, the resonant peaks in the range of 6.6 to 8.5 ppm (attributed to the aromatic rings) are contributed from the benzoic acid groups of structure **A** (peaks a and b) and the five phenyl rings of structure **B** (peaks c, d, e, f, g, h and i). To recognize the molar (**m/n**) ratios of copolymers, the integral values of ^{1}H NMR peaks from structures **A** and **B** in each copolymers were calculated the integral values of NMR peaks a - b, (from structure **A**) along with c - d, and i (from structure **B**). Based on this calculating way, copolymers **A16B1**, **A10B1**, **A4B1**, **A1B2**, **A1B5** and **A1B13** and homopolymers **A1B0** and **A0B1** were characterized. In addition, the number average molecular weights (Mn) and polydispersity index (PDI) values of all polymers were acquired by GPC experiments as shown in Table 4.1, where the PDI

values were in the range of 1.13 – 1.29 and Mn values were in the range of 5.1 -

12.7×10^3. The Mn values were increased at higher values of **n** (part **B** ratio) duo to the

higher molecular weight of part **B**.
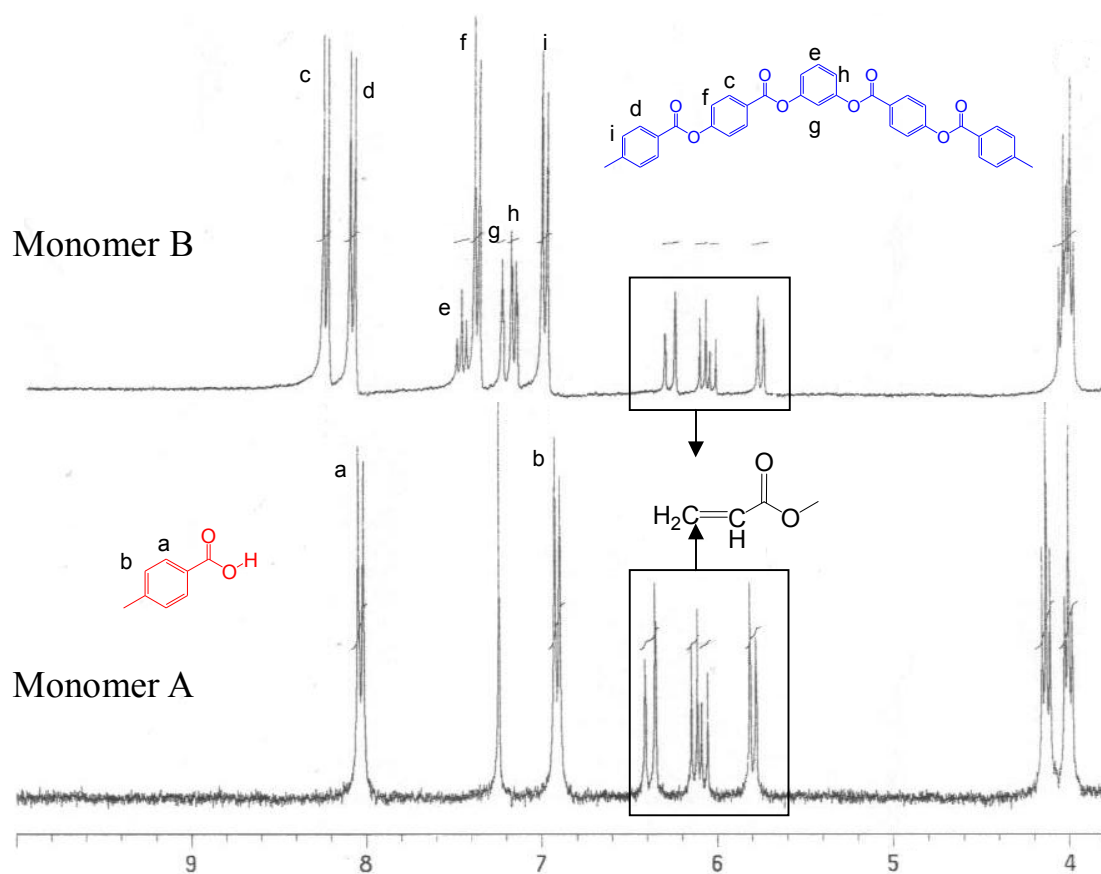
Figure 4.2. NMR spectra of monomers **A** and **B**.
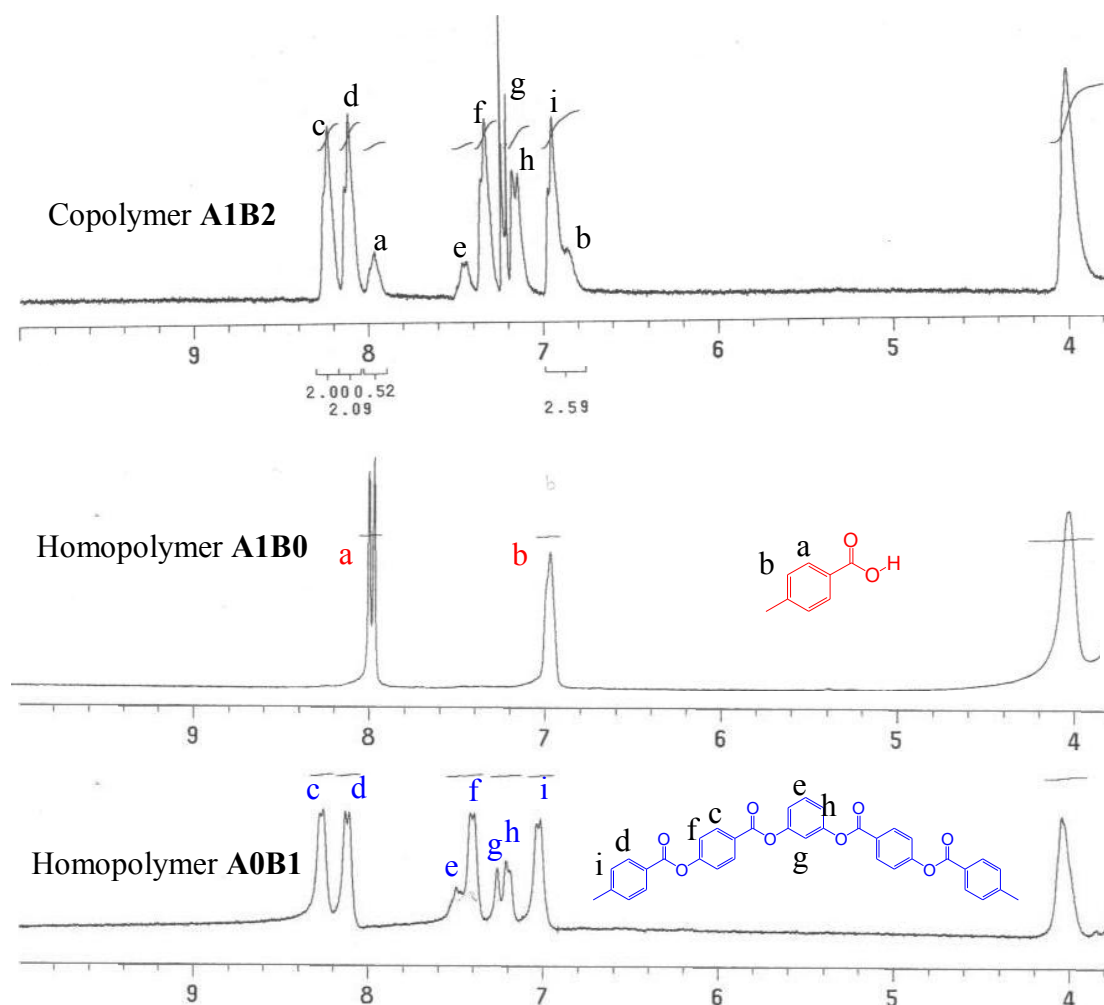
Figure 4.3. NMR patterns of side-chain polymers **A1B2** (copolymers), **A1B0** (homopolymers), and **A0B1** (homopolymers).

4.3.2. IR Characterization

The existence and stability of H-bonds in polymer complexes were characterized by IR spectra, and the IR spectra of H-donor polymer **A10B1** (with acidic groups) and pyridyl H-Acceptor (**N**) were compared with that of complex copolymer **A10B1-N** to examine the existence of H-bonds as shown in Figure 4.4. In contrast to the O-H bands of pure **A10B1** at 2666 and 2568 cm^{-1}, weaker O-H band observed at 2514 and 1952 cm^{-1} in complex **A10B1-N** was indicative of hydrogen bonding between the pyridyl group of **N** and acidic group of **A**. On the other hand, a C=O stretching vibrations appeared at 1728 cm^{-1} (shoulder) and 1687 cm^{-1} in complex **A10B1-N**,

141

which showed that the carbonyl group is in a less associated state than in pure **A10B1** with weaker C=O stretching vibrations appeared at 1687 and 1671 cm^{-1}.[38a,53] The results suggested that H-bonds of polymer complex **A10B1-N** are formed between copolymer **A10B1** and H-acceptor **N**. In addition, the other polymer complexes were also confirmed to exhibit H-bonded frameworks as polymer complex **A10B1-N**, so the supramolecular structures were established in all polymer complexes.
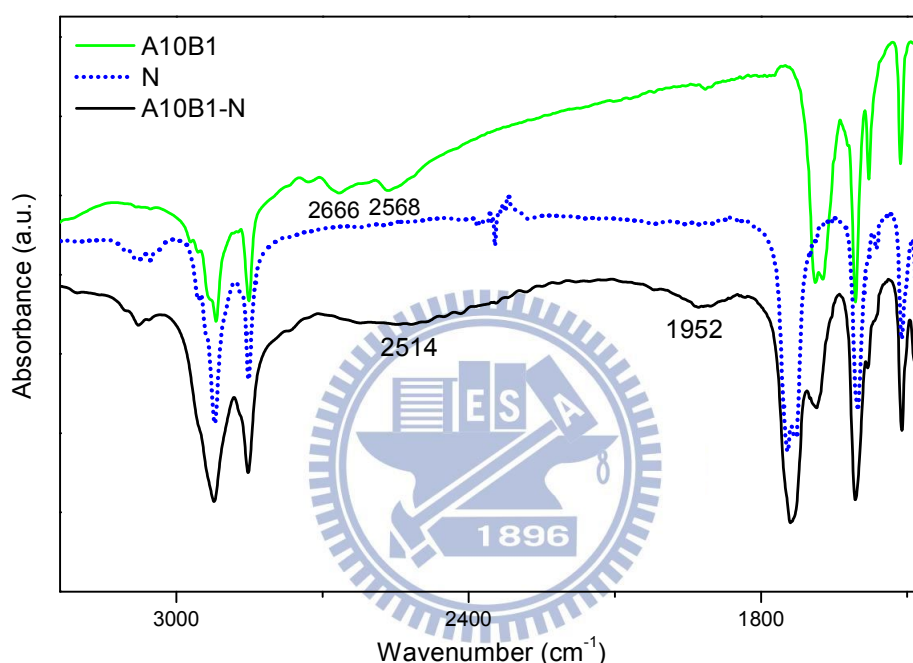
Figure 4.4. IR spectra of polymer **A10B1**, pyridyl H-acceptor **N**, and polymer complex **A10B1-N**.

4.3.3. Mesophasic and Thermal Properties

4.3.3.1. Side-Chain Polymers AmBn. In order to understand the influence of the molar ratio of covalent-bonded bent-core units on the mesomorphic, molecular stacking, and thermal properties, side-chain polymers **AmBn** were investigated by POM, DSC, and XRD measurements. The thermal properties and phase behaviors of side-chain polymers **AmBn** are illustrated in Figure 4.7a and Table 4.2. Polymers **A1B0**, **A16B1**, and **A10B1** with higher **m/n** molar ratios (lower densities of covalent-bonded bent-core units) possessed the tilted smectic (SmC) phases, which

were verified by POM to show the enantiotropic schlieren texture and grainy domain. For instance, the schlieren texture and grainy domain of polymers **A1B0** and **A10B1** are demonstrated in Figures 4.5a and 4.5b, respectively. However, polymer **A4B1** revealed a nematic phase in both heating and cooling processes, and the POM texture of polymer **A4B1** is shown in Figure 4.5c. Regarding the mesophases of polymers **A1B2**, **A1B5**, **A1B13**, and **A0B1** with lower **m/n** molar ratios (higher densities of covalent-bonded bent-core units), the same enantiotropic smectic phase (SmC) was obtained, where one of the POM texture of **A1B13** is shown in Figure 4.5d.

Table 4.2. Phase transition temperatures and tnthalpies of side-chain polymers

polymer	phase transition temperature/°C [enthalpy/kJ/g] heating (top) / cooling (bottom)
A1B0	**K** 71.2 [1.3] **K'** 96.3 [1.7] **SmC₁** 162.2 [22.4] **I**
	I 155.1 [-27.5] **SmC₁** 76.2 [-4.5] **K**
A16B1	**K** 141.2 [1.3] **SmC₁** 159.7 [10.4] **I**
	I 153.6 [-12.9] **SmC₁** 140.9 [-1.8] **K**
A10B1	**K** 140.2 [6.4] **SmC₁** 154.3 [1.7] **I**
	I 153.3 [-7.6][a] **SmC₁** 138.7[a] **K**
A4B1	**K** 112.3 [0.6] **N** 129.8 [4.5] **I**
	I 129.7 [-3.6] **N** 105.3 [-1.0] **K**
A1B2	**K** 71.3 [3.5] **SmC₂** 96.0 [5.7] **I**
	I 90.1 [-2.8] **SmC₂** 74.3 [-0.7] **K'** 59.2 [-1.4] **K**
A1B5	**K** 75.9 [6.9] **SmC₂** 98.8 [2.5] **I**
	I 88.7 [-4.69] **SmC₂** 74.8 [-4.5] **K**
A1B13	**K** 120.4 [18.5] **SmC₂** 140[b] **I**
	I 135[b] **SmC₂** 115.4 [-15.3] **K**
A0B1	**K** 136.3 [23.5] **SmC₂** 150[b] **I**
	I 148[b] **SmC₂** 130 [-19.4] **K**

The phase transitions were measured by DSC at the 2nd scan with a cooling rate of 5 °C/min. I = isoptropic state; N = nematic phase; SmC_1 and SmC_2 = tilted smectic phases; K = crystalline state. [a] means the enthalpy values of two cover transition peaks. [b] means the temperature data is observed in POM only. Phase transitions of monomer **A** was obtained as **I** 106.4 [20.6] **SmC** 55.4 [8.59] **K**. Phase transition of monomer **B** was obtained as **I** 90.3 [34.8] **K**.
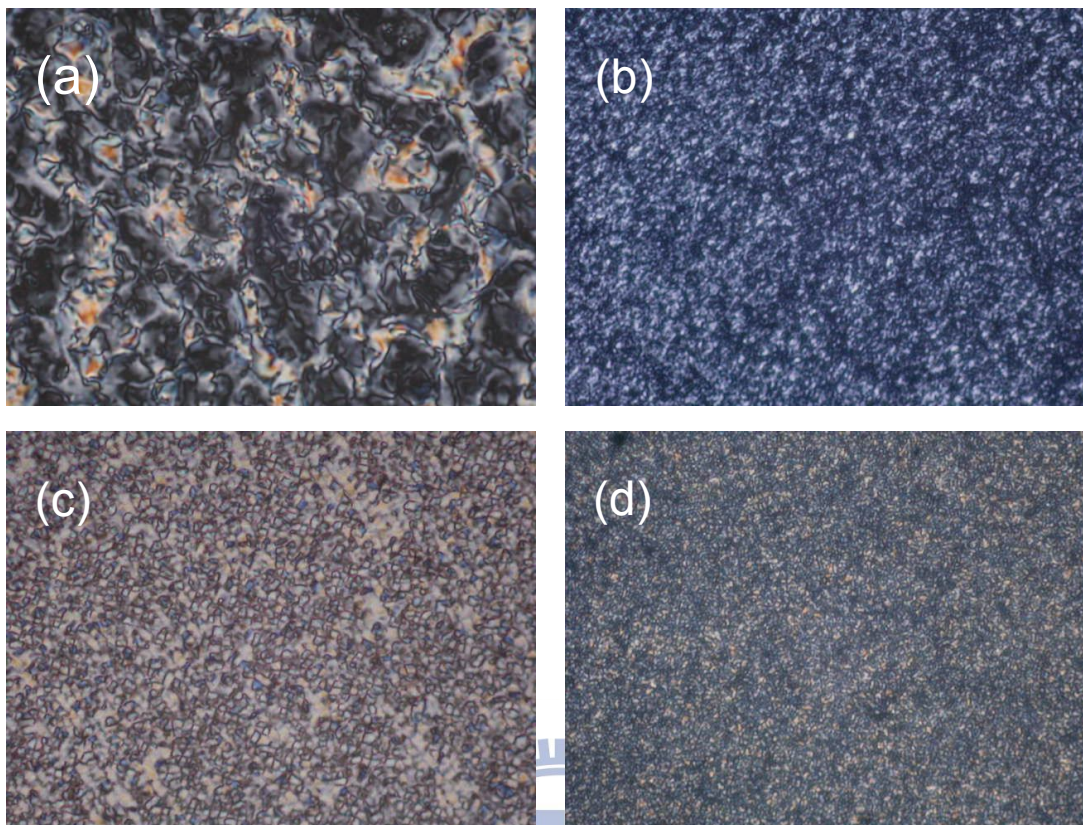
Figure 4.5. POM textures at the cooling process: (a) the tilted smectic phase with schlieren texture of polymer **A1B0** at 150 °C; (b) the tilted smectic phase with grainy domain of polymer **A10B1** at 150 °C; (c) the nematic phase with schlieren texture of polymer **A4B1** at 125 °C; (d) the tilted smectic phase with grainy domain of polymer **A1B13** at 130 °C.

Comparing the phase transition temperatures of all side-chain polymers **AmBn**, homopolymers **A1B0** and **A0B1** revealed the highest isotropization temperatures for polymers **AmBn** with higher and lower **m**/**n** molar ratios (lower and higher densities of covalent-bonded bent-core units), respectively. Higher isotropization temperatures of homopolymers **A1B0** and **A0B1** indicated that the tighter molecular staking of intermolecular H-bonded linear-cores or bent-cores in homopolymeric systems, which also suggested that the looser molecular stackings were formed in copolymers duo to the disorder arrangements of both H-bonded linear-cores and covalent-bonded bent-cores. Especially, copolymer **A4B1** reached the largest randomness to lose the lamellar packings for both H-bonded linear-cores and covalent-bonded bent-cores,

and the nematic phase was preferred instead. Hence, three cartoon diagrams were drawn in Figure 4.6 to explain possible intermolecular arrangements in polymers **AmBn**. Based on the molar ratios of bent-core units, polymers **A1B0**, **A16B1**, and **A10B1** with the high density of benzoic acidic groups displayed the smectic stacking by the intermolecular acidic H-bonds (with H-bonded cross-linking structures) as shown in Figure 4.6a, and the stacking order was reduced by decreasing **m**/**n** molar ratio. As **m**/**n** ratio reached 4/1 (polymer **A4B1**), the acidic H-bonded linear-cores (H-bonded cross-links) would be separated into a more random stacking by the introduction of covalent-bonded bent-core unit **B** as shown in Figure 4.6b. Afterwards, to the other extreme of more covalent-bonded bent-core units (**B**), polymers **A1B2**, **A1B5**, **A1B13**, and **A0B1** demonstrated another smectic arrangement due to the major intermolecular stackings of bent-core units (see Figure 4.6c).
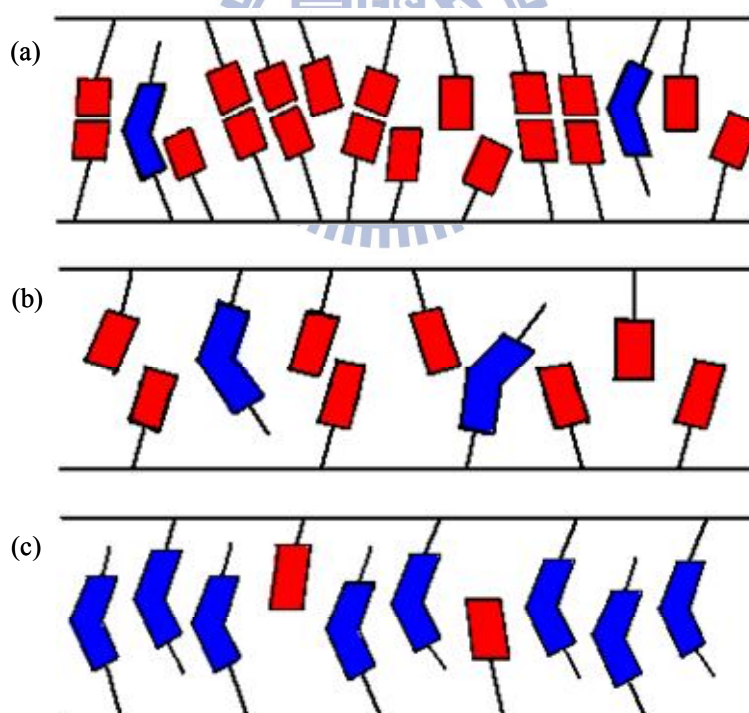
Figure 4.6. Cartoon diagrams of possible intermolecular arrangements of (a) polymers **A1B0**, **A16B1**, and **A10B1** with larger **m/n** molar ratios mainly contributed from the self H-bonded acidic dimmers, (b) polymer **A4B1** with a medium **m/n** molar ratio, and (c) polymers **A1B2**, **A1B5**, **A1B13**, and **A0B1** with smaller **m/n** molar ratios mainly contributed from the major component of covalent-bonded bent-cores.
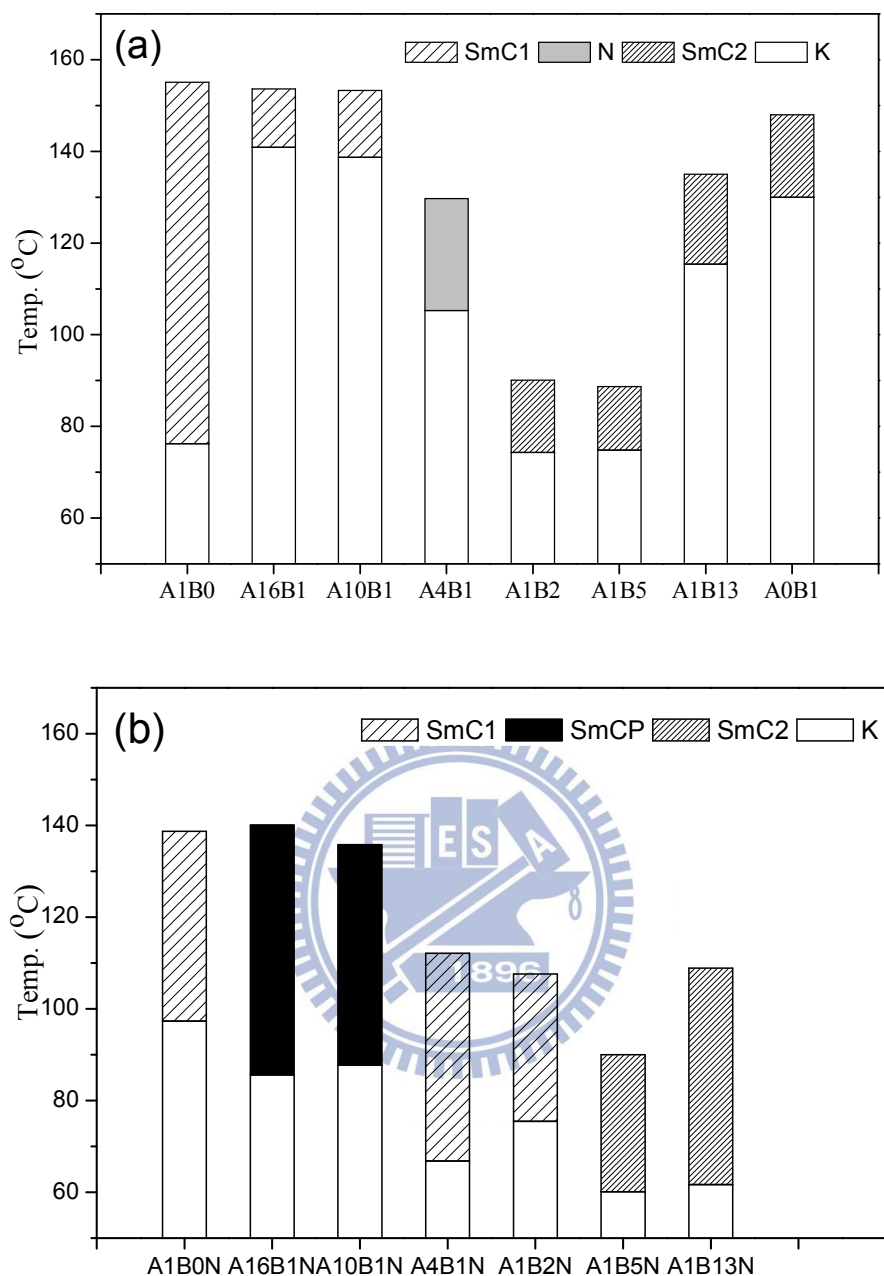
Figure 4.7. Phase diagrams (upon 2nd cooling) of (a) side-chain polymers **AmBn** and (b) bent-core side-chain polymer complex **AmBn-N**.

4.3.3.2. Bent-Core Side-Chain Polymer Complexes AmBn-N. The influence of molar ratios of bent-core covalent- and H-bonded units on the mesomorphic, molecular stacking, and thermal properties of bent-core side-chain polymer complexes **AmBn-N** were also investigated by POM, DSC, and XRD measurements. The thermal properties and phase behaviors of bent-core side-chain polymer

146

complexes **AmBn-N** are illustrated in Figure 4.7b and Table 4.3. According to Figure S1 of the supporting information, compound **S12** and supramolecular analogue **H12** (H-bonded complex) both exhibited the SmCP phase, so bent-core side-chain polymer complexes **AmBn-N** via the copolymerization of these two units (**S12** and **H12**) were prepared and surveyed for the generation of the SmCP phase. However, due to the addition of acrylate termini in their similar structures, **B** and **A-N** units did not possess any SmCP phase, where the phase transition temperatures of monomers **A** and **B** along with complex **A-N** were obtained as **A**: **I** 106.4 °C **SmC** 55.4°C **K**, **B**: **I** 90.3 °C **K**, and **A-N**: **I** 76.7 °C **K**, respectively.
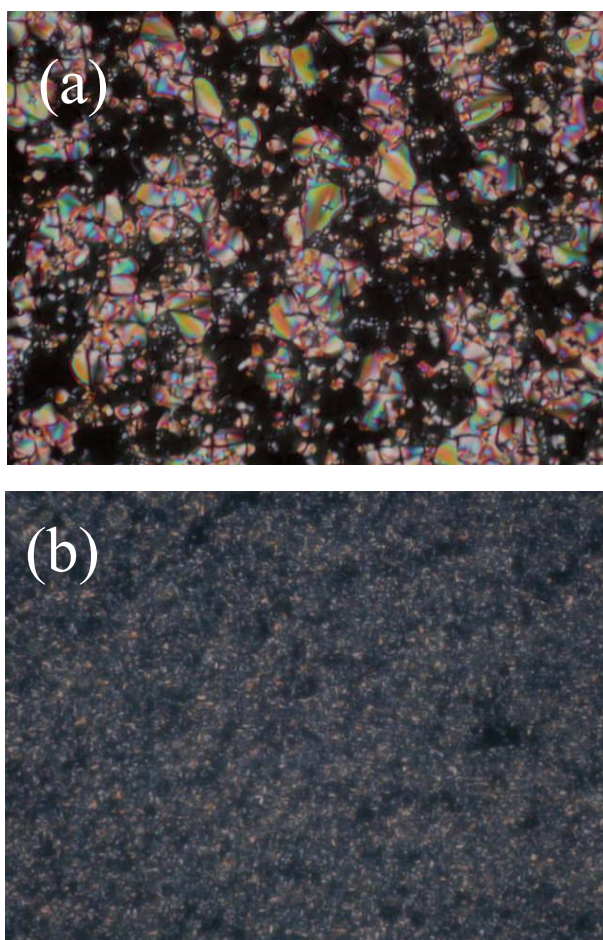
Figure 4.8. POM textures at the cooling process: (a) the polar smectic phase with fan-like texture of polymer complex **A10B1-N** at 130 °C; (b) the tilted smectic phase with grainy domain of polymer complex **A1B13-N** at 85 °C.

Table 4.3. Phase transition temperatures and enthalpies of bent-core side-chain polymer complexes

polymer complex	phase transition temperature/°C [enthalpy/kJ/g] heating (top) / cooling (bottom)
A1B0-N	**K** 125.6 [43.3] **SmC$_1$** 158.0 [2.5] **I** **I** 138.7 [1.9] **SmC$_1$** 97.3 [36.8] **K**
A16B1-N	**K** 80.0 [2.7] **K'** 112.7 [13.3] **SmCP** 145.5 [15.0] **I** **I** 140.1 [-12.2] **SmCP** 85.6 [-1.8] **K'** 59.4 [-9.0] **K**
A10B1-N	**K** 85.4 [2.8] **K'** 116.1 [18.7] **SmCP** 143.0 [3.2] **I** **I** 135.8 [-17.0] **SmCP** 87.7 [-2.3] **K'** 66.7 [-10.6] **K**
A4B1-N	**K** 78.5 [5.4] **SmC$_1$** 117.3 [11.4] **I** **I** 112.1 [-8.4] **SmC$_1$** 66.8 [-2.7] **K**
A1B2-N	**K** 77.4 [6.0] **SmC$_1$** 110.8 [14.3] **I** **I** 107.6 [-7.0] **SmC$_1$** 75.5 [-14.7] **K**
A1B5-N	**K** 79.9 [9.9] **SmC$_2$** 95.7 [17.1] **I** **I** 90.0 [-19.7] **SmC$_2$** 60.1 [-9.0] **K**
A1B13-N	**K** 75.9 [1.6] **SmC$_2$** 115.2 [12.9] **I** **I** 108.9 [-13.9] **SmC$_2$** 61.7 [-1.2] **K**

The phase transitions were measured by DSC at the 2nd scan with a cooling rate of 5 °C/min. I = isoptropic state; SmCP = polar smectic phase; SmC$_1$ and SmC$_2$ = tilted smectic phase2; K = crystalline state. Phase transitions of complex **A-N** was obtained as **I** 76.7 [36.4] **K**.

In comparison with side-chain polymers **AmBn**, bent-core side-chain polymer complexes **AmBn-N** have lower isotropization temperatures due to their H-bonded pendants assembled by pyridyl and acidic groups, which have less intermolecular acidic H-bonds (with less H-bonded cross-links). Therefore, the novel enantiotropic polar smectic (SmCP) phase was surprisingly generated in some compositions of bent-core side-chain polymer complexes **AmBn-N**. Regarding the mesophasic types, the enantiotropic tilted smectic phase was observed in polymer complexes **A1B0-N**, **A4B1-N**, **A1B2-N**, **A1B5-N**, and **A1B13-N**, and the enantiotropic polar smectic (SmCP) phase was achieved in polymer complexes **A16B1-N** and **A10B1-N**. The mesophasic textures were observed by POM experiments, for instance, polymer

complex **A10B1-N** revealed the polar smectic phase with a fan-like texture in Figure 4.8a, and polymer complex **A1B13-N** exhibited the tilted smectic (SmC) phase with a grainy domain in Figure 4.8b, which were the characteristics of the tilted smectic phases.

With regard to the variation of mesophasic transition temperatures of polymer complexes **AmBn-N**, the isotropization temperatures and mesophasic ranges were reduced as the **m**/**n** molar ratio decreased (except **A1B13-N**). Side-chain copolymers **AmBn** with higher **m**/**n** ratios possessed more H-donor groups exhibited more extensive mesophasic ranges and higher isotropization temperatures, which indicated that the acidic H-bonded linear-cores (H-bonded cross-links) would extend and stabilize the mesophase. However, due to the intermolecular acidic H-bonds (with H-bonded cross-linking structures) of side-chain copolymers **AmBn** being replaced with side-chain H-bonded pendants of the analogous polymer complexes **AmBn-N**, bent-core side-chain polymer complexes **AmBn-N** with higher **m**/**n** molar ratios did not exhibit more extensive mesophasic ranges but still possessed higher isotropization temperatures. Compared with side-chain copolymers **AmBn**, the corresponding polymer complexes **AmBn-N** generally exhibited more extensive mesophasic ranges and lower transition temperatures, except polymer complexes **A1B2-N** and **A1B5-N**. In addition, the nematic phase in copolymer **A4B1** was replaced by a tilted smectic phase in polymer complex **A4B1-N**. More excitingly, the polar smectic phase (the switching current behaviors will be demonstrated later) was achieved in polymer complexes **A16B1-N** and **A10B1-N**, though the individual components of H-donor side-chain copolymers **A16B1** and **A10B1** as well as H-acceptor **N** did not possess the SmCP phase (see Tables 4.2 and 4.3). Hence, it suggested that the mesomorphic and thermal properties of polymer complexes **AmBn-N** were strongly dependent on the **m**/**n** molar ratios of bent-core covalent- and H-bonded units (i.e., **B** and **A-N** units,

respectively), where the bent-core H-bonded units were formed by the acidic H-donor groups (**A** groups from side-chain polymers **AmBn**) incorporated with H-acceptor **N**. Therefore, we have discovered a special technique that the construction (or stabilization) of the SmCP phase can be acquired by copolymerization of bent-core covalent- and H-bonded units in side-chain polymer complexes (with proper **m**/**n** molar ratios) from both bent-core covalent- and H-bonded monomers (i.e., **B** and **A-N** units, respectively) without the SmCP phase (see Figure 4.9).
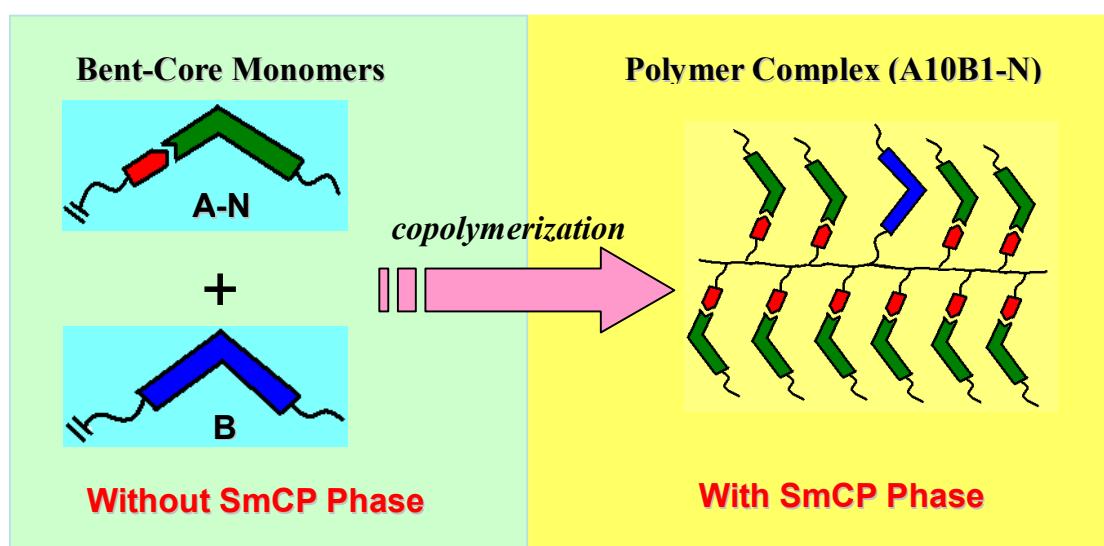
Figure 4.9. The SmCP phase was introduced by copolymerized frameworks bearing both bent-core covalent- and H-bonded monomers (**B** and **A-N** units with proper **m**/**n** molar ratios) without the SmCP phase.

4.3.4. Powder XRD Analyses

4.3.4.1. Side-Chain Polymers AmBn. The molecular arrangements of side-chain polymers **AmBn** in different mesophases were investigated by XRD measurements at various temperatures upon cooling (see Figures 4.10-4.11). As shown in Figure 4.10a (also see Figures S4.3a of the supporting information), the 2D XRD pattern of polymer **A16B1** at 150 °C during the cooling process revealed a diffuse peak at wide angles corresponding to a d-spacing value of 4.6 Å, which

demonstrated that similar liquid-like in-plane orders with average intermolecular distances were prevalent inside the layers of bent-core units. Two single sharp peaks were observed at corresponding d-spacing values of $d_1 = 35.4$ Å and $d_2 = 17.7$ Å in small angle regions, where the longest d-spacing value d_1 was indexed as (001). The d-spacing value (d_1) is shorter than the theoretical coplanar molecular length (L) (about 47 Å) of self H-bonded benzoic acidic dimmer to indicate the tilted smectic arrangement. In addition, temperature dependent XRD results of polymer **A16B1** were also provided in Figure 4.10b. Two sharp peaks appeared during the cooling process from the isotropic to mesophasic states. An additional peak with a corresponding d-spacing value (~ 46 Å) similar to its theoretical molecular length was obtained as the temperature was equivalent to or lower than 130 °C, and the orthogonal arrangement of the crystalline phase or highly ordered smectic phase was generated. Polymers **A1B0** and **A10B1** illustrated similar XRD results as shown in the supporting information (see Figures S4.2a and S4.4a) to indicate the analogous smectic mesophase.

Polymer **A4B1** did not obtain any sharp diffraction peak at small angle regions in the mesophasic temperature (120 °C) to reveal one dimension order of nematic phase as shown in Figure S4.5 of the supporting information, but two broad peaks were observed at the corresponding d-spacing values of 17.1 Å and 4.6 Å. Until the temperature reaching the crystalline state (100 °C), a d-spacing value of 66.5 Å was produced to indicate the orthogonal arrangement of the crystalline phase or highly ordered smectic phase. The powder XRD results of polymer **A4B1** in various temperatures was also provided in Figure S4.5a of the supporting information to reveal its phase transition in the cooling process from the isotropic to crystalline states.

As the shown pattern of polymer **A1B13** at 120 °C (see Figure S4.8a of the

supporting information), several sharp peaks were detected at corresponding values of $d_1 = 37.5$ Å, $d_2 = 25.4$ Å, and $d_3 = 19.1$ Å in small angle regions (along with some other undefined sharp peaks). The ratio of d_1 to d_3 was 2 : 3 : 4 to index (002), (003) and (004), and a d-spacing value ca. 76 Å was correspondent to the essential peak indexed as (001), which might be lost duo to the limitation of the XRD instrument. A broad peak was gained at the wide angle regions to account for the natural mesogenic stacking width. This similar result was reported in the literature[17] to mean the long range ordered smectic structure of SmC_2. The XRD investigations of polymer **A1B13** at various temperatures from the isotropic to crystalline states were performed in Figure S4.7a of the supporting information, and polymers **A1B2**, **A1B5**, and **A0B1** exhibited similar XRD results with those of **A1B13** in the supporting information (see Figures S4.6a, S4.8a, and S4.9).

In comparison the variation of d-spacing values in all side-chain polymers **AmBn** as shown in Table 4.4 (also see Figures S4.10a of the supporting information), the d-spacing values of copolymers were larger than those of homopolymers to indicate that more tilted smectic arrangements were produced in both homopolymers **A1B0** and **A0B1**, which meant that less tilted smectic arrangement existed in copolymers with both H-bonded acidic dimers and covalent-bonded bent-cores. Hence, the variations of molecular arrangements, including two kinds of tilted smectic orders (i.e., SmC_1 and SmC_2), in side-chain polymers were further identified by the XRD experiments.
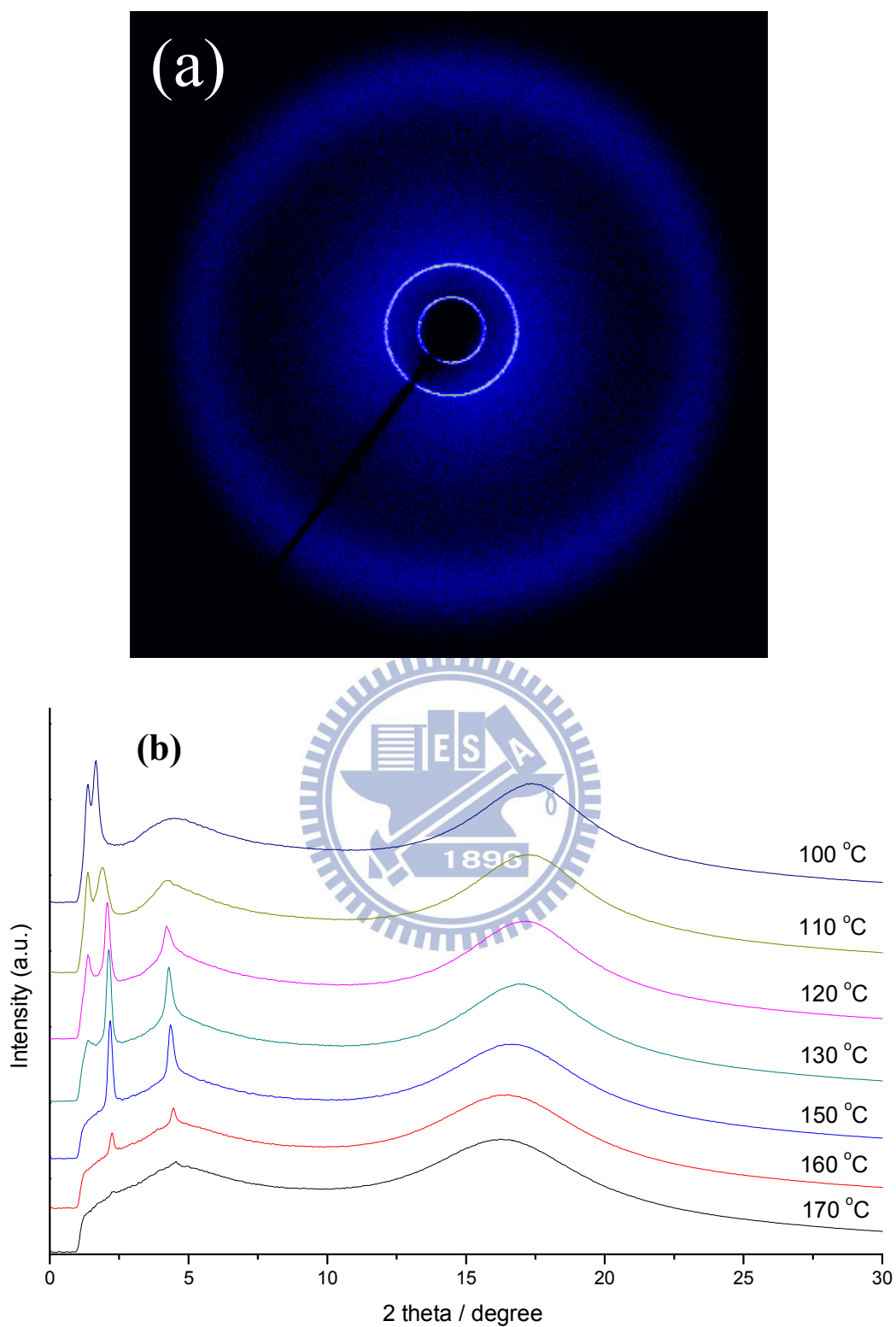
Figure 4.10. Powder X-ray data of polymer **A16B1**: (a) 2D pattern in the tilted smectic phase (150 °C); (b) Powder X-ray diffraction intensity against angle profiles at various temperatures upon cooling from the isotropic to crystalline phases.

Table. 4.4. Powder XRD data of side-chain polymers

polymer	cooling temp. (°C)	2 theta (degree)	d-spacing (Å)
A1B0	140	2.24	34.1
		4.47	17.1
A16B1	150	2.16	35.4
		4.33	17.7
A10B1	140	2.12	36.1
		4.25	18.0
A4B1	120	4.37 (br)	17.5
A1B2	90	2.06	37.1
		2.70	28.3
		3.82	20.0
		4.09	18.7
A1B5	90	2.00	38.2
		2.83	27.0
		3.78	20.2
		6.04	12.7
A1B13	120	2.04	37.5
		3.08	24.8
		3.80	20.1
		4.45	17.2
A0B1	140	2.10	36.4
		3.14	24.3
		3.85	19.9
		4.48	17.1
		5.20	14.7

4.3.4.2. Bent-Core Side-Chain Polymer Complexes AmBn-N. The molecular arrangements of bent-core side-chain polymer complexes **AmBn-N** were also surveyed by XRD measurements and their related results are illustrated in Table 4.5. Compared with side-chain copolymers **AmBn**, the corresponding polymer complexes **AmBn-N** generally exhibited larger d-spacing values (except polymer complex **A1B2-N**), which might be due to the coexistence of bent-core covalent- and H-bonded units in side-chain polymer complexes, and thus to have less ordered smectogenic packings and to induce lower phase transition temperatures. Similar to side-chain copolymers **AmBn**, most polymer complexes **AmBn-N** in Table 4.5 (also see Figures S4.10b of the supporting information) generally demonstrated larger d-spacing values than homopolymer complex **A1B0-N** (with bent-core H-bonded units only), which might have better and homogeneous packing of bent-core H-bonded units in the tilted smectic arrangement of the homopolymer complex. Similarly, smaller d-spacing values were observed in **A1B13** (d_1 = 37.5 Å), **A1B13-N** (d_1 = 38.0 Å), and **A0B1** (d_1 = 36.4 Å), which might be attributed to the major component of bent-core covalent-bonded structure **B**, and the influence of co-stacking effect contributed from bent-core H-bonded structure **A-N** was much less.

Polymer complex **A16B1-N** displayed two sharp peaks at the associated d-spacing values of d_1 = 43.2 Å and d_2 = 21.6 Å in small angle regions and a broad peak at the related d-spacing value d = 4.5 Å at 130 °C (upon cooling) as shown in Figure 4.11a (also see Figures S4.3b of the supporting information). The largest d-spacing value (d_1 = 43.2 Å) is less than the theoretical length of bent-core H-bonded structure **A-N** (about 58 Å) to indicate the tilted smectic arrangement of polymer complex **A16B1-N**. The XRD results of **A16B1-N** at various temperatures upon cooling from the isotropic to crystalline phases were demonstrated in Figure 4.11b. Two sharp peaks of a characteristic smectic mesophase appeared as the temperature

reached 140 °C during the cooling process. Afterwards, an additional peak developed when the temperature was lower than 80 °C, where the new d-spacing value of 35.1 Å was correspondent to the crystalline state. Polymer complexes **A10B1-N**, **A4B1-N** and **A1B2-N** revealed similar X-ray diffraction patterns (see Figures S4.4b, S4.5b, and S4.6b of the supporting information) to indicate the analogous type of the tilted smectic mesophase. Polymer complex **A1B13-N** manifested the long range ordered smectic organization in mesophasic and crystalline temperatures duo to the exhibition of several sharp diffraction peaks (see Figure S4.7b of the supporting information). In addition, polymer complex **A1B5-N** revealed X-ray diffraction patterns (see Figure S4.8b of the supporting information) similar to that of **A1B13-N**, which suggested the analogous type of the tilted smectic phase in both polymer complexes.

Table 4.5. Powder XRD Data of bent-core side-chain polymer complexes

polymer complex	cooling temp. (°C)	2 theta (degree)	d-spacing (Å)
A1B0-N	140	2.19	34.9
		4.43	17.3
A16B1-N	130	1.77	43.2
		3.54	21.6
A10B1-N	120	1.71	44.7
		3.40	22.5
A4B1-N	100	1.70	45.0
		3.40	22.5
A1B2-N	100	2.16	35.4
		4.32	17.7
A1B5-N	70	1.76	43.4
		2.65	28.8
		4.42	17.3
		5.32	14.4
A1B13-N	65	2.01	38.0
		3.04	25.1
		3.73	20.5
		4.39	17.4
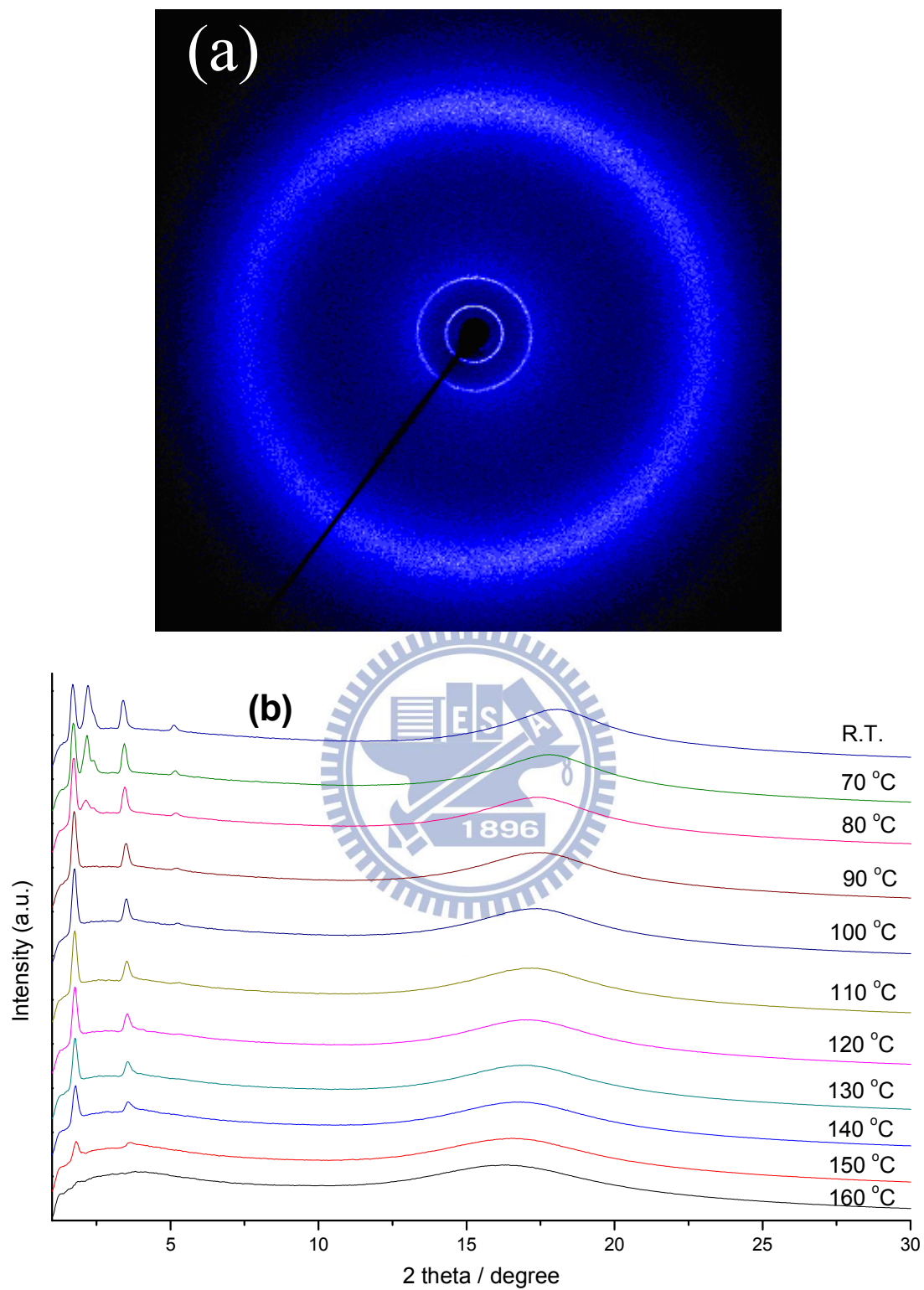
Figure 4.11. Powder X-ray data of polymer complex **A16B1-N**: (a) 2D pattern in the tilted smectic phase (130 °C); (b) Powder X-ray diffraction intensity against angle profiles at various temperatures upon cooling from the isotropic to crystalline phases.

4.3.5. Switching Current Behaviors and Spontaneous Polarization (Ps) of Bent-Core Side-Chain Polymer Complexes

In order to evaluate the polar switching properties of the SmCP phase in all side-chain polymers and bent-core side-chain polymer complexes, the triangular wave method[22] was applied to measure the switching current behavior (i.e., the spontaneous polarization, Ps) in parallel rubbing cells with a cell gap of 4.25 μm. The triangular voltages were applied on all polymers and polymer complexes, and only bent-core side-chain polymer complexes **A10B1-N** and **A16B1-N** possess the switching current behaviors with specific Ps values. For instance, as shown in Figure 4.12a, polymer complex **A10B1-N** responded under a simple (continuous) triangular voltage to give a single current peak per half-period in the switching current response (Vpp = 310 V and f = 150 Hz, at T = 100 °C). However, as shown in Figure 4.12b, the current response was separated into two repolarisation peaks under the modified triangular wave (i.e., a single pulsed triangular wave, Vpp = 310 V and f = 30 Hz, at T = 100 °C), where a plateau equivalent to a triangular wave period is introduced at zero voltage, and antiferroelectric switching current responses were observed in both polymer complexes **A10B1-N** and **A16B1-N**. Here, the characteristic behavior of a sequential electric response was due to a ferroelectric state switched into an antiferroelectric ground state and back to the opposite ferroelectric state, which confirmed the $SmCP_A$ (A = anti-ferroelectric behavior) structure of the B2 phase,[53] and the existing $SmCP_A$ state was hidden under the continuous triangular wave measurements due to the quick exchange of $SmCP_F \rightarrow SmCP_A \rightarrow SmCP_F$.

According to the triangular wave method, the Ps values (the saturated values at high voltages) of polymer complexes **A16B1-N** and **A10B1-N** could be calculated as 15 and 60 nC/cm^2, respectively. As shown in Figure 4.13, the spontaneous polarization (Ps) values of polymer complex **A10B1-N** in the SmCP phase at various

applied electric fields and temperatures were surveyed. With respect to Ps values as a function of applied voltages (at f = 60Hz and T = 100 °C) in Figure 4.13a, the Ps values were steeply enhanced to reach a maximum at Vpp ~ 130-180 V by increasing the applied electric fields, and the Ps values were gradually dropped as the applied electric fields were above Vpp ~ 200 V, which were reproducible for several cycles. It was speculated that the reduction of Ps values at high applied voltages was duo to the weak H-bonds of bent-core H-bonded component **A-N** in polymer complex **A10B1-N**, and the Ps behavior of the SmCP phase was mainly contributed from bent-core H-bonded component **A-N** rather than from bent-core covalent-bonded component **B** (due to a large molar ratio of **m/n** in **A10B1-N**). Hence, the novel example of bent-core side-chain polymer complex **A10B1-N** was evidenced to possess the voltage-sensitive switching polar behavior, which was provided by the major soft bent-core skeleton (H-bonded unit) and the minor rigid bent-core skeleton (covalent-bonded unit). In addition, as shown in Figure 4.13b, the Ps values of polymer complex **A10B1-N** at various temperatures (except the transition teperatures) were acquired as a constant value around Ps = 60 nC/cm^2 in the SmCP phase. However, the switching current phenomena were not clearly acquired in bent-core H-bonded homopolymer complex (**A1B0-N**), covalent-bonded homopolymer (**A0B1**), and the other copolymer complexes (**A4B1-N**, **A1B2-N**, **A1B5-N**, and **A1B13-N**), which indicated that the suitable **A-N/B** (i.e., **m/n**) molar ratio in the tilted smectic phases should be in the range of **m/n** = 16/1 to 10/1 to induce the polar switching behavior by the favorable molecular stackings of bent-core H-bonded (major) and covalent-bonded (minor) components with proper molar ratios of **m/n** (ca. 16/1~10/1).
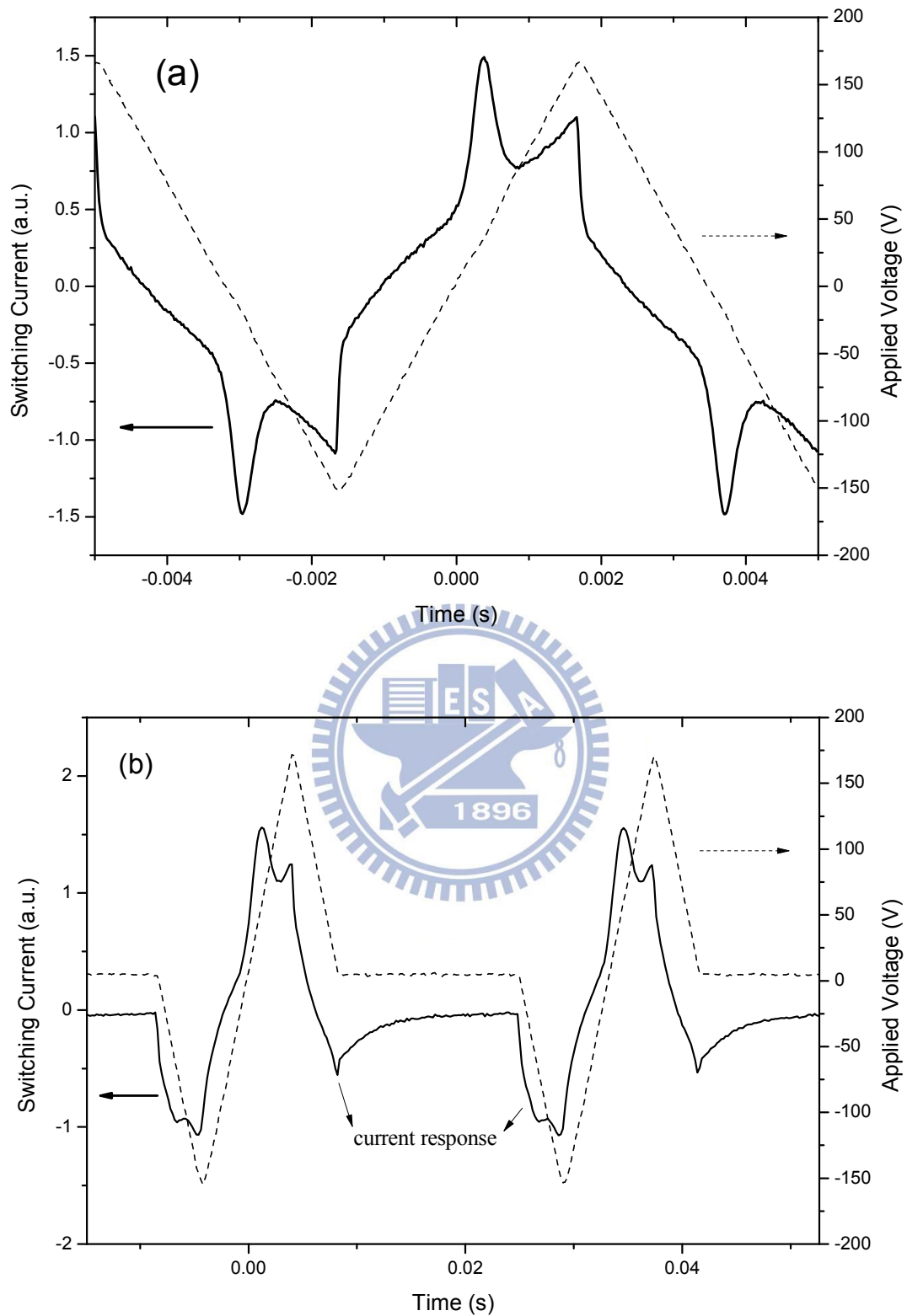
Figure 4.12. Switching current responses of polymer complex **A10B1-N** under (a) the triangular wave method (at Vpp = 310 V, f = 150 Hz, and T = 100 °C) and (b) the modified triangular wave method (at Vpp = 310 V, f = 30 Hz, and T = 100 °C).
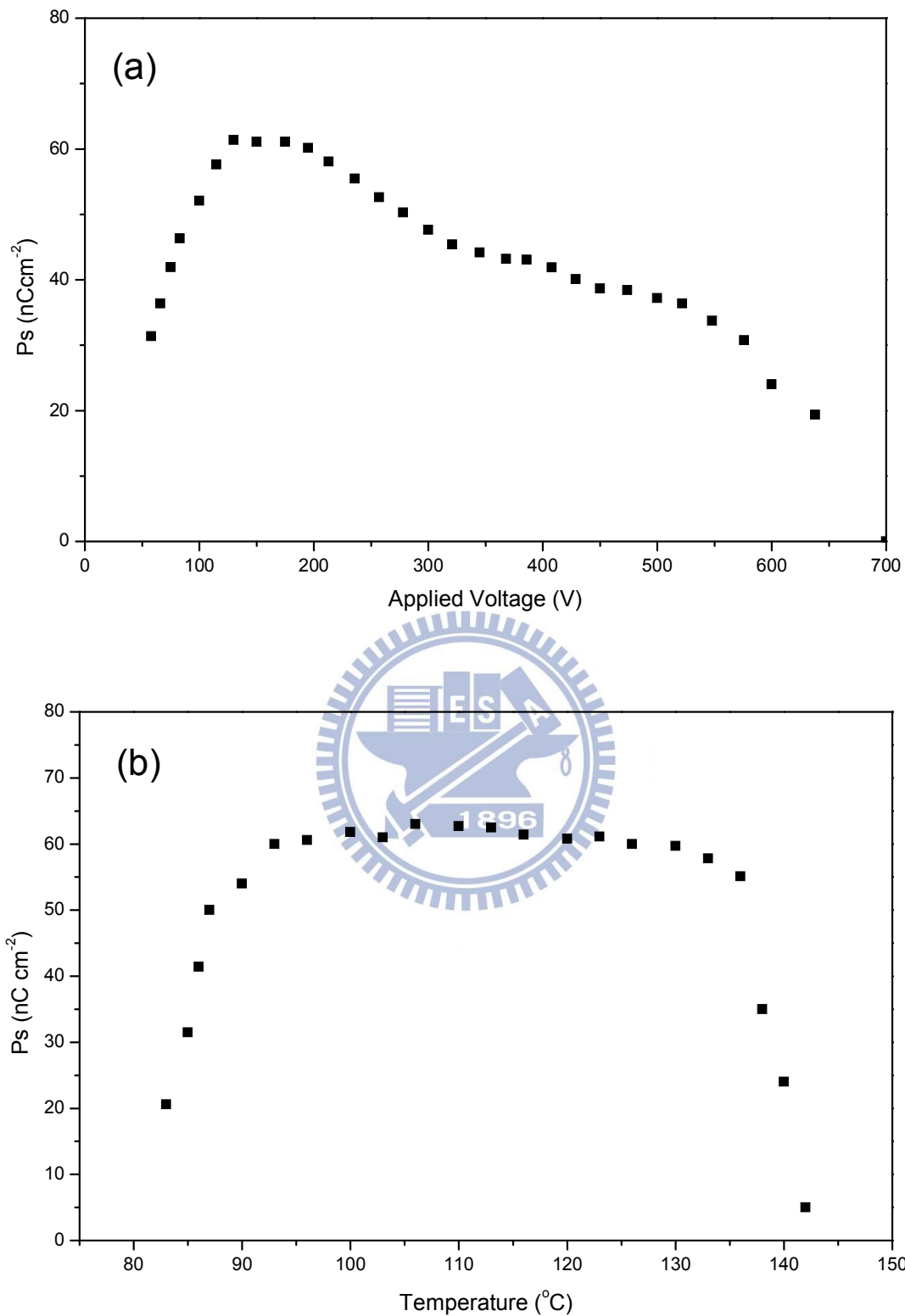
Figure 4.13. (a) Ps values of polymer complex **A10B1-N** as a function of applied voltages (at f = 60 Hz and T = 100 °C). (b) Ps values of polymer complex **A10B1-N** as a function of temperatures (at Vpp = 200 V and f = 200 Hz).

4.4. Conclusions

In summary, several novel side-chain banana-shaped liquid crystalline copolymers with various molar ratio of covalent- and H-bonded bent-core components were developed by the free radical polymerization and their polymer complexes were self-assembled by appropriate molar ratios of proton donor (H-donor) polymers and pyridyl proton acceptor (H-acceptor) bent-cores. The mesomorphic and electro-optical properties in the side-chain banana-shaped liquid crystalline polymers and their corresponding polymer complexes were influenced by the molar ratios of bent-core H-bonded components effectively. The voltage-dependent anti-ferroelectric properties of spontaneous polarization (Ps) values in the polar smectic phase of the supramolecular side-chain banana-shaped copolymers were also first observed in this study. Several kinds of nematic and tilted smectic phases were obtained in bent-core side-chain homopolymers/copolymers and polymer complexes, which depended on the **m**/**n** molar ratio (i.e., hydrogen- and covalent-bonded units). The nematic and tilted smectic phases were verified by XRD measurements, and the SmCP phase was further identified by the triangular wave method. Overall, the anti-ferroelectric behaviors of the polar semctic phase were introduced in bent-core side-chain polymer complexes **AmBn-N** by tuning the suitable **m**/**n** molar ratios in the range of 16/1 to 10/1. It would be seemingly summarized that strict packing conditions between each bent-core covalent-bonded unit were present to reduce molecular oscillating, but loose packing conditions between each bent-core H-bonded unit would induce molecular fluctuations and become dynamically unstable under electric fields. The polar switching behaviors were diminished if just only either bent-core covalent-bonded or H-bonded structures were organized in the side chains of polymers. Therefore, rigid bent-core covalent-bonded components uniformly dispersed and copolymerized among soft bent-core H-bonded ingredients in the side-chain polymers are necessary

for the polar switching behaviors. This study offers some valuable information to achieve the polar switching properties by blending bent-core host-guest supramolecular systems with a combination of low molecular weight molecules (as H-acceptors) and polymers (homopolymers/copolymers as H-donors), which could be utilized for supramolecular mixtures in the future.

4.5. Electronic Supplementary Information
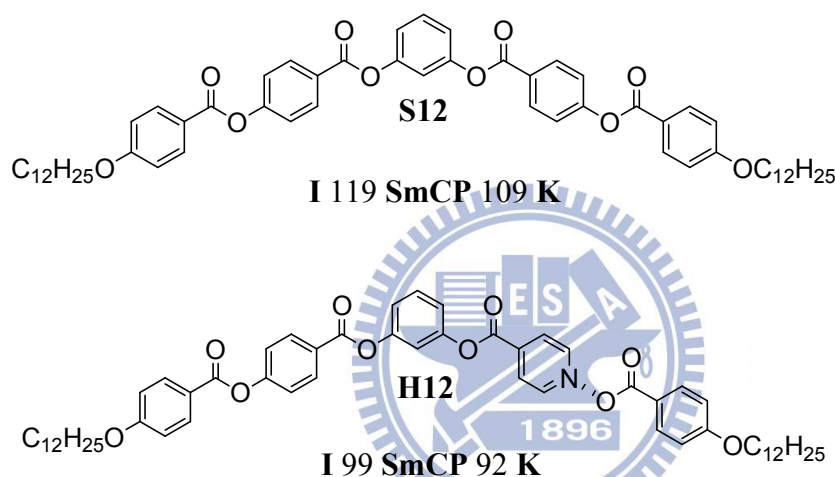
Figure S4.1. The single H-bonded five-ring banana-shaped supramolecule (complex **H12**) and fully covalent-bonded five-ring banana-shaped material (compound **S12**).
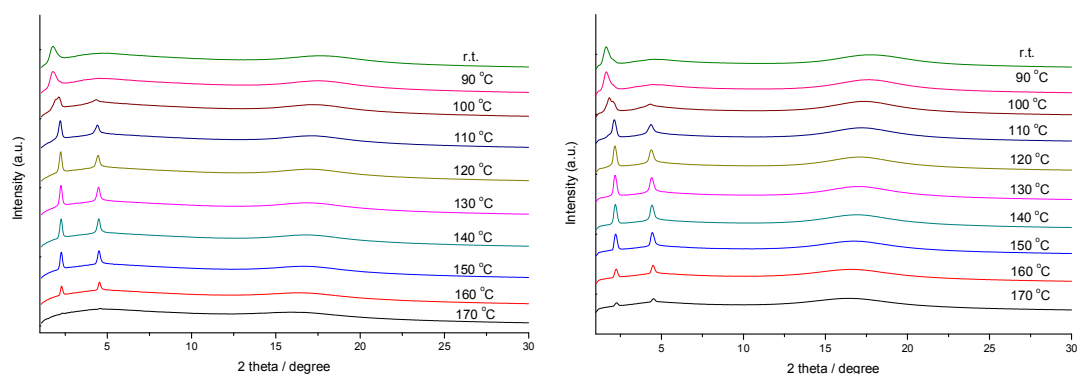
Figure S4.2. Powder X-ray diffraction intensity against angle profiles of (a) polymer **A1B0** and (b) complex polymer **A1B0-N** at various temperatures upon cooling from the isotropic to crystalline phases.
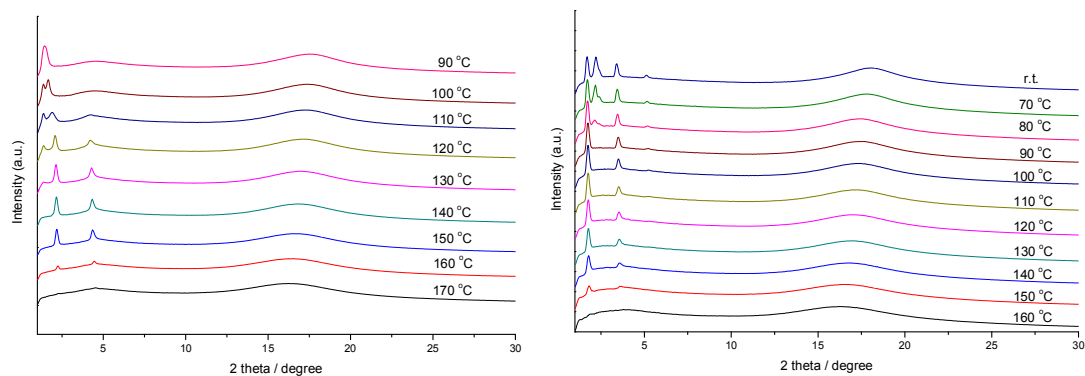
Figure S4.3. Powder X-ray diffraction intensity against angle profiles of (a) polymer **A16B1** and (b) complex polymer **A16B1-N** at various temperatures upon cooling from the isotropic to crystalline phases.
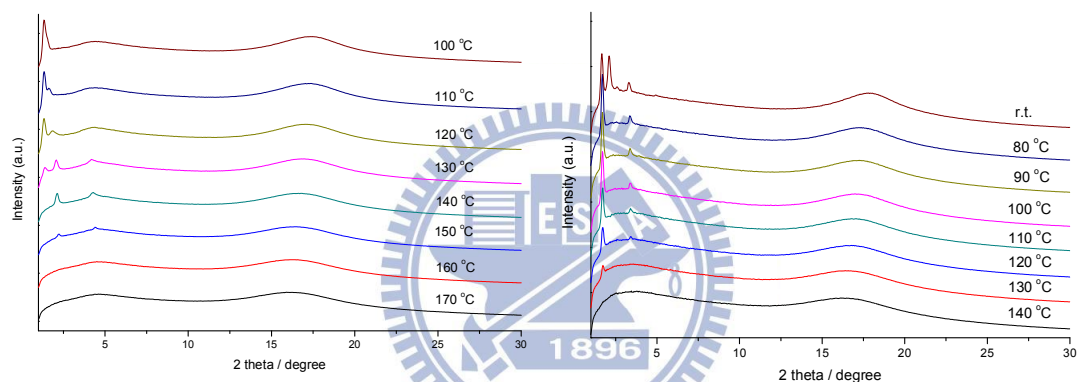
Figure S4.4. Powder X-ray diffraction intensity against angle profiles of (a) polymer **A10B1** and (b) complex polymer **A10B1-N** at various temperatures upon cooling from the isotropic to crystalline phases.
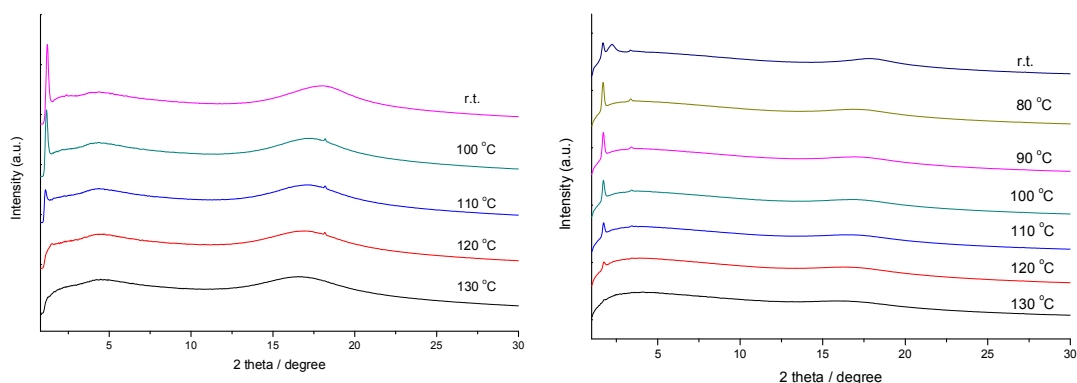
Figure S4.5. Powder X-ray diffraction intensity against angle profiles of (a) polymer **A4B1** and (b) complex polymer **A4B1-N** at various temperatures upon cooling from the isotropic to crystalline phases.
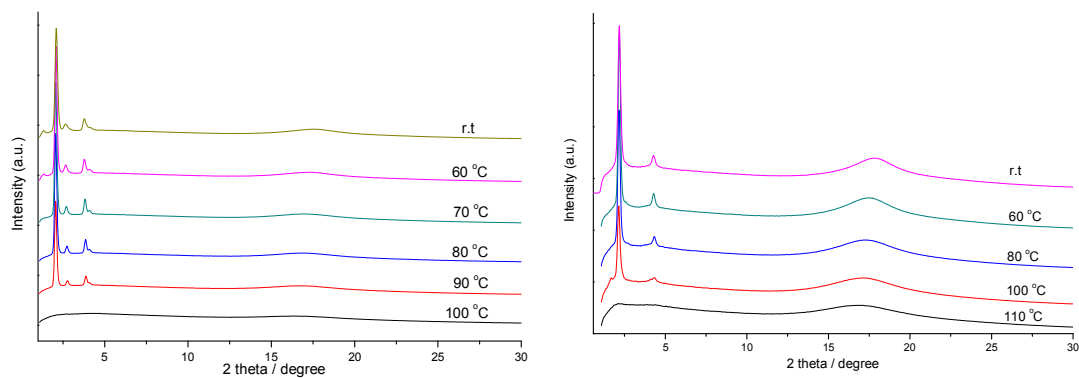
Figure S4.6. Powder X-ray diffraction intensity against angle profiles of (a) polymer **A1B2** and (b) complex polymer **A1B2-N** at various temperatures upon cooling from the isotropic to crystalline phases.
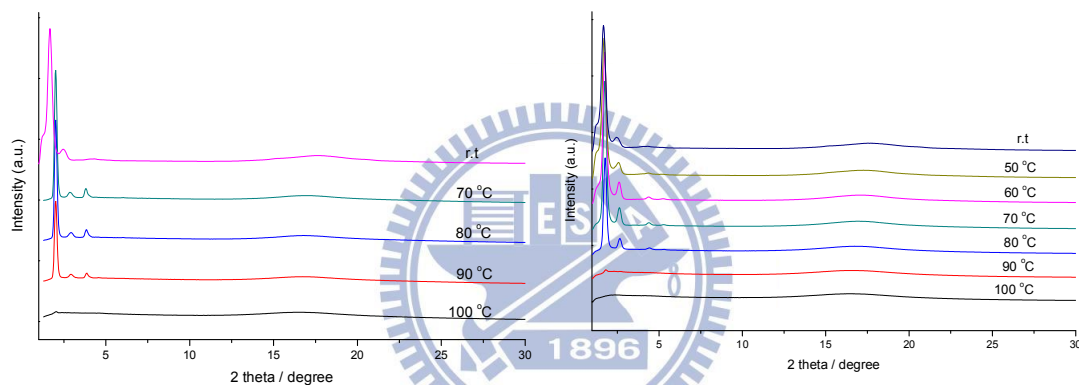
Figure S4.7. Powder X-ray diffraction intensity against angle profiles of (a) polymer **A1B5** and (b) complex polymer **A1B5-N** at various temperatures upon cooling from the isotropic to crystalline phases.
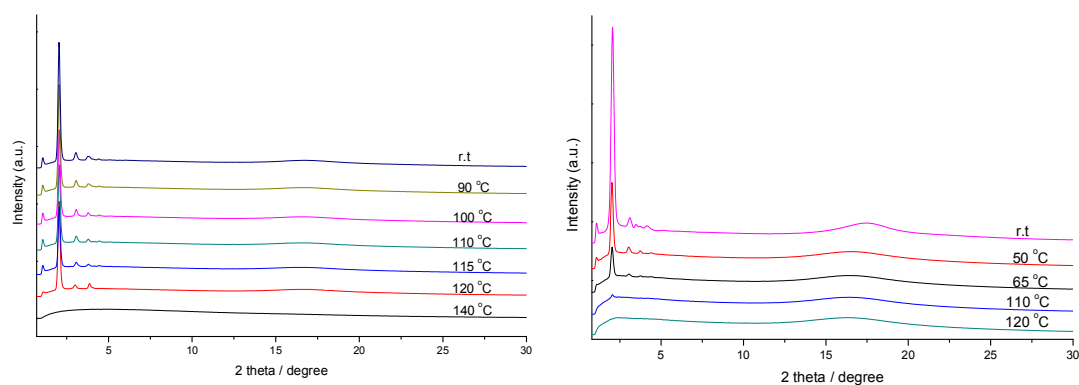
Figure S4.8. Powder X-ray diffraction intensity against angle profiles of (a) polymer **A1B13** and (b) complex polymer **A1B13-N** at various temperatures upon cooling from the isotropic to crystalline phases.
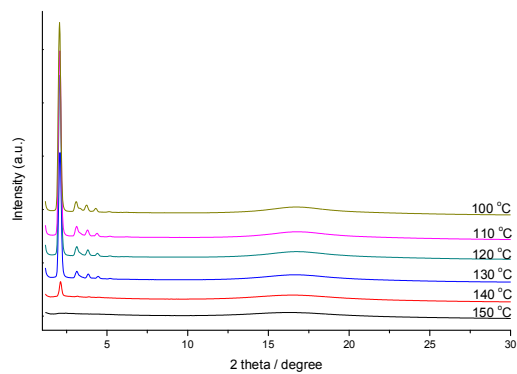
Figure S4.9. Powder X-ray diffraction intensity against angle profiles of polymer **A0B1** at various temperatures upon cooling from the isotropic to crystalline phases.
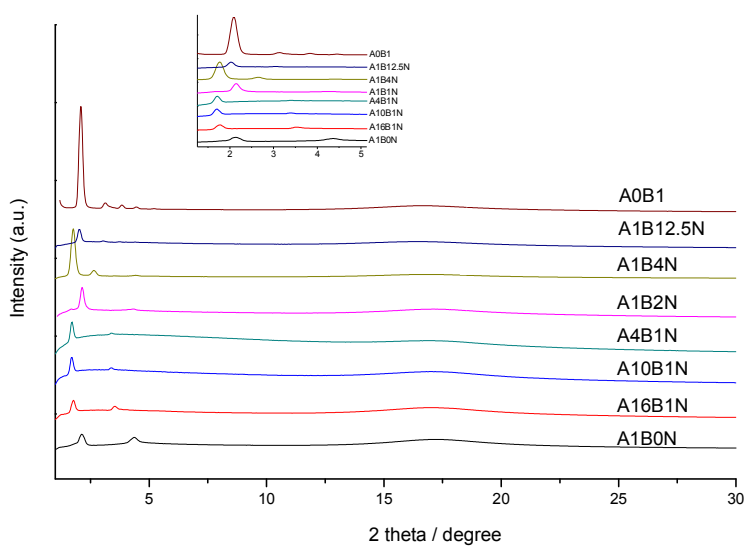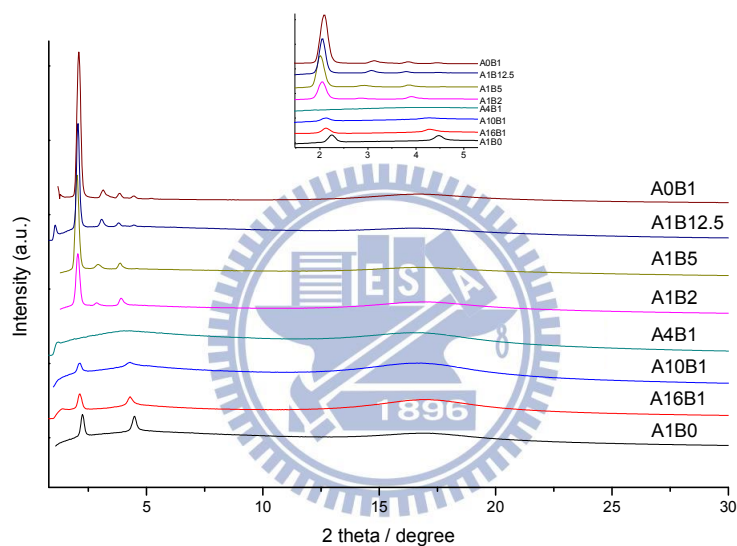

Figure S4.10. Powder X-ray diffraction intensity against angle profiles of (a) polymer **AmBn** and (b) complex polymer **AmBn-N**.

166

Chapter 5

Polymeric Dopant Effects of Bent-Core Covalent- and Hydrogen-Bonded Structures on Banana-Shaped Liquid Crystalline Complexes

5.1. Introduction

Liquid crystalline (LC) materials bearing banana-shaped mesogens become interesting topics duo to their special electro-optical properties, such as spontaneous polarized capabilities and nonlinear optics.[42,61] Based on various intermolecular arrangements, several kinds of special mesophases in accordance with banana-shaped (or bent-core) molecular designs with particular mesophases, including columnar stacking, tilted smectic, and three dimensional structures, named as B1 to B7 phases were developed and identified.[4] Traditionally, electro-optical switching behaviors were observed in the smectic B1, B2, B5, and B7 phases, where the B2 (SmCP) phase had been prevailingly investigated. Depending on the polar direction and molecular tilted direction in neighboring layers of the SmCP phase, ferroelectric (F) and antiferroelectric (A) states possessed identical/inverse polarizations and synclinic (S)/anticlinic (A) arrangements with alike/opposite molecular tilted aspects between layer to layer, respectively. Hence, four kinds of different supramolecular architectures denoted SmC_AP_A, SmC_SP_A, SmC_AP_F, and SmC_SP_F were recognized as homochiral (SmC_AP_A and SmC_SP_F) and racemic (SmC_SP_A and SmC_AP_F) conditions separately.[8] With respect to the bent-core molecular architectures, the traditional banana-shaped liquid crystals were generally formed by two bent-substituted rigid arms connected to a central cyclic ring (through polar or non-polar functional groups)

with a suitable bent angle and linking, where appropriate lengths of flexible chains were attached.[5] Among these bent-shaped modeling frameworks, the structural variations of achiral molecular designs, such as the central parts,[6] lateral substituents,[25a] linking groups,[62] terminal chains,[63] and the number of rings,[7] would affect their physical properties to different extents in small molecular systems. Recently, poly-molecular systems, i.e., dimeric,[31] main-chain polymeric,[32d] side-chain polymeric,[33a] and dendritic structures,[34b] were also developed to investigate the influence of molecular configurations on mesomorphic and electro-optical properties. Moreover, some novel supramolecular bent-core interactions or their nanocomposite architectures have been integrated into organic or inorganic parts to display special electro-optical characteristics, for instance, bent-core derivatives embedded with nanoparticles,[37] bent-core H-bonded supramolecules,[38] and bent-core structures with silyl and siloxyl linkages.[21]

To retain the electro-optical switching behavior in the bent-core structures is constantly the important assignment in the field of banana-shaped LC research. However, even if many kinds of bent-core small molecular systems displayed particular polar switching current behaviors, duo to the higher viscosities and larger inter-/intra-molecular interactions in polymers, such switching current behaviors were not easy to be obtained (or detected) in analogous bent-core polymer derivatives.[33b-c,64] Interestingly, the switching current behavior of the SmCP phase in the monomeric units was sustained and the ferro-electricity could be modified by the polymer structural design of dimethylsiloxane diluted polysiloxane side-chain copolymer frameworks.[33a] According the previous works, bent-core H-bonded small molecules could yield lower mesophasic transition temperatures, enthalpies, and threshold voltages than those of fully covalent-bonded five-ring banana-shaped molecular analogues and H-bonded side-chain polymeric derivatives, which

suggested that softer bent-core intermolecular arrangements were present in both H-bonded and small molecular designs.[2,38a,39] Regarding the small molecular systems containing two different fully covalent-bonded components, unusual molecular arrangements and mesomorphic behaviors were developed by blending rod-like liquid crystals with bent-core LC dopants.[65] Meanwhile, the blended polymeric systems (mainly side-chain polymers) were expanded by doping,[60] copolymerization,[66] and H-bonded complexation[67] with chiral/achiral liquid crystalline components to induce the particular mesomorphic and electro-optical properties.

As shown in Figure 5.1, in order to investigate the polymeric dopant effects of bent-core covalent- and H-bonded structures on the mesomorphic and electro-optical properties of banana-shaped LC complexes, two series of H-bonded complexes **HPm/CBn** (i.e., bent-core H-bonded side-chain homopolymer **HP** mixed with bent-core covalent-bonded small molecule **CB**) and **CPm/HBn** (i.e., bent-core covalent-bonded side-chain homopolymer **CP** mixed with bent-core H-bonded small molecular complex **HB**) with various **m/n** molar ratios (**m/n** = 15/1, 10/1, 15/1, 1/1, 1/5, 1/10, and 1/15) were developed. The mesomorphic and electro-optical properties of the H-bonded complexes were investigated and characterized by polarizing optical microscopy (POM), differential scanning calorimetry (DSC), powder X-ray diffraction (XRD), and electro-optical (EO) switching current experiments. Herein, the polar smectic (SmC$_A$P$_A$) phase with switching current behavior (or spontaneous polarization) was introduced and stabilized in some of the banana-shaped LC H-bonded complexes **HPm/CBn** and **CPm/HBn** by blending various **m/n** molar ratios of soft H-bonded bent-core moieties with rigid covalent-bonded bent-core moieties, where one of the moieties was homopolymerized as side-chain H-bonded homopolymer (**HP**) or covalent-bonded homopolymer (**CP**), respectively. Finally,

their mesophasic ranges and spontaneous polarization (Ps) values could be adjusted by the **m/n** molar ratios (polymeric moieties vs. small molecular moieties) in the banana-shaped LC H-bonded complexes **HPm/CBn** and **CPm/HBn**.
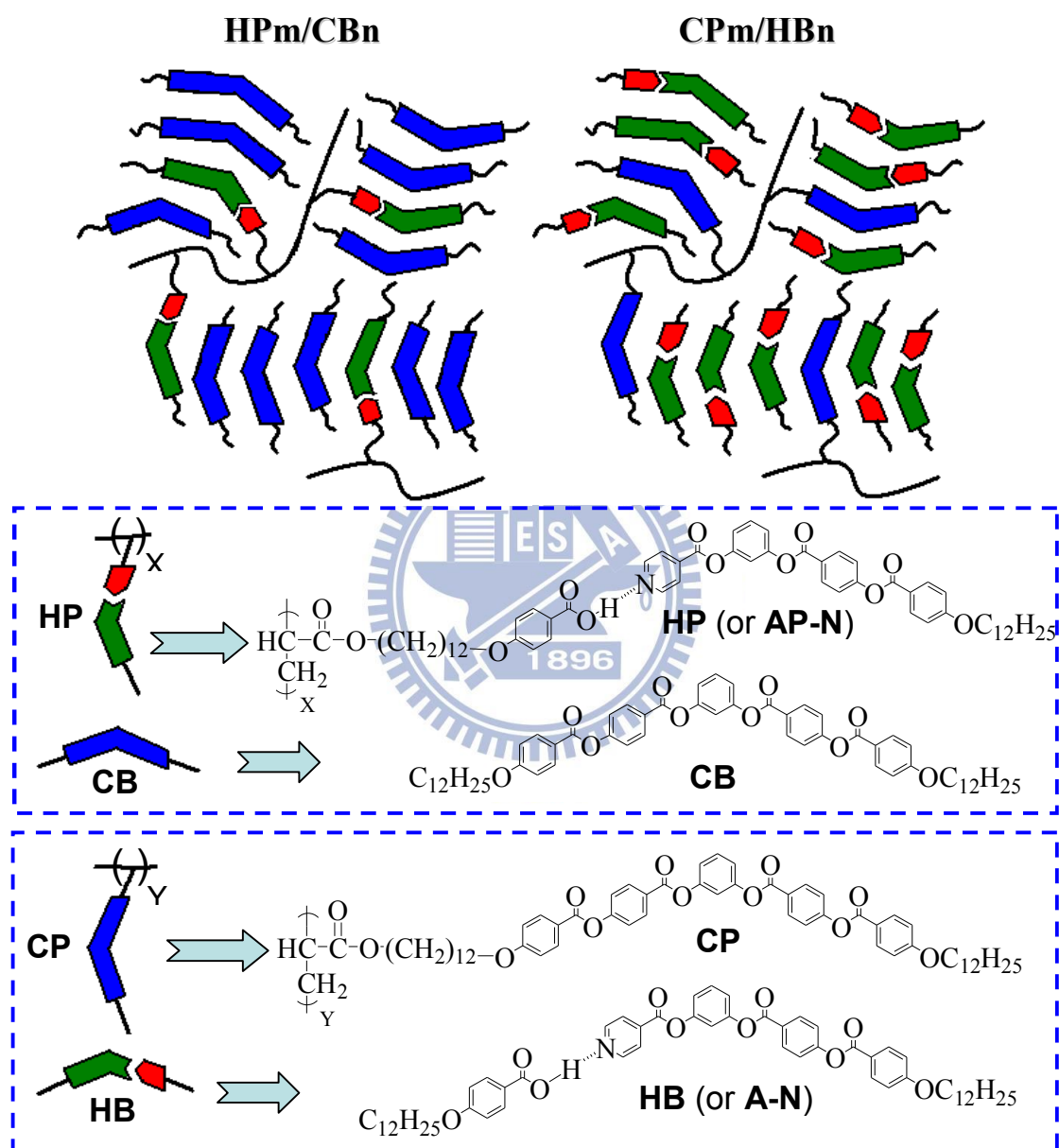
Figure 5.1. Chemical structures of banana-shaped LC H-bonded complexes **HPm/CBn** and **CPm/HBn** (where **m/n** = 15/1, 10/1, 15/1, 1/1, 1/5, 1/10, and 1/15) and their composing H-bonded and covalent-bonded bent-core side-chain homopolymers (**HP** and **CP**, respectively) as well as H-bonded and covalent-bonded bent-core small molecules (**HB** and **CB**, respectively).

5.2. Eeperimental

5.2.1. Methods

^{1}H NMR spectra were recorded on a Varian Unity 300 MHz spectrometer using d_6-dioxane and $CDCl_3$ as solvents and mass spectra were determined on a Micromass TRIO-2000 GC-MS. Elemental analyses (EA) were performed on a Heraeus CHN-OS RAPID elemental analyzer. Gel permeation chromatography (GPC) analyses were conducted on a Waters 1515 separation module using polystyrene as a standard and THF as an eluant. Mesophasic textures were characterized by polarizing optical microscopy (POM) using a Leica DMLP equipped with a hot stage. Infrared (IR) spectra were investigated by Perk-Elmer Spectrum 100 instrument. Temperatures and enthalpies of phase transitions were determined by differential scanning calorimetry (DSC, model: Perkin Elmer Pyris 7) under N_2 at a heating and cooling rate of 10 °Cmin^{-1}. Synchrotron powder X-ray diffraction (XRD) measurements were performed at beamline BL17A of the National Synchrotron Radiation Research Center (NSRRC), Taiwan, where the wavelength of X-ray was 1.33366 Å. The powder samples were packed into a capillary tube and heated by a heat gun, whose temperature controller was programmable by a PC with a PID feedback system. The scattering angle theta was calibrated by a mixture of silver behenate and silicon. The electro-optical properties were determined in commercially available ITO cells (from Mesostate Corp., thickness = 4.25 μm, active area = 1 cm^2) with rubbed polyimide alignment coatings (parallel rubbing direction). A digital oscilloscope (Tektronix TDS-3012B) was used in these measurements, and a high power amplifier connected to a function generator (GW Model GFG-813) with a d.c. power supply (Keithley 2400) was utilized in the d.c. field experiments. During electro-optical measurements, the modulations of textures by applying electric fields were observed by POM.

5.2.2. Synthesis of Monomers

All synthetic procedures of monomers **A'** (H-donor monomer) and **B'** (bent-core covalent-bonded monomer) as well as pyridyl H-acceptor **N** are demonstrated in Scheme S1 of the supporting information. The synthetic details of all compounds in Scheme S1 are shown in the supporting information.

5.2.3. Synthesis of Polymers (H-donor homopolymer AP and covalent-bonded homopolymer CP) and Preparation of H-Bonded Complexes (HPm/CBn and CPm/HBn)

The side-chain proton donor (H-donor) homopolymer **AP** and bent-core covalent-bonded homopolymer **CP** were carried out by free radical coupling reactions of monomers **A'** and **B'**, respectively, with initiator 2,2'-azobis-isobutyronitrile (AIBN) in Scheme 1. All reactions were proceeded in dry THF solvent under N_2 at the reflux temperature for 24 hours. The accomplished organic liquid was dropped into strong stirring diethyl ether (EA) solvent to precipitate products, which were purified again by THF and EA to acquire pure compounds. The H-bonded complexes (**HPm/CBn** and **CPm/HBn**) were constructed by blending appropriate molar ratios of proton donors **AP** (H-donor polymers) and acceptors **N** (H-acceptors) in the solutions of chloroform/THF (ca. 1:1 vol.), which were self-assembled into supramolecules by evaporating solvents slowly. Hence, two series of H-bonded complexes **HPm/CBn** (**HP15/CB1**, **HP10/CB1**, **HP5/CB1**, **HP1/CB1**, **HP1/CB5**, **HP1/CB10** and **HP1/CB15**) and **CPm/HBn** (**CP15/HB1**, **CP10/HB1**, **CP5/HB1**, **CP1/HB1**, **CP1/HB5**, **CP1/HB10** and **CP1/HB15**) with various **m/n** molar ratios (**m/n** = 15/1, 10/1, 5/1, 1/1, 1/5, 1/10, and 1/15) were prepared.
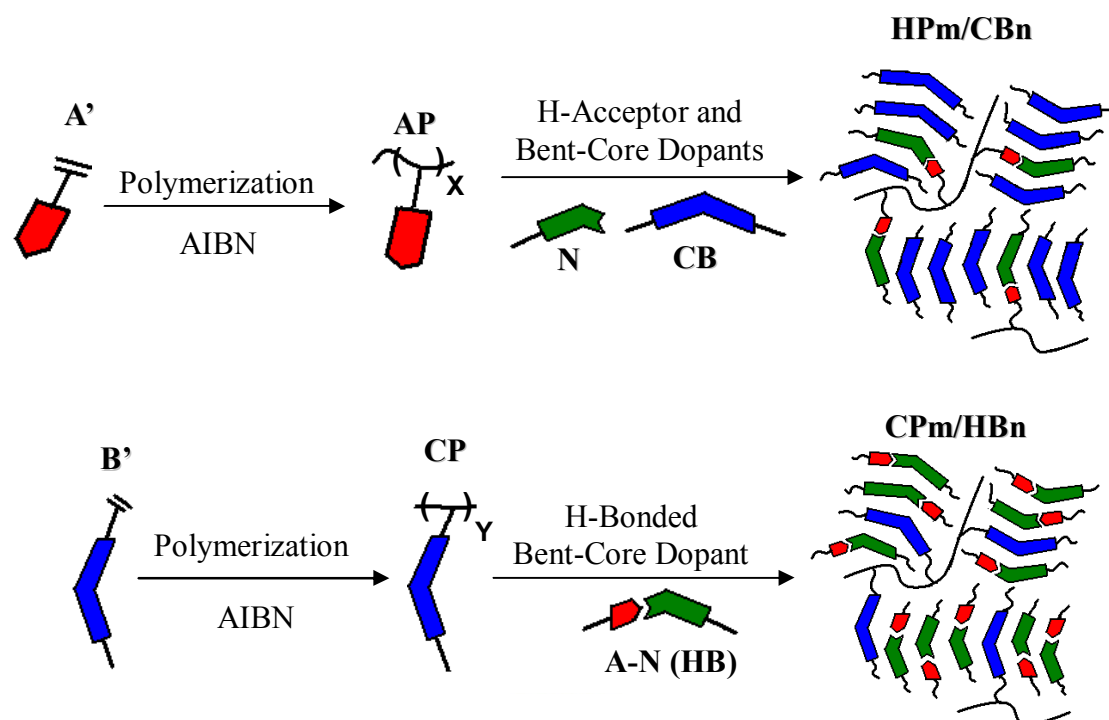
Scheme 5.1. Homopolymerization and complexation of banana-shaped LC H-bonded complexes **HPm/CBn** and **CPm/HBn**.

5.3. Results and Disscussion

5.3.1. Polymer Characterization

In order to identify the chemical structures of all components in this study, the side-chain proton donor (H-donor) homopolymer **AP** and bent-core covalent-bonded homopolymer **CP** along with their corresponding monomeric moieties **A'** (H-donor monomer) and **B'** (bent-core covalent-bonded monomer) were characterized by ^{1}H NMR measurements. Both monomers **A'** and **B'** were confirmed by the resonant peaks in the chemical shift range of 5.7-6.4 ppm, which belong to the signals of acryl groups and demonstrate in Figure S5.1a of the supporting information. However, the chemical shift peaks in the range of 5.7-6.4 ppm were disappeared in the corresponding side-chain polymers **AP** and **CP** to prove the complete polymerization of monomers **A'** and **B'** (see Figure S5.1b). Compared with monomers **A'** and **B'**, the resonant peaks (a and b) of H-donor polymer **AP** in the range of 6.6 ppm to 8.5 ppm

(attributed to aromatic rings) did not shift clearly, and the resonant peaks (c, d, e, f, g, h, and i) of bent-core covalent-bonded homopolymer **CP** belonged to the five bent-core benzoic rings as those of monomer **B'**. Furthermore, the number average molecular weights (Mn) and polydispersity index (PDI) values measured by GPC experiments for side-chain polymers **AP** and **CP** were 5.1×10^3 (with PDI = 1.13) and 12.7×10^3 (with PDI = 1.29), respectively.

5.3.2. IR Characterization

The existence and stability of H-bonds in side-chain polymeric H-bonded complex **HP** (i.e., **AP-N**: H-donor homopolymer **AP** supramolecularly complexed with H-acceptoror **N**) and small molecular H-bonded complex **HB** (i.e., **A-N**: H-donor **A** supramolecularly complexed with H-acceptor **N**) were characterized by IR spectra. The IR spectra of H-bonded complexes **HP** (i.e., polymeric complex **AP-N**) and **HB** (i.e., small molecular complex **A-N**) and their corresponding H-acceptor **N**, H-donor **A**, and H-donor homopolymer **AP** in Figure 5.2 were compared to examine the existence of H-bonds. In contrast to the O-H band of pure H-donor homopolymer **AP** at 2555 cm^{-1} in Figure 5.2a, weaker O-H bands observed at 2515 and 1926 cm^{-1} in side-chain polymeric H-bonded complex **HP** (i.e., **AP-N**) were indicative of hydrogen bonding between the acidic groups of H-donor homopolymer **AP** and the pyridyl groups of H-acceptor **N**.[39] As shown in Figure 5.2b, the formation of H-bonds between H-donor **A** and H-acceptor **N** was also confirmed in small molecular H-bonded complex **HB** (i.e., **A-N**), where O-H bands of H-bonded complex **HB** observed at 2536 and 1912 cm^{-1} were weaker than that of pure H-donor **A** observed at 2556 cm^{-1}. These results suggested that supramolecular frameworks of H-bonded complexes **HP** (i.e., **AP-N**) and **HB** (i.e., **A-N**) were formed by acid H-donor polymer **AP** and H-donor **A**, respectively, with pyridyl H-acceptor **N**.
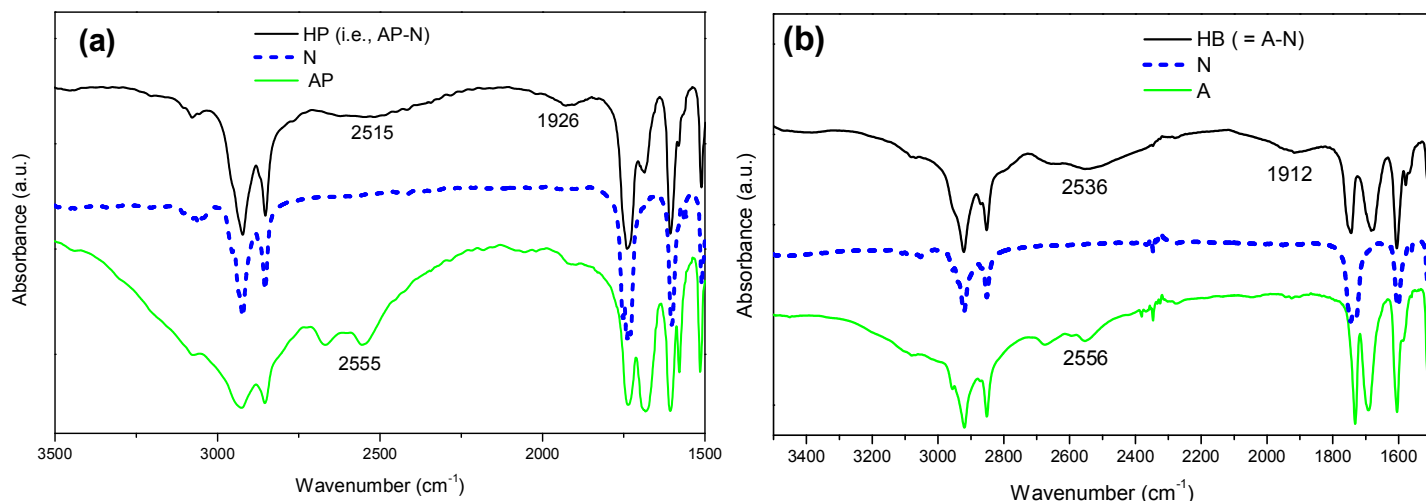
Figure 5.2. IR spectra of (a) H-bonded bent-core side-chain polymer complex **HP** and its components **N** (H-acceptor) and **AP** (H-donor homopolymer), and (b) H-bonded bent-core small molecular complex **HB** and its components **N** (H-acceptor) and benzoic acid derivative **A** (H-donor).

5.3.3. Mesophasic and Thermal Properties of Banana-Shaped H-Bonded Complexes HPm/CBn and CPm/HBn

In order to investigate the polymeric dopant effects of covalent- and H-bonded structures on banana-shaped H-bonded complexes, the mesomorphic and thermal properties of H-bonded complexes **HPm/CBn** and **CPm/HBn** with various **m/n** molar ratios (i.e., 15/1, 10/1, 5/1, 1/1, 1/5, 1/10 and 1/15) were investigated by POM and DSC measurements. The thermal properties and phase behaviors of banana-shaped LC H-bonded complexes **HPm/CBn** and **CPm/HBn** are illustrated in Figures 5.3-5.4 and Tables 5.1-5.2. Banana-shaped H-bonded complexes **HPm/CBn** (i.e., bent-core H-bonded side-chain homopolymer **HP** mixed with bent-core covalent-bonded small molecule **CB**) mostly possessed the enantiotropic tilted smectic (SmC) phases, which were verified by POM to show the grainy domain, schlieren, and fan-like textures. For instance, the grainy domain of H-bonded complex **HP5/CB1** is demonstrated in Figure 5.3a, and H-bonded complexes **HPm/CBn** (**m/n** = 15/1, 10/1, 5/1, 1/1, and 1/5) exhibited the similar mesophasic type to indicate the
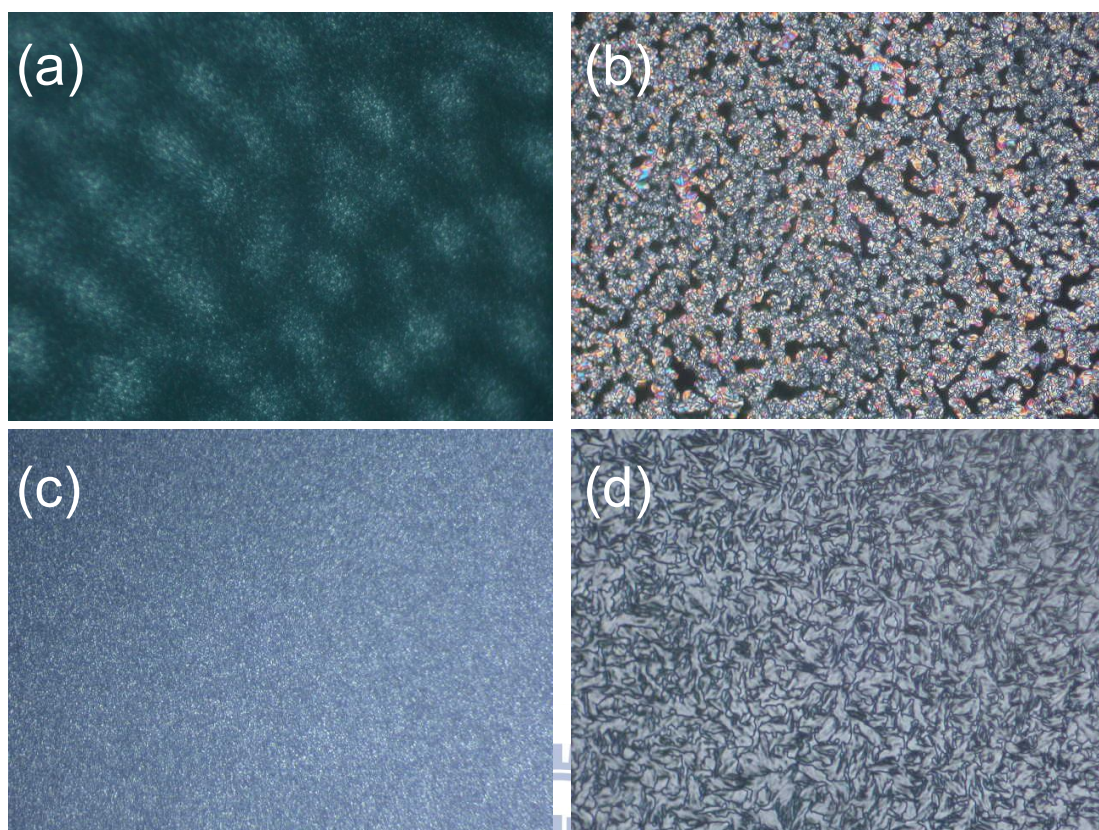
Figure 5.3. POM textures at the cooling process: (a) the tilted smectic phase with grainy domain and birefringence of H-bonded complex **HP5/CB1** at 100 °C; (b) the polar smectic phase with schlieren and fan-like textures of H-bonded complex **HP1/CB15** at 90 °C; (c) the tilted smectic phase with birefringence of H-bonded complex **CP1/HB5** at 80 °C; (d) the polar smectic phase with schlieren and fan-like textures of H-bonded complex **CP1/HB15** at 90 °C.

tilted smectic phase. Regarding H-bonded complexes **HP1/CB10** and **HP1/CB15** with low **m/n** molar ratios, an enantiotropic polar smectic phase (SmCP) was obtained as that of bent-core covalent-bonded small molecule **CB**, but H-bonded complexes **HP1/CB10** and **HP1/CB15** possessed lower melting and isotropization temperatures. The schlieren and fan-like textures of H-bonded complex **HP1/CB15** as characteristic textures of the SmCP phase are shown in Figure 5.3b. Comparing all phase transition temperatures of H-bonded complexes **HPm/CBn** in Table 5.1 and Figure 5.4a, side-chain H-bonded homopolymer **HP** (i.e., **AP-N**) revealed the highest isotropization temperatures and the widest mesophasic range (the SmC phase), and

some H-bonded complexes **HPm/CBn** (as **m/n** = 1/10 and 1/15) with less polymeric dopants exhibited lower isotropization temperatures than that of bent-core covalent-bonded molecule **CB** (see Figure 5.4a). In addition, only H-bonded complexes **HP1/CB10** and **HP1/CB15** doped with less polymeric configurations (alike bent-core covalent-bonded small molecule **CB**) would display the SmCP phase and the lowest isotropization temperatures. Therefore, the SmCP phase in bent-core compound **CB** was stabilized by H-bonded complexes **HPm/CBn** (**m/n** = 1/10 and 1/15) with less H-bonded homopolymeric dopants, but it was replaced with the tilted smectic phase in H-bonded complexes **HPm/CBn** (**m/n** = 15/1, 10/1, 5/1, 1/1, and 1/5) with higher amounts of polymeric frameworks, which was favored by bent-core H-bonded side-chain homopolymer **HP**.

With respect to banana-shaped H-bonded complexes **CPm/HBn** (i.e., bent-core covalent-bonded side-chain homopolymer **CP** mixed with bent-core H-bonded small molecular complex **HB**), the mesophase was not clearly acquired in most H-bonded complexes **CPm/HBn** (including **m/n** = 15/1, 10/1, 5/1, and 1/1). However, the birefringence of an enantiotropic tilted smectic phase was recovered in H-bonded complex **CP1/HB1** (see Figure 5.3c). In addition, the polar smectic (SmCP) phase of H-bonded complexes **CP1/HB10** and **CP1/HB15** was acquired as that of bent-core H-bonded small molecular complex **HB** (i.e., **A-N**), which were clarified by the schlieren and fan-like textures of **CP1/HB15** as shown in Figure 5.3d. Comparing the phase transition temperatures of H-bonded complexes **CPm/HBn** and their corresponding components **CP** (bent-core covalent-bonded polymer) and **HB** (bent-core H-bonded molecular complex) illustrated in Table 5.2 and Figure 5.4b, the isotropization temperatures of all H-bonded complexes **CPm/HBn** were lower than that of polymer **CP**, and some H-bonded complexes **CPm/HBn** (as **m/n** = 1/5, 1/10, and 1/15) with less polymeric dopants exhibited lower isotropization temperatures

than that of H-bonded molecular complex **HB** (see Figure 5.4b). Therefore, the SmCP

phase in bent-core H-bonded molecular complex **HB** was stabilized by H-bonded

complexes **CPm/HBn** (**m/n** = 1/10 and 1/15) with less polymeric dopants, but it was

replaced with the tilted smectic phase or even became non-mesomorphic in H-bonded

complexes **CPm/HBn** (**m/n** = 15/1, 10/1, 5/1, 1/1, and 1/5) with higher amounts of

polymeric frameworks.

Table 5.1. Phase Transition Temperatures and Enthalpies of Banana-Shaped
H-Bonded Complexes, Side-Chain H-Bonded Homopolymer **HP** (i.e., **AP-N**), and
Bent-Core Covalent-Bonded Molecule **CB**

Complex/ compound	Phase transition temperature/°C [Enthalpy/kJ/g] Heating(up) / Cooling (down)
HP	**Cr** 96.3 [3.0] **SmC** 162.2 [22.4] **Iso** **Iso** 155.1 [-27.5] **SmC** 76.2 [-4.5] **Cr**
HP15/CB1	**Cr** 92.5(4.7) **SmC** 120.1(8.8) **Iso** **Iso** 120.4(-13.1) **SmC** 74.7(-3.7) **Cr**
HP10/CB1	**Cr** 91.5(-6.7) **SmC** 118.3(-10.5) **Iso** **Iso** 119.4(-17.1) **SmC** 71.5(-5.2) **Cr**
HP5/CB1	**Cr** 90.3 (14.5) **SmC** 117.6(11.1) **Iso** **Iso** 115.4(-20.1) **SmC** 74.7(-11.0) **Cr**
HP1/CB1	**Cr** 98.3(27.0)**SmC** 127.0(10.0)**Iso** **Iso** 124.5(-10.4) **SmC** 96.8(-16.9) **Cr**
HP1/CB5	**Cr** 96.2 (24.8) **SmC** 128.3(9.2) **Iso** **Iso** 125.3(-12.7) **SmC** 95.4(-13.7) **Cr**
HP1/CB10	**Cr** 97.8 (67.0) **SmCP** 118.2 (19.2) **Iso** **Iso** 96.1(-16.9)**SmCP** 73.7(-43.7) **Cr**
HP1/CB15	**Cr** 100.3(46.3) **SmCP** 110.5(14.8) **Iso** **Iso** 105.7(-19.8) **SmCP** 76.7 (-47.9) **Cr**
CB	**Cr** 101.7 (73.5) **SmCP** 115.4 (44.2) **Iso** **Iso** 112.7 (-43.8) **SmCP** 83.3 (-73.7) **Cr**

The phase transitions were measured by DSC at the 2nd scan with a cooling rate of 5
°C/min. I = isoptropic state; SmC = tilted smectic phase; SmCP = polar smectic phase;
K = crystalline state.

Table 5.2. Phase Transition Temperatures and Enthalpies of Banana-Shaped
H-Bonded Complexes, Bent-Core Covalent-Bonded Side-Chain Homopolymer **CP**,
and H-Bonded Small Molecular Complex **HB**

Complex/ compound	Phase transition temperature/°C [Enthalpy/kJ/g] Heating(up) / Cooling (down)
CP	**Cr** 136.3(23.5) **SmC** 150[b] **Iso** **Iso** 148[b] **SmC** 130(-19.4) **Cr**
CP15/HB1	**Cr** 124.2(26.0) **Iso** **Iso** 119.7(-27.6) **Cr**
CP10/HB1	**Cr** 122.6 (38.3) **Iso** **Iso** 116.7(-39.9) **Cr**
CP5/HB1	**Cr** 119.9(32.7) **Iso** **Iso** 114.7(-28.5) **Cr**
CP1/HB1	**Cr** 121.8(33.7) **Iso** **Iso** 116.2(-27.2) **Cr**
CP1/HB5	**Cr** 83.3(13.7) **SmC** 95.5(19.4) **Iso** **Iso** 95.0(-36.7) **SmC** 72.0(-15.9) **Cr**
CP1/HB10	**Cr** 84.6(19.1) **SmCP** 98.1(39.8) **Iso** **Iso** 95.5(-47.9) **SmCP** 77.8(-19.5) **Cr**
CP1/HB15	**Cr** 89.2(17.6) **SmCP** 99.3(56.5) **Iso** **Iso** 96.8(-45.2) **SmCP** 80.8(-15.9) **Cr**
HB	**Cr** 107.2(79.0) **SmCP** 110.1[a] **Iso** **Iso** 109.6(-35.4) **SmCP** 90.7 (-16.2) **Cr**

The phase transitions were measured by DSC at the 2nd cooling scan with a cooling rate of 5 °C/min. I = isoptropic state; SmC = tilted smectic phase; SmCP = polar smectic phase; K = crystalline state. [a] the enthalpy values of two overlapped transition peaks. [b] the temperature was observed by POM.

Overall, due to the stronger intermolecular interactions and tighter stackings of covalent- and H-bonded bent-cores in homopolymers (**CP** and **HP**, respectively), bent-core homopolymers **CP** and **HP** had higher isotropization temperatures than their H-bonded complexes **HPm/CBn** and **CPm/HBn**. The looser molecular stackings of H-bonded complexes **HPm/CBn** and **CPm/HBn** provided H-bonded complex systems (as **m/n** = 1/10 and 1/15 possessing less polymeric dopants) with

suitable disordered arrangements of both covalent- and H-bonded structures to stabilize the SmCP phase, which would induce lower transition temperatures (and possibly wider mesophasic ranges) as well as tunable Ps values (to be shown later) in the proper polymeric molar ratios of banana-shaped H-bonded complexes.
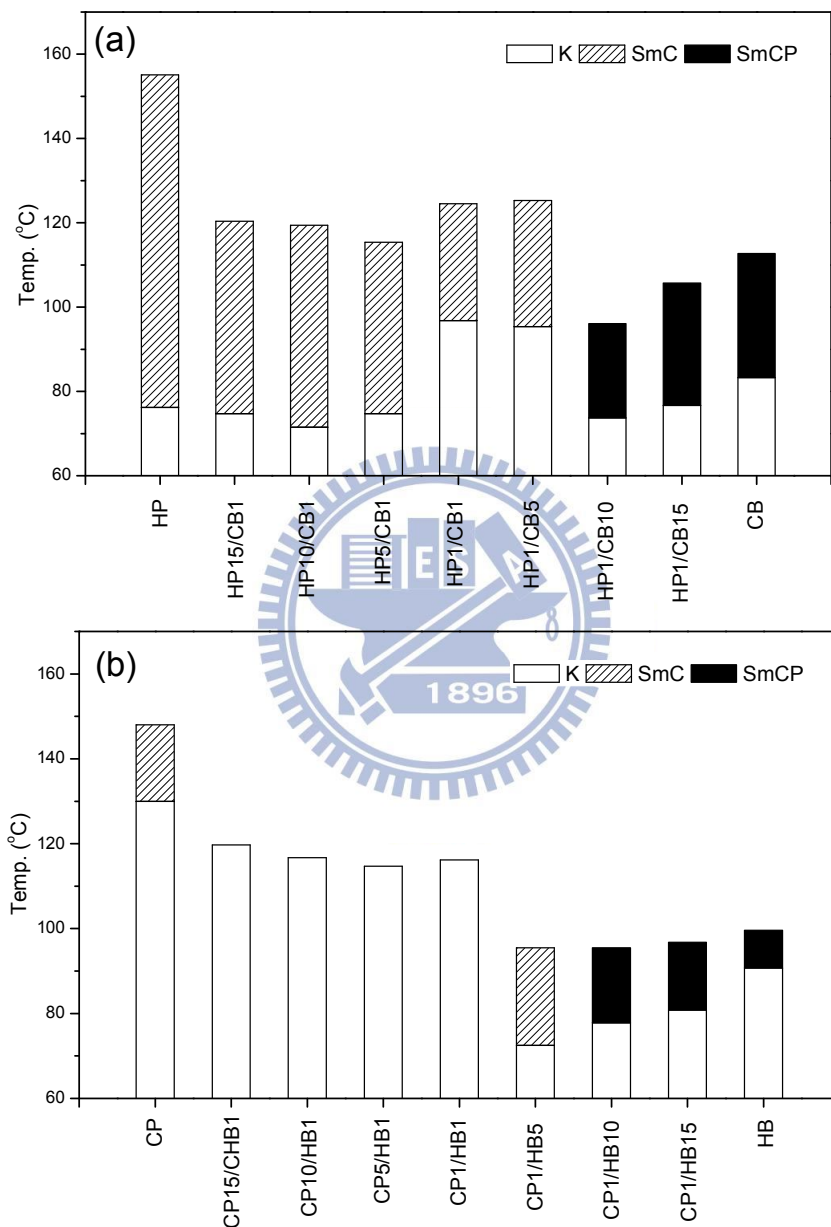
Figure 5.4. Phase diagrams (upon 2nd cooling): (a) banana-shaped H-bonded complexes **HPm/CBn**, consisting of side-chain H-bonded homopolymer **HP** (i.e., **AP-N**) and bent-core covalent-bonded molecule **CB**; (b) banana-shaped H-bonded complexes **CPm/HBn**, consisting of covalent-bonded side-chain homopolymer **CP** and H-bonded small molecular complex **HB**.
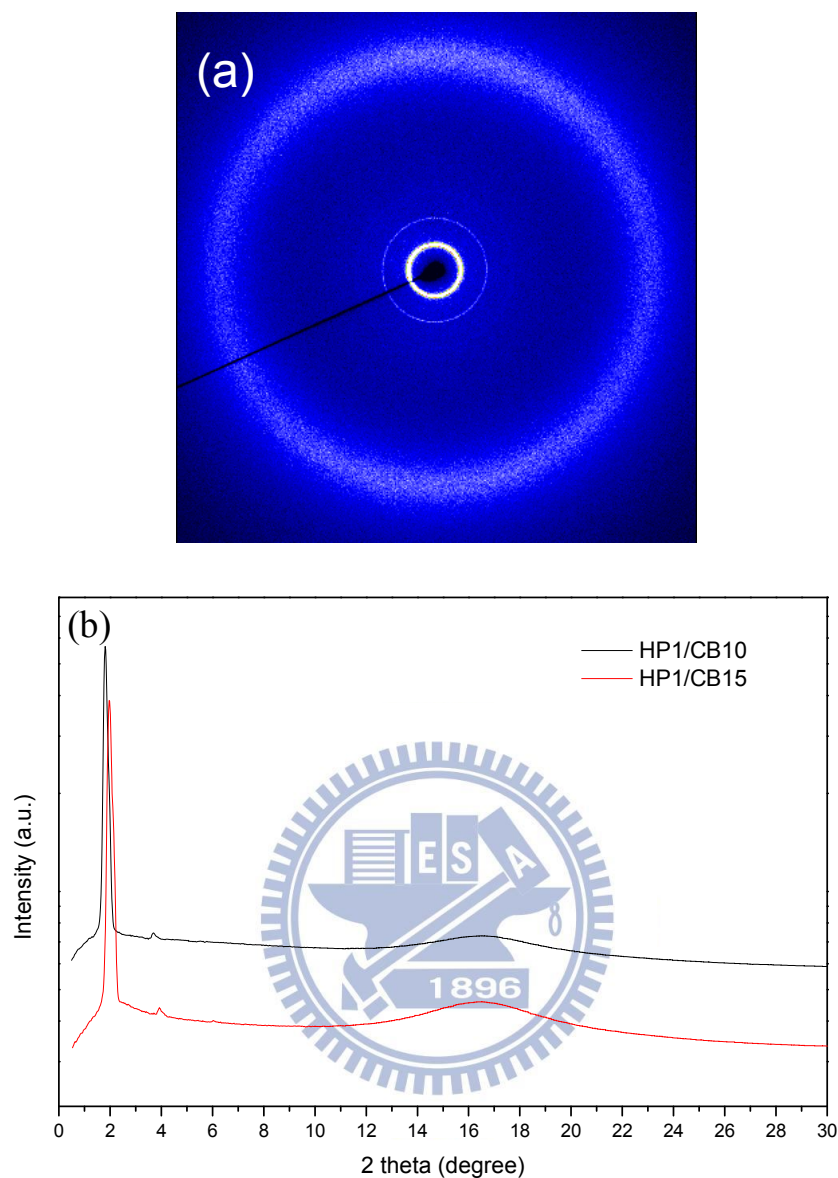
Figure 5.5. (a) Powder X-ray 2D pattern of H-bonded complex **HP1/CB10** (at 80 °C cooling); (b) Powder X-ray diffraction intensities against angle profiles of H-bonded complexes **HP1/CB10** and **HP1/CB15** in the polar smectic phase (at 90 °C cooling).

5.3.4. Powder XRD Analyses of Bent-Core H-Bonded Complexes HPm/CBn and CPm/HBn

The molecular organizations of banana-shaped H-bonded complexes **HPm/CBn** and **CPm/HBn** in different mesophases, especially the layered structures of the smectic phases, could be characterized by XRD measurements, and their results are demonstrated in Tables 5.3 and 5.4. The formation of bent-core H-bonded complexes

were further confirmed by the different d-spacing values of the smectic phases from those of their constituents. For instance, new sharp XRD peaks indexed as (001) in the small angle region were obtained in bent-core H-bonded complexes **HPm/CBn** and **CPm/HBn**, respectively. In addition, no separated diffraction peaks in H-bonded complexes **HPm/CBn** and **CPm/HBn** were observed to prove no phase separations occurred between their components. Wide angle diffuse peaks corresponding to a d-spacing value of 4.6 Å indicated that similar liquid-like in-plane orders with average intermolecular distances were prevalent inside the smectic layers of bent-core side-chain polymer complexes. As shown in Tables 5.3 and 5.4 (also see Figures 5.5-5.6 and Figure S5.2 of the supporting information), the d-spacing values of bent-core H-bonded complexes **HPm/CBn** and **CPm/HBn** were mostly longer than those of bent-core homopolymers (**HP** and **CP**) and small molecules (**CB** and **HB**) owing to the less tilted and looser arrangements of the mixtures from both H-bonded and covalent-bonded structures.

Generally, bent-core H-bonded complexes **CPm/HBn** had larger d-spacing values than H-bonded polymer complexes **HPm/CBn**. This phenomenon of smaller d-spacing values in H-bonded polymer complexes **HPm/CBn** might be explained by that the higher flexibility of bent-core H-bonded homopolymer **HP** and its larger compatibility with bent-core covalent-bonded small molecule **CB** to induce the better interactions and more compact stackings of both components, which also explained

the better mesomorphic properties of H-bonded polymer complexes **HPm/CBn** (with wider SmCP phasic ranges and more constituted complexes possessing the SmC phase) than those of H-bonded complexes **CPm/HBn** demonstrated in Figure 5.4. In addition, several sharp peaks were accomplished in covalent-bonded polymer **CP** to mean the long range ordered smectic structure,[21] and H-bonded homopolymer **HP**

displayed a sharp diffraction peak to reveal tilted molecular organization. The largest d-spacing value of H-bonded complexes **HPm/CBn** and **CPm/HBn** (d_1 = 42.0 Å for **HP1/CB10** and d_1 = 51.6 Å for **CP1/HB15**, respectively) were shorter than the theoretical length of small molecular H-bonded complex **HB** (about 58 Å) to indicate the tilted smectic arrangement of polymer H-bonded complexes **HPm/CBn** and **CPm/HBn**. For example, the two-dimensional structures of the SmCP phase in bent-core H-bonded complexes **HP1/CB10** and **CP1/HB10** were also confirmed to be tilted smectic structures by the XRD results (see Figures 5-6).

Table. 5.3. Powder XRD Data of Banana-Shaped H-Bonded Complexes and Their Corresponding Components

Complex/ compound	Cooling Temp. (°C)	2 theta	d-spacing(Å)
HP	140	2.17	35.2
		4.40	17.4
HP15/CB1	110	2.00	38.2
		4.05	18.9
HP10/CB1	110	1.92	39.8
		3.84	19.9
HP5/CB1	105	1.90	40.2
		3.80	20.1
HP1/CB1	110	1.87	40.9
		3.76	20.3
HP1/CB5	110	1.84	41.5
		3.90	19.6
HP1/CB10	80	1.82	42.0
		3.72	20.7
HP1/CB15	90	1.96	39.0
		3.98	19.2
		6.00	12.7
CB	100	2.23	34.3
		4.41	17.3
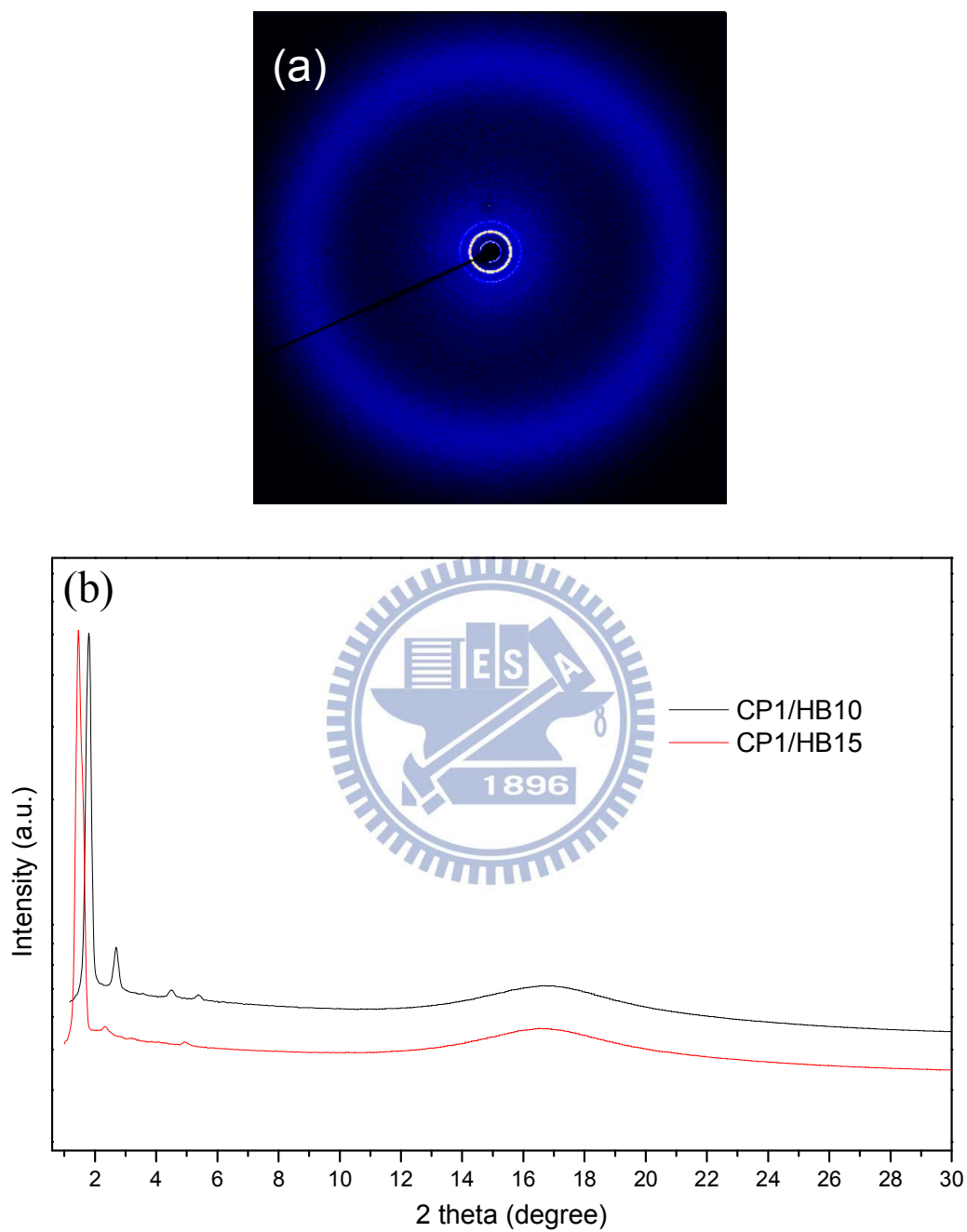
Figure 5.6. (a) Powder X-ray 2D pattern of H-bonded complex **CP1/HB10** (at 90 °C cooling); (b) Powder X-ray diffraction intensities against angle profiles of H-bonded complexes **CP1/HB10** and **CP1/HB15** in the polar smectic phase (at 90 °C cooling).

Table. 5.4. Powder XRD Data of Banana-Shaped H-Bonded Complexes and Their Corresponding Components

Complex/ compound	Cooling Temp. (°C)	2 theta	d-spacing(Å)
CP	140	2.10	36.4
		3.14	24.3
		3.85	19.9
		4.48	17.1
		5.20	14.7
CP1/HB5	80	1.51	50.6
		2.40	31.8
		4.20	18.2
		5.08	15.1
CP1/HB10	90	1.80	42.5
		2.70	28.3
		4.49	17.1
		5.49	13.9
CP1/HB15	90	1.48	51.6
		2.38	32.1
		3.18	24.0
		4.94	15.5
HB	100	1.62	47.2

5.3.5. Electro-Optical Properties of Bent-Core Mixtures HPm/CBn and CPm/HBn

In order to evaluate the polar switching current properties of the SmCP phase in all banana-shaped H-bonded complexes **HPm/CBn** and **CPm/HBn**, the triangular wave method was applied to measure the switching current behavior (i.e., the spontaneous polarization) in parallel rubbing cells with a cell gap of 4.25 μm. Regarding the spontaneous polarization (Ps) behaviors of H-bonded complexes **HPm/CBn**, two current peaks per half-period of an applied triangular voltage were

observed in the switching current response curves of the SmCP phase in H-bonded complexes **HP1/CB10** and **HP1/CB15**. The two-peak switching current response curve of H-bonded complex **HP1/CB15** in the SmCP phase is shown in Figure 5.7a, where the characteristic behavior of a sequential electric response was due to a ferroelectric state switched into an antiferroelectric ground state and back to the opposite ferroelectric state again. These phenomena confirmed the SmCP$_A$ (A = anti-ferroelectric behavior) structure of the B2 phase in the bent-core H-bonded complex.[55] As shown in Figure 5.7b, the Ps values of 280 and 450 nC/cm^2 were saturated at high voltages (Vpp > 200 V) for H-bonded complexes **HP1/CB10** and **HP1/CB15**, respectively. Compared with H-bonded complexes, the saturated Ps value of 500 nC/cm^{-2} in **CB** (the bent-core covalent-bonded small molecule) was obtained at a much higher voltage above Vpp = 320 V in our previous study.[24] This might be explained by that the host system of covalent-bonded molecule **CB** doped with H-bonded polymer **HP** would reach saturated Ps values at lower voltages due to the softer bent-core mixed configurations in H-bonded complexes **HP1/CB10** and **HP1/CB15**. Moreover, the electro-optical properties in the SmC phase of H-bonded complexes **HPm/CBn** with **n/m** ratios between 15/1 and 1/5 were proven to be no polar switching current responses under AC fields.

With respect to the Ps values of H-bonded complexes **CPm/HBn**, for instance, H-bonded complex **CP1/HB15** revealed two-peak switching current response curves in Figure 5.8a to prove the anti-ferroelectric behavior of the polar smectic phase, and H-bonded complex **CP1/HB10** displayed a similar polar switching current behavior to indicate the existence of the SmCP$_A$ phase. As shown in Figure 5.8b, the Ps values at high voltages (i.e., Vpp > 200 V) were both saturated at 350 nC/cm^2 for H-bonded complexes **CP1/HB15** and **CP1/HB10**. On the contrary, the saturated Ps value of 115 nC/cm^{-2} in bent-core H-bonded small molecular complex **HB** (i.e., **A-N**) was obtained

at a higher voltage of Vpp = 210 V in our previous study.[24] The Ps values of banana-shaped H-bonded complexes and their corresponding components are summarized. The higher Ps values of SmCP phase in bent-core H-bonded complexes **CP1/HB15** and **CP1/HB10** than that of H-bonded molecular complex **HB** indicated that the polar switching current behavior was not only contributed from H-bonded molecular complex **HB** but also provided by covalent-bonded polymer dopant **CP**. Therefore, the mesophasic range, Ps value, and stability of the SmCP phase could be enhanced by doping H-bonded molecular complex **HB** with small molar ratios of bent-core covalent-bonded side-chain homopolymer **CP**.

A switching process could also be checked through the rotation of the extinction crosses (Figure 5.9) by applying (or after removing) opposite d.c. electric fields in the banana-shaped H-bonded complexes with the SmCP phase. For instance, circular domains of H-bonded complex **CP1/HB15** were formed in the SmCP mesophasic range, in which the smectic layers were circularly arranged around the centers of the domains, which were organized according to the domain models proposed by Link et al.[8.24] As shown in Figure 5.9, the rotation of the extinction crosses during the switched on and off states in H-bonded complex **CP1/HB15** demonstrated the chiral domain behavior.[10] In view of Figure 5.9a and 5.9c, by applying d.c. electric fields (with reverse polarities), the extinction crosses rotated either counterclockwise or clockwise (i.e., rotated oppositely with positive and negative fields), indicating a synclinic tilt in the ferroelectric state (SmC_SP_F). By removing electric fields (off state), the extinction crosses were reoriented back to the crossed polarizer directions (see Figure 5.9b), where an anticlinic tilt existed in the antiferroelectric ground state (SmC_AP_A). Hence, the anti-clinic and anti-ferroelectric polar smectic (SmC_AP_A) arrangement in the ground state of H-bonded complex **CP1/HB15** were identified, and the other H-bonded complexes possessing the anti-ferroelectric polar smectic

(SmC$_A$P$_A$) phase were also confirmed.
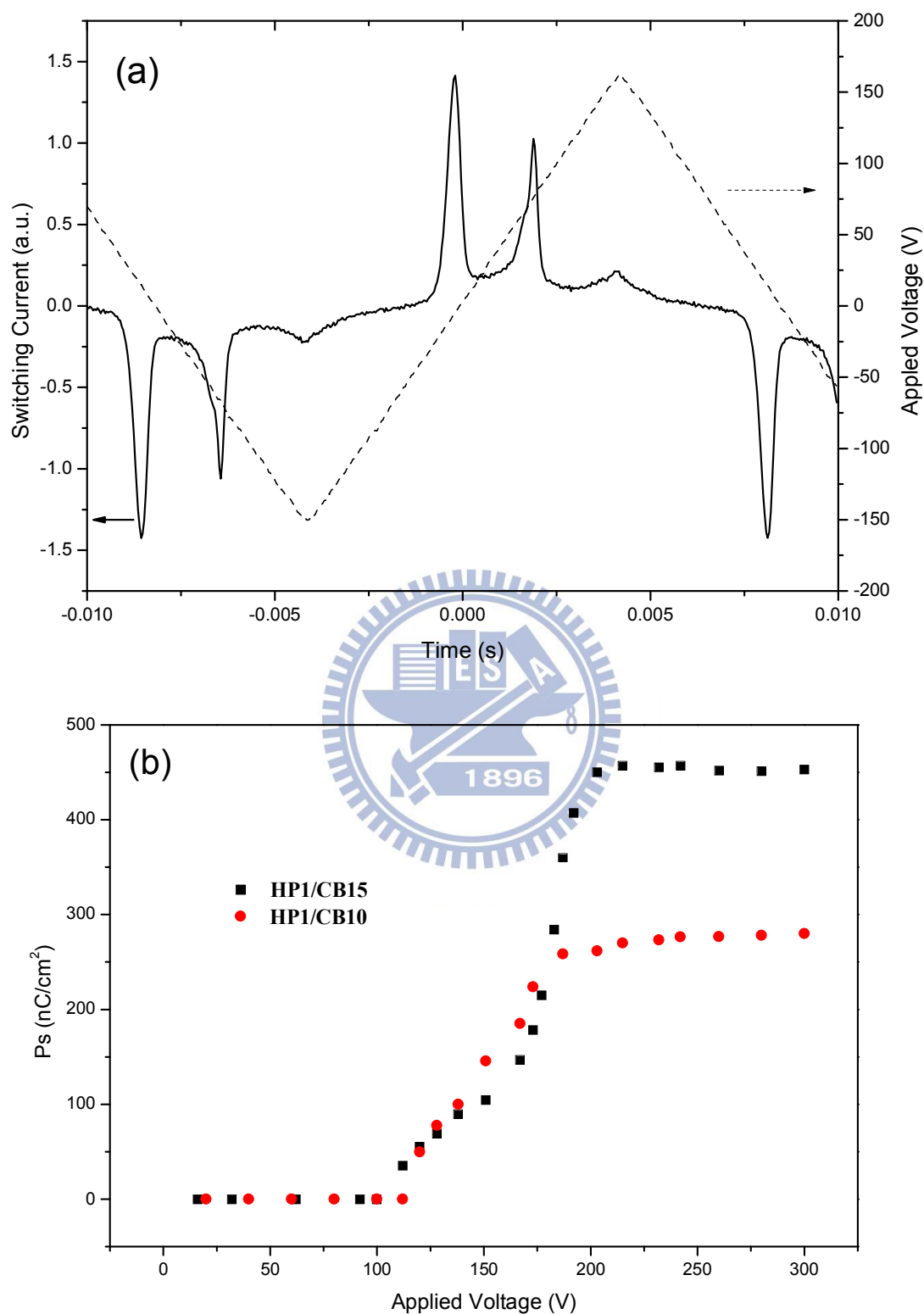
Figure 5.7. (a) Switching current responses of banana-shaped H-bonded complex **HP1/CB15** (at 80 °C cooling) under the triangular wave method (as Vpp = 240 V and f = 200 Hz). (b) Ps values as a function of applied voltages (as f = 200 Hz) in the SmCP phase of banana-shaped H-bonded complexes **HP1/CB15** and **HP1/CB10** (at

90 °C cooling).
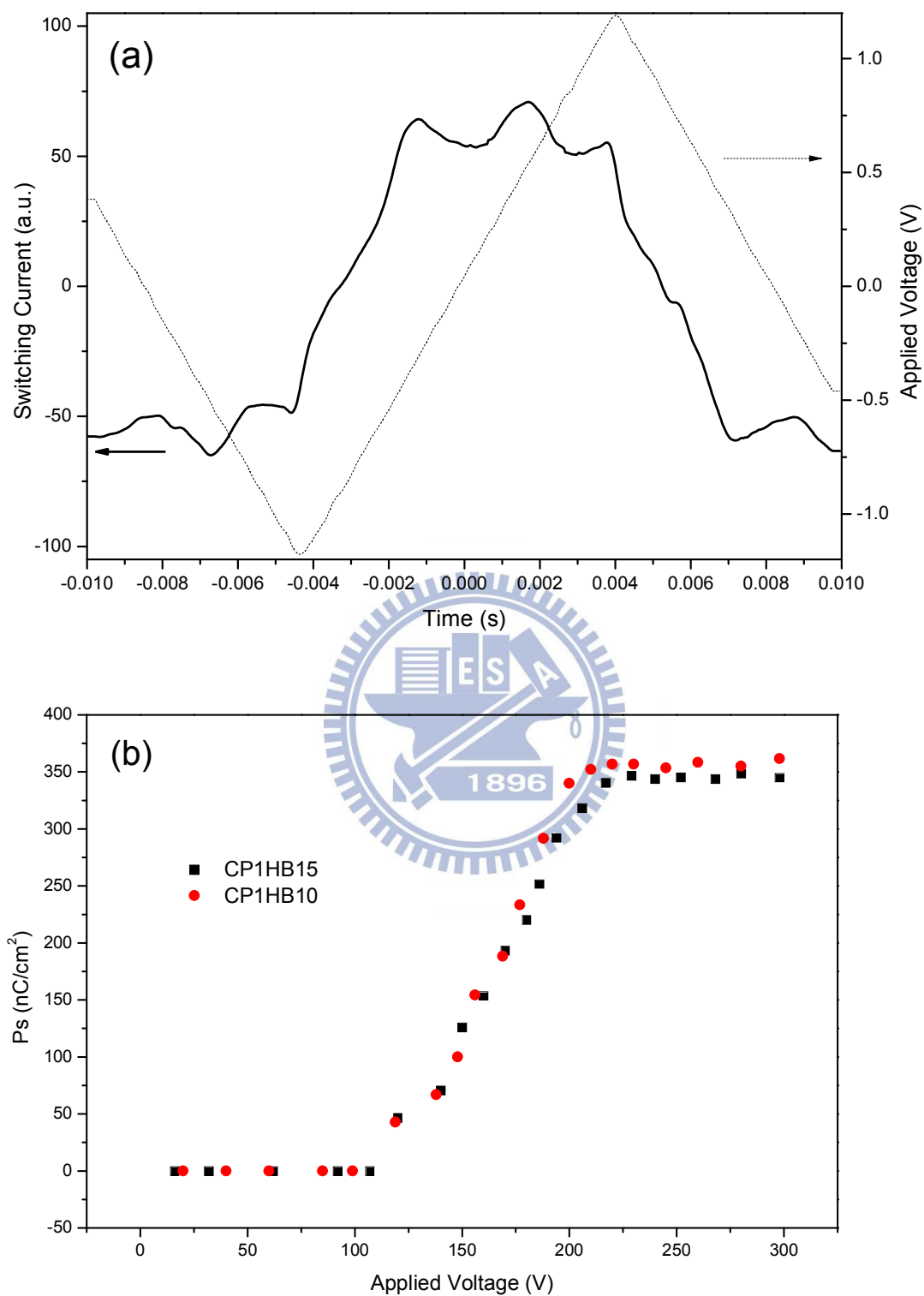
Figure 5.8. (a) Switching current responses of banana-shaped H-bonded complex **CP1/HB15** (at 85 °C cooling) under the triangular wave method (as Vpp = 240 V and f = 200 Hz). (b) Ps values as a function of applied voltages (as f = 200Hz) in the SmCP phase of banana-shaped H-bonded complexes **CP1/HB15** and **CP1/HB10** (at

90 °C cooling).
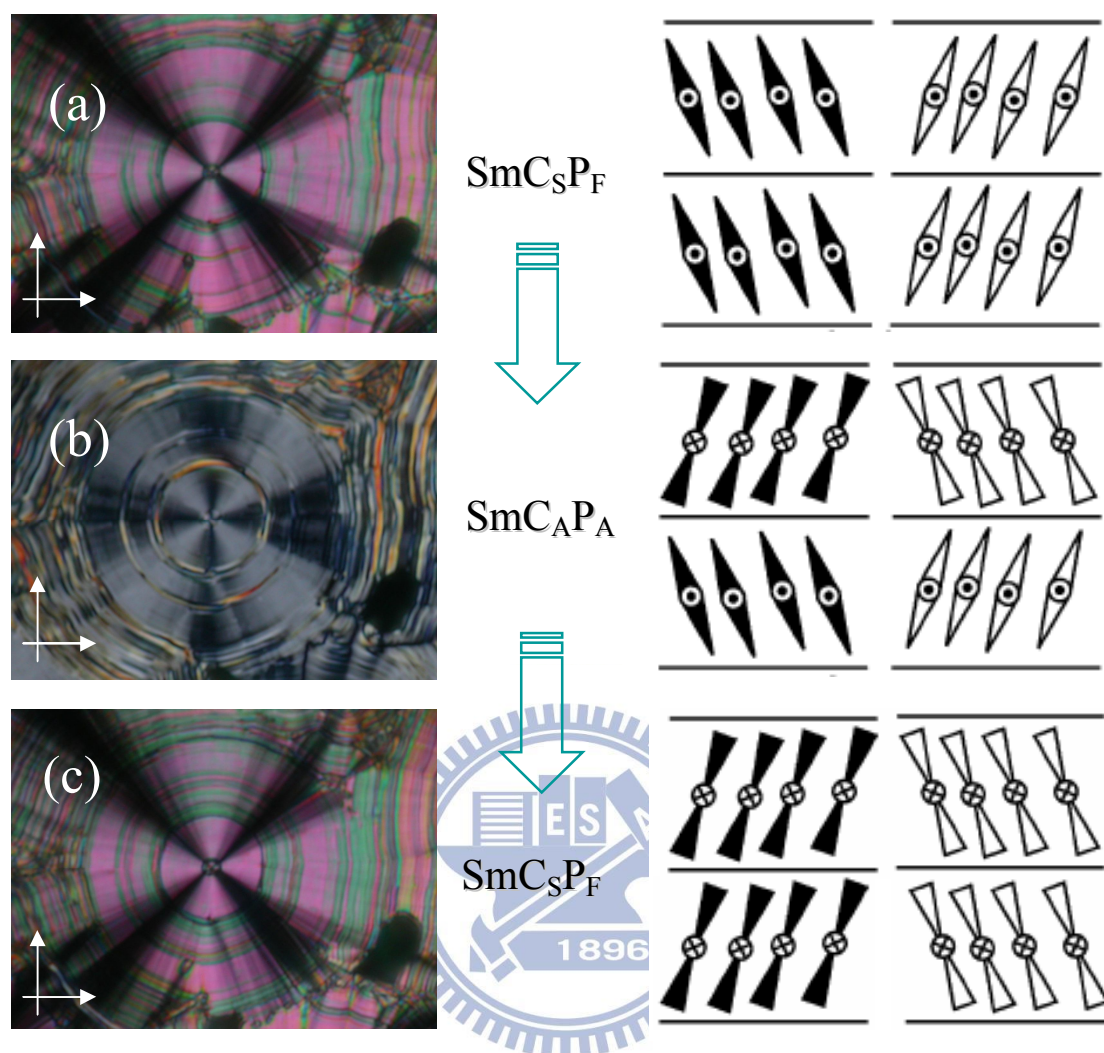
Figure 5.9. POM textures of the anti-ferroelectric SmC_AP_A chiral domain (in a parallel rubbing cell with a cell gap of 4.25 μm, where white arrows are the directions of polarizers and analyzers) in banana-shaped H-bonded complex **CP1/HB15** by applying d.c. electric fields from (a) -30 V → (b) 0 V → (c) +30 V (at 90 °C cooling).

5.4. Conclusions

In summary, banana-shaped liquid crystalline (LC) H-bonded complexes **HPm/CBn** and **CPm/HBn** (with various **m/n** molar ratios) were developed by mixing both H-bonded and covalent-bonded moieties in combination with polymeric and small molecular structures, where either H-bonded or covalent-bonded structural units were homopolymerized in the banana-shaped side-chain H-bonded LC polymer complexes **HPm/CBn** and **CPm/HBn**, respectively, to stabilize the polar smectic

(SmC_AP_A) phase. Due to the stronger intermolecular interactions and tighter stackings of H-bonded and covalent-bonded bent-cores in homopolymers (**HP** and **CP**), bent-core homopolymers **HP** and **CP** had higher isotropization temperatures than their H-bonded complexes **HPm/CBn** and **CPm/HBn**, respectively. The looser molecular stackings of H-bonded complexes **HPm/CBn** and **CPm/HBn** provided H-bonded complex systems (as **m/n** = 1/10 and 1/15 possessing less polymeric dopants) with suitable disordered arrangements of both covalent- and H-bonded structures to stabilize the SmCP phase, which would induce lower transition temperatures (and possibly wider mesophasic ranges) as well as tunable Ps values in the proper polymeric molar ratios of banana-shaped H-bonded complexes. Hence, lower Ps values were obtained in H-bonded complexes **HPm/CBn** and **CPm/HBn** with higher ratios of H-bonded moieties (larger **m/n** molar ratios), correspondingly. Because of the higher flexibility of bent-core H-bonded homopolymer **HP** and its larger compatibility with bent-core covalent-bonded small molecule **CB** to induce the better interactions and more compact stackings of both components, the better mesomorphic properties of H-bonded polymer complexes **HPm/CBn** (with wider SmCP phasic ranges and more constituted complexes possessing the SmC phase) than those of H-bonded complexes **CPm/HBn**. According to the XRD measurements and switching current responses (including the chirality investigation), the polar smectic (SmC_AP_A) phase were verified to be achieved and stabilized by smaller contents of polymeric dopants in banana-shaped LC H-bonded complexes, such as **HP1/CB10**, **HP1/CB15**, **CP1/HB10**, and **CP1/HB15**. Overall, the mesomorphic and electro-optical properties of banana-shaped LC materials could be efficiently adjusted by mixing either H-bonded or covalent-bonded bent-core side-chain homopolymers with low molecular weight bent-core LC materials possessing covalent-bonded or H-bonded designs opposite to the previous homopolymers.

5.5. Electronic Supplementary Information

5.5.1. Synthesis

The synthetic procedures of H-donor monomer **A'**, bent-core monomer **B'**, and pyridyl H-acceptor **N** were proceeded according to scheme S1.

5.5.1.1. Synthesis of 12-bromododecanol (1). Doecan 1,12-diol (1e.q) and HBr (1e.q.) were dissolved in toluene solvent to react at 60°C for 24 hours, and side product H_2O could be removed by dean stark installation. After then, the reacted solution was extracted by ethyl acetate (EA) and water, and the organic liquid layer was purified by column chromatography to give a liquid product. Yield: 56%. ^{1}H NMR (300 MHz, CDCl$_3$) δ (ppm): 3.57 (t, J = 6.6 Hz, 2H, -OCH$_2$-), 3.39 (t, J = 6.9 Hz , 2H, Br-CH$_2$-), 3.19 (s, 1H, -OH), 2.04-1.80 (m, 2H, Br-CH$_2$CH$_2$-), 1.56-1.49 (m, 2H, HO-CH$_2$CH$_2$-), 1.44-1.21 (m, 16H, -CH$_2$-).

5.5.1.2. Synthesis of compound (cpd) 2. 12-bromododecanol (**1**) (1.1 e.q), methyl 4-hydroxybenzoate and potassium carbonate (K$_2$CO$_3$) (1.5 eq.) were dissolved in acetone solvent to react at reflux temperature for 20 hours. After that, water was added to dissolve the inorganic salt and a white precipitation was produced. Subsequently, the white powder was washed by hexane to get a pure product. Yield: 91 %. ^{1}H NMR (300 MHz, CDCl$_3$) δ (ppm): 7.95 (d, J = 9.0 Hz, 2H, Ar-H), 6.87 (d, J = 9.0 Hz, 2H, Ar-H), 3.97 (t, J = 6.3 Hz, 2H, -OCH$_2$-), 3.85 (s, 3H, -OCH$_3$), 3.61 (m, 2H, -CH$_2$OH), 1.79 (s, 1H, -OH), 1.26(m, 20H, -CH$_2$-).

5.5.1.3. Synthesis of cpd 3. Cpd **2** (1 e.q.) and potassium hydroxide (KOH) (4 e.q.) were dissolved in ethanol solvent to reflux and react for 16 hours. After cooling reacted liquid to room temperature, HCl (10 vol% in water) solution was added to react 30 minutes. The precipitation was filtered and a white powder was formed. The powder was recrystallized by ethanol and hexane (1:3 vol) to collect a pure white product. Yield: 95 %. ^{1}H NMR (300 MHz, CDCl$_3$) δ (ppm): 7.92 (d, J = 8.7 Hz, 2H,

Ar-H), 6.92 (d, J = 8.7 Hz, 2H, Ar-H), 4.00 (t, J = 6.6 Hz, 2H, -O$\underline{CH_2}$-), 3.45 (t, J = 6.3 Hz, 2H, -$\underline{CH_2}$OH), 2.06(s, 1H, -$\underline{OH}$), 1.78 (m, 2H, -CH$_2$$\underline{CH_2}$OH), 1.29 (m, 18H, -$\underline{CH_2}$-).

5.5.1.4. Synthesis of H-donor monomer (A'). T The addition of terminal acryl group on cpd **2** was proceeded by the reaction of acryloyloxy chloride (1.5 e.q.) and cpd **2** (1 e.q.) in 1,4-dioxane solvent with an organic base of dimethylaniline (DMA) (1.1 e.q.) under nitrogen to react at room temperature for 24 hours. When the reaction was finished, a dilute HCl solution (10 vol% in water) was added to the reacted solution to form a white powder. The product was purified by column chromatography to give a white product. Yield: 55 %. ^{1}H NMR (300 MHz, CDCl$_3$) δ (ppm): 8.03 (d, J = 9.0 Hz, 2H, Ar-H), 6.91 (d, J = 9.0 Hz, 2H, Ar-H), 6.41 (d, J = 18 Hz, 1H, -CH=$\underline{CH_2}$), 6.35 (m, 1H, =$\underline{CH}$-), 6.07 (d, J = 9.0 Hz, 1H, -CH=$\underline{CH_2}$), 4.13 (t, J = 6.6 Hz, 2H, Ar-O$\underline{CH_2}$-), 4.00 (t, J = 6.3 Hz, 2H, C=C-O$\underline{CH_2}$-), 1.79 (m, 2H, Ar-OCH$_2$$\underline{CH_2}$-), 1.63 (m, 2H, C=C-OCH$_2$$\underline{CH_2}$-), 1.26 (m, 16H, -$\underline{CH_2}$-). MS (EI): m/z [M+] 377; calcd m/z [M+] 376.5. EA: Calcd for C$_{22}$H$_{32}$O$_5$: C, 70.18; H, 8,57. Found: C, 70.33; H, 8.52.

5.5.1.5. Synthesis of cpd 5. Cpd **4** (1 e.q.), resorcinol (1 e.q.), N,N-dicyclohexylcarbodiimide (DCC) (1.1 eq), and a catalytic amount of 4-(N,N-dimethylamino) Pyridine (DMAP) were dissolved in dry dichloromethane (DCM) under nitrogen to react at room temperature for 15 hours. The precipitated dicyclohexylurea (DCU) was filtered off and washed with an excess of DCM (20 ml). The filtrate was extracted with water and DCM, and the organic liquid layer was dried over anhydrous magnesium sulphate. After removal of the solvent by evaporation under reduced pressure, the residue was recrystallized from ethanol to give a white solid. Yield: 44 %. ^{1}H NMR (300 MHz, CDCl$_3$) δ (ppm) : 8.25 (d, J = 8.7 Hz, 2H, Ar-H), 8.14 (d, J = 9.0 Hz, 2H, Ar-H), 7.40 (d, J = 8.7 Hz, 2H, Ar-H), 7.22 (t, J = 8.1

Hz, 1H, Ar-H), 7.03 (d, J = 9.0 Hz, 2H, Ar-H), 6.71-6.66 (m, 3H, Ar-H), 4.06 (t, J = 6.6 Hz, 2H, O$\underline{CH_2}$), 1.80 (m, 2H, OCH$_2\underline{CH_2}$), 1.47-1.28 (m, 18H, $\underline{CH_2}$), 0.88 (t, J = 6.3 Hz, 3H, $\underline{CH_3}$).

5.5.1.6. Synthesis of pyridyl H-Acceptor (N). A mixture of cpd **5** (1 e.q.), isonicotinoyl chloride hydrochloride (1.1 e.q.), and triethylamine (1.2 e.q.) were dissolved in dry DCM under nitrogen to react at room temperature for 8 hours. After work up, the solvent was extracted with water and DCM, and organic liquid layer was dried over anhydrous magnesium sulphate. After removal of the solvent by evaporation under reduced pressure, the residue was purified by column chromatography and recrystallized by DCM and hexane (1:4 vol) to give a white solid. Yield: 95 %, ^{1}H NMR (300 MHz, CDCl$_3$): δ 8.89 (d, J = 4.2 Hz, 2H, Ar-H), 8.22 (d, J = 8.7 Hz, 2H, Ar-H), 8.08(d, J = 8.7 Hz, 2H, Ar-H), 8.01 (d, J = 4.2 Hz, 2H, Ar-H), 7.59 (t, J = 8.1 Hz, 1H, Ar-H), 7.51 (d, J = 9.0 Hz, 2H, Ar-H), 7.41 (s, 1H, Ar-H), 7.32 (br, 2H, Ar-H), 7.10 (d, J = 9.0 Hz, 2H, Ar-H); 4.07 (t, J = 6.3 Hz, 2H, O$\underline{CH_2}$), 1.74 (br, 2H, OCH$_2\underline{CH_2}$), 1.23 (br, 18H, $\underline{CH_2}$), 0.84 (t, J = 6.3 Hz, 3H, $\underline{CH_3}$). MS (EI): m/z [M+] 624; calcd m/z [M+] 623.7. EA: Calcd for C$_{38}$H$_{41}$NO$_7$: N, 2.25 C, 73.17; H, 6.63;. Found: N, 2.44 C, 73.25; H, 6.75.

5.5.1.7. Synthesis of cpd 7. Methyl 4-hydroxybenzoate (cpd **6**) (1eq.), benzyl bromide (1.1eq.), and K$_2$CO$_3$ (1.5eq.) were dissolved in acetone solvent and reacted at reflux temperature for 10 hours. After removing acetone at reduced pressure, water was added and a precipitate was produced immediately. The crude product was recrystallized by acetone and hexane (1:4 vol) to give a white solid. Yield: 97%, ^{1}H NMR (300 MHz, CDCl$_3$) δ 7.03 (d, J = 9.0 Hz, 2H, Ar-H), 6.63-6.50 (m, 5H, Ar-H), 6.35 (d, J = 9.0 Hz, Ar-H), 4.38 (s, 2H, O$\underline{CH_2}$), 2.49 (s, 3H, O$\underline{CH_3}$).

5.5.1.8. Synthesis of cpd 8. Cpd **7** (1eq.) and KOH (4eq.) were dissolved in ethanol and reacted at reflux temperature for 10 hours. HCl solution (10 vol% in

water) was added to produce a precipitate, and the crude product was recrystallized by THF and hexane (1:10 vol) to give a white solid. Yield: 98 %, ^{1}H NMR (300 MHz, DMSO) δ 7.87 (d, J = 9.0 Hz, 2H, Ar-H), 7.46-7.33 (m, 5H, Ar-H), 7.07 (d, J = 9.0 Hz, 2H, Ar-H), 5.17 (s, 2H, O$\underline{CH_2}$).

5.5.1.9. Synthesis of cpd 9. Cpd **8** (1.1 e.q.) and cpd **4** (1 e.q.) were dissolved in dry DCM solvent and reacted with a catalytic amount of DMAP (0.2 e.q.) and DCC (1.1 eq) under nitrogen for 24 hours. The organic solution was extracted by DCM and water (1:1 vol) and recrystallized by DCM and ethanol (1:10 vol) to yield a white solid. Yield: 57%. ^{1}H NMR (300 MHz, d-dioxane) δ (ppm) : 8.26 (d, J = 9.0 Hz, 2H, Ar-H), 8.13 (d, J = 9.0 Hz, 2H, Ar-H), 7.44-7.29 (m, 10H, Ar-H), 6.97 (d, J = 9.0 Hz, 2H, Ar-H)，6.91-6.81 (m, 7H, Ar-H), 5.06(s, 1H, -Ar-O-$\underline{CH_2}$-Ar), 4.04(t, J = 6.6 Hz, 2H, O$\underline{CH_2}$), 1.81(t, J = 6.3 Hz, 2H, O$CH_2\underline{CH_2}$)，1.46-1.25(m, 18H, -$\underline{CH_2}$-), 0.86 (t, J = 6.3 Hz, 3H, $\underline{CH_3}$).

5.5.1.10. Synthesis of cpd 10. Cpd **9** and Pd/C catalyst were mixed in THF solvent under hydrogen to react at room temperature for 20 hours. The catalyst was removed by filtration through Celite and washed with THF. The solvent was removed by evaporation under reduced pressure, and the crude product was recrystallized by THF and hexane (1:10 vol) to produce a white solid. Yield: 80 %. ^{1}H NMR (300 MHz, d-dioxane): δ(ppm) : 8.28 (d, J = 9.0 Hz, 2H, Ar-H), 8.13 (d, J = 9.0 Hz, 2H, Ar-H), 8.05 (d, J = 8.7 Hz, 2H, Ar-H), 7.47 (t, J = 8.1 Hz, 1H, Ar-H), 7.41 (d, J = 8.7 Hz, 2H, Ar-H), 7.22 (s, 1H, Ar-H), 7.19-7.14 (m, 4H, Ar-H), 7.03 (d, J = 9.0 Hz, 2H, Ar-H), 6.86 (d, J = 8.7 Hz, 2H, Ar-H), 4.05 (t, J = 6.3 Hz, 2H, -O$\underline{CH_2}$-)，1.80(m, 2H, -OCH$_2\underline{CH_2}$-)，1.28(m, 18H, -CH_2-)，0.88(t, J = 6.3 Hz, 3H, -CH_3).

5.5.1.11. Synthesis of bent-core covalent-bonded monomer (B'). Cpd **A'** (1.1 e.q.), cpd **10** (1 e.q.), DCC (1.1 e.q.), and DMAP (0.2 e.q.) were dissolved in THF solvent under nitrogen to react at room temperature for 24 hours. The solution was

extracted by DCM and water, and purified by column chromatography to acquire a white solid. Yield: 60 %. ^{1}H NMR (300 MHz, d-dioxane) δ (ppm) : 8.25 (d, J = 9.0 Hz, 2H, Ar-H), 8.10 (d, J = 8.7 Hz, 2H, Ar-H), 7.48 (d, J = 8.1 Hz, 1H, Ar-H), 7.38 (d, J = 9.0 Hz, 2H, Ar-H), 7.25(s, 1H, Ar-H), 7.17 (d, J = 8.1 Hz, 1H, Ar-H), 7.01 (d, J = 8.7 Hz, 2H, Ar-H), 6.29 (d, J = 17.1 Hz, 1H, -CH=C$\underline{H}_2$), 6.08(m, 1H, -C$\underline{H}$=)，5.77 (d, J = 10.2 Hz, 1H, -CH=C$\underline{H}_2$), 4.08-4.00 (m, 6H, -OC$\underline{H}_2$-)，1.78-1.71(m, 4H, -OC$\underline{H}_2$C$\underline{H}_2$-)，1.59-1.56(m, 2H, -OCH$_2$C$\underline{H}_2$-), 1.43-1.26 (m, 34H, -C$\underline{H}_2$-), 0.84 (t, J = 6.3 Hz, 3H, -CH$_3$). MS (EI): m/z [M+] 998; calcd m/z [M+] 997.2. EA: Calcd for C$_{61}$H$_{72}$O$_{12}$: C, 73.47; H, 7.28;. Found: C, 73.82; H, 6.95.

Figure S5.2. Powder X-ray diffraction intensities against angle profiles of bent-core side-chain homopolymers **HP** and **CP** and bent-core small molecular structures **CB** and **HB**.
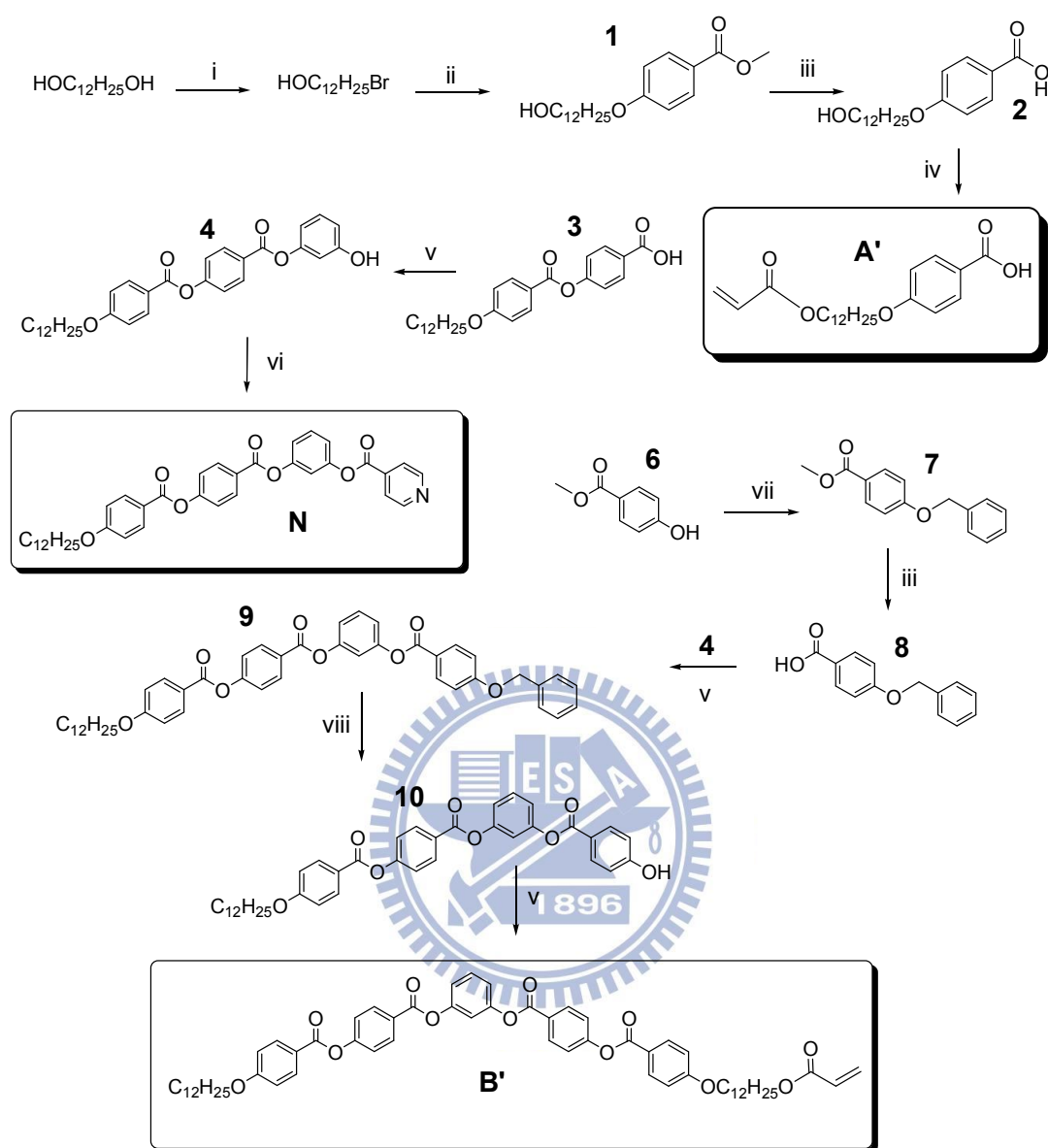
Scheme S5.1. Synthetic procedures of monomers **A'**, **B'**, and H-acceptor **N**. (i): HBr, toluene, (ii): methyl 4-hydroxybenzoate, K₂CO₃, Acetone; (iii) KOH, ethanol; (iv) acryloyloxy chloride, DMA, 1,4-dioxane; (v) DCC, DMAP, DCM; (vi) isonicotinoyl chloride hydrochloride, triethylamine, DCM; (vii) benzyl bromide, K₂CO₃, Acetone; (viii) Pd/C, H₂, THF.
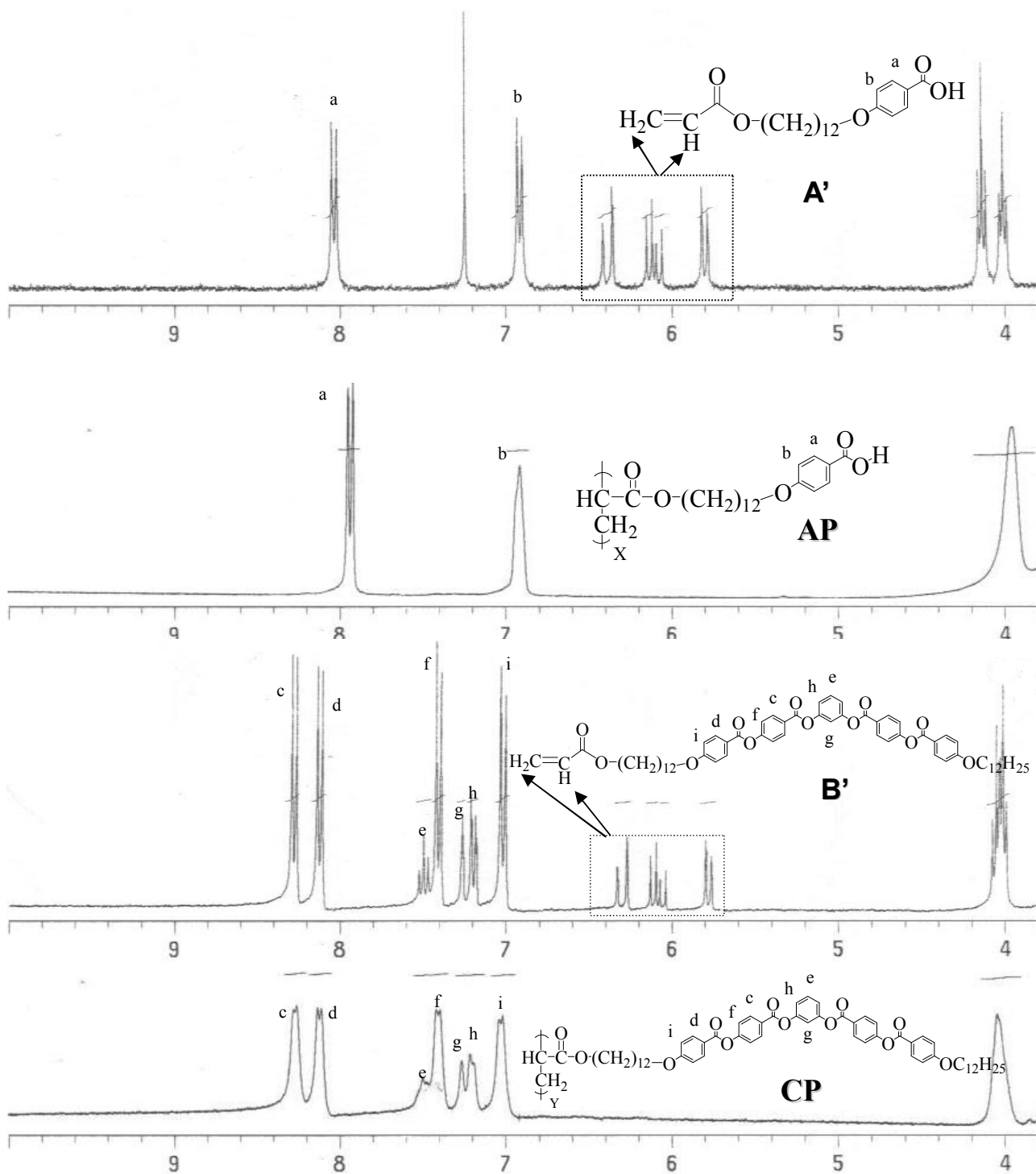
Figure S5.1. NMR spectra of monomers **A'** and **B'** and side-chain H-donor homopolymer **AP** and bent-core side-chain homopolymer **CP**.

Chapter 6

Dopant Effect of Covalent Structures on H-bonded

Banana-shaped Liquid Crystals

6.1. Introduction

Banana-shaped liquid crystals, which were framed by a bent-shaped achiral structure, displayed interesting special mesomorphic and electro-optical properties due to the peculiar intermolecular arrangements.[11] Originally, the spontaneous polarization (Ps) behaviors of electro-optical properties were only displayed in liquid crystalline mesogens with a chiral center part.[42] However, since the first example of bent-core structure, which built with resorcinol derivative linking through polar functional groups with a suitable bent angle as well as appropriate lengths of flexible chains was developed,[1a,12a] Ps behaviors were achieved in bent-shaped molecules duo to the various molecular polar and tilt directions in neighboring layers.[3-5] Naturally, their particular mesophases, including column stacking, tilt smectic phases, and three dimension structures, named as B1 to B7 were adequately developed and identified.[3-5] Among these phases with switching properties, B2 phase, so called polar smectic phase (SmCP) was the most frequently examined. Based on the molecular polar and tilt directions in neighboring layers, ferroelectric (F) and antiferroelectric (A) states are accomplished cause of the identical and inverse polarization between layer to layer, respectively. Synclinic (S) and anticlinic (A) status are executed duo to the alike and opposite molecular tilt aspect between layer to layer, respectively. Hence, the supramolecular architectures of homochiral domains (SmC_AP_A and SmC_SP_F) and racemic domains (SmC_SP_A and SmC_AP_F) were developed.

In order to perform the electro-optical applications of bent-core liquid crystalline materials, such as spontaneous polarized capabilities, nonlinear optics,[42] and fast responsive LCD devices,[65a,68] the most important and interesting issue of bent-core molecule is to retain and extend the lamellar organization with spontaneous polarization and electric-optical switching properties. However, high and narrow mesophasic transition temperatures were observed in traditional five-ring bent-core symmetric materials.[2,4] In order to stabilize the switching current behaviors of SmCP phase and reduce mesophasic transition temperatures, the varieties of bent-shaped molecular designs were developed, including fluoro lateral substitutes,[28] siloxyl and silyl derivatives,[25b,35,45b-c] and hydrogen bonds (H-bonds)[5,38,47,48] in bent-core structures. In addition, the influence of bent-core molecular dopant effect on the mesomorphic and electro-optical properties were also studied to induce or stabilize the particular smectic arrangements and chirality by doping with rod-like chiral/achiral liquid crystals in bent-core blending systems.[65b, 68]

In our previous works, on the contrast of mesophasic behaviors of traditional five-ring covalent-bonded bent-core materials,[39] bent-core H-bonded complexes with single far-central H-bonded sites at the rigid cores exhibited lower phase transition temperatures and threshold voltages of SmCP phase, where was indicated the single H-bonded injection in bent-core materials was performed the softer intermolecular arrangement. However, the SmCP phase of H-bonded complexes was disappeared in the bent-core H-bonded complexes bearing two H-bonds or single near-central H-bond. Based on our reported results, the production and enhancement of spontaneous polarization behaviors in bent-core small molecular liquid crystals was focused to be the primary purpose in this study.

In our conception, the bent-core small molecular blending systems were proposed to adjust the spontaneous polarization behavior by mixing with soft (H-bonded) and
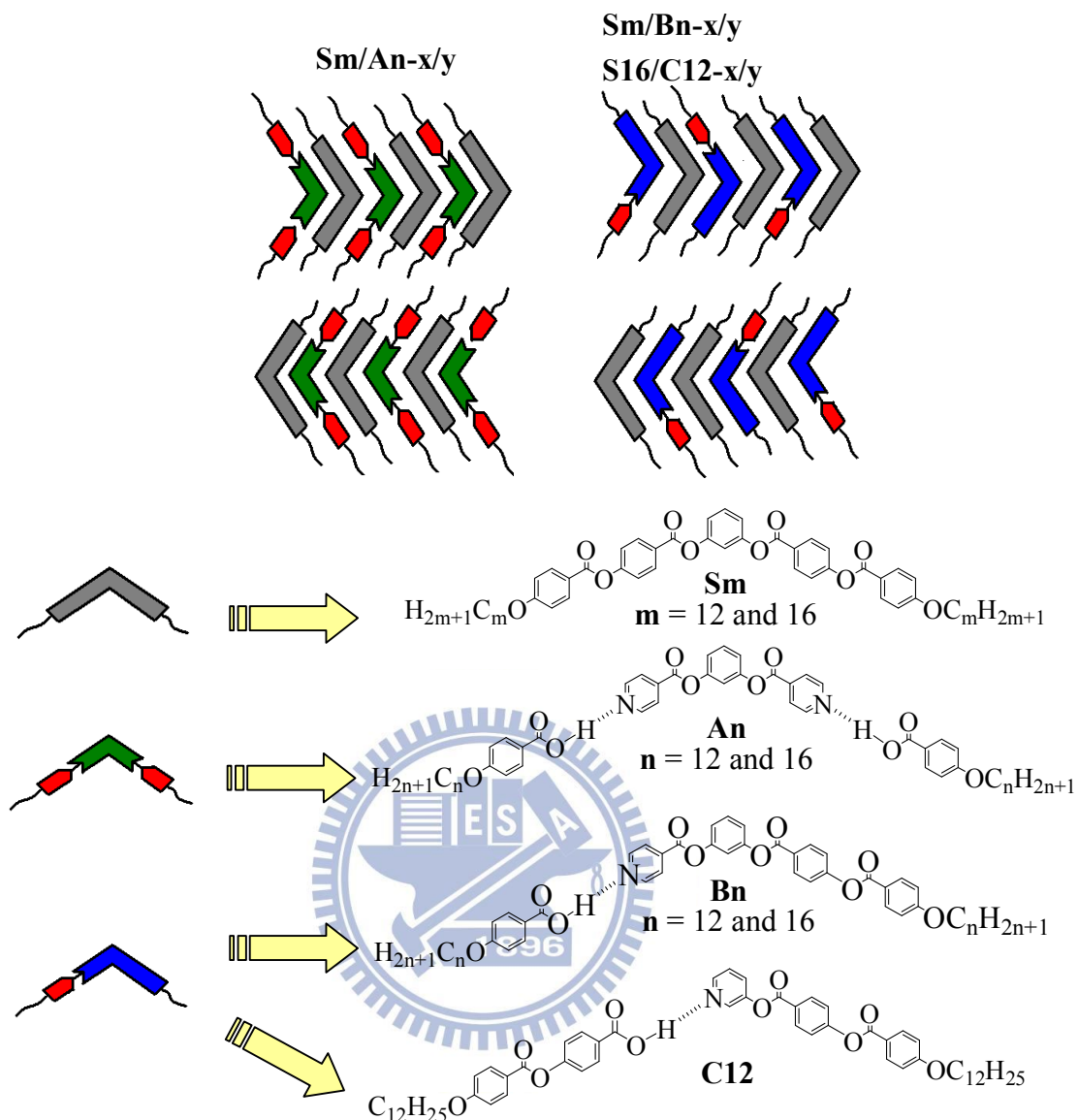
Figure 6.1. The molecular arranged models of complexes **Sm/An-x/y**, **Sm/Bn-x/y**, and **S16/C12-x/y** and their individual covalent- and H-bonded composited chemical structures **Sm**, **An**, **Bn**, and **C12**.

rigid (covalent-bonded) interacted bent-core structures. Hence, four bent-core covalent- and H-bonded structures **Sm**, **An**, **Bn**, and **C12** were prepared. Compounds **Sm** (m = 12 and 16) are the five-ring fully covalent bent-core structures connected by ester linkages.[2] Complexes **An** (n = 12 and 16) are the five-ring bent-core symmetric timers with in two sides of H-bonded linkages. Complexes **Bn** (n = 12 and 16) and **C12** are the five-ring bent-core asymmetric hetero-dimers with a single side of far-

and near-central H-bonded linkages, respectively. Three series of bent-core covalent- and H-bonded complexes **Sm/An-x/y**, **Sm/Bn-x/y**, and **S16/C12-x/y**, which were composed with several covalent- and H-bonded (**x/y**) molar doping ratios 1/0, 9/1, 8/2, 7/3, 6/4, 5/5, 4/6, 3/7, 2/8, 1/9, and 0/1 as shown in Figure 6.1. The variations of mesomorphic and electro-optical properties influenced by the molar doping (**x/y**) ratios of bent-core covalent- and H-bonded structures in bent-core mixtures were mainly investigated, and their mesomorphic and electro-optical properties were examined and characterized by polarizing optical microscopy (POM), differential scanning calorimetry (DSC), powder X-ray diffraction (XRD), and electro-optical (EO) switching current experiments.

6.2. Experimental

6.2.1. Characterization methods

^{1}H NMR spectra were recorded on a Varian Unity 300 MHz spectrometer using d_6-dioxane and $CDCl_3$ as solvents and mass measurements were determined on a Micromass TRIO-2000 GC-MS. Elemental analyses (EA) were performed on a Heraeus CHN-OS RAPID elemental analyzer. Mesophasic textures were characterized by polarizing optical microscopy (POM) using a Leica DMLP equipped with a hot stage. Temperatures and enthalpies of phase transitions were determined by differential scanning calorimetry (DSC, model: Perkin Elmer Pyris 7) under N_2 at a heating and cooling rate of 10 °Cmin^{-1}. Synchrotron powder X-ray diffraction (XRD) measurements were performed at beamline BL17A of the National Synchrotron Radiation Research Center (NSRRC), Taiwan, where the wavelength of X-ray was 1.33366 Å. The powder samples were packed into capillary tubes and heated by a heat gun, whose temperature controller was programmable by a PC with a PID feedback system. The scattering angle theta was calibrated by a mixture of silver behenate and

silicon. The electro-optical properties were determined in commercially available ITO cells (from Mesostate Corp., thickness = 4.25 μm, active area = 1 cm^2) with rubbed polyimide alignment coatings (parallel rubbing direction). A digital oscilloscope (Tektronix TDS-3012B) was used in these measurements.

6.2.2. Sample preparation

All the bent-core covalent- and H-bonded complexes were constructed by H-bonded components (H-donors and H-accepters) and covalent structure **Sn** from mixed solutions of chloroform by evaporating solvents slowly, where those components were synthesized according to the previous works,[39] and three series of blending systems were formed: (1) **S12/A12-x/y**, **S12/A16-x/y**, **S16/A12-x/y**, **and S16/A16-x/y**; (2) **S12/B12-x/y**, **S12/B16-x/y**, **S16/B12-x/y**, and **S16/B16-x/y**; (3) **S16/C12-x/y**, where the covalent- and H-bonded (**x/y**) ratios were 1/0, 9/1, 8/2, 7/3, 6/4, 5/5, 4/6, 3/7, 2/8, 1/9, and 0/1.

6.3. Result and Discussion

6.3.1. Mesophasic and thermal properties: (1) bent-core covalent- and H-bonded complexes Sm/An-x/y

In order to realize the influences of bent-core dopant effects and blending ratios as well as varieties of flexible chain lengths on mesomorphic, molecular stacking, and thermal properties, bent-core complexes **Sm/An**, which joined by four series of complexes **S12/A12**, **S12/A16**, **S16/A12**, and **S16/A16** with various molar doping ratios (**x/y**) were investigated by POM and DSC measurements. The thermal properties and phase behaviors of bent-core complexes **Sm/An** (**m,n** = 12 and 16) were illustrated in Figures 6.2-6.4 and Tables S6.1-S6.4. Even the pure component **An** (**n** = 12 and 16) possessed the non-polar switchable smectic C (SmC) phase, the complexes **Sm/An** with low **x/y** ratios (**x/y** = 4/6, 3/7, 2/8, and 1/9) revealed only the

crystalline phase during the heating and cooling processes. However, the polar smectic (SmCP) phase was obtained in the complexes **Sm/An** with high x/y ratios (**x/y** = 5/5, 6/4, 7/3, 8/2, and 9/1). For instance, the fan-like texture of SmCP phase in the complex **S12/A12-6/4** was demonstrated in Figure 6.2a and the crystalline texture of the complex **S12/A12-1/9** was shown in Figure 6.2b. Regarding the phase transitions of complexes **Sm/An**, their phase transition temperatures and enthalpy values were shown in Tables S6.1-S6.4 and Figures 6.3-6.4. To contrast mesophasic transition temperatures in the series of complexes **S12/A16**, the SmCP phase was enhanced in the complexes with high **x/y** ratios (**x/y** $\geqq$ 5/5), and these mesophasic ranges and phase transition temperatures of SmCP phase were extended and lower than those of the pure component **S12**. As shown in Figures 6.3 and 6.4, other series of complexes **S12/A12**, **S16/A12**, and **S16/A16** exhibited the similar phase transition phenomena as complexes **S12/A16**. To compare the tendencies of mesophasic transition temperatures in all complexes **Sm/An**, the extensies of SmCP phase were most and fewest distinguished in series of complexes **S12/A16** and **S16/A16**, respectively. The lowest freezing temperature ($T_f \sim$ 71 °C) of SmCP phase was achieved in the complex **S12/A16-9/1**. Meanwhile, the most extensive SmCP range in series of complexes **S16/A12** were carried out in **x/y** = 6/4, indicating few doping amount of the covalent-bonded component **S16** (with longer flexible chain) is necessary for the H-bonded symmetric trimer **A12** (with shorter flexible chain).

6.3.2. (2) Bent-core covalent- and H-bonded complexes Sm/Bn-x/y

The series of comparable bent-core covalent- and H-bonded complexes **Sm/Bn** were investigated for the influence of dopant effect on their mesophasic types and phase transition temperatures as shown in Tables S6.5-S6.8 and Figures 6.5-6.7. With respect to the mesophasic types, the enantiotropic SmCP phase was obtained in all series of complexes, i.e., **S12/B12**, **S16/B12**, **S12/B16**, and **S16/B16** (**x/y** = 1/0 to 0/1).

The mesophasic textures were examined by POM observations, for instance, complexes **S12/B16-3/7** and **S12/B16-7/3** revealed fan-like textures in Figure 6.5. Comparing the phase transition temperatures of four series of complexes **Sm/Bn** with their pure components **Sm** and **Bn**, complexes **Sm/Bn** revealed more extensive SmCP ranges by the blending of bent-core covalent- and H-bonded dopants and the lower isotropization (T_i) and freezing (T_f) temperatures were acquired due to the relatively higher molar doping ratios (**x/y** ~ 7/3 or 8/2). For example, the complex **S12/B16-8/2** exhibited the most extensive SmCP range and the lowest T_f value (Figure 6.7 and Figure 6.6b). As shown in Figure 6, the tendencies of phase transitions influenced by the molar doping ratio effect in four series of complexes **Sm/Bn** were analogous. However, the best and worst extensive efficiencies of SmCP phase were executed in complexes **S12/B16** and **S16/B16**, respectively as shown in Figure 6.7.
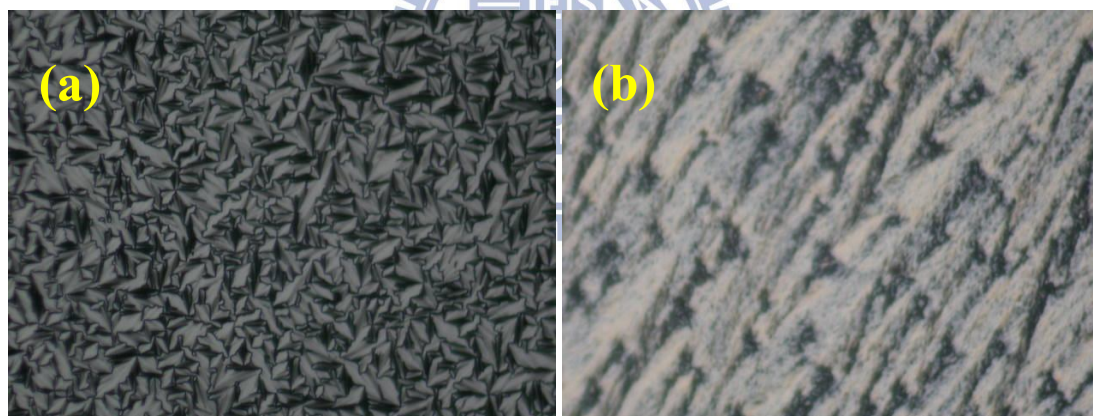
Figure 6.2. The POM textures of (a) the complex **S12/A12-6/4** in 90 °C and (b) the complex **S12/A12-1/9** in 90 °C.

According to the comparisons of phase transitions in series of bent-core covalent- and H-bonded complexes **Sm/An** and **Sm/Bn**, the influences of the molar doping ratio and the length of flexible chain in bent-core complexes on the phase transitions of SmCP phase were collected. In general, the eminently mesophasic expansion would be achieved through the covalent- and H-bonded dopants with

different lengths of flexible chain, and the mesophasic properties were mainly decided by the components with longer flexible chain.[25c] Hence, less doping amount of the covalent-bonded component with longer flexible chain (the stable SmCP contribution) was necessary to extend the SmCP phase for series of complexes **S16/A12** and **S16/B12**, respectively and the most effective expansions and lowest of T_f temperatures of SmCP ranges were displayed in series of complexes **S12/A16** and **S12/B16**, respectively due to the effective H-bonded components **A16** and **B16** (the soft (H-bonded) interacted bent-core molecules).
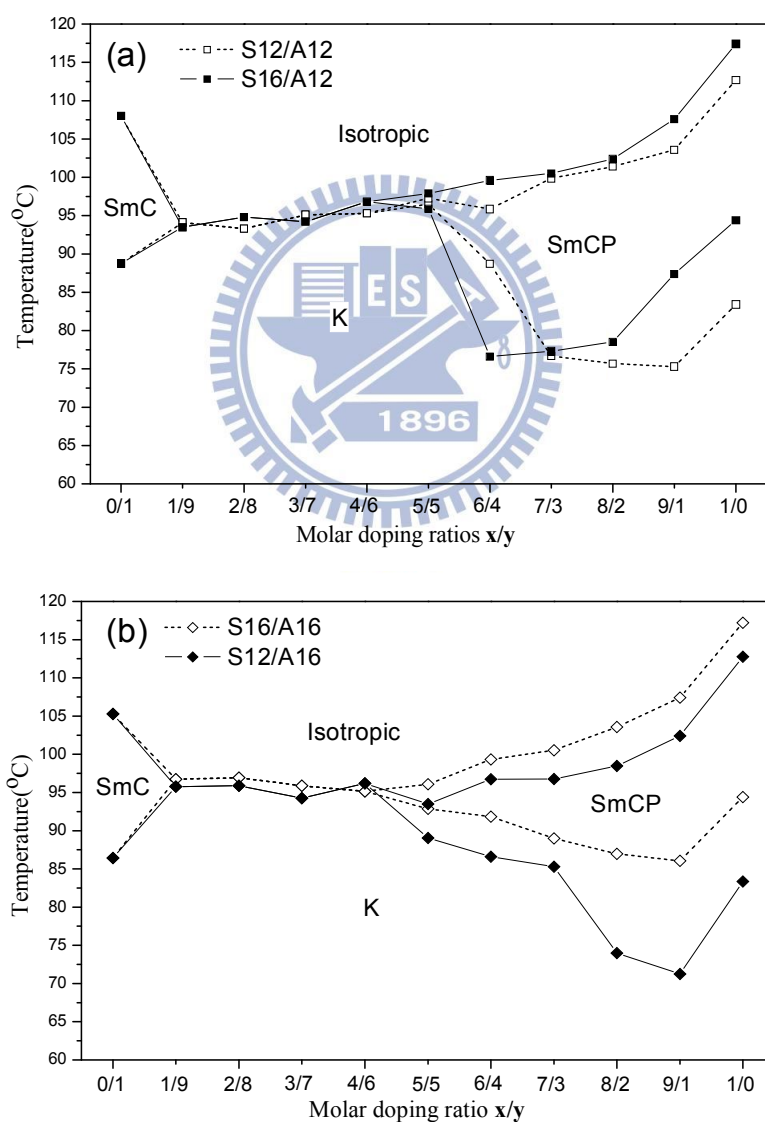
Figure 6.3. The phase transition temperatures of complexes **Sm/An** in various molar doping (**x/y**) ratios (by DSC).
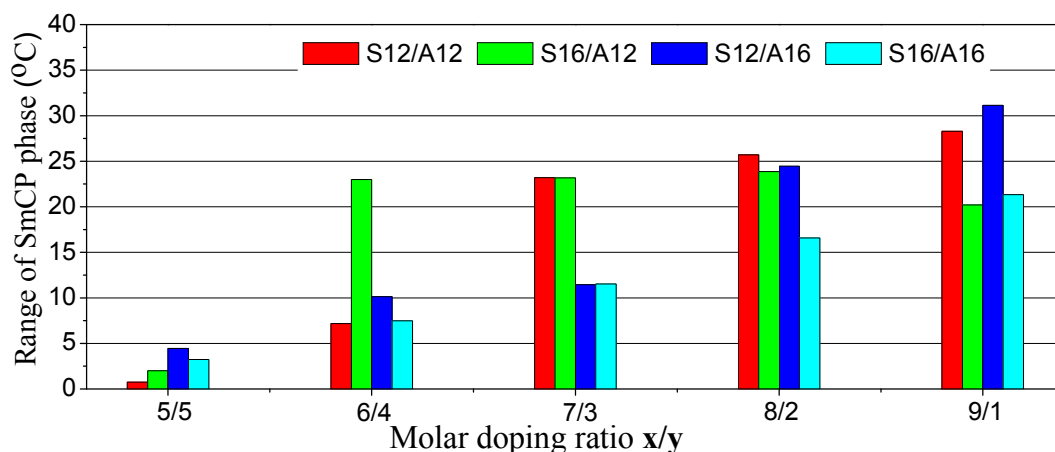
Figure 6.4. The SmCP ranges of series of complexes **Sm/An** in various molar doping (**x/y**) ratios.
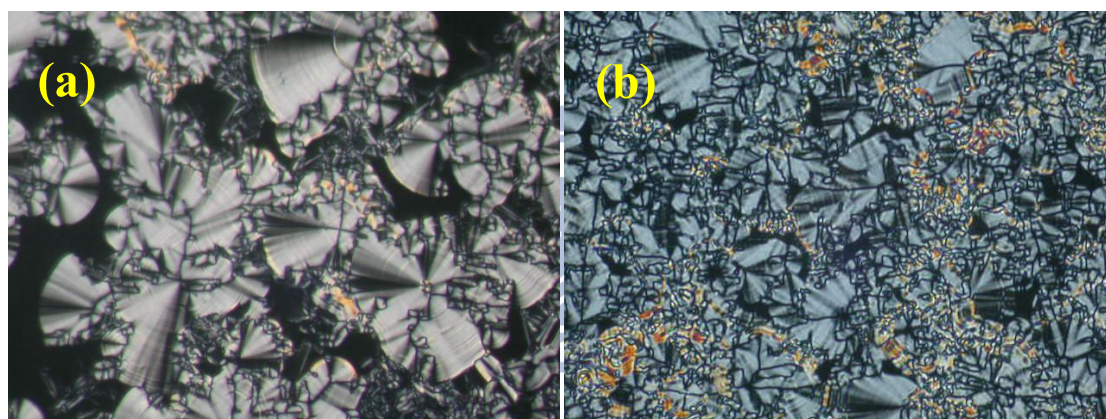
Figure 6.5. The POM textures of (a) the complex **S12/A16-3/7** in 90 °C and (b) the complex **S12/A16-7/3** in 90 °C.

6.3.3. (3) Bent-core covalent- and H-bonded complexes S16/C12-x/y

In order to enhance the polar switchable mesophase of the heterodimer **C12** which exhibited non-polar switchable SmA phase, the series of bent-core covalent- and H-bonded complexes **S16/C12-x/y** were prepared to investigated the influences of dopant effects on varieties of mesophasic types and phase transitions as shown in Figures 6.8-6.9 and Table S6.9. Complexes **S16/C12** with lower **x/y** ratios (1/9, 2/8, and 3/7) possessed non-polar switching SmA phase, and the SmCP phase of the complexes **S16/C12** was exhibited in molar doping ratios as **x/y** = 4/6, 5/5, 6/4, 7/3,
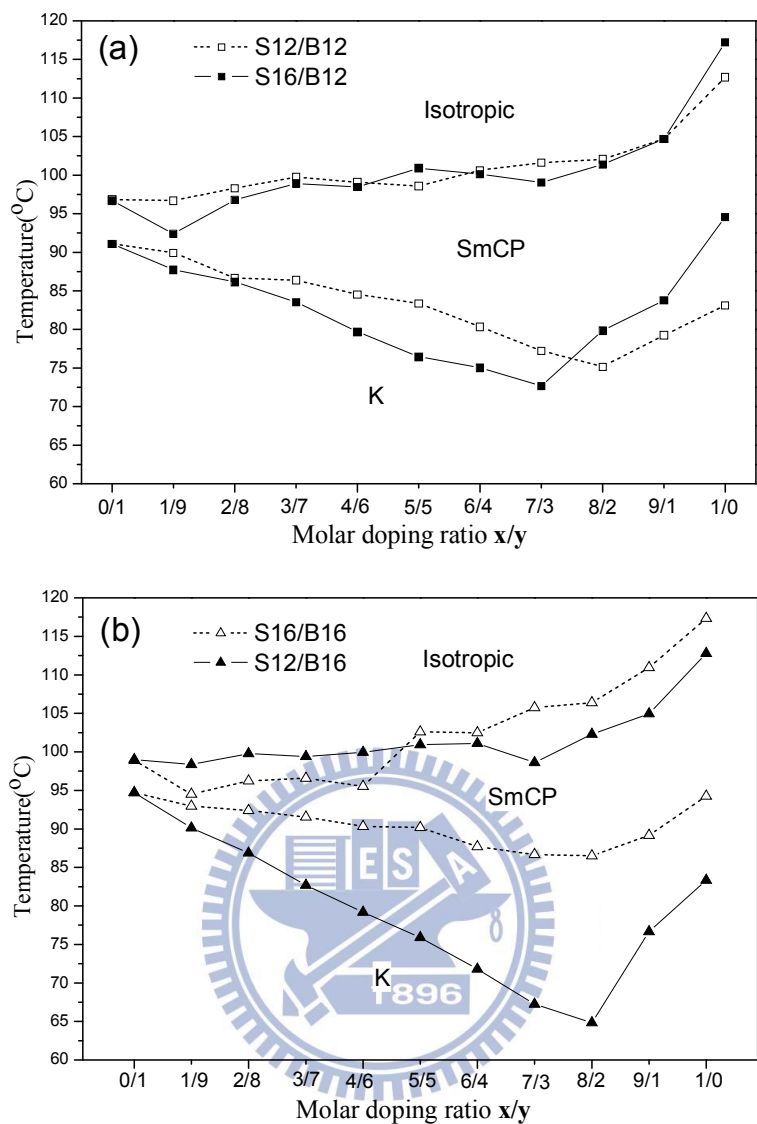
Figure 6.6. The phase transition temperatures of complexes **Sm/Bn** in various molar doping (**x/y**) ratios (by DSC).
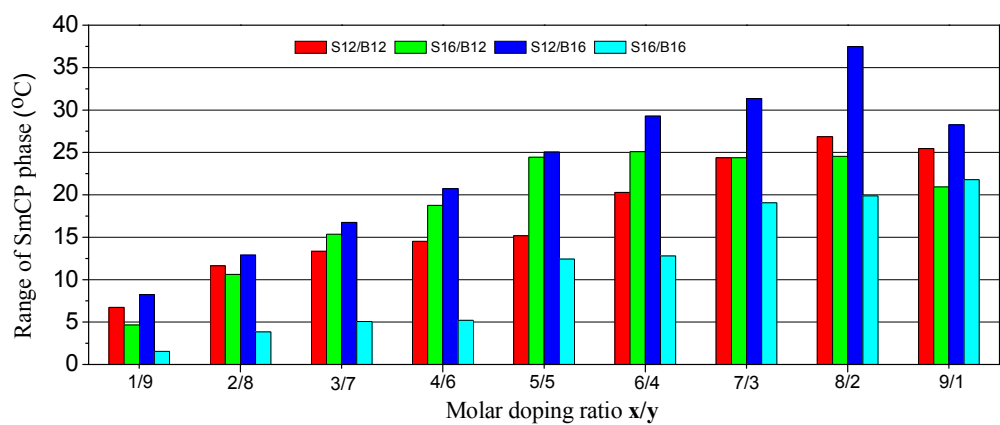
Figure 6.7. The SmCP ranges of series of complexes **Sm/Bn** in various molar doping (**x/y**) ratios.

8/2, and 9/1. In addition, the nematic phase of complexes **S16/C12** was obtained in molar doping ratios **x/y** = 4/6 and 5/5., For example, the POM observations of SmA and SmCP phases in complexes **S16/C12-3/7** and **S16/C12-6/4** were verified to show the fan-like textures as shown in Figure 6.8. Comparing the phase transition temperatures of series of complexes **S16/C12** with their covalent- and H-bonded components **S16** and **C12**, the SmCP phase was enhanced in the complexes with the increasing of **x/y** ratios (**x/y** ≧ 4/6), and these mesophasic ranges and phase transition temperatures of SmCP phase were extended and lower than those of the pure component **S16**. As shown in Figure 6.9, the lowest isotropization (T_i) and freezing (T_f) temperatures were acquired in the complex **S16/C12-6/4** and the most extensive range of SmCP phase was obtained in the complex **S16/C12-7/3**. There results were proven the flexible-chain-length effect again, which indicated the mesophasic properties were mainly decided by the components with longer flexible chain (**S16**) and less doping amount of the covalent-bonded component with longer flexible chain was necessary to achieve the SmCP phase.
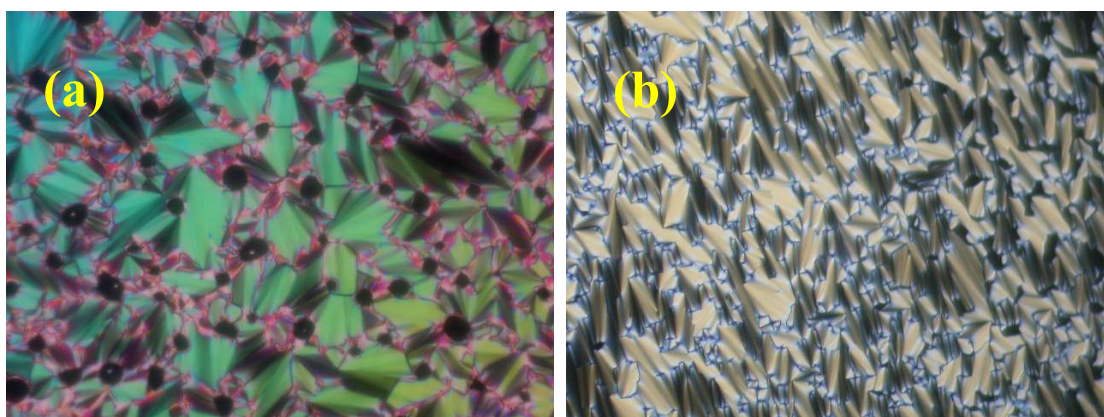
Figure 6.8. The POM textures of (a) the complex **S16/C12-3/7** in 105 °C and (b) the complex **S16/C12-6/4** in 90 °C.
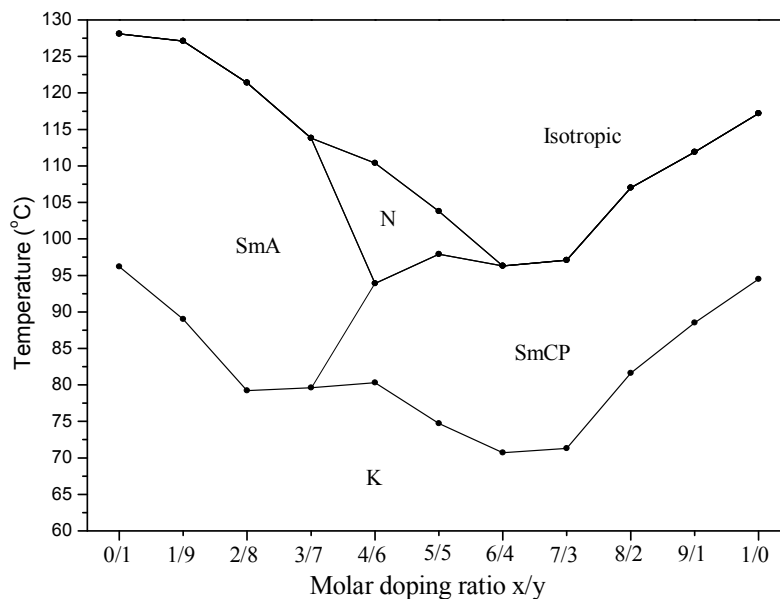
Figure 6.9. The phase transition temperatures of complexes **S16/C12** in various molar doping (**x/y**) ratios (by DSC).

6.3.4. Powder XRD analyses of bent-core covalent- and H-bonded complexes Sm/An-x/y, Sm/Bn-x/y, and S16/C12-x/y

In order to realize the molecular organizations of bent-core covalent- and H-bonded complexes **S12/A12**, **S16/A12**, **S12/A16**, and **S16/A16** with various **x/y** ratios (**x/y** = 0/1 to 1/0), their XRD measurements were examined as shown in Figure 6.10, Figure S6.1-S6.3 (in supporting information), and Table 6.1. As shown in Figure 6.10, the bent-core complexes **S16/A12-4/6**, **S16/A12-7/3**, **S16/A12-8/2**, and **S16/A12-9/1** possessed broad diffuse scattering peaks in wide angle region, which indicated the similar liquid-like, in-plane orders with average intermolecular distances. One set of reflection peaks of complexes **S16/A12-4/6**, **S16/A12-7/3**, **S16/A12-8/2**, and **S16/A12-9/1** were observable in small angle region, describing the smectic lamellar order of uniformly mixed systems (without the phase separation). Comparing corresponding d-spacing values to those of their two bent-core covalent- and H-bonded components **S16** and **A12**, sharp peaks indexed as (001) in the small-angle region at the associated d-spacing values of d_1 = 46.7, 45.8, 44.0, and 41.5 Å were

calculated for complexes **S16/A12-4/6**, **S16/A12-7/3**, **S16/A12-8/2**, and **S16/A12-9/1**, respectively, which were larger than those of two components **S16** and **A12** (40.9 and 32.5 Å, respectively) to mean that the existence of less tilted angles were examined in bent-core complex systems. The similar XRD results of other series of complexes **S12/A12**, **S12/A16**, and **S16/A16** were displayed, where the uniformly mixed systems and lamellar order were further confirmed as shown in Table 6.1 and Figure S6.1-S6.3.

Table 6.1. Powder XRD Data of series of bent-core complexes **S12/A12, S16/A12, S12/A16, and S16/A16** with molar doping ratios **x/y** = 6/4, 7/3, 8/2, and 9/1

Complex	d-spacing（Å）	Complex	d-spacing（Å）	Complex	d-spacing（Å）	Complex	d-spacing（Å）
S12/A12-6/4	42.2	**S16/A12-6/4**	46.7	**S12/A16-6/4**	43.9	**S16/A16-6/4**	48.1
S12/A12-7/3	41.5	**S16/A12-7/3**	45.8	**S12/A16-7/3**	43.1	**S16/A16-7/3**	46.0
S12/A12-8/2	39.3	**S16/A12-8/2**	44.0	**S12/A16-8/2**	39.2	**S16/A16-8/2**	42.9
S12/A12-9/1	35.9	**S16/A12-9/1**	41.5	**S12/A16-9/1**	37.3	**S16/A16-9/1**	41.8
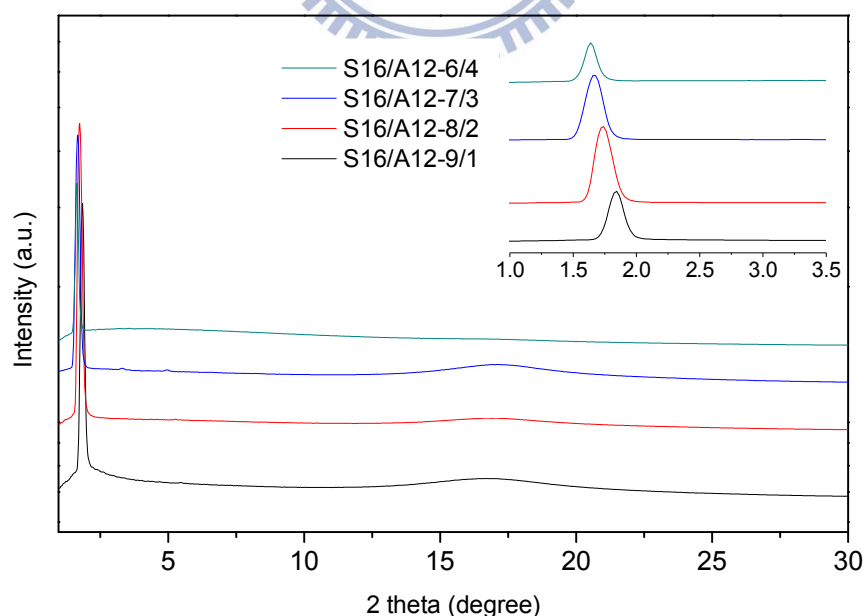
Figure 6.10. Powder X-ray diffraction intensities against angle profiles of bent-core complexes **S16/A12** with molar doping ratios **x/y** = 6/4, 7/3, 8/2, and 9/1.

The structural arrangements of bent-core covalent- and H-bonded complexes **S12/B12**, **S16/B12**, **S12/B16**, and **S16/B16** investigated by XRD measurements were shown in Table 6.2, Figure 6.11, and Figures S6.4-S6.6 (in supporting information). As shown in Figure 6.11 and Table 6.2, complexes **S16/B16-2/8**, **S16/B16-5/5**, and **S16/B16-8/2** exhibited one set of sharp peaks as index of (001) at the corresponding d-spacing values d_1 = 48.0, 43.9, and 41.1 Å, respectively, in small angle region and broad diffuse scattering peaks in wide angle region to indicate the uniformly mixed systems and lamellar order at the SmCP phase cooling temperature. In addition, the corresponding d-spacing values of complexes **S16/B16-2/8**, **S16/B12-5/5**, and **S16/B16-8/2** were smaller than that of the component **B12** and larger than that of the component **S12**, indicating the gradually tilted arrangements by the increasing amount of covalent-bonded component doping. Other series of bent-core complexes **S12/B12**, **S12/B16**, and **S16/B12** revealed the analogous XRD results as complexes **S16/B16** to mean the lamellar arrangements (see Table 6.2 and Figure S6.4-S6.6).

Regarding the powder XRD analyses of series bent-core covalent- and H-bonded complexes **S16/C12**, their XRD results were collected in Figure 6.12 and Table 6.3. The complexes **S16/C12-2/8**, **S16/C12-5/5**, and **S16/C12-8/2** revealed broad diffuse scattering peaks in wide angle region to indicate the similar liquid-like, in-plane orders with average intermolecular distances. The formations of bent-core H-bonded complexes were further confirmed by the different d-spacing values of the smectic phases from those of their constituents. Sharp XRD peaks indexed as (001) in the small angle region were obtained in complexes **S16/C12-2/8**, **S16/C12-5/5**, and **S16/C12-8/2**, respectively. To compare the associated d-spacing values of bent-core complexes **S16/C12-2/8**, **S16/C12-5/5**, **S16/C12-8/2**, and their components **S16** and **C12**, The d-spacing values of bent-core complexes **S16/C12-2/8**, **S16/C12-5/5**, and **S16/C12-8/2** were longer than that of covalent-bonded component **S16** and shorter

than that of H-bonded component **C12**. For instance, the d-spacing value $d_1 = 47.8$ Å of the complex **S16/C12-2/8**, which was closed to the d-spacing value of H-bonded component **C12** ($d_1 = 51.9$ Å), were obtained to indicate the less tilted molecular arrangement. The d-spacing values $d_1 = 43.2$ and 40.0 Å of the complexes **S16/C12-5/5** and **S16/C12-8/2**, respectively, were acquired to indicate the tilted lamellar orders.

Table 6.2. Powder XRD Data of series of bent-core complexes **S12/B12, S16/B12, S12/B16, and S16/B16** with molar doping ratios **x/y** = 2/8, 5/5, and 8/2

Complex	d-spacing (Å)	Complex	d-spacing (Å)	Complex	d-spacing (Å)	Complex	d-spacing (Å)
S12/B12-2/8	42.5	**S16/B12-2/8**	47.2	**S12/B16-2/8**	47.8	**S16/B16-2/8**	48.0
S12/B12-5/5	40.2	**S16/B12-5/5**	44.4	**S12/B16-5/5**	42.5	**S16/B16-5/5**	43.9
S12/B12-8/2	37.6	**S16/B12-8/2**	43.2	**S12/B16-8/2**	37.1	**S16/B16-8/2**	41.1
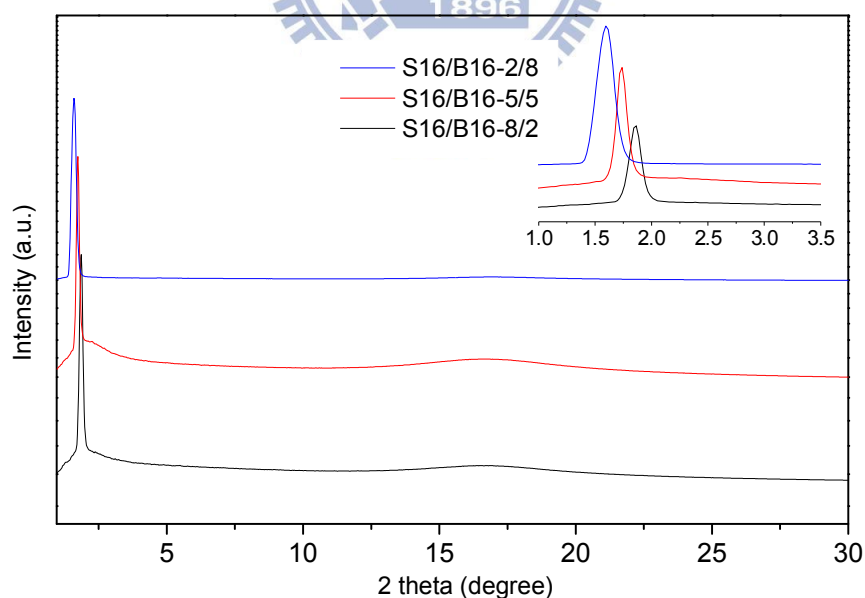
Figure 6.11. Powder X-ray diffraction intensities against angle profiles of bent-core complexes **S16/B16** with molar doping ratios **x/y** = 2/8, 5/5, and 8/2.

Table 6.3. Powder XRD Data of series of bent-core complexes **S16/C12** with molar doping ratios **x/y** = 2/8, 5/5, and 8/2

Complex	Phase	d-spacing（Å）
S16/C12-2/8	SmA	47.8
S16/C12-5/5	SmCP	43.2
S16/C12-8/2	SmCP	39.8
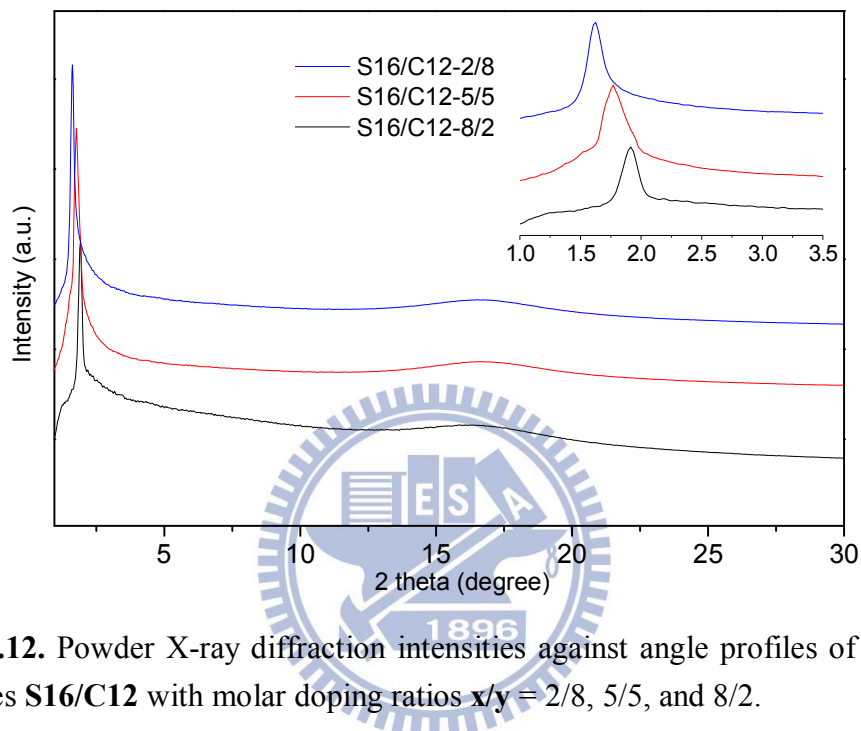
Figure 6.12. Powder X-ray diffraction intensities against angle profiles of bent-core complexes **S16/C12** with molar doping ratios **x/y** = 2/8, 5/5, and 8/2.

6.3.5. Electro-optical properties of bent-core covalent- and H-bonded complexes Sm/An-x/y, Sm/Bn-x/y, and S16/C12-x/y

In order to evaluate the polar switching current properties of the SmCP phase in all bent-core covalent- and H-bonded complexes **Sm/An**, **Sm/Bn**, and **S16/C12**, the triangular wave method[22] was applied to measure the switching current behavior (i.e., the spontaneous polarization) in parallel rubbing cells with a cell gap of 4.25 μm. Regarding the spontaneous polarization (Ps) behaviors of bent-core complexes **Sm/An**, two current peaks per half-period of an applied triangular voltage were observed in the switching current response curves of the SmCP phase in complexes

214

Sm/An with molar doping ratios **x/y** ≧ 5/5. For example, the two-peak switching current response curve of the complex **S12/A16-7/3** in the SmCP phase is shown in Figure 6.13a, where the characteristic behavior of a sequential electric response was due to a ferroelectric state switched into an antiferroelectric ground state and back to the opposite ferroelectric state. These phenomena confirmed the SmCP$_A$ (A = antiferroelectric behavior) structure of the B2 phase in the bent-core H-bonded complex.[55] However, all bent-core complexes of **Sm/An** (**m,n** = 12 and 16, respectively) with lower molar doping ratios **x/y** ≦ 4/6 did not displayed polar smectic phase in cooling temperature processes. As shown in Figure S6.7-S6.10 (in supporting information), the Ps values of complexes **Sm/An** (**x/y** ≧ 5/5), which were saturated probably at Vpp ≧ 300 V (see Figures S6.7-S6.10 of supporting information), could be turned by the molar doping ratios as shown in Figure 6.13b-6.13c. With respect to the Ps behaviors of bent-core complexes **Sm/Bn**, the anti-ferroelectric behaviors of B2 phase were also determined in all series of complexes **Sm/Bn** with molar doping ratios **x/y** from 0/1 to 1/0. For instance, two current peaks per half-period of an applied triangular voltage were observed in the switching current response curves of the SmCP phase in the complex **S12/B16-7/3**, where the characteristic behavior of a sequential electric response was due to a ferroelectric state switched into an antiferroelectric ground state and back to the opposite ferroelectric state again. As shown in Figure 6.14, the Ps values of complexes **Sm/Bn** were straight rising by the increasing of the covalent-bonded amounts and the maximized Ps values were saturated probably at Vpp ≧ 260 V, which are lower than those of pure covalent-bonded components **Sm** (**m** = 12 and 16) as shown in Figure S6.11-S6.14. It was indicated that the H-bonded bent-core dopants in covalent-bonded bent-core molecules would not only decrease the phase transition temperatures but also reduce the voltages of the saturated Ps values due to the softer

rigid-core configurations in the H-bonded complexes.
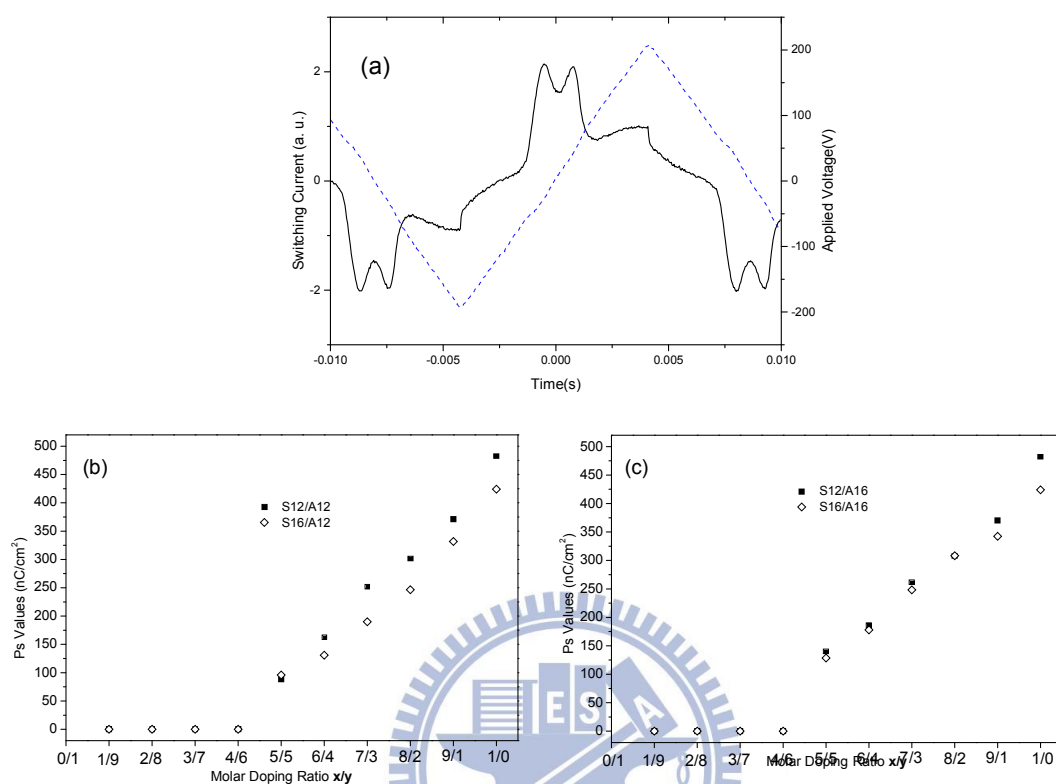
Figure 6.13. (a) Switching current responses of complex **S12/A16-7/3** at 90°C (as V pp = 400 V, f = 60 Hz); (b) the Ps values as a function of molar doping ratio x/y (at the SmCP phases as f = 100Hz) for complexes **S12/A12** and **S16/A12**; (c) the Ps values as a function of molar doping ratio **x/y** (at the SmCP phases as f = 100Hz) for complexes **S12/A16** and **S16/A16**.

The antiferroelectricity was also further evidenced by the dielectric permittivity studies, and series of complexes **Sm/An-8/2** and **Sm/Bn-8/2** (**m**,**n** = 12 and 16, respectively) were were investigated under their cooling processes at a frequency of 5 kHz in nonrubbing cells (9 μm cell gap) as shown in Figure 6.15 and Figures S6.15-S6.16. In cooling processes, higher permittivity values (ε ~ 12-16) of SmCP phases were observed than those of the isotropic and crystalline states in complexes **S16/A12-8/2** and **S16/B12-8/2**, which indicates the antiferroelectric polar

smectic phase.[57] Similar higher permittivity values of SmCP phase in components **S16** (ε ~ 17-21) and **B12** (ε ~ 12) were obtained. However, no higher permittivity values were achieved in the SmC phase of complex **A12** to further prove the tilt smectic phase without polar switching behavior. The analogous results of SmCP phase in other complexes **Sm/An-8/2** and **Sm/Bn-8/2** were also displayed in Figures S6.15-S6.16. There phenomena were further proved the spontaneous polarization behaviors of polar switchable smectic phase in bent-core complexes again.
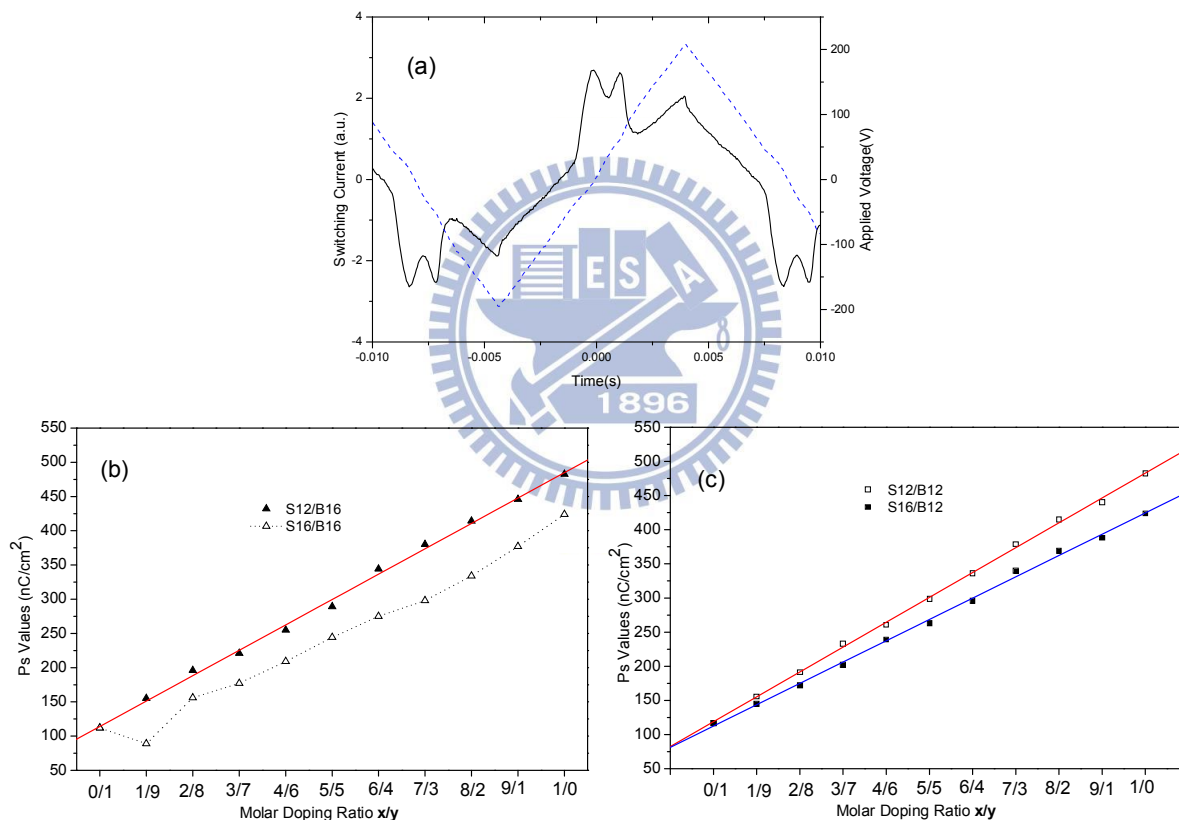
Figure 6.14. (a) Switching current responses of complex **S12/B16-7/3** at 90°C (as V pp = 400 V, f = 60 Hz); (b) the Ps values as a function of molar doping ratio x/y (at the SmCP phases as f = 100Hz) for complexes **S12/B12** and **S16/B12**; (c) the Ps values as a function of molar doping ratio **x/y** (at the SmCP phases as f = 100Hz) for complexes **S12/B16** and **S16/B16**.
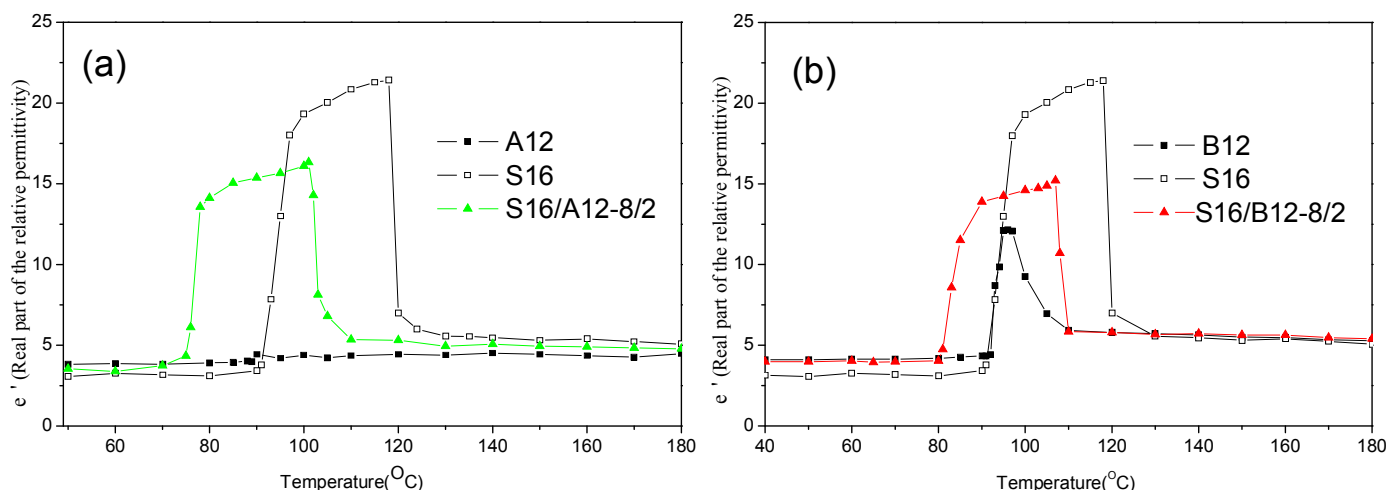
Figure 6.15. Dielectric permittivity studies of (a) the complex **S16/A12-8/2** and its components and (b) the complex **S16/B12-8/2** and its components in cooling processes.

6.3.6. Chirality Investigation

A switching process could also be checked through the rotation of the extinction crosses (Figure 6.16) by applying (or after removing) opposite d.c. electric fields in the bent-core complexes with the SmCP phase. For instance, the extinction crosses of broken circular domains in the complex **S16/B12-7/3** were formed in the SmCP mesophasic range, in which the smectic layers were circularly arranged around the centers of the domains, which were organized according to the domain models proposed by Link et al. [8,24] As shown in Figure 6.16, the rotation of the extinction crosses during the switched on and off states in the complex **S16/B12-7/3** demonstrated the chiral domain behavior. In view of Figure 6.16a and 6.16c, by applying d.c. electric fields (with reverse polarities), the extinction crosses rotated, indicating a synclinic tilt in the ferroelectric state (SmC$_S$P$_F$). By removing electric fields (off state), the extinction crosses were reoriented back to the crossed polarizer directions (see Figure 6.16b), where an anticlinic tilt existed in the antiferroelectric ground state (SmC$_A$P$_A$). Hence, the anti-clinic and anti-ferroelectric polar smectic (SmC$_A$P$_A$) arrangement in the ground state of bent-core complex **S16/B12-7/3** was

identified.[7]

With respect to the chirality investigations of series complexes **Sm/An** with the SmCP phase, the extinction crosses of circular domains were hard to retained under the d.c. electric fields applying to determine their chiral behaviors. However, chiral domain behavior could also be proven by the method of rotating the polarizer under the triangular-wave applying electric fields. For instance, the polarizer was rotated clockwise by a small angle of 10° from the crossed position in complex **S12/A16-6/4**, then the dark and bright domains become clearly distinguishable (Figure 6.17b). On rotating the polarizer counterclockwise by the same angle (10°) from the crossed position, the previously observed dark domains turned to bright domains, and vice versa (see Figure 6.17c). This observation was also indicative of the occurrence of chiral domains with opposite handedness, even through the chiral domain of SmCP phase was disappeared by the removing of applied triangular-wave voltage by the rotating of polarizer (Figure 6.17d).
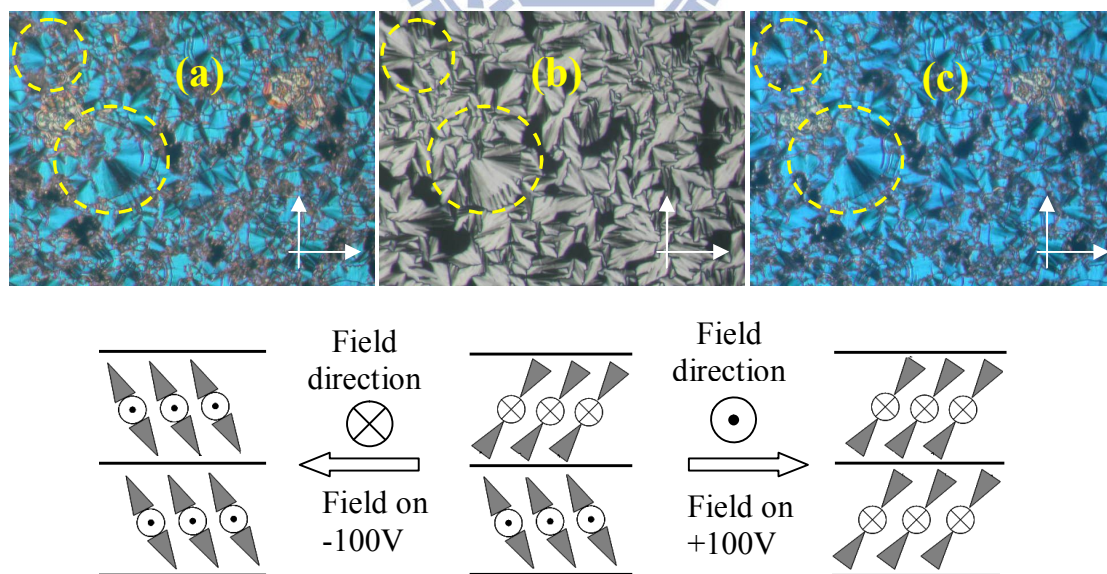
Figure 6.16. POM textures of the antiferroelectric SmC$_A$P$_A$ chiral domain (in a parallel rubbing cell with a cell gap of 4.25 μm) in the complex **S16/B12-7/3** by applying dc electric fields from (a) -100 to (b) 0 to (c) +100 V. (White arrows are the directions of polarizers and analyzers).

Figure 6.17. The chiral domain textures of the complex **S12/A16-6/4** under applied triangular-wave voltage (Vpp = 180V). During the applied voltage, the observations of chiral domain were revealed via (a) crossed polarizer to (b) and (c) opposite directions of polarizer rotating conditions. The chiral domain was disappeared by the removing of applied voltage.

6.4. Conclusion

In summary, banana-shaped liquid crystalline (LC) covalent- and H-bonded complexes **Sm/An**, **Sm/Bn**, and **S16/C12** (with various **x/y** molar ratios) were developed by mixing both H-bonded and covalent-bonded moieties in combination with small molecular structures to stabilize the polar smectic (SmC_AP_A) phase. Due to the stronger intermolecular interactions of component **An**, SmCP phase was not enhanced in series of complexes **Sm/An** with lower **x/y** molar ratios (**x/y** $\leqq$ 5/5). However, more extensive and lower phase transition temperatures of SmCP phase in series of complexes **Sm/An** with higher **x/y** molar ratios (**x/y** $\geqq$ 5/5) were obtained, where the lowest and most extensive SmCP phase could be achieved in complexes

220

with **x/y** molar ratios in 7/3 or 8/2. With respect to the phase transition temperatures of series of complexes **Sm/Bn,** which all complexes possessed SmCP phase, the similar mesophasic tendencies of SmCP phase were also displayed. In addition, the eminently mesophasic expansion would be achieved through the covalent- and H-bonded dopants with different lengths of flexible chain, and the mesophasic properties were mainly decided by the components with longer flexible chain. It meant that less doping amount of the covalent-bonded component with longer flexible chain (the stable SmCP contribution) was necessary to extend the SmCP phase. Hence, the SmCP phase was successfully enhanced in series of complexes S16/C12 with low **x/y** molar ratios (**x/y** $\geqq$ 4/6). The antiferroelectric and anticlinic intermolecular arrangement of SmC_AP_A ground state was exhibited in all bent-core complexes with polar switchable B2 phase. The tunable maximized Ps values of bent-core complexes were saturated in lower applied electric fields due to the H-bonded bent-core dopants.
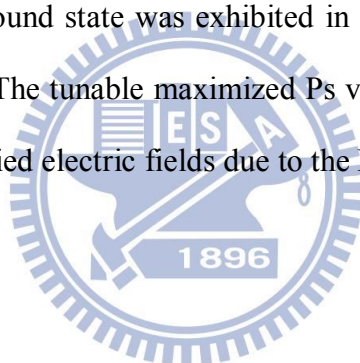
6.5. Electronic Supplementary Information
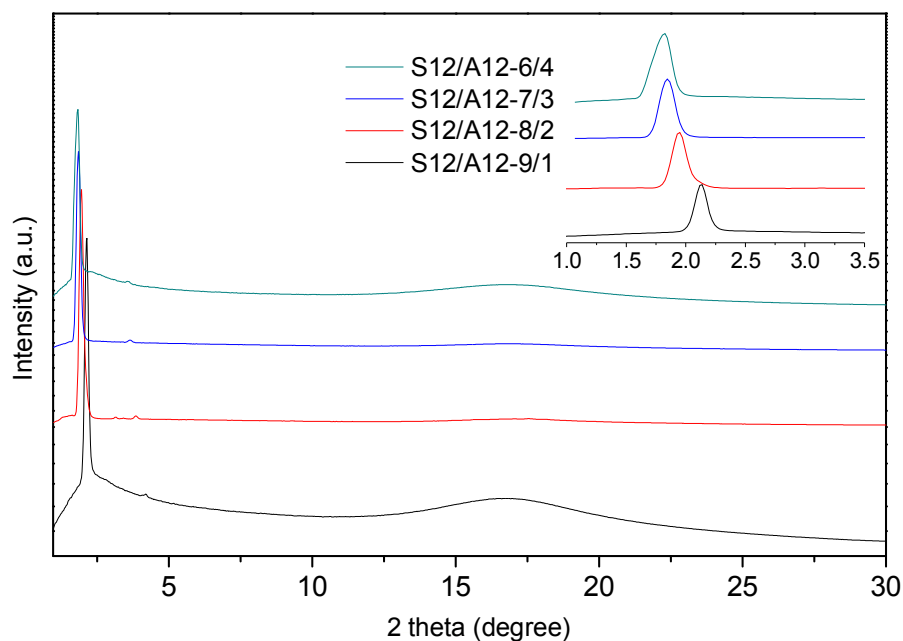
Figure S6.1. Powder X-ray diffraction intensities against angle profiles of bent-core complexes **S12/A12** with molar doping ratios **x/y** = 6/4, 7/3, 8/2, and 9/1.
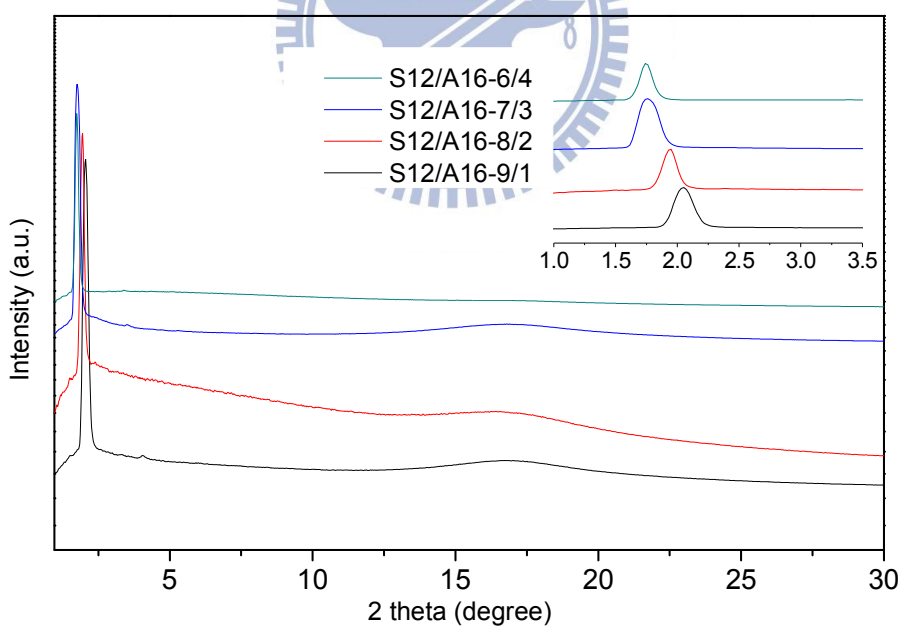
Figure S6.2. Powder X-ray diffraction intensities against angle profiles of bent-core complexes **S12/A16** with molar doping ratios **x/y** = 6/4, 7/3, 8/2, and 9/1.
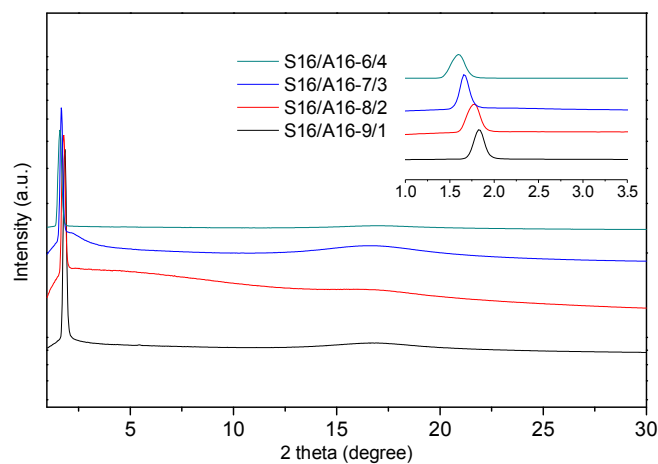
Figure S6.3. Powder X-ray diffraction intensities against angle profiles of bent-core complexes **S16/A16** with molar doping ratios **x/y** = 6/4, 7/3, 8/2, and 9/1.
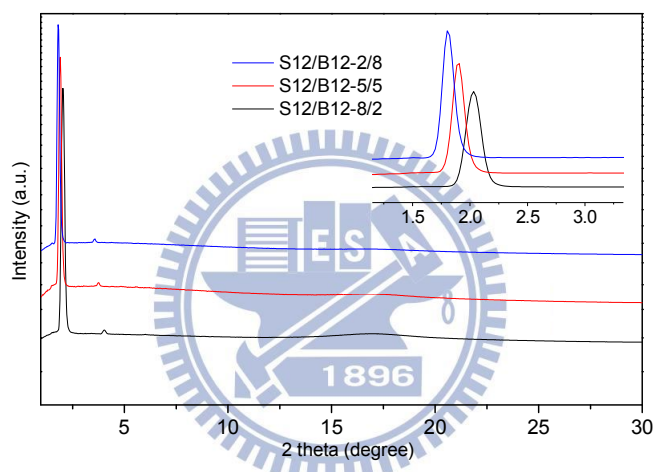
Figure S6.4. Powder X-ray diffraction intensities against angle profiles of bent-core complexes **S12/B12** with molar doping ratios **x/y** = 2/8, 5/5, and 8/2.
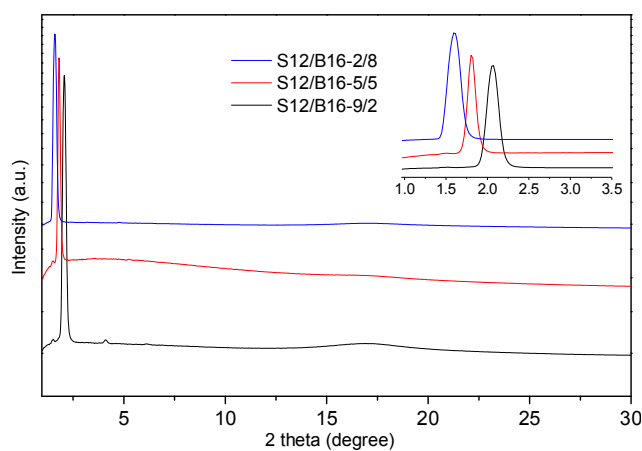
Figure S6.5. Powder X-ray diffraction intensities against angle profiles of bent-core complexes **S12/B16** with molar doping ratios **x/y** = 2/8, 5/5, and 8/2.
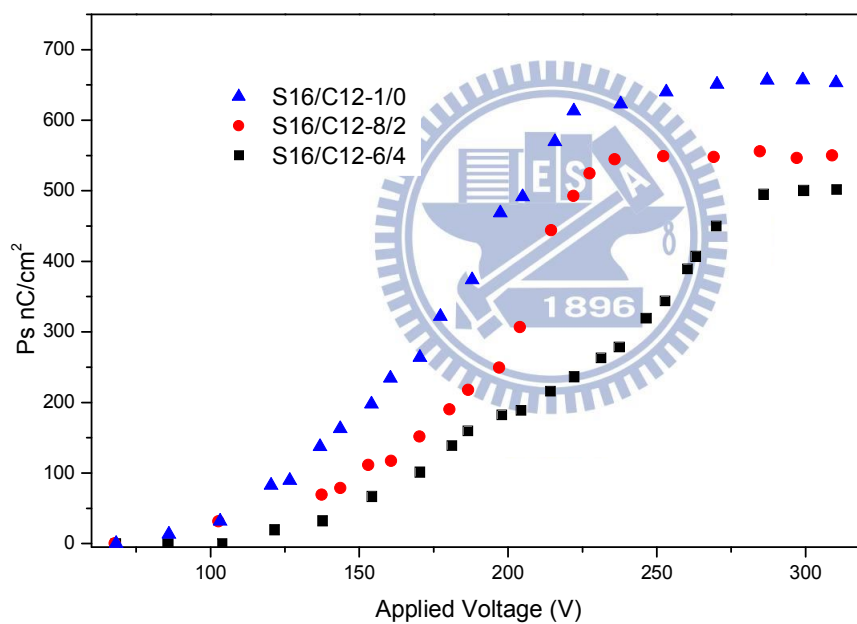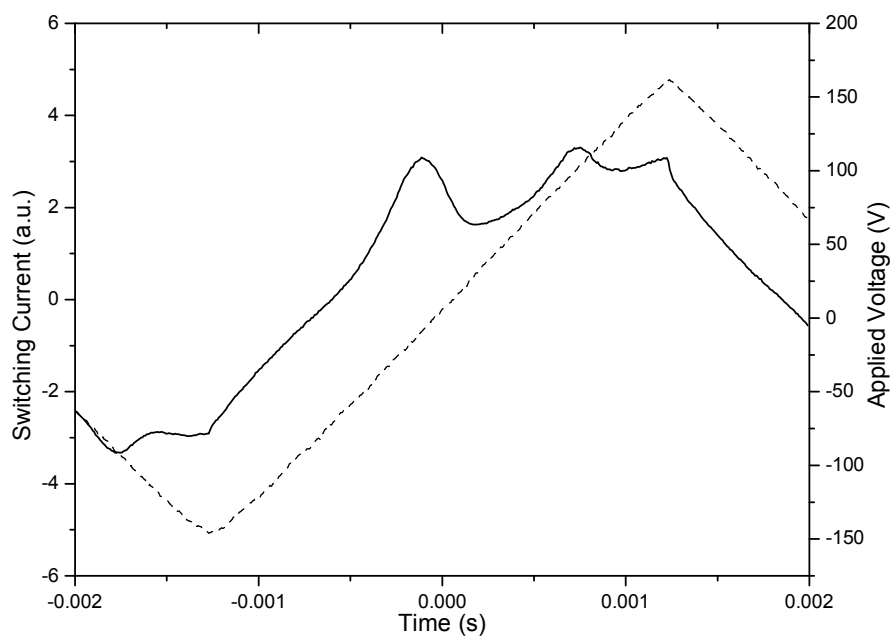
Figure S6.6. (a) Switching current responses of complex **S16/C12-4/6** at 90°C (as V pp = 300 V, f = 60 Hz). (b) Ps values as a function of applied voltages (at the SmCP phase as f = 60 Hz) for bent-core complexes **S16/C12** (**x/y** = 1/0, 8/2, and 6/4).
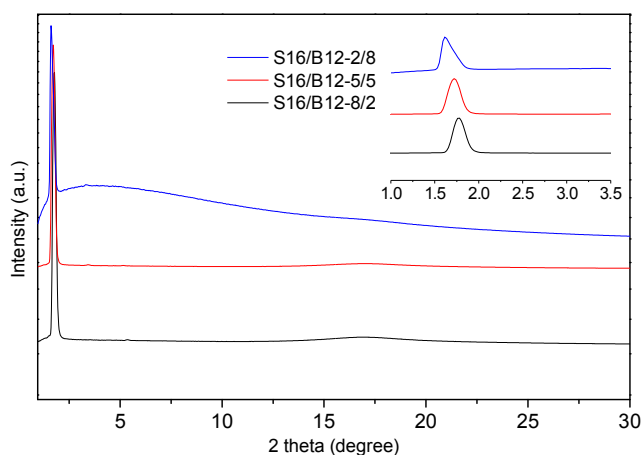
Figure S6.7. Powder X-ray diffraction intensities against angle profiles of bent-core complexes **S16/B12** with molar doping ratios **x/y** = 2/8, 5/5, and 8/2.
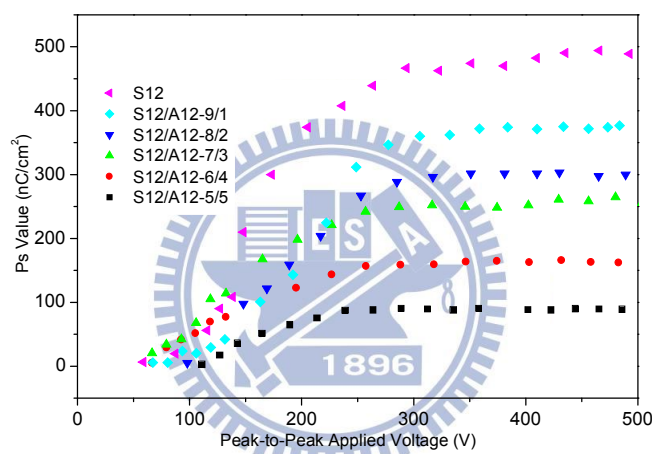
Figure S6.8. Ps values as a function of applied voltages (at the SmCP phase as f = 100 Hz) for bent-core complexes **S12/A12** (**x/y** = 1/0, 9/1, 8/2, 7/3, 6/4, and 5/5).
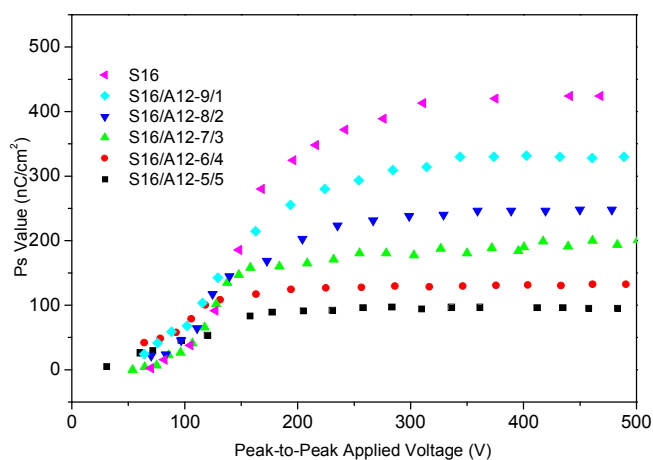
Figure S6.9. Ps values as a function of applied voltages (at the SmCP phase as f = 100 Hz) for bent-core complexes **S16/A12** (**x/y** = 1/0, 9/1, 8/2, 7/3, 6/4, and 5/5).
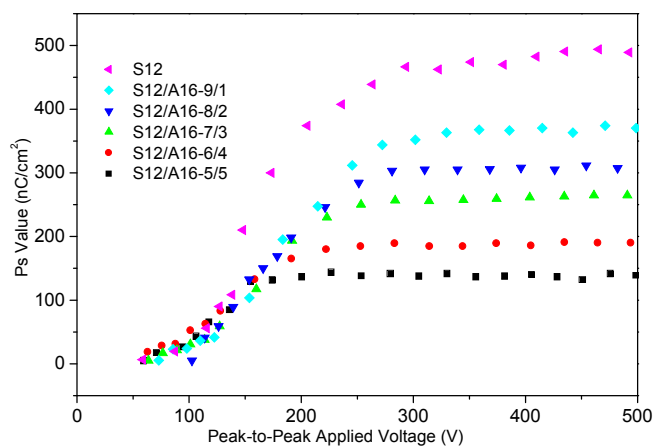
Figure S6.10. Ps values as a function of applied voltages (at the SmCP phase as f = 100 Hz) for bent-core complexes **S12/A16** (**x/y** = 1/0, 9/1, 8/2, 7/3, 6/4, and 5/5).
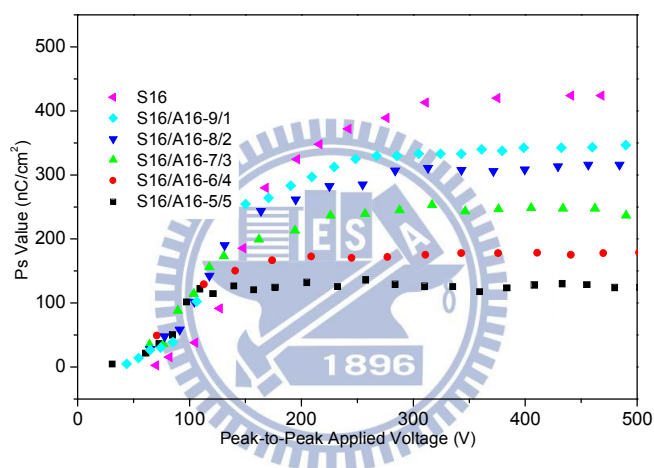
Figure S6.11. Ps values as a function of applied voltages (at the SmCP phase as f = 100 Hz) for bent-core complexes **S16/A16** (**x/y** =1/0, 9/1, 8/2, 7/3, 6/4, and 5/5).
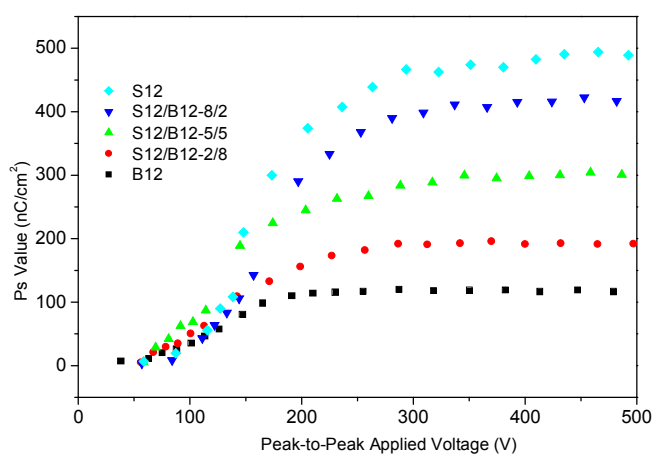
Figure S6.12. Ps values as a function of applied voltages (at the SmCP phase as f = 100 Hz) for bent-core complexes **S12/B12** (**x/y** = 1/0, 8/2, 5/5, 2/8, and 0/1).
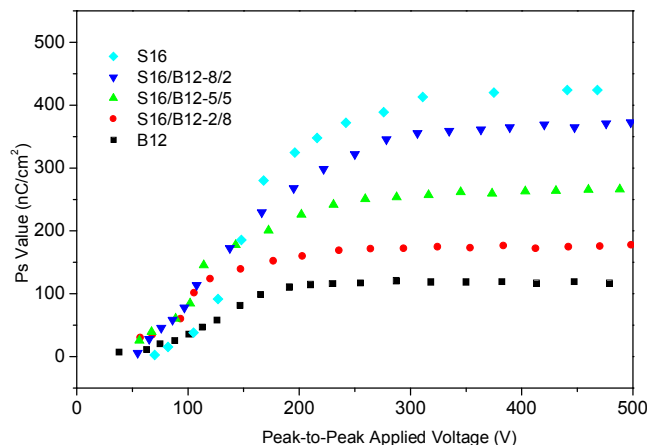
Figure S6.13. Ps values as a function of applied voltages (at the SmCP phase as f = 100 Hz) for bent-core complexes **S16/B12** (**x/y** = 1/0, 8/2, 5/5, 2/8, and 0/1).
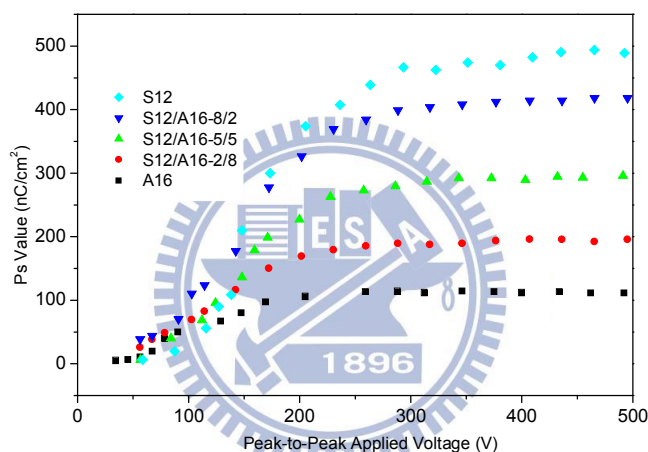
Figure S6.14. Ps values as a function of applied voltages (at the SmCP phase as f = 100 Hz) for bent-core complexes **S12/B16** (**x/y** = 1/0, 8/2, 5/5, 2/8, and 0/1).
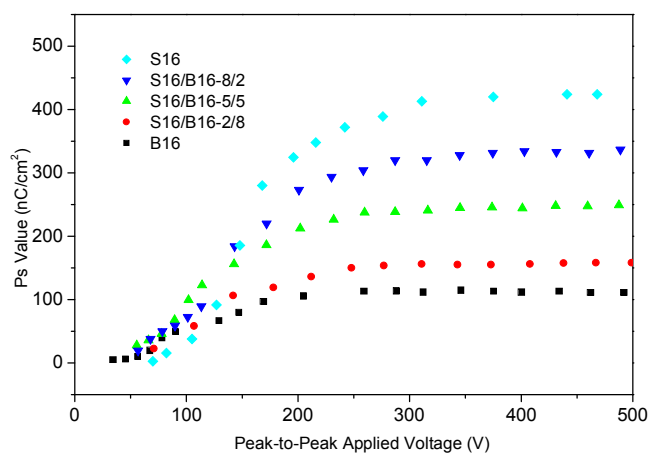
Figure S6.15. Ps values as a function of applied voltages (at the SmCP phase as f = 100 Hz) for bent-core complexes **S16/B16** (**x/y** = 1/0, 8/2, 5/5, 2/8, and 0/1).
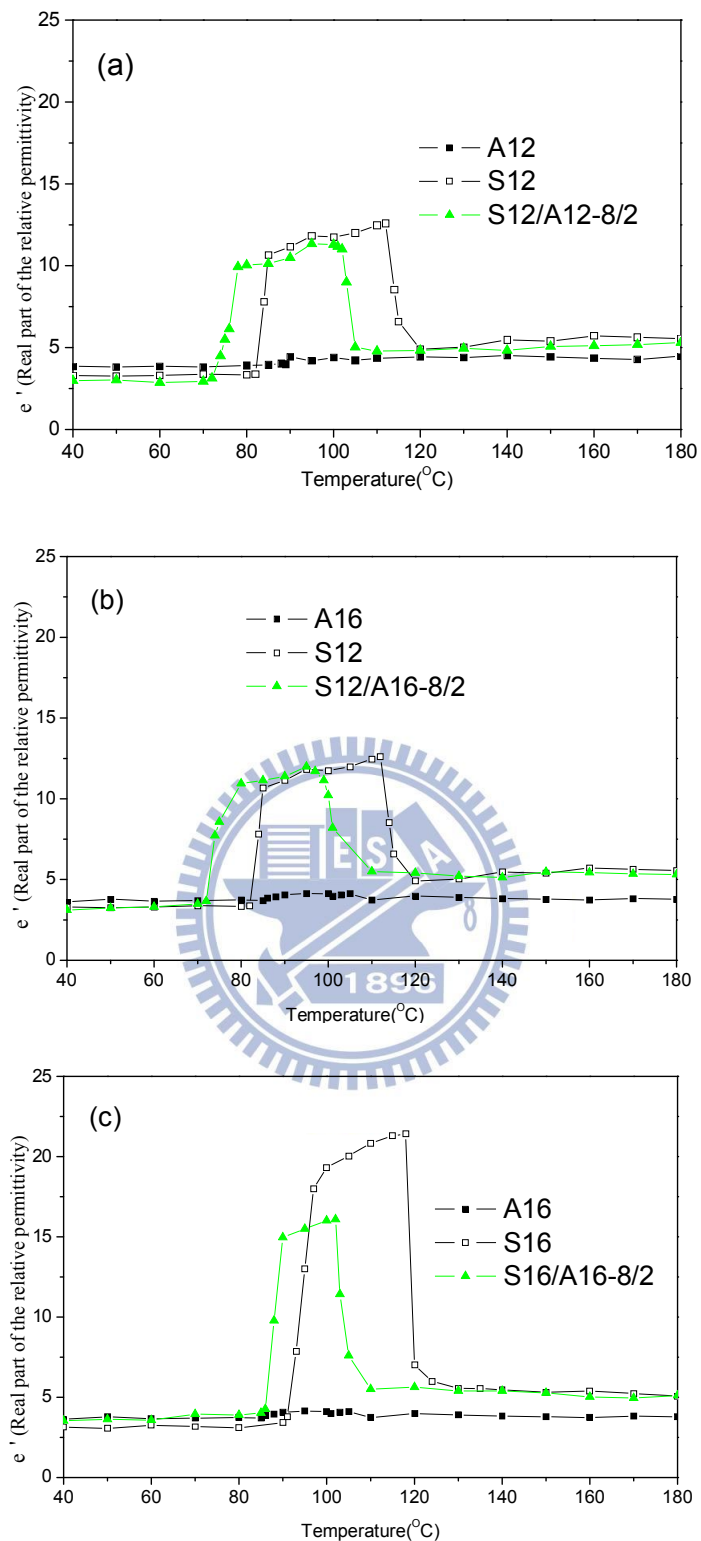
Figure S6.16. Dielectric permittivity studies of (a) the complex **S12/A12-8/2** and its components, (b) the complex **S12/A16-8/2** and its components, and (c) the complex **S16/A16-8/2** and its components in cooling processes.
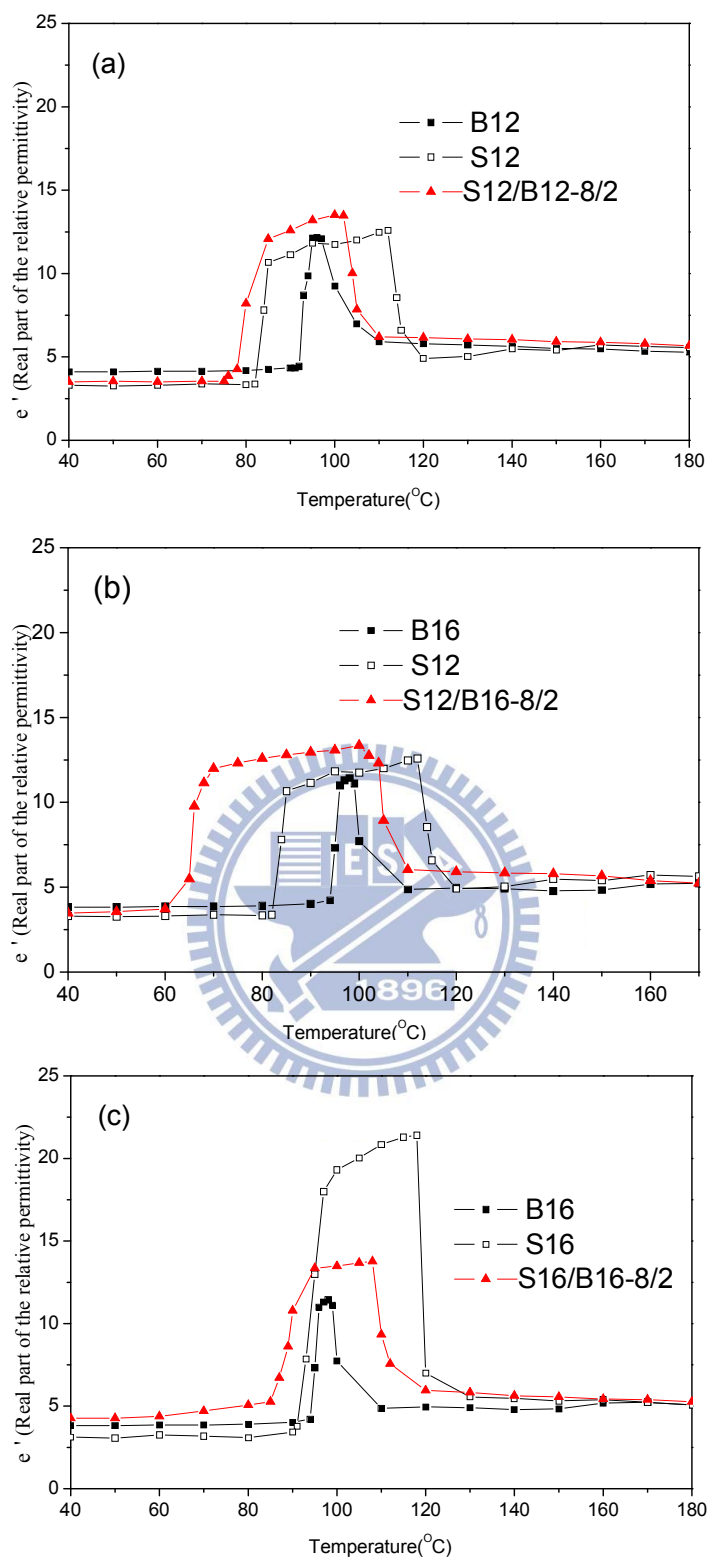
Figure S6.17. Dielectric permittivity studies of (a) the complex **S12/B12-8/2** and its components, (b) the complex **S12/B16-8/2** and its components, and (c) the complex **S16/B16-8/2** and its components in cooling processes.

Table S6.1. Phase Transition Temperatures and Enthalpies of complexes **S12/A12**

Compound		Phase transition temperature/^{o}C [Enthalpy/kJ/g]			
A12	**I**	108[4.4]	**SmCP**	88.7[32]	**K**
S12/A12-10/90	**I**	94.1[142.9]	**SmCP**	—	**K**
S12/A12-20/80	**I**	90.4[109.1]	**SmCP**	—	**K**
S12/A12-30/70	**I**	95.8[99.9]	**SmCP**	—	**K**
S12/A12-40/60	**I**	96[82.6]	**SmCP**	—	**K**
S12/A12-50/50	**I**	97.3	**SmCP**	96.6[72.4][a]	**K**
S12/A12-60/40	**I**	95.9[44.9]	**SmCP**	88.6[14.8]	**K**
S12/A12-70/30	**I**	100[56.3]	**SmCP**	76.7[46.7]	**K**
S12/A12-80/20	**I**	101.6[53.5]	**SmCP**	75.3[55.9]	**K**
S12/A12-90/10	**I**	103.6[45.7]	**SmCP**	76[59.2]	**K**
S12	**I**	112.7[43.8]	**SmCP**	83.3[73.7]	**K**

I = isoptropic state; SmCP = polar tilt smectic phase; K = crystalline state. The phase transitions were measured by DSC at the 2nd cooling scan with a cooling rate of 5°Cmin^{-1}.

Table S6.2. Phase Transition Temperatures and Enthalpies of complexes **S16/A12**

Compound		Phase transition temperature/^{o}C [Enthalpy/kJ/g]			
A12	**I**	108[4.4]	**SmCP**	88.7[32]	**K**
S16/A12-10/90	**I**	93.3[125.9]	**SmCP**	—	**K**
S16/A12-20/80	**I**	94.8[109.8]	**SmCP**	—	**K**
S16/A12-30/70	**I**	94.1[80.3]	**SmCP**	—	**K**
S16/A12-40/60	**I**	98.3[85.1]	**SmCP**	—	**K**
S16/A12-50/50	**I**	98.2	**SmCP**	95.9[91.6][a]	**K**
S16/A12-60/40	**I**	99.5[56.2]	**SmCP**	77.4[14.8]	**K**
S16/A12-70/30	**I**	100.6[49.2]	**SmCP**	76.9[39.0]	**K**
S16/A12-80/20	**I**	101.9[51.5]	**SmCP**	77.9[62.3]	**K**
S16/A12-90/10	**I**	108.0[47.0]	**SmCP**	87.4[83.2]	**K**
S16	**I**	117.2[41.5]	**SmCP**	94.5[91.2]	**K**

I = isoptropic state; SmCP = polar tilt smectic phase; K = crystalline state. The phase transitions were measured by DSC at the 2nd cooling scan with a cooling rate of 5°Cmin^{-1}.

Table S6.3. Phase Transition Temperatures and Enthalpies of complexes **S12/A16**

Compound		Phase transition temperature/°C [Enthalpy/kJ/g]			
A16	**I**	105.4[18.3]	**SmCP**	86.3[133.7]	**K**
S12/A16-10/90	**I**	95.7[132.2]	**SmCP**	—	**K**
S12/A16-20/80	**I**	95.8[95.5]	**SmCP**	—	**K**
S12/A16-30/70	**I**	94.1[112.3]	**SmCP**	—	**K**
S12/A16-40/60	**I**	96.4[82]	**SmCP**	—	**K**
S12/A16-50/50	**I**	93.4	**SmCP**	89.1[70.9][a]	**K**
S12/A16-60/40	**I**	98.7[60.3]	**SmCP**	86.2[23.2]	**K**
S12/A16-70/30	**I**	99.9[54.3]	**SmCP**	85.3[23.4]	**K**
S12/A16-80/20	**I**	98.4[43.6]	**SmCP**	73.9[51.3]	**K**
S12/A16-90/10	**I**	102.4[46.6]	**SmCP**	71.3[59.2]	**K**
S12	**I**	112.7[43.8]	**SmCP**	83.3[73.7]	**K**

I = isoptropic state; SmCP = polar tilt smectic phase; K = crystalline state. The phase transitions were measured by DSC at the 2nd cooling scan with a cooling rate of 5°Cmin⁻¹.

Table S6.4. Phase Transition Temperatures and Enthalpies of complexes **S16/A16**

Compound		Phase transition temperature/°C [Enthalpy/kJ/g]			
A16	**I**	105.4[18.3]	**SmCP**	86.3[133.7]	**K**
S16/A16-10/90	**I**	96[146.3]	**SmCP**	—	**K**
S16/A16-20/80	**I**	96.5[129.2]	**SmCP**	—	**K**
S16/A16-30/70	**I**	95.9[134.1]	**SmCP**	—	**K**
S16/A16-40/60	**I**	96[117.6]	**SmCP**	—	**K**
S16/A16-50/50	**I**	96.1	**SmCP**	92.0[129][b]	**K**
S16/A16-60/40	**I**	99.5[48.7]	**SmCP**	91.9[68.8]	**K**
S16/A16-70/30	**I**	100.4[47.8]	**SmCP**	89.0[80.4]	**K**
S16A16-80/20	**I**	103.6[51.8]	**SmCP**	86.8[87.4]	**K**
S16/A16-90/10	**I**	107.5[46.4]	**SmCP**	86.1[87.0]	**K**
S16	**I**	117.2[41.5]	**SmCP**	94.5[91.2]	**K**

I = isoptropic state; SmCP = polar tilt smectic phase; K = crystalline state. The phase transitions were measured by DSC at the 2nd cooling scan with a cooling rate of 5°Cmin⁻¹.

Table S6.5. Phase Transition Temperatures and Enthalpies of complexes **S12/B12**

Compound	Phase transition temperature/°C [Enthalpy/kJ/g]				
B12	**I**	96.8[35.4]	**SmCP**	90.7[21.7]	**K**
S12/B12-10/90	**I**	96.4[29.2]	**SmCP**	89.9[35.5]	**K**
S12/B12-20/80	**I**	98.3[30.5]	**SmCP**	86.8[23.9]	**K**
S12/B12-30/70	**I**	99.7[31.7]	**SmCP**	86.4[26.8]	**K**
S12/B12-40/60	**I**	99.2[28.2]	**SmCP**	84.6[27.4]	**K**
S12/B12-50/50	**I**	98.5[24.9]	**SmCP**	83.4[26.8]	**K**
S12/B12-60/40	**I**	100.5[54.1]	**SmCP**	80.2[59.5]	**K**
S12/B12-70/30	**I**	101.7[48.6]	**SmCP**	77.3[63.6]	**K**
S12/B12-80/20	**I**	102[52.1]	**SmCP**	75.2[59.0]	**K**
S12/B12-90/10	**I**	104.6[45.6]	**SmCP**	79.4[68.7]	**K**
S12	**I**	112.7[43.8]	**SmCP**	83.3[73.7]	**K**

Table S6.6. Phase Transition Temperatures and Enthalpies of complexes **S12/B16**

Compound	Phase transition temperature/°C [Enthalpy/kJ/g]				
S12	**I**	112.7[43.8]	**SmCP**	83.3[73.7]	**K**
S12/B16-10/90	**I**	92.3	**SmCP**	87.7[85]	**K**
S12/B16-20/80	**I**	96.7[50]	**SmCP**	86.8[23.9]	**K**
S12/B16-30/70	**I**	99.1[57]	**SmCP**	86.4[26.8]	**K**
S12/B16-40/60	**I**	98.3[55.8]	**SmCP**	84.6[27.4]	**K**
S12/B16-50/50	**I**	100.8[54.2]	**SmCP**	83.4[26.8]	**K**
S12/B16-60/40	**I**	100[45.8]	**SmCP**	80.2[59.5]	**K**
S12/B16-70/30	**I**	97[30.7]	**SmCP**	77.3[63.6]	**K**
S12/B16-80/20	**I**	105.4[42.3]	**SmCP**	75.2[59]	**K**
S12/B16-90/10	**I**	104.6[31.5]	**SmCP**	79.4[68.7]	**K**
B16	**I**	97.4[38.8]	**SmCP**	94.7[63.5]	**K**

Table S6.7. Phase Transition Temperatures and Enthalpies of complexes **S16/B12**

Compound		Phase transition temperature/°C [Enthalpy/kJ/g]			
S16	**I**	117.2[41.5]	**SmCP**	94.5[91.2]	**K**
S16/B12-10/90	**I**	98.3[56.9]	**SmCP**	90.2[85.3]	**K**
S16/B12-20/80	**I**	99.7[54.5]	**SmCP**	86.8[67.5]	**K**
S16/B12-30/70	**I**	99.4[52.1]	**SmCP**	82.6[60.8]	**K**
S16/B12-40/60	**I**	99.9[44.8]	**SmCP**	79.2[42.5]	**K**
S16/B12-50/50	**I**	100.9[53.5]	**SmCP**	75.9[42.8]	**K**
S16/B12-60/40	**I**	100.9[50]	**SmCP**	71.6[50.9]	**K**
S16/B12-70/30	**I**	98.4[45.4]	**SmCP**	67.3[46.2]	**K**
S16/B12-80/20	**I**	102.1[45.4]	**SmCP**	64.7[48.8]	**K**
S16/B12-90/10	**I**	104.9[43.2]	**SmCP**	76.4[63.5]	**K**
B12	**I**	96.8[35.4]	**SmCP**	90.7[21.7]	**K**

Table S6.8. Phase Transition Temperatures and Enthalpies of complexes **S16/B16**

Compound		Phase transition temperature/°C [Enthalpy/kJ/g]			
S16	**I**	117.2[41.5]	**SmCP**	94.5[91.2]	**K**
S16/B16-10/90	**I**	94.5	**SmCP**	92.9[118.1][b,]	**K**
S16/B16-20/80	**I**	96.2	**SmCP**	92.4[135.2][b]	**K**
S16/B16-30/70	**I**	96.6	**SmCP**	91.5[129.7][b]	**K**
S16/B16-40/60	**I**	95.5	**SmCP**	90.3[123.2][b]	**K**
S16/B16-50/50	**I**	102.6[44.4]	**SmCP**	90.2[73.3]	**K**
S16/B16-60/40	**I**	100.4[43.7]	**SmCP**	87.8[86.3]	**K**
S16/B16-70/30	**I**	105.8[48.5]	**SmCP**	86.7[100.3]	**K**
S16/B16-80/20	**I**	106.5[48.1]	**SmCP**	86.5[96.5]	**K**
S16/B16-90/10	**I**	110.9[41.6]	**SmCP**	89.1[91.4]	**K**
B16	**I**	97.4[38.8]	**SmCP**	94.7[63.5]	**K**

Table S6.9. Phase Transition Temperatures and Enthalpies of complexes **S16/C12**

Compound		Phase transition temperature/°C [Enthalpy/kJ/g]					
C12	**I**	128.1[8.2]	**N**	—	**SmA**	96.2[157.2]	**K**
S16/C12-10/90	**I**	127.1[8.0]	**N**	—	**SmA**	89.0[85.7]	**K**
S16/C12-20/80	**I**	121.4[6.4]	**N**	—	**SmA**	79.2[81.3]	**K**
S16/C12-30/70	**I**	113.8[5.6]	**N**	—	**SmA**	79.6[73.6]	**K**
S16/C12-40/60	**I**	110.4[3.4]	**N**	93.9[3.6]	**SmCP**[a]	80.3[57.4]	**K**
S16/C12-50/50	**I**	103.8[1.1]	**N**	97.9[9.0]	**SmCP**[a]	74.7[58.0]	**K**
S16/C12-60/40	**I**	96.3[14.2]	**N**	—	**SmCP**[a]	70.7[44.2]	**K**
S16/C12-70/30	**I**	97.1[13.2]	**N**	—	**SmCP**	71.3[29.9]	**K**
S16/C12-80/20	**I**	107.0[21.2]	**N**	—	**SmCP**	81.6[47.6]	**K**
S16/C12-90/10	**I**	111.9[21.3]	**N**	—	**SmCP**	88.5[48.8]	**K**
S16	**I**	117.2[41.5]	**N**	—	**SmCP**	94.5[91.2]	**K**

Table S6.10. Powder XRD Data of doping components **An**, **Bn**, **C12**, and **Sm**

Compound	Phase	Miller index	d-spacing（Å）
A12	SmC	001	32.5
A16	SmC	001	40.9
B12	SmCP	001	42.3
B16	SmCP	001	52.7
C12	SmA	001	51.9
S12	SmCP	001	35.7
S16	SmCP	001	40.9

Reference

[1] (a) T. Niori, F. Sekine, J. Watanabe, T. Furukawa, H. Takezoe, J. Mater. Chem., 1996, 6, 1231. (b) T. Niori, F. Sekine, J. Watanabe, T. Furukawa, H. Takezoe, Mol. Cryst. Liq. Cryst., 1997, 301, 337. (c) F. Sekine, Y. Takanashi, T. Niori, H. Takezoe, Jpn. J. Appl. Phys., 1997, 36, 1201.

[2] M. W. Schroder, S. Diele, G. Pelzl, W. Weissflog, Chem. Phys. Chem., 2004, 5, 99.

[3] H. Takezoe, Y. Takanishi, Jpn. J. Appl. Phys., 2006, 45, 597.

[4] G. Pelzl, S. Diele, W. Weissflog, Adv. Mater., 1999, 11, 707.

[5] R. A.Reddy, C. Tschierske, J. Mater. Chem., 2006, 16, 907.

[6] D. Shen, S. Deiele, G. Pelzl, I. Wirth, C. Tschierske, J. Mater. Chem., 1999, 9, 661.

[7] D. Shen, A. Pegenau, S. Diele, I. Wirth, C. Tschierske, J. Am. Chem. Soc., 2000, 122, 1593.

[8] D.R. Link, G. Natale, R. Shao, J.E. Maclennan, N.A. Clark, E. Korblova, D.M. Walba. Science, 1997, 278, 1924.

[9] T. Sekine, Y. Takanishi, T. Niori, J. Watanabe, H. Takezoe, Jpn. J. Appl. Phys., 1997, 36, 1201.

[10] (a) S. W. Choi, J. Watanabe, H. Takezoe, Jpn. J. Appl. Phys., 1998, 37, 3408. (b) F. Kentischer, R. Macdonald, P. Warnick, G. Heppke, Liq. Cryst., 1998, 25, 341.

[11] T. Sekine, T. Niori, M. Sone, J. Watanabe, S. W. Choi, Y. Takanishi, H. Takezoe, Jpn. J. Appl. Phys., 1997, 36, 6455.

[12] (a) T. Sekine, T. Niori, J. Watanabe, T. Furukawa, S. W. Choi, H. Takezoe, J. Mater. Chem., 1997, 7, 1307. (b) J. W. Goodby, M. A. Waugh, S. M. Stein, E. Chin, R. Pindak, J. S. Patel, Nature, 1989, 337, 449.

[13] J. Thisayukta, Y. Nakayama, S. Kawauchi, H. Takezoe, J. Watanabe, J. Am. Chem. Soc., 2000, 122, 7441.

[14] (a) S. Diele, H. Grande, H. Kruth, Ch. Lischka, G. Pelzl, W. Weissflog, I. Wirth, Ferroelectrics, 1998, 212, 169. (b) H. Nadasi, W. Weissflog, A. Eremin, G. Pelzl, S. Diele, B. Das, S. Grande, J. Mater. Chem., 2002, 12, 1316.

[15] W. Weissflog, I. Wirth, S. Diele, G. Pelzl, H. Schmalfuss, T. Schoss and A. Wurflinger, Liq. Cryst., 2001, 28, 1603. (b) J. C. Rouillon, J. P. Marcerou, M. Laguerre, H. T. Nguyen, M. F. Achard, J. Mater. Chem., 2001, 11, 2946. (c) H. N. S. Murthy, B. K. Sadashiva, Liq. Cryst., 2002, 29, 1223.

[16] J. P. Bedel, J. C. Rouillon, J. P. Marcerou, M. Laguerre, H. T. Nguyen, M. F. Achard, J. Mater. Chem., 2002, 12, 2214.

[17] (a) G. Pelzl, S. Diele, A. Jakli, Ch. Lischka, I. Wirth, W. Weissflog, Liq. Cryst., 1999, 26 135. (b) C. K. Lee, A. Primak, A. Jakli, E. J. Choi, W. C. Zin, L. C.Chien, Liq. Cryst., 2001, 28, 1293. (c) R. A. Reddy, B. K. Sadashiva, Liq. Cryst., 2003, 30, 273. (d) H. N. S. Murthy, B. K. Sadashiva, Liq. Cryst., 2003, 30,1051. (e) G. Heppke, D. D. Parghi, H. Sawade, Liq. Cryst., 2000, 27, 313. (f) A. Jakli, Ch. Lischka, W. Weissflog, G. Pelzl, A. Saupe, Liq. Cryst., 2000, 27, 1405.

[18] D. A. Coleman, J. Fernsler, N. Chattham, M. Nakata, Y. Takanishi, E. Korblova, D. R. Link, R. F. Shao, W. G. Jang, J. E. Maclennan, O. Mondainn-Monval, C. Boyer, W. Weissflog, G. Pelzl, L. C. Chien, J. Zasadzinski, J. Watanabe, D. M. Walba, H. Takezoe, N. A. Clark, Science, 2003, 301, 1204.

[19] A. Eremin, S. Diele, G. Pelzl, H. Nadasi. W. Weissflog, Phys. Rev. E, 2003, 67, 21702.

[20] J. P. Bedel, J. C. Rouillon, J. P. Marcerou, M. Laguerre, H. T. Nguyen, M. F. Achard, Liq. Cryst., 2001, 28, 1285.

[21] C. Keith, R. A. Reddy, A. Hauser, U. Baumeister, C. Tschierske, J. Am. Chem. Soc., 2006, 128, 3051.

[22] K. Miyasato; S. Abe, H. Takazoe, A. Fukuda, E. Kuze. Jpn. J. Appl. Phys., 1983, 22, 661.

[23] I. C. Pintre, J. L. Serrano, M. B. Ros, J. Ortega, I. Alonso, J. M. Perdiguero, C. L. Folcia, J. Etxebarria, F. Goc, D. B. Amabilino, P. L. Josep G. N. Elba, Chem. Commun., 2008, 2523.

[24] D. M. Walba, E. Korblova, R. Shao, J. E. Maclennan, D. R. Link, M. A. Glaser, N. A. Clark, Science, 2000, 288, 2181.

[25] (a) G. Dantlgraber, D. Shen, S. Diele, C. Tschierske, Chem. Mater., 2002, 14, 1149. (b) C. Keith, R. A. Reddy, H. Hahn, H. Lang, C. Tschierske, Chem. Commun., 2004, 1898. (c) K. Kumazawa, M. Nakata, F. Araoka, Y. Takanishi, K. Ishikawa, J. Watanabe, H. Takezoe, J. Mater. Chem., 2004, 14, 157. (d) G. Pelzl, M. W. Schroder, U. Dunemann, S. Diele, W. Weissflog, C. Jones, D. Coleman, N. A. Clark, R. Stannarius, J. Li, B. Das, S. Grande. J. Mater. Chem., 2004, 14, 2492.

[26] (a) S. Kang, Y. Saito, N. Watanabe, M. Tokita, Y. Takanishi, H. Takezoe, J. Watanabe, J. Phys. Chem. B, 2006, 110, 5205. (b) S. K. Lee, Y. Naito, L. Shi, M. Tokita, H. Takezoe, J. Watanabe, Liquid Crystals, 2007, 34, 935. (c) S. K. Lee, L. Shi, M. Tokita, J. Watanabe, J. Phys. Chem. B, 2008, 112, 6762.

[27] (a) R. Amaranatha Reddy, B. K. Sadashiva, Liq. Cryst., 2003, 30, 1031. (b) H. T. Nguyen, J. C. Rouillon, J. P. Marcerou, J. P. Bedel, P. Barois, S. Sarmento, Mol. Cryst. Liq. Cryst., 1999, 328, 177. (c) R. Amaranatha Reddy, M. W. Schroder, M. Bodyagin, H. Kresse, S. Diele, G. Pelzl, W. Weissflog, Angew. Chem., Int. Ed., 2005, 44, 774. (d) H. N. Shreenivasa Murthy, B. K. Sadashiva, J. Mater. Chem., 2005, 15, 2056.

[28] (a) R. Amaranatha Reddy, B. K. Sadashiva, J. Mater. Chem., 2002, 12, 2627. (b) R. Amaranatha Reddy, V. A. Raghunathan, B. K. Sadashiva,Chem. Mater., 2005, 17, 274. (c) R. Amaranatha Reddy, B. K. Sadashiva, J. Mater. Chem., 2004, 14, 1936.

[29] (a) W. Weissflog, H. Nadasi, U. Dunemann, G. Pelzl, S. Diele, A. Eremin, H. Kresse, J. Mater. Chem., 2001, 11, 2748. (b) I. Dierking, H. Sawade, G. Heppke, Liq. Cryst., 2001, 28, 1767.

[30] P. Pyc, J. Mieczkowski, D. Pociecha, E. Gorecka, B. Donnio and D. Guillon, J. Mater. Chem., 2004, 14, 2374. (b) J. Szydlowska, J. Mieczkowski, J. Matraszek, D. W. Bruce, E. Gorecka, D. Pociecha and D. Guillon, Phys. Rev. E, 2003, 67, 031702. (c) J. Mieczkowski, J. Szydlowska, J. Matraszek, D. Pociecha,E. Gorecka, B. Donnio, D. Guillon, J. Mater. Chem., 2002, 12, 3392. (d) J. Mieczkowski, K. Gomola, J. Koseska, D. Pociecha,J. Szydlowska, E. Gorecka, J. Mater. Chem., 2003, 13, 2132.

[31] (a) G. Dantlgraber, S. Diele, C. Tschierske, Chem. Commun., 2002, 2768. (b) S. Umadevi, B. K. Sadashiva, H. N. S. Murthy, V. A. Raghunathan, Soft Matter, 2006, 2, 210. (c) B. Kosata, G. M. Tamba, U. Baumeister, K. Pelz, S. Diele, G. Pelzl, G. Galli,S. Samaritani, E. V. Agina, N. I. Boiko, V. P. Shibaev, W. Weissflog, Chem. Mater., 2006, 18, 691.

[32] (a) C. D. Keum, A. Kanazawa, T. Ikeda, Adv. Mater., 2001, 13, 321; (b) A. C. Sentman, D. L. Gin, Angew. Chem., Int. Ed., 2004, 42, 1815; (c) E. J. Choi, J. C. Ahn, L. C. Chien, C.K. Lee, W. C. Zin, D.C. Kim, S.T. Shin, Macromolecules, 2004, 37, 71. (d) J. Barbera, N. Gimeno, L. Monreal, R. Pinol, M. B. Ros, J. L. Serrano, J. Am. Chem. Soc., 2004, 126, 7190.

[33] (a) C. Keith, R. A. Reddy, C. Tschierske, Chem. Commun., 2005, 871. (b) X. F. Chen, K. K. Tenneti, C. Y. Li, Y. W. Bai, X. H. Wan, X. H. Fan, Q. F. Zhou, L.

Rong, B. S. Hsiao, Macromolecules, 2007, 40, 840. (c) E. J. Choi, J. C. Ahn, L. C. Chien, C. K. Lee, W. C. Zin, D. C. Kim, S. T. Shin, Macromolecules, 2004, 37, 71. (d) K. K. Tenneti, X. F. Chen, C. Y. Li, X. H. Wan, X. H. Fan, Q. F. Zhou, L. Rong, B. S. Hsiao, Macromolecules, 2007, 40, 5095.

[34] (a) D. Kardas, M. Prehm, U. Baumeister, D. Pociecha, R. A. Reddy, G. H. Mehl, C. Tschierske, J. Mater. Chem., 2005, 15, 1722. (b) H. Hahn, C. Keith, H. Lang, R. A. Reddy, C. Tschierske, Adv. Mater., 2006, 18, 2629. (c) G. Dantlgraber, U. Baumeister, S. Diele, H. Kresse, B. Luhmann, H. Lang, C. Tschierske, J. Am. Chem. Soc., 2002, 124, 14852. (d) Q. W. Pan, X. F. Chen, X. H. Fan, Z. H. Shen, Q. F. Zhou, J. Mater. Chem., 2008, 18, 3481.

[35] (a) C. Keith, G. Dantlgraber, R. A. Reddy, U. Baumeister, C. schierske, Chem. Mater., 2007, 19, 694. (b) C. Keith, R. A. Reddy, A. Hauser, U. Baumeister, C. Tschierske, J. Am. Chem. Soc. 2006, 128, 3051. (c) R. A. Reddy, U. Baumeister, C. Tschierske. Chem. Commun., 2009, 4236. (d) C. Keith, R. A. Reddy, A. Hauser, U. Baumeister, C. schierske, J. Am. Chem. Soc., 2006, 128, 3051.

[36] H. Nozary, C. Piguet, J. P. Rivera, P. Tissot, P. Y. Morgantini, J. Weber, G. Bernardinelli, J. C. G. Bunzli, R. Deschenaux, B. Donnio, D. Guillon, Chem. Mater., 2002, 14, 1075-1090.

[37] V. M. Marx, H. Girgis, P. A. Heiney, T. Hegmann, J. Mater. Chem., 2008, 18, 2983.

[38] (a) N. Gimeno, M. B. Ros, J. L. Serrano, M. R. Fuente. Angew. Chem. Int. Ed., 2004, 43, 5235. (b) J. Barbera, N. Gimeno, I. Pintre, M. B. Ros, J. L. Serrano. Chem. Commun., 2006, 1212. (c) N. Gimeno, M. B. Ros, J. L. Serrano, M. R. Fuente. Chem. Mater. 2008, 20, 1262. (d) A. perez, N. Gimeno, F. Vera, M. B. Ros, J. L. Serrano, M. R. Fuente, Eur. J. Org. Chem., 2008, 826.

[39] L. Y. Wang, I. H. Chiang, P. J. Yang, W. S. Li, I. T. Chao, H. C. Lin, J. Phys.

Chem. B (in Press).

[40] (a) O. Ikkala, G. T. Brinke, Science, 2002, 295, 2407. (b) S. I. Stupp, S. Son, H. C. Lin, L. S. Li, Science, 1993, 259, 59. (c) T. Kato, N. Mizoshita, K. Kishimoto, Angew. Chem. Int. Ed., 2006, 45, 38. (d) U. J. Kumar, M. J. Frechet, T. Kato, S. Ujiie, K. Iimura, Angew. Chem. Int. Ed., 1992, 31, 1531. (e) S. Tsonchev, K. L. Niece, G. C. Schatz, M. A. Ratner, S. I. Stupp, J. Phys. Chem. B, 2008, 112, 441. (f) Y. R. Velichko, S. I. Stupp, M. O. Cruz, J. Phys. Chem. B, 2008, 112, 2326.

[41] (a) H. Hofmeier, U. S. Schubert, Chem. Commun., 2005, 2423. (b) J. M. Pollino, M. Weck, Chem. Soc. Rev., 2005, 34, 193. (c) B. Moulton, M. J. Zaworotko, Chem. Rev., 2001, 101, 1629. (d) T. Kato, T. Matsuoka, M. Nishii, Y. Kamikawa, K. Kanie, T. Nishimura, E. Yashima, S. Ujiie, Angew. Chem. Int. Ed., 2004, 43, 1969.

[42] (a) M. Nakata, R. F. Shao, J. E. Maclennan, W. Weissflog, N. A. Clark, Phys. Rev. Lett., 2006, 96, 067802. (b) M. Rickard, M. Nakata, H. Takezoe, J. Watanabe, N. A. Clark, Phys. Rev. Lett., 2005, 87, 261115. (c) R. B. Meyer, L. Liebert, L. Strzelecki, P. J. Keller, Phys. (Paris) Lett., 1975, 36, 69. (d) A. D. L. Chandani, Y. Ouchi, H. Takezoe, A. Fukuda, K. Terashima, K. Furukawa, A. Kishi, Jpn. J. Appl. Phys., 1989, 28, 1261. (e) A. Fukuda, Y. Takanishi, T. Isokaki, K. Ishikawa, H. Takezoe, J. Mater. Chem., 1994, 4, 997.

[43] (a) S. Kang, Y. Saito, N. Watanabe, M. Tokita, Y. Takanishi, H. Takezoe, J. Watanabe, J. Phys. Chem. B, 2006, 110, 5205. (b) D. Pociecha, K. Ohta, A. Januszko, P. Kaszynski, Y. Endo, J. Mater. Chem., 2008, 18, 2978. (c) S. K. Lee, S. Heo, J. G. Lee, K. T. Kang, K. Kumazawa, K. Nishida, Y. Shimbo. Y. Takanishi, J. Watanabe, T. Doi, T. Takahashi, H. Takazoe, J. Am. Chem. Soc., 2005, 127, 11085. (d) R. A. Reddy, G. Dantlgraber, U. Baumeister, C. Tschierske, Angew. Chem. Int. Ed., 2006, 45, 1. (e) U. M. Dunemann, W. Schroder, R. A.

Reddy, G. Pelzl, S. Diele, W. Weissflog, J. Mater. Chem. 2005, 15, 4051. (f) R. A.
Reddy, B. K. Sadashiva, V. A. Raghunathan, Chem. Mater., 2004, 16, 4050. (g) P.
J. Yang, H. C.Lin, Liq. Cryst., 2006, 33, 587.

[44] (a) C. V. Yelamaggad, I. S. Shashikala, Q. Li, Chem. Mater., 2007, 19, 6561. (b)
P. Kumar, U. S. Hiremath, C. V. Yelamaggad, A. G. Rossberg, K. S.
Krishnamurthy, J. Phys. Chem. B, 2008, 112, 9270. (c) P. Kumar, Y. G. Marinov,
H. P. Hinov, U. S. Hiremath, C. V. Yelamaggad, K. S. Krishnamurthy, A. G.
Petrov, J. Phys. Chem. B, 2009, 113, 9168.

[45] (a) C. Keith, R. A. Reddy, U. Baumeister, H. Hahn, H. Lang, C. Tschierske, J.
Mater. Chem., 2006, 16, 3444. (b) G. Dantlgraber, A. Eremin, S. Diele, A. Hauser,
H. Kresse, G. Pelzl, C. Tschierske, C. Angew. Chem. Int. Ed., 2002, 41, 2408. (c)
R. A. Reddy, U. Baumeister, C. Keith, C. Tschierske, J. Mater. Chem., 2007, 17,
62.

[46] (a) M. Sepelj, A. Lesac, U. Baumeister, S. Diele, D. W. Bruce, Z. Hamersak,
Chem. Mater., 2006, 18, 2050. (b) M. G. Tamba, B. Kosata, K. Pelz, S. Diele, G.
Pelzl, Z. Vakhovskaya, H. Kresse, W. Weissflog, Soft Matter, 2006, 2, 60.

[47] M. B. Ros, J. L. Serrano, M. R. de la Fuente, C. L. Folcia, J. Mater. Chem. 2005,
15, 5093.

[48] P. J. Martin, D. W. Bruce, Liq. Cryst., 2007, 6, 767.

[49] (a) F. Mohamandi, N. G. J. Richards, W. C. Guida, R. Liskamp, M. Liption, C.
Caufield, G. Chang, T. Hendrickson, W. C. Still, J. Comput. Chem., 1990, 11,
400. (b) S. J. Weiner, P. A. Kollman, D. A. Case, U. C. Singh, C. Chio, G.
Alagona, S. Profeta, P. J. Weiner, Am. Chem. Soc., 1984, 106, 765. (c) S. J.
Weiner, P. A. Kollman, D. A. Case, J. Comput. Chem., 1986, 7, 230. (d) W. C.
Still, A. Tempczyk, R. C. Hawley, T. Hendrickson, J. Am. Chem. Soc., 1990, 112,
6127.

[50] M. J. Frisch, G. W. Trucks, H. B. Schlegel, G. E. Scuseria, M. A. Robb, J. R. Cheeseman, J. A. Montgomery, T. Jr. Vreven, K. N. Kudin, J. C. Burant, J. M. Millam, S. S. Iyengar, J. Tomasi, V. Barone, B. Mennucci, M. Cossi, G. Scalmani, N. Rega, G. A. Petersson, H. Nakatsuji, M. Hada, M. Ehara, K. Toyota, R. Fukuda, J. Hasegawa, M. Ishida, T. Nakajima, Y. Honda, O. Kitao, H. Nakai, M. Klene, X. Li, J. E. Knox, H. P. Hratchian, J. B. Cross, V Bakken, C. Adamo, J. Jaramillo, R. omperts, R. E. Stratmann, O. Yazyev, A. J. Austin, Cammi, R. C. Pomelli, J. W. Ochterski, P. Y. Ayala, K. Morokuma, G. A. Voth, P. Salvador, J. J. Dannenberg, V. G. Zakrzewski, S. Dapprich, A. D. Daniels, M. C. Strain, O. Farkas, D. K. Malick, A. D. Rabuck, K. Raghavachari, J. B. Foresman, J. V. Ortiz, Q. Cui, A. G. Baboul, S. Clifford, J. Cioslowski, B. B. Stefanov, G. Liu, A. Liashenko, P. Piskorz, I. Komaromi, R. L. Martin, D. J. Fox, Keith, T.; M. A. Al-Laham, C. Y. Peng, A. Nanayakkara, M. Challacombe, P. M. W. Gill, B. Johnson, W. Chen, M. W. Wong, C. Gonzalez, J. A. Pople, Gaussian 03, Revision D.02, Gaussian, Inc., Wallingford CT, 2004.

[51] C. Cativiela, J. L. Serrano, M. M. Zurbano, J. Org. Chem., 1995, 60, 3074.

[52] H. Dehne, M. Potter, S. Sokolowski, W. Weissflog, S. Diele, G. Pelzl, I. Wirth, H. Kresse, H. Schmalfuss, S. Grande. Liq. Cryst. 2001, 28, 1269.

[53] (a) C. W. Wu, H. C. Lin, Macromolecules, 2006, 39, 7985. (b) H. C. Lin, H. Y. Sheu, C. L. Chang, C. Tsai, J. Mater. Chem., 2001, 11, 2958.

[54] (a) V. Prasad, S. W. Kang, S. Kumar, J. Mater. Chem., 2003, 13, 1259. (b) H. N. S. Murthy, B. K. Sadashiva, Liq. Cryst., 2004, 31, 1337.

[55] M. Zenyoji, Y. Takanishi, K. Ishikawa, J. Thisayukta, H. Watanabe, J. Takezoe, J. Mater. Chem., 1999, 9, 2775.

[56] (a) J. Mieczkowski, K. Gomola, J. Koseska, D. Pociecha, J. Szydlowska, E. Gorecka. J. Mater. Chem., 2003, 13, 2132. (b) E. Gorecka, N. Vaupotic, D.

Pociecha, M. Cepic, J. Mieczkowski, J. Chem. Phys. Chem., 2005, 6, 1087. (c) K. Pelz, W. Weissflog, U. Baumeister and S. Diele, Liq. Cryst., 2003, 30, 1151.

[57] (a) E. Gorecka, D. Pociecha, F. Araoka, D. R. Link, M. Nakata, J. Y. Thisayukta, Takanishi, K. Ishikawa, J. Watanabe, H. Takezoe, Phys. Rev. E 2000, 62, 4524. (b) M. Nakata, D. R. Link, J. Thisayukta, Y. Takanishi, K. Ishikawa, J. Watanabe, H. Takezoe, J. Mater. Chem., 2001, 11, 2694.

[58] I. Cacelli, G. Prampolini, Chem. Phys., 2005, 314, 283.

[59] X. Chen, K. K. Tenneti, C. Y. Li, Y. Bai, R. Zhou, X. Wan, X. Fan, Q. F. Zhou, Macromolecules, 2006, 39, 517.

[60] E. B., Barmatov, A. Y. Bobrovsky, D. A. Pebalk, M. V. Barmatova, V. P. Shibaev, J. Polym. Sci. Part A: Polym. Chem., 1999, 37, 3215.

[61] H. Takezoe, Y. Takanishi, Jpn J Appl Phys, 2006, 597.

[62] S. Anand, R. Krishnan, W. Weissflog, G. Pelzl, S. Diele, H. Kresse, Z. Vakhovskaya, R. Friedemann, Phys. Chem. Chem. Phys., 2006, 8, 1170.

[63] G. Pelzl, M. G. Tamba, F. T. Sonja, M. W. Schroder, U. Baumeister, S. Diele, W. Weissflog, J. Mater. Chem., 2008, 18, 3017.

[64] K. K. Tenneti, X. F. Chen, C. Y. Li, Z. H. Shen, X. H. Wan, X. H. Fan, Q. F. Zhou, L. Rong, B. S. Hsiao, Macromolecules, 2009, 42, 3510.

[65] (a) G. Nair, C. A. G. Bailey, S. Taushanoff, F. C. A. KatalinVajda, Z. Varga, A. Bota, A. Jakli, Adv. Mater., 2008, 20, 3138. (b) K. Kishikawa, N. Muramatsu, S. Kohmoto, K. Yamaguchi, M. Yamamoto, Chem. Mater., 2003, 15, 3443.

[66] (a) J. H. Liu, H. J. Hung, P. C. Yang, K. H. Tien, J. Polym. Sci. Part A Polym. Chem., 2008, 46, 6124. (b) J. H. Liu, P. C. Yang, Y. H. Chiu, Y. Suda, J. Polym. Sci. Part A Polym. Chem., 2007, 45, 2026. (c) L. C. Gao, X. H. Fan, Z. H. Shen, X. F. Chen, Q. F. Zhou, J. Polym. Sci. Part A Polym. Chem., 2009, 47, 319. (d) M. J. Lee, H. N. Ji, Y. K. Han, J. Polym. Sci. Part A Polym. Chem., 2008, 46, 6734. (e)

V. Shibaev, A. Medvedev, A. Bobrovsky, J. Polym. Sci. Part A Polym. Chem., 2008, 46, 6532. (f) L. C. Gao, Q. W. Pan, C. Wang, Y. Yi, X. F. Chen, X. H. Fan, Q. F. Zhou, J. Polym. Sci. Part A Polym. Chem., 2007, 45, 5949.

[67] F. Vera, C. Almuzara, I. Orera, J. Barbera, L. Oriol, J. L. Serrano, T. Sierra, J. Polym. Sci. Part A Polym. Chem. 2008, 46, 5528.

[68] (a) J. Thisayukta, Y. Nakayama, S. Kawauchi, H. Takezoe, J. Watanabe, J. Am. Chem. Soc. 2000, 122, 7441. (b) I.I. Smalyukh, R. Pratibha, N. V. Madhusudana, O.D. Lavrentovich, Eur. Phys. J. E, 2005, 16, 179. (c) J. Thisayukta, H. Niwano, H. Takezoe, J. Watanabe, J. Am. Chem. Soc. 2000, 122, 3354. (d) J. Thisayukta, H. Niwano, H. Takezoe, J. Watanabe, J. Mater. Chem., 2001, 11, 2717. (e) M. R. Dodge, R. G. Petschek, C. Rosenblatt, Physical Review E, 2003, 68, 031703.

Introduction to the Author

學經歷資料

- 姓名：王怜詠 (Ling-Yung Wang)
- 性別：男
- 生日：1981 年 08 月 02 號
- 電子郵件信箱：wevily@gmail.com
- 聯絡電話：(家) 06-2337879　(手機) 0928-769958
- 聯絡地址：台南縣永康市中正路 155 巷 10 弄 19 號

學歷

博士：國立交通大學材料科學與工程學系	2005.9 ~ 2009.11
碩士：國立暨南國際大學應用化學系	2003.9 ~ 2005.6
學士：國立暨南國際大學應用化學系	1999.9 ~ 2003.6

論文發表

期刊論文(博)

1. Ling-Yung Wang, I-Hung Chiang, Po-Jen Yang, Wan-Sheung Li, I-To Chao, and Hong-Cheu Lin, "Configuration Effects of H-Bonded Sites and Rigid Core Lengths on H-Bonded Banana-Shaped Liquid Crystalline Supramolecules Consisting of Symmetric Trimers /and Asymmetric Heterodimers", Journal of Physical Chemistry B, 2009, 113, 14648.

2. Ling-Yung Wang, Chieh-Yin Tang, and Hong-Cheu Lin, "Polymeric Dopant Effects of Bent-Core Covalent- and Hydrogen-Bonded Structures on Banana-Shaped Liquid Crystalline Complexes", Journal of Polymer Science Part A: Polymer Chemistry, 2009, (Accepted).

3. Hong-Cheu Lin, Ling-Yung Wang, Shin-Yi Tsai, Szu-Fen Chen, and Chi-Neng Mo, "Improvement of Fast Responsive LC Materials by Bent-Core Dopants in Optical Compensated Bend (OCB) Mode Liquid Crystal Displays" Journal of the Chinese Institute of Engineers, 2009, (Accepted).

4. Ling-Yung Wang, Hsin-Yi Tsai, and Hong-Cheu Lin. "Novel Supramolecular Side-Chain Banana-Shaped Liquid Crystalline Polymers Containing Covalent- and Hydrogen-Bonded Bent-Cores", Macromolecules (To be Submitted).

5. Ling-Yung Wang, Jing-Yuan Chiou and Hong-Cheu Lin, "H-Bonded Banana-Shaped Liquid Crystalline Dimeric Complexes and Main-Chain Polymers Containing Bent-Core Pyridyl Acceptors and Siloxane Diacid Donors", Chemistry

Materials (To be Submitted).

6. <u>Ling-Yung Wang</u>, I-Hung Chiang and Hong-Cheu Lin, "Dopant Effect of Covalent Structures on H-bonded Banana-shaped Liquid Crystals", (To be Submitted).

國際研討會論文發表

1. <u>Ling-Yung Wang</u>, Shin-Yi Tsai, Szu-Fen Chen, Chi-Neng Mo, and Hong-Cheu Lin, "Improvement of Fast Response LC Materials by Bent-Core Dopants in Optical Compensated Bend (OCB) Mode Liquid Crystal Displays" Society for Information Display, 2008, session 5.4 (Oral).